Architectures multi-photochromiques : structures et fonctions

Agostino Galanti

UNIVERSITÉ DE STRASBOURG

ÉCOLE DOCTORALE DES SCIENCES CHIMIQUES

UMR 7006 – Institut de Science et d'Ingénierie Supramoléculaires (I.S.I.S)

THÈSE

présentée par :

Agostino GALANTI

soutenue le : **4 Décembre 2018**

pour obtenir le grade de : **Docteur de l'université de Strasbourg**

Discipline/ Spécialité : Chimie / Chimie physique

Multi-Photochromic Architectures: from Structure to Function

THÈSE dirigée par :

M. SAMORÌ Paolo	Professeur, Université de Strasbourg

RAPPORTEURS :

M. DE FEYTER Steven	Professeur, Katholieke Universiteit Leuven
M. MONTALTI Marco	Professeur, Università di Bologna

AUTRES MEMBRES DU JURY :

M. HERMANS Thomas	Maître de conférences, Université de Strasbourg

Resumé

L'objectif de cette thèse a été axé sur le développement des systèmes capable de répondre à des stimuli externes, basés sur des unités photochromiques. Au cours des dernières décennies, d'énormes progrès ont été effectués quant à la réalisation des systèmes synthétiques contenant des interrupteurs moléculaires contrôlables à distance, notamment en utilisant préférentiellement la lumière comme stimulus. Le but d'une telle quête est d'augmenter la complexité des dispositifs et des machines moléculaires synthétiques, dans l'objectif ultime d'imiter les processus naturels.[1] Par ailleurs, du point de vue technologique, il est très attractif d'obtenir des matériaux ou des complexes *host-guest* capables de modifier leurs propriétés macroscopiques (par ex. changement de morphologie, ou capture/relargage d'un *guest*) ou de stocker des informations utilisant des photons comme stimulus. Les familles d'unités photochromiques employées les plus souvent comprennent les azobenzènes, les diaryléthènes et les spiropyranes, qui typiquement sont des interrupteurs moléculaires binaires, modulables par irradiation lumineuse entre deux états (méta) stable. Afin d'amplifier l'effet via le changement des propriétés physicochimiques de tels interrupteurs moléculaires, il est généralement convenable de les combiner avec d'autres unités fonctionnelles, soit moléculaires ou bien avec des nanomatériaux. Ce faisant, il a été démontré qu'il est possible d'obtenir des dispositifs électroniques de mémoire,[2] ou d'observer des propriétés émergentes dans des systèmes hybrides plasmoniques-moléculaires[3] avec des stimuli lumineux. Avec l'objectif de développer des dispositifs et des machines artificiels de plus en plus complexes, un intérêt croissant est consacré à la réalisation de systèmes comprenant de multiples interrupteurs moléculaires dont le comportement est indépendant de l'état des unités voisines.[4] La synthèse d'unités multi-photochromiques présente un intérêt particulier, car en principe il pourrait permettre de réaliser un système commutable entre 2^n états (où n est égal au nombre de photochromes actifs, s'ils sont différenciables). En vue de la

réalisation de cette thèse, des nouveaux systèmes multi-photochromiques, où hybrides photochrome/nanomatériaux contenant des fragments azobenzène, diaryléthène ou spiropyrane ont été réalisés et étudiés.

La première partie du travail expérimental effectué dans ce cadre porte sur l'étude de nouveaux dérivés photochromiques à base d'azobenzènes contenant jusqu'à trois interrupteurs dans la même molécule. Les composés ont été réalisés en collaboration avec le groupe du Prof. M. Mayor (*Karlsruher Institut für Technologie*), synthétisés par J. Santoro and Dr. M. Valášek. De telles molécules ont été réalisées comme composants de base pour la génération de matériaux sensibles à la lumière, utilisables pour le stockage, tels que des polymères de coordination et des réseaux moléculaires covalents 2D et 3D, pour ainsi étudier leur auto-assemblage dans des réseaux formés via des liaisons hydrogène.[5]

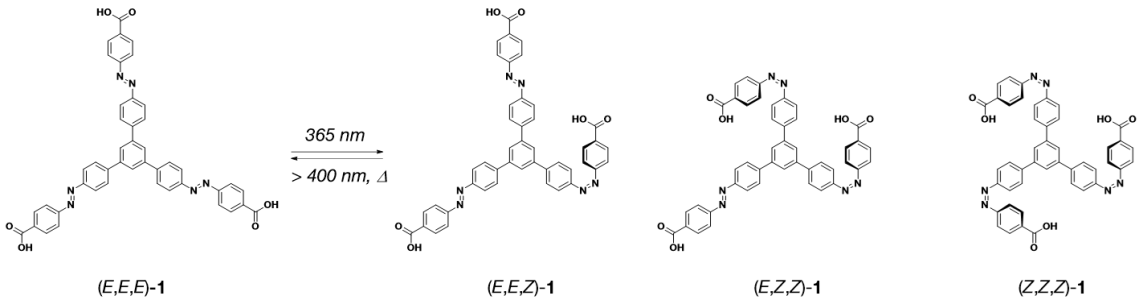

Figure 1. Isomérisation du tris(azobenzène) **1**.

Les édifices moléculaires étudiés ici sont constitués de noyaux « *star-shaped* » rigides, leur géométrie étant dictée par la présence d'une squelette aromatique et par des unités photochromiques se ramifiant à partir d'un cycle benzène central 1,3,5-trisubstitué. Un tel motif de substitution places les bras réciproquement en position *méta*, abaissant ainsi la conjugaison de ces systèmes multi-chromophoriques. Ce projet est motivé par l'étude du multi-photochromisme de tels systèmes, de ce fait une caractérisation détaillée des multiples états isomériques a été effectuée. Le multi-photochromisme du dérivé tris(azobenzène) **1** a été étudié par comparaison avec des composés bis(azobenzène) et mono(azobenzène) présentant une géométrie et une rigidité similaire, en utilisant plusieurs techniques analytiques, comprenant la séparation par chromatographie de

chaque état et leur caractérisation par spectrométrie de masse à mobilité ionique. Les composés modèles bis(azobenzène) et mono(azobenzène) ont été réalisés en substituant progressivement le groupe diazene-1,2-diyl par des unités ethyn-1,2-diyl, donnant ainsi des branches similaires en géométrie et dimension, mais non photosensibles. L'auto-assemblage du dérivé tris(azobenzène) **1** en réseaux bidimensionnels a été étudié par microscopie à effet tunnel (STM), corroborée par la modélisation moléculaire (cette dernière a été effectuée en collaboration avec le groupe du Prof. J. Cornil, Université de Mons). L'exploration de l'auto-assemblage dynamique de tels systèmes en architectures supramoléculaires ordonnées a permis d'identifier des motifs résultant de multiples isomères, démontrant ainsi que le multi-photochromisme est conservé lorsque les molécules sont confinées en deux dimensions.

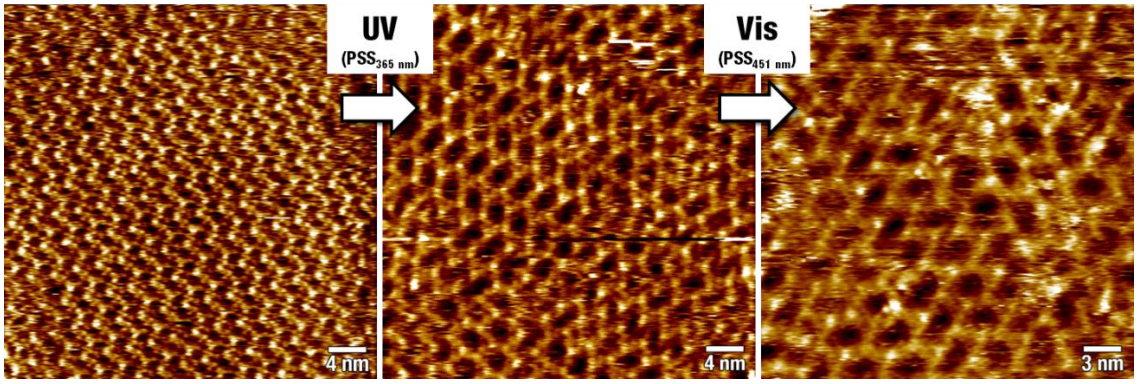

Figure 2. Images STM de **1** enregistrées à l'interface entre un substrat de graphite (HOPG) et une solution (c = 10 µM) de **1** en acide 1- heptanoïque. *À gauche*, pas de rayonnement lumineux. *Centre*, irradiation *in-situ* avec lumière UV à l'état photostationnaire (PSS, λ_{max} = 367 nm). *À droite*, irradiation ultérieure *in-situ* avec lumière visible (PSS, λ_{max} = 451 nm).

Le deuxième système étudié dans ce travail est basé sur des systèmes contenant plusieurs diaryléthènes. Les édifices moléculaires présentés ici sont basés sur une architecture de type dyade contenant un noyau fluorescent et symétrique constitué par une porphyrine et quatre diaryléthènes. Ces diaryléthènes sont, plus précisément, des dithyénylethènes pontés par un groupement perfluorocyclopentène (DTE) dans sa périphérie. Les composés décrits ci-dessus ont été designés et synthétisés par l'équipe de Prof. J. Weiss (Université de Strasbourg), par Dr. T. Biellmann. Ces systèmes ont été conçus pour exploiter la porphyrine centrale à la fois comme échafaudage symétrique pour les photochromes ainsi que pour ses propriétés photophysiques attractives. Les unités DTE employés sont

connectées à la position *méta* d'un noyau de tétraphénylporphyrine : une telle connectivité a été choisie non seulement pour empêcher la formation d'atropoisomères, mais surtout pour découpler électroniquement les interrupteurs moléculaires afin de conserver leur photoréactivité. Quatre porphyrines tétra-substituées par unités DTE **2** ont été étudiées, la base libre et les complexes de Zn(II), Ni(II) et Co(II). La conversion photochimique efficace et réversible des quatre dérivés du système **2** a été démontrée par spectroscopie d'absorption UV-Vis et ^{1}H-RMN (cette dernière a été faite en collaboration avec l'équipe de Prof. V. Guerchais, Université de Rennes I). Il est intéressant de noter que la base libre et le complexe de zinc ayant toutes les unités DTE sous forme ouverte présente des propriétés photophysiques similaires à celles de leurs analogues non photochromiques : la tétraphénylporphyrine base libre et le complexe de zinc. A l'inverse, la conversion photochimique déclenchée par les UV des unités DTE en leurs isomères fermés correspondant apporte une annihilation presque complète de l'émission initiale des fluorophores.

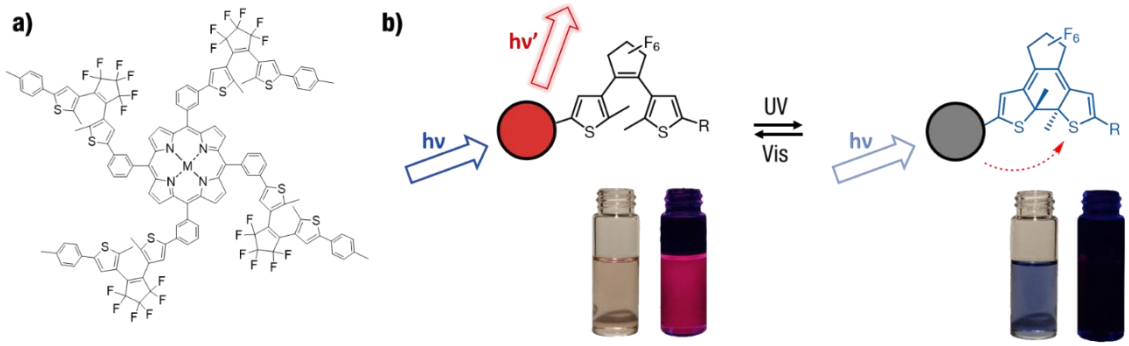

Figure 3. a) Formule de structure des dérivés de porphyrine **2** tétra-substitués avec unités DTE étudiés. M = H_2, Zn(II) montrent une émission commutable réversible. b) Schéma simplifié de l'extinction des émissions par transfert d'énergie vers l'isomère fermé de l'unité DTE. *Gauche*, DTE-ouvert : fluorescence ON. *Droite*, DTE-fermé : fluorescence OFF.

La luminescence peut être commuté dans un état ON et un état OFF de façon réversible sur plusieurs cycles d'irradiation, tant en solution que dans les couches minces dopées par **2**, ce qui nous a permis de démontrer que ces composés pouvaient être utilisés comme colorants fluorescents photo-réinscriptibles. Il est important de souligner que la detection de la fluorescence de ces composés peut être effectuée sans modifier l'état des commutateurs modulant la fluorescence. Le contraste élevé obtenu dans la modulation de

fluorescence est dû à la présence d'un grand nombre (à savoir quatre) d'interrupteurs autour du noyau émissif.

Dans le dernier chapitre expérimental, l'accent a été mis sur les systèmes hybrides constitués de jonctions de spiropyranes photosensibles avec des nanoparticules plasmoniques, à savoir des nanorods d'or (AuNR). Une telle combinaison a été choisie afin d'étudier la variation des propriétés optiques des nanoparticules anisotropes et de vérifier un éventuel effet sur la stabilité de la dispersion colloïdale lors de l'isomérisation de l'unité photochromique. Les interrupteurs moléculaires utilisés ici ont été immobilisés sur la surface des AuNR en exploitant la chimie des thiols. Le dérivé de spiropyrane ponté par le dodécanethiol utilisé dans cette étude a été synthétisé dans le groupe du Prof. S. Hecht (*Humboldt-Universität zu Berlin*), par J. Boelke et B. Zyska. Les unités spiropyranes ont été choisies suite à la variation importante de leur moment dipolaire lors de l'isomérisation de la forme spiropyrane (SP) vers l'isomère mérocyanine (MC).[6] L'une des propriétés les plus attrayantes des AuNR est liée à leurs propriétés optiques: possédant non seulement une bande de résonance plasmonique de surface (SPR) dans la gamme de la lumière visible ($\lambda \approx 520$ nm) commune à tous les colloïdes d'or, ils sont également caractérisés par un second mode SPR aux énergies inférieures (nommé *longitudinal SPR*, LSPR). Ce dernier est généralement une bande fine et intense, et sa longueur d'onde maximale peut être ajustée du visible au proche infrarouge du spectre électromagnétique en faisant varier le rapport entre la longueur et le diamètre des nanoparticules anisotropes. Les propriétés spectrales des nanoparticules plasmoniques sont très sensibles à la variation de leur environnement diélectrique, en particulier celles présentant des propriétés anisotropes telles que AuNR.[7] Nous avons utilisé des méthodes présentes dans la littérature pour synthétiser des dispersions colloïdales d'AuNR stabilisées par des tensioactifs avec différents rapports longueur et diamètre, sélectionnés sur la base du recouvrement spectral de leur mode LSPR avec la bande d'absorption de la forme MC à anneau ouvert de l'unité photochromique. Cela a été fait afin de vérifier l'apparition de propriétés émergentes sur le système hybride réalisé en couplant les AuNR au photochrome une fois immobilisé sur ses surfaces. Les interrupteurs moléculaires à terminaison thiol ont également été utilisés dans le but de stabiliser la dispersion colloïdale dans des solvants organiques.

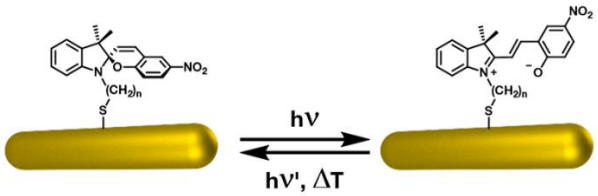

Figure 4. Représentation schématique de l'isomérisation du dérivé de spiropyrane à terminaison thiolate **3**.

La fonctionnalisation des nanoparticules anisotropes (AuNR) a été réalisée en substituant le tensioactif stabilisant le colloïde après sa synthèse avec la chemisorption du thiol fonctionnel à la surface des AuNR, en veillant particulièrement à éviter la variation de la morphologie des nanoparticules après cette étape. Le photochromisme des systèmes hybrides a été étudié en dispersion colloïdale par spectroscopie d'absorption UV-Vis, où aucune agrégation évidente du colloïde induite par la lumière n'était évidente. Néanmoins, une variation évidente dans les spectres d'extinction dépendante de la longueur d'onde du mode LSPR et du recouvrement spectrale avec MC a été observée lors d'une irradiation UV. Afin de mieux caractériser notre système hybride et d'obtenir une compréhension plus détaillée du comportement de l'unité photochromique une fois immobilisée sur les nanoparticules plasmoniques, nous avons réalisé une étude spectroscopique sur les particules sur support solide par diffusion de la lumière en champ sombre et par spectroscopie Raman, en collaboration avec Prof. H. Uji-i and Dr. S. Toyouchi (*Katholieke Universiteit Leuven*). L'isomérisation du SP sur AuNR a pu être étudiée grâce aux grands facteurs d'amplification Raman présentés par ces nanomatériaux, suivant l'empreinte vibrationnelle de SP et MC par *surface-enhanced Raman scattering* (SERS). Néanmoins, les preuves spectroscopiques obtenues montrent que le thiol photochromique n'est pas capable de s'isomériser lorsqu'il est immobilisé à la surface du colloïde d'or, étant alors uniquement présent sous la forme MC (photochromisme négatif). Nous attribuons cette défaillance à la fois à la très faible distance de l'interrupteur moléculaire à la surface des nanoparticules et à leur encombrement dans la monocouche auto-assemblée, cette dernière conduisant très probablement à la stabilisation de la forme MC.

Dans le but de développer de nouveaux systèmes sensibles aux stimuli, nous avons présenté ici trois exemples de systèmes optiquement commutables basés sur des blocs photochromiques. L'ingénierie de dispositifs constitués par la combinaison de commutateurs moléculaires avec des unités fonctionnelles organiques et des

nanostructures est très attractive, car elle permet de contrôler à distance une propriété physico-chimique sélectionnée, sans accumulation de déchets. Dans ce cadre, nous avons utilisé ici trois familles différentes d'unités photochromiques, en fonction de la propriété du système que nous voulions faire varier par des stimuli optiques.

Dans le premier cas, l'azobenzène était l'unité de choix, après son changement de forme important lors de la conversion de l'isomère *E* en isomère *Z* déclenché par la lumière ultraviolette. En intégrant de multiples unités azobenzéniques dans des édifices moléculaires pseudo-planaires en forme d'étoile, nous avons montré qu'il est possible de réaliser des molécules rigides relativement petites ayant des unités photochromiques efficaces et totalement indépendantes en les connectant simplement en position *méta* sur un noyau benzénique trisubstitué. Ces molécules présentent à l'état photostationnaire de multiples isomères, du fait de la présence de trois commutateurs au maximum dans la même structure, chaque espèce étant isolée et entièrement caractérisée par chromatographie liquide et spectrométrie de masse à mobilité ionique. Ces systèmes sont capables de subir de grands réarrangements géométriques lors de la photoisomérisation, preuve corroborée par microscopie à effet tunnel, ce qui prouve que l'assemblage de différents isomères (générés par des stimuli lumineux) à l'interface solide-liquide produit des assemblages cristallins 2D à liaisons hydrogène avec une morphologie sensiblement différente. Nous prévoyons que de tels composés multi-azobenzéniques pourraient être utilisés à l'avenir comme éléments constitutifs des matériaux *host-guest* ou *metal-organic frameworks* contrôlables par des stimuli lumineux.

Dans un second exemple, des commutateurs photochromiques de type dithiényléthène (DTE) ont été utilisés pour déclencher l'émission d'un fluorophore organique. Cela a été possible en exploitant l'important changement survenant sur le système π-électronique lors de l'isomérisation entre la forme ouverte et la forme fermée du DTE, accompagnée de l'altération de ses niveaux électroniques. De cette manière, le noyau émissif, à savoir la base libre ou la tétraphénylporphyrine de zinc (II), n'est pas perturbé lorsque les unités DTE résident dans la forme ouverte. A l'inverse, le transfert d'énergie se produit en présence de la forme fermée, résultant en l'annihilation de la fluorescence. La dyade formée par le noyau porphyrine lié par liaisons covalentes à quatre unités DTE a montré une modulation réversible de son émission par irradiation ultraviolette et visible, affichant un contraste particulièrement élevé dû à la présence de plusieurs agents capables d'annihiler l'émission autour du cœur émissif lorsque les unités

DTE sont commutées en la forme fermée. La possibilité de moduler la fluorescence et de la détecter à des longueurs d'ondes très distinctes, même lorsqu'ils sont dispersés dans une matrice polymère et déposés en tant que films minces, rends de tels dérivés particulièrement intéressants pour leurs applications dans le stockage de mémoire optique et l'imagerie par microscopie à fluorescence.

Comme dernier exemple, un dérivé de spiropyrane a été utilisé comme unité photosensible en raison de la variation considérable du moment dipolaire électrique de ses deux isomères: le spiropyrane et la mérocyanine. Un tel interrupteur moléculaire activé par la lumière a été combiné avec des nanoparticules d'or anisotropes (nanorods d'or, AuNR), exploitant la correspondance de leurs bandes de résonance plasmoniques de surface et la grande sensibilité de ces dernières à la variation de leur milieu diélectrique. Différents AuNR avec des proportions variables ont été utilisés afin d'étudier l'effet du recouvrement spectral entre les spectres d'absorption et d'émission des mérocyanines et les bandes de résonance de plasmon de surface des nanomatériaux. En induisant l'isomérisation de l'interrupteur moléculaire dans les dispersions colloïdales AuNR en liquide, nous avons visualisé une grande variation du spectre d'extinction des colloïdes, dépendante de la longueur d'onde du mode LSPR et du recouvrement spectrale avec le *photoswitch*. Néanmoins, l'utilisation de la technique SERS a montré que l'isomérisation du commutateur moléculaire n'était pas possible à la surface des nanomatériaux, ce qui montre à quel point la réalisation de systèmes hybrides capables de répondre à des stimuli lumineux est difficile.

Abstract

The work described within the present thesis is centred on the development of stimuli-responsive systems based on photochromic units. During the course of the last decades, enormous progress has been made in the realisation of remotely addressable, switchable synthetic systems, with a special interest in using light as an input. The scope of such a quest is to obtain molecular devices and machines of increasing complexity with the ultimate goal of mimicking natural processes.[1] Moreover, from the technological point of view it is highly appealing to obtain materials or host-guest complexes capable of varying their macroscopic properties (*e.g.* morphology change, guest uptake/release), or to store information using photons as a remote control. The most widely employed families of photochromic compounds include azobenzene, diarylethenes and spiropyran derivatives, and typically are binary switches, being interconvertible between two states with a photochemical reaction. In order to exploit and/or to amplify the effect of different physicochemical properties of such molecular switches, it is generally suitable to combine them with other molecular functional units, or alternatively with nanomaterials. By doing so, it has been shown possible to obtain photoswitchable memory devices,[2] or to observe emerging properties in hybrid plasmonic-molecular systems.[3] With the aim of developing increasingly complex artificial devices and machines, growing interest is currently being devoted to the development of molecular, and/or hybrid systems including multiple and independent responsive units.[4] The synthesis of multi-photochromic units is of particular interest, since in principle it could allow to realise a system that is switchable between 2^n states (where n equals to the number of the active photochromes, if they are distinguishable). The work conducted towards the realisation of this thesis has been focussed on the study and development of novel photoswitchable systems containing either azobenzene, diarylethene, or spiropyran moieties.

The first part of the experimental work performed here lies on the study of novel azobenzene-based photochromic derivatives containing up to three switches within the same molecular backbone. The compounds were realised in collaboration with the group of Prof. M. Mayor (Karlsruhe Institute of Technology), synthesised by J. Santoro and Dr. M. Valášek. Such molecules were realised as promising building blocks for the generation of light-responsive materials, such as 2D and 3D metal-organic materials and covalent-organic frameworks, as well as to study their self-assembly in hydrogen-bonded networks.[5] The molecular scaffolds studied here consist of rigid star-shaped cores, being their geometry dictated by the presence of an aromatic backbone and by the photochromic units branching from a central, 1,3,5-trisubstituted benzene ring. Such a substitution pattern results in the arms being reciprocally in *meta*- position, thus lowering the conjugation of the multi-chromophoric systems. We were interested in studying such systems for their multi-photochromism, therefore we performed an in-depth characterisation of their multiple isomeric states.

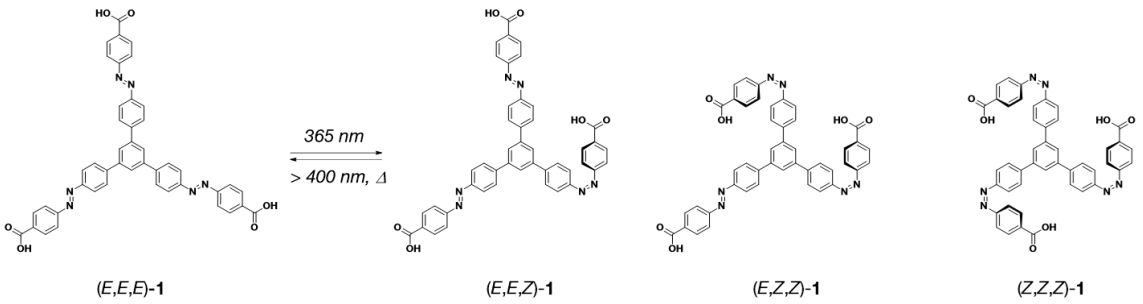

Figure 1. Isomerisation of tris(azobenzene) **1**

A detailed study over the multi-photochromism of the tris(azobenzene) derivative **1** by comparison with bis(azobenzene) and mono(azobenzene) compounds showing similar geometry and rigidity has been performed with multiple analytical techniques. The model bis(azobenzene) and mono(azobenzene) compounds were realised by progressively substituting the diazene-1,2-diyl groups with ethyn-1,2-diyl units, thus yielding similar, yet non-photoresponsive branches. The self-assembly of the tris(azobenzene) in 2D networks has been studied by scanning tunnelling microscopy (STM), corroborated by molecular modelling (the latter in collaboration with the group of Prof. J. Cornil, Université de Mons). The exploration of the dynamic self-assembly of such systems into ordered

supramolecular architectures allowed to identify patterns resulting from multiple isomers, thereby demonstrating that the multi-photochromism is retained when the molecules are confined in two-dimensions.

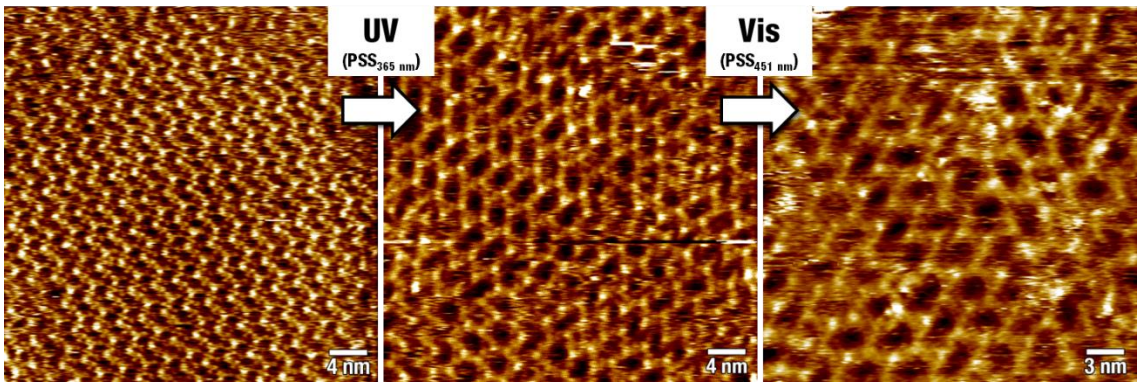

Figure 2. STM images of **1** recorded at the interface between an HOPG substrate and a 10 μM solution of **1** in 1-heptanoic acid. *Left*, no light irradiation. *Centre*, *in-situ* UV light irradiation to the photostationary state (PSS, λ_{max} = 367 nm). *Right*, subsequent in-situ visible light irradiation (PSS, λ_{max} = 451 nm).

The second system explored throughout this work is based on multi diarylethene-containing systems. The derivatives presented here are based on a dyad architecture containing a fluorescent porphyrin core and four diarylethene, and specifically perfluorocyclopentene-bridged dithienylethene photoswitches (DTE) on its periphery. The photochromic tetra-substituted porphyrins were designed and synthesised in the group of Prof. J. Weiss (Université de Strasbourg), realised by Dr. T. Biellmann. Such a system was conceived to exploit the central porphyrin unit both as a symmetrical scaffold for the photochromes and for its appealing photophysical properties (*e.g.* fluorescence). The dithienylethene (DTE) units employed are connected at the *meta*-position of a tetraphenylporphyrin core: such a connectivity pattern has been chosen not only to prevent the formation of atropoisomers, but most importantly to electronically decouple the switches in order to retain their photoreactivity.

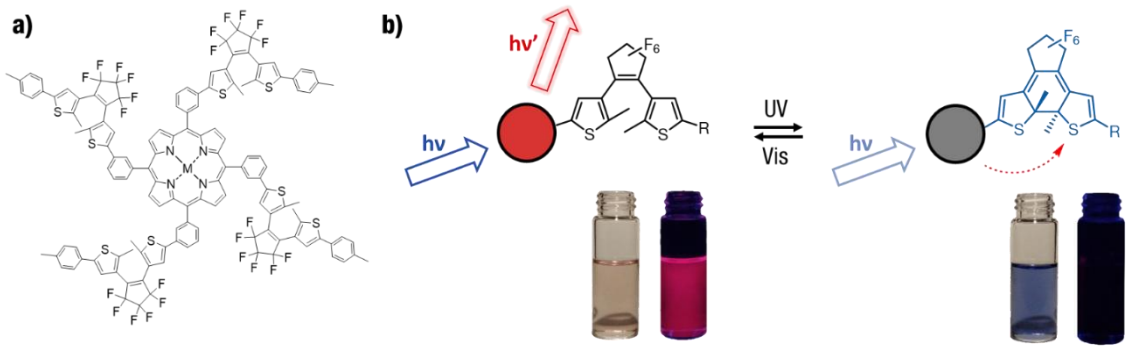

Figure 3. a) Structure formula of the tetra-DTE-substituted porphyrin derivatives **2** studied. M = H_2, Zn(II) show reversibly switchable emission. b) Simplified scheme of the emission quenching by energy transfer to the closed DTE isomer. *Left*, open-DTE: fluorescence ON. *Right*, closed-DTE: fluorescence OFF.

Four tetra(dithienylethene)-substituted porphyrins **2** were studied, being the free base, and the Zn(II), Ni(II) and Co(II) complexes. The effective and reversible photochemical conversion of the four derivatives of the system reported here was studied by UV-Vis absorption and emission spectroscopy and ^{1}H-NMR (the latter in collaboration with the group of Prof. V. Guerchais, Université de Rennes I). Interestingly, the free base and the zinc complex having all the DTE units in the open form display analogous photophysical properties to their non-photochromic analogues free base- and zinc tetraphenylporphyrin. Conversely, UV-triggered photochemical conversion of the DTE units to their corresponding closed isomer(s) results in almost complete quenching of the original emission of the aforementioned compounds. The luminescence showed to be reversibly on- and off-switched over several irradiation cycles both in solution and in dye-doped polystyrene thin films, allowing us to demonstrate that such compounds could be used as photo-rewritable fluorescent dyes, which fluorescence read-out could be performed without altering the state of the switches modulating the fluorescence. The high contrast obtained in the fluorescence modulation is due by the presence of a high amount (*i.e.* four) of photoswitches around the emissive core.

In the last experimental chapter, the focus has been shifted from multi-photochromic molecules towards hybrid systems made up by joining spiropyran photoswitches with plasmonic nanoparticles, namely gold nanorods (AuNR). Such a combination has been chosen in order to study the variation of the optical properties of the anisotropic nanoparticles and to verify an eventual effect on the stability of the colloidal dispersion upon isomerisation of the photochromic unit. The photoswitches used here have been grafted on the surface of AuNR by exploiting thiol chemistry. The dodecanethiol-bridged

spiropyran derivative **3** used in this study was synthesised in the group of Prof. S. Hecht (Humboldt University, Berlin) by Jan Boelke and Björn Zyska. Spiropyran photochromes were chosen following the notably large variation of their molecular dipole moment upon isomerisation from the spiropyran (SP) form to the merocyanine (MC) isomer.[6] One of the most appealing properties of AuNR is related to their optical properties: alongside with the surface plasmon resonance band (SPR) in the visible light range ($\lambda \approx 520$ nm) common to all gold colloids, they are characterised by a second SPR mode at lower energies (named longitudinal SPR, LSPR). The latter is commonly a sharp, intense band, and its maximum wavelength can be tuned from the visible to the near-infrared range of the electromagnetic spectrum by varying the aspect ratio of the anisotropic nanoparticles.

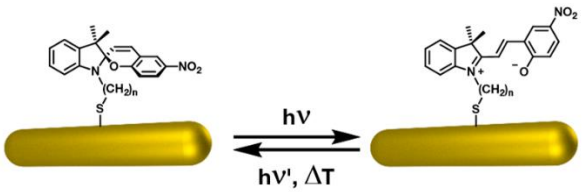

Figure 4. Schematic representation of the isomerisation of thiolate-terminated spiropyran derivative **3**.

The spectral properties of plasmonic nanoparticles are highly sensitive towards the variation of their dielectric environment, and especially the ones presenting anisotropic properties such as AuNR.[7] We have employed well-established literature methods to synthesise surfactant-stabilised colloidal dispersions of AuNR with different aspect ratio, which were selected on the basis of the spectral overlap of their LSPR mode with the absorption band of the open-ring MC form of our photochromic unit. This was done in order to verify the appearance of emerging properties on the hybrid system realised by coupling AuNR with the photochrome once grafted on its surface. The thiol-terminated photoswitches were used also with the purpose of stabilising the colloidal dispersion in organic solvents. Functionalisation of the aforementioned anisotropic nanoparticles was performed by substituting the surfactant stabilising the as-synthesised colloid upon chemisorption of the functional thiol on the surface of AuNR, with particular care in avoiding variation of nanoparticle morphology subsequent to this step. Photochromism of the hybrid systems was studied in colloidal dispersion by UV-Vis absorption spectroscopy, where no evident light driven aggregation of the colloid was evident, though clear plasmon-dependent variation of the extinction spectra was seen occurring upon UV

irradiation. In an attempt to further characterise our hybrid system and to obtain a more detailed understanding on the behaviour of the photochromic unit grafted on the plasmonic nanoparticles, we have performed a spectroscopic study on the solid-supported particles by dark field light scattering and Raman spectroscopy, in collaboration with Prof. H. Uji-i and Dr. S. Toyouchi (Katholieke Universiteit Leuven). Isomerisation of the photochromic unit grafted on AuNR could be studied taking advantage of the large Raman enhancement factors presented by such nanomaterials, thus by tracking the vibrational fingerprint of SP and MC using the surface-enhanced Raman scattering (SERS) technique. Nevertheless, the spectroscopic evidence obtained shows that the photochromic thiol is not capable of isomerising when immobilised on the surface of the gold colloid, being present only in the MC form (negative photochromism). We impute this failure both in the vicinity of the photoswitch to the nanoparticles surface, and to their crowding in the self-assembled monolayer, the latter most likely leading to the stabilisation of the open-ring MC form.

With the objective of developing novel stimuli-responsive systems, we have presented here three examples of optically switchable systems based on photochromic building blocks. The engineering of devices made up by the combination of photoswitches with molecular functional units and nanostructures is highly appealing since it gives the possibility of remotely controlling a selected physicochemical property in a reversible fashion without the build-up of waste products. In this framework, we have utilised here three different families of photochromic units, according to the property of the system we wanted to be varied by optical stimuli.

In the first case, azobenzene was the unit of choice, following its large shape change occurring upon conversion from the *E* to the *Z* isomer triggered by ultraviolet light. Upon embedding multiple azobenzene units within rigid, pseudo-planar star-shaped molecular scaffolds we have shown that it is possible to realise relatively small rigid molecules having efficient, fully independent photochromic units by simply connecting them in *meta*-position on a central trisubstituted benzene ring. Such molecules present at the photostationary state multiple isomers, due to the presence of up to three switches within the same structure, being each species isolated and fully characterised by means of liquid chromatography and ion-mobility mass spectrometry. The star-shaped systems are

capable to undergo large geometrical rearrangements upon photoisomerisation, evidence which was given also by scanning tunnelling microscopy, evidencing that the assembly of different (light-generated) isomers at the solid-liquid interface between graphite and their solutions gave yield to hydrogen bonded 2D crystalline assemblies with notably different morphology. We envision that such multi-azobenzene compounds could be employed in the future as building blocks for light-triggered host-guest systems or metal-organic frameworks.

In a successive example, photochromic dithienylethene (DTE) switches were employed to gate the emission of an organic fluorophore. This was made possible by exploiting the large change occurring on the π-electronic system upon isomerisation between the open- and the closed-form of DTE accompanied by the alteration of its electronic levels. In such a way, the emissive core, namely free base or zinc (II) tetraphenylporphyrin, is not perturbed when the DTE unit(s) reside in the open form, while energy transfer occurs from the excited state of the fluorophore to the DTE in the closed form. The dyad formed by the porphyrin core covalently linked to four DTE units showed reversible modulation of its emission upon ultraviolet and visible light irradiation, displaying notably high contrast due by the presence of multiple quenchers around the emissive core when the DTE units are switched to the closed form. The possibility of switching the system and detecting its fluorescence at very distinct wavelengths together with its capability of being converted between the on- and off-forms also when dispersed in a polymeric matrix and deposited as thin films makes such derivatives particularly appealing for their application in all-optical memory storage and fluorescence microscopy imaging.

As last example, a spiropyran derivative was employed as photoswitchable unit owing to the considerable variation of the electrical dipole moment of its two isomers: the bulky spiropyran, and the planar, conjugated merocyanine. Such a light-activated switch was combined with anisotropic gold nanoparticles (gold nanorods, AuNR), exploiting the tunability of their surface plasmon resonance bands and the high sensitivity of the latter towards the variation of their dielectric medium. Different AuNR with varying aspect ratio were employed, in order to study the effect of the spectral overlap between the absorption and emission spectra of merocyanine and the surface plasmon resonance bands of the nanomaterial. Upon inducing the isomerisation of the switch in AuNR colloidal dispersions in liquid, we could visualise a large, plasmon wavelength-dependent variation

of the colloid extinction spectrum. Nevertheless, the use of SERS technique showed that isomerisation of the photoswitch could not be attained on the nanomaterial surface, thus enlightening how challenging is the realisation of hybrid systems capable of responding to light stimuli.

TABLE OF CONTENTS

Chapter 1.

INTRODUCTION

The realisation of architectures capable of responding to external stimuli attracts great scientific interest, with the ultimate goal of building-up materials whose macroscopic properties could be remotely controlled. On this regard, Nature and more specifically the biological world represents probably the first and most important source of inspiration for the research in this field. Living cells are the greatest example of complex machines known, being capable of performing a vast variety of different functions with high spatial and temporal control, as a result of external stimuli. Tremendous efforts in chemical research and nanoscience have been made in order to employ the concepts given by biology and biochemistry, mastering the abilities of synthetic chemistry in combination with supramolecular concepts to obtain self-assembled, or self-organised systems that can perform functions whose complexity is still not even comparable to their natural counterparts.

Within the broad scientific community that includes synthetic and supramolecular chemistry, soft matter nanoscience and materials science, the field aimed at engineering synthetic molecular (and supramolecular) systems capable of responding to external stimuli is extremely active and in rapid expansion.[1, 8] Recently, these efforts have also been recognised by awarding to Sauvage, Stoddart and Feringa the 2016 Nobel Prize for chemistry, for their pioneering work aimed at the realisation of synthetic molecular machines and devices.[9]

Stimuli-responsive molecular and supramolecular systems are species capable of changing their conformation as a consequence of an external trigger, and such a conformational change has an impact on their overall properties.[10] From such definition, it is of fundamental importance to distinguish between the different types of "machines" that can arise from these synthetic systems. On the one hand, switches as a result of the change in their atomic connectivity and conformation can be used to tune the overall properties of the system studied, analogously as their macroscopic counterpart. However, any work performed upon switching from one state to another will be lost while returning to the original conditions. On the contrary, more complex devices such as motors are capable of performing mechanical work at the end of their cycle, as the movement generated by their conformational changes is directional.[8c] Thus, molecular motors take advantage of random thermal fluctuations (Brownian motion) to realise

directional motions through ratcheting mechanisms such as energy-[11] and information ratchets.[12] In this regard, motors and Brownian ratchets are more complex entities which take advantage of the molecular movement produced by a switch, but enabling to control the directionality of the motion generated at the molecular level. Artificial molecular motors are just one – yet probably the most visionary – example on how molecules and supramolecules can be employed as sophisticated nanomachines which can be controlled with external inputs.

The whole supramolecular chemistry is based on the concepts of self-assembly and self-organisation occurring between building blocks which are encoded with a wealth of chemical information (*e.g.* molecular conformation, atom connectivity, functional groups allowing intermolecular interactions, to name a few).[13] Though generally the self-assembly processes approach a condition of thermodynamic equilibrium where the most stable species is formed, thus reaching the global energy minimum of the potential energy surface describing the system. On the contrary, Nature, and in particular living systems are constituted by complex assemblies that, upon consumption of chemical fuel, reside out of this potential energy well, hence they are in an out-of-equilibrium state. Recently, the realisation of synthetic supramolecular systems which can be driven far away from chemical equilibrium conditions is being embraced as a major challenge by several research groups.[14] Chemical systems are pushed away from thermodynamic equilibrium via the supply of energy, achieved with external stimuli (*e.g.* light),[15] or chemical fuels. In this context, switches are also of paramount importance, as they often constitute the molecular building blocks that allow to externally control and drive the system out of the global energy minimum in kinetically trapped, or alternatively far-from-equilibrium conditions.

Switches are not only the principal building block for the construction of nanomachines and increasingly complex, life-inspired systems, but can also be employed in a plethora of applications in materials science and optoelectronics. For instance, there is a constantly growing amount of reports showing that nowadays it is possible to realise smart materials whose macroscopic properties (*e.g.* shape) could be changed by external stimuli, thus enabling to make macroscopic actuators also capable of performing mechanical work.[16] Moreover, the combination of switches with (organic) semiconductors enabled to realise sophisticated devices capable of *e.g.* storing information, as optically reconfigurable memory elements.[2, 17] Switches have shown their importance also in the development of efficient fluorescent probes,[18] to perform controlled drug delivery,[19] and to remotely control chemical reactions.[20]

With the aim of developing artificial chemical systems of increasing complexity, one of the hardest challenges still open to date consists in the integration of multiple and independent responsive units within a single molecular system. Chemical, electrochemical or photochemical switches, are typically systems which, analogously as their macroscopic counterpart, can exist into two states showing remarkably different properties, and their interconversion is externally governed. Switches are therefore binary objects, nonetheless the integration of multiple switchable units within the same molecule could allow to obtain a system capable to switch between a higher number of states, thus to break the traditional 0/1 barrier in a single object. This in principle could amount up to 2^n, where n equals to the number of binary switches, if each is distinguishable. Among various inputs, the use of photons has been regarded as one of

the most promising for technological applications thanks to the possibility of being remotely exploited with high spatiotemporal resolution, without build-up of waste products.[21]

Motivation

Photoswitchable nanoarchitectures based on photochromic compounds constitute an extremely appealing substrate for the development of remotely controllable dynamic materials. Light represents the stimulus of choice due to its non-invasive character. This work is aimed at the development and the study of novel systems containing multiple photochromic components kept together by different scaffolds. Such studies have been performed in order to establish whether the integration of several switchable components enables the observation of emerging properties that could not be attained by employing only the single parts. This includes the presence of multiple states, thus going beyond their dual functionality, or to increase the contrast in the photoresponse of the system. In this framework, photochromic units coming from the three main classes of photoswitches available, being azobenzene, diarylethene, and spiropyran have been combined in multiphotochromic arrays by covalently binding the functional fragments to a specific "scaffold". One among the greatest challenges to obtain fully working multiphotochromic systems relies on the choice of a suitable bridge between the switches, which at the same time should ensure acceptable switching performance of the single components, but also allowing the appearance of emerging properties. In fact, in the present work the term "scaffold" has a very broad definition, as for the bridging unit between the switches different objects having heterogeneous nature and dimensions have been used, ranging from simple 1,3,5-trisubstituted benzene connectors, to tetraphenylporphyrins, and even to anisotropic gold nanoparticles.

The first multiphotochromic system tackled in this work at Chapter 4 consists of a multi(azobenzene) derivative, containing up to three switches within the same molecular backbone. Here the use of a simple 1,3,5-trisubstituted benzene ring to bridge the chromophores granted full photochromism of the system, with the observation of multiple states as the product of the isomerisation of each light-activated unit, but at the same time providing the molecular rigidity needed in order to employ azobenzenes as molecular actuators. Building upon the widely studied surface-confined self-assembly behaviour of aromatic carboxylic acids, we have studied the dynamic self-assembly of our multi-azobenzene system in 2D supramolecular networks, and have also been able to identify multiple isomeric states by scanning tunnelling microscopy. In the second project, reported in Chapter 5, a tetra(diarylethene) system represented the focus of our investigation, where a tetraphenylporphyrin moiety was used as scaffold, by tethering the photochromes to its periphery. The use of such architecture provided a photoswitchable fluorophore which highly contrasted photoresponse was due to the presence of multiple surrounding switches capable of gating its emission. The last experimental work described here at Chapter 6 consists of a hybrid system obtained by combining a photochromic spiropyran derivative with anisotropic gold nanoparticles, and specifically gold nanorods. In this framework, the introduction of the concept of multiphotochromism for such an example falls

on a different length scale, and does not refer to each photochrome in a single molecule, as the photoswitches are not distinguishable from one another being present in large number on the gold nanorods (particles with dimensions ranging between 20 – 130 nm), but can be intended from the anisotropic character of the colloid. Gold nanorods are distinguished by the presence of two surfaces with different curvature radius, being the apex and the longitudinal face; thanks to the facile tunability of their synthetic method allowing to obtain nanorods in a wide range of different dimensions, thus having different ratio between the area of the longitudinal faces vs. the one of the apices. In this way the use of photochromic units that are highly sensitive to their local environment (*e.g.* spiropyrans) could result in the observation of a distinct photoresponse related to the presence of photoswitches tethered to the different faces of the anisotropic gold colloid.

This thesis is organised as follows:

- Chapter 2 offers a brief description of the theoretical background of this work, including the materials employed;
- Chapter 3 provides an overview over the central techniques employed for the experimental work reported here;
- Chapter 4 describes our investigations on the star-shaped multi(azobenzene) compounds, focussed at studying their multi-photochromism and the dynamic surface-confined self-assembly of the tris(azobenzene) derivative;
- Chapter 5 is focussed on a reversibly switchable fluorophore-diarylethene system composed of a tetraphenylporphyrin emissive core and four diarylethene units allowing to control its emission in highly contrasted fashion;
- Chapter 6 deals with the covalent functionalisation of gold nanorods with spiropyran photochromic derivatives and the study of the photochromism of the hybrid system upon varying the nanorods aspect ratio;
- Chapter 7 provides a summary of the presented work, together the outlooks for its future development.

Chapter 2.

THEORETICAL BACKGROUND AND MATERIALS

1. Light-activated switches: photochromic compounds

Phototriggered phenomena are ubiquitous in Nature, being the most notable examples photosynthesis, vision, phototropism and phototaxis. On the other hand, organic photochromism, being the reversible phenomenon of conversion between two forms of a chromophore under light stimuli is known since slightly more than a century. The first examples of photochromic reactions were suggested nearly at the end of the nineteenth century, and first described as *phototropism*,[22] but the term *photochromism* was first used by Hirshberg in 1950.[23] Such a name derives from the combination of the Greek words used to define light and colour, referring to the phenomenon of reversible colour change obtained from light irradiation. One among the first class of photochromic molecules being discovered was the spiropyrans, by Fischer and Hirshberg, in 1952.[24] Soon after, Hirshberg's idea of "photochemical erasable memory"[25] literally kickstarted active research in this field. Nowadays, the definition of photochromism does not refer only to compounds capable of reversible light-induced colour change: it probably represents the most studied and versatile method to introduce nanoscale optical manipulations into systems going from the molecular scale to the macroscopic level. The switching between different states induced by light is determined by the interconversion to a different isomer of the photochromic compound. This event is accompanied by distinct changes in the physicochemical properties of such states, which range from the variation of the absorption spectra, energy of excited states and molecular orbitals, shape, luminescence, refractive index, dielectric constant, electron delocalisation, electrical conductance, molecular dipole moment, solubility, to name a few.

For any system undergoing a reversible photochemical reaction, upon continuous irradiation at a specific wavelength a steady state is reached when the two components (reagent and product) absorb the excitation light and are converted into their respective form. This

situation is called photostationary state (PSS) and its formation is an intrinsic characteristic of any photochromic compound. The PSS composition depends on the quantum yields of the forward and backward reactions together with the absorption of the two isomers at the irradiation wavelength. The PSS, together with the fatigue resistance, constitutes the main figure of merit to evaluate the performance of a photochromic system.

Several different classes of organic compounds giving rise to photochromism have been developed on the basis of a number of reversible photochemical reactions. Organic photochromism takes advantage of molecules that upon light irradiation typically give rise to pericyclic reactions, *E-Z* isomerisation of double bonds, hydrogen transfer, or also homolytic bond cleavage. In the case of pericyclic reactions, several classes of photochromes, such as diarylethenes, spiropyrans and spirooxazines, furyl fulgides and fulgimides give rise to 6π-electrocyclisations, while polycyclic hydrocarbons such as anthracene and helianthrene give rise to [4+4] and [4+2] cycloadditions. Isomerisation over double bonds represents the main photoinduced phenomenon for azobenzenes, imines and hydrazones, and stilbenes, together with the naturally occurring retinal. On the other hand, the less common anils are characterised by photoinduced hydrogen transfer reactions, and triarylimidazole dimers undergo homolytic bond cleavage.

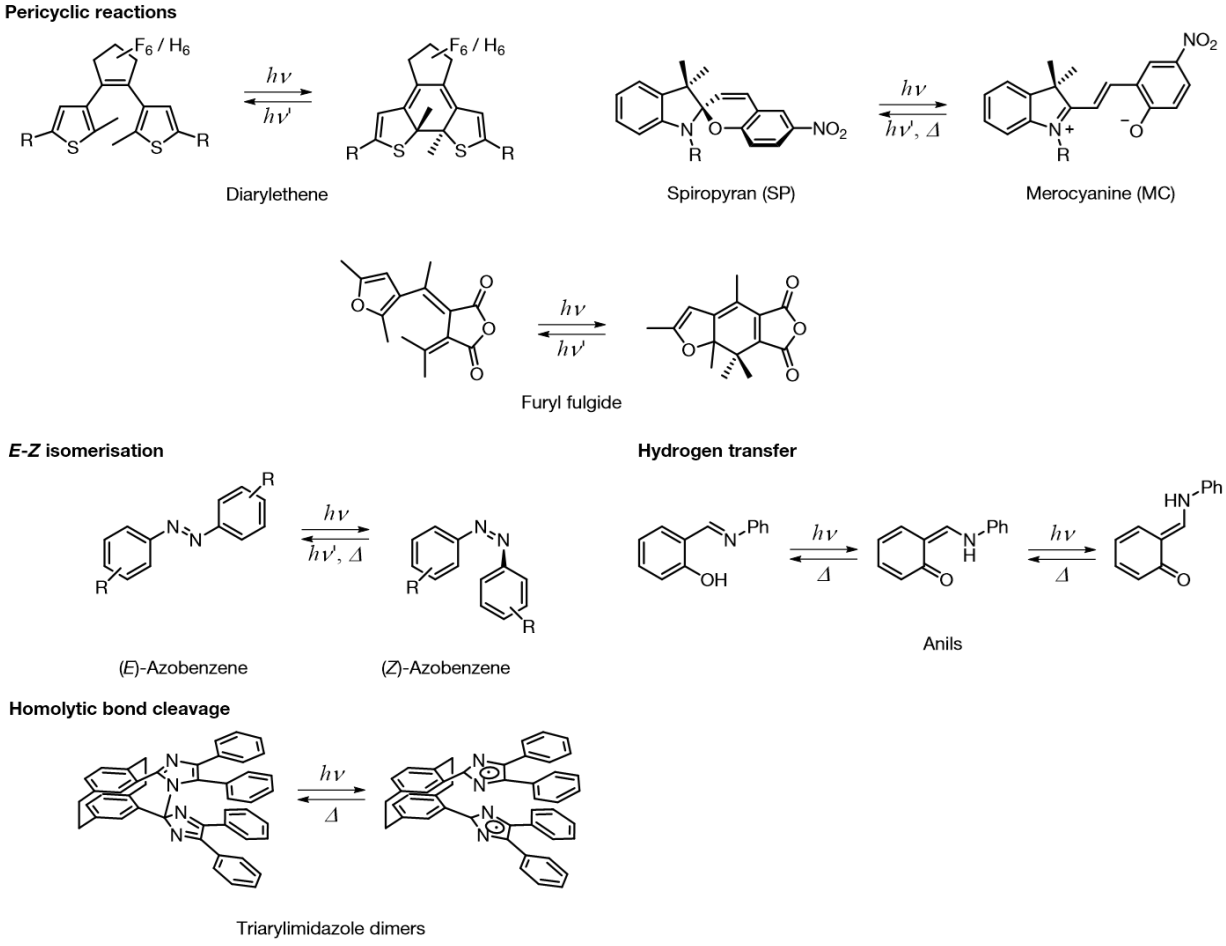

Figure 1. Most common classes of photochromic compounds classified according to their photochemical reactions.

Photochromic compounds have been applied in various fields of natural sciences, as they allowed to achieve remotely controlled functionalities with the use of photons in a reversible

fashion. This could be achieved by coupling them with other chemical functionalities, or alternatively with luminophores, and even with biological systems, to name a few. In the next sections the most common families of photoswitches will be briefly treated, highlighting few examples of their applications related to the present work.

1.1. Azobenzene

Azobenzene consists of two phenyl rings bridged by a central diazene N=N moiety, being structurally similar to stilbene, the latter not containing heteroatoms. Such compounds may undergo isomerisation around the central double bond, thus can be present in the two *E* and *Z* isomers. For unsubstituted azobenzene, the energetic barrier for the *E* – *Z* isomerisation in the ground state is relatively high – it thus results that the *E* isomer does not convert to *Z*, while the opposite occurs being the latter isomer less thermodynamically stable. The thermal $Z \rightarrow E$ conversion is generally a slow reaction, but its activation barrier may be drastically lowered when the *Z* isomer is in its radical anion form.[26] The high energetic barrier for the isomerisation in the ground state can be circumvented by populating the excited state of both forms with the absorption of UV-visible light. The photochromism of both stilbene and azobenzene organic compounds is thus based on the *E*-*Z* photoisomerisation of their central double bond. For the sake of simplicity, from now on we will discuss only about azobenzene derivatives, as they represent the focus of part of this work. Azobenzene derivatives are yellow-orange coloured, and have long been known and used as industrial dyes. Their characteristic colour is due to the presence of two absorption bands in both *E* and *Z* isomers: the π-π^* in the ultraviolet range, and the n-π^* lying in the visible range, the latter with low intensity being symmetry forbidden.

Absorption of light through the π-π^* and n-π^* transitions leads to the population of S_2 and S_1 excited states, respectively. The variation in the absorption spectra of the two isomers is generally limited, since the differences in electron delocalisation between the two forms are small. Both isomers show overlapping spectra, with a change in the respective intensity of the two: the π-π^* is weaker, but the n-π^* is more intense for the *Z* isomer. The irradiation of azobenzene in either of the two transitions can lead to the *E*-*Z* isomerisation in the two directions, depending on the wavelength of the light used: due to the aforementioned absorption spectral differences, irradiation with light of a wavelength centred on the π-π^* transition leads to a photostationary state more rich of the *Z*-isomer, while the opposite situation is achieved by irradiating on the n-π^* band. The occurrence of similar absorption spectra is the main reason for the invisibility of the colour change by naked eye (but also because the main variations occur in the ultraviolet range), nevertheless the spectral overlap also results in the formation of photostationary states rich of both isomers, thus preventing the quantitative formation of one by light irradiation. On the contrary, a situation in which ~ 100 % of one form (the *E*-isomer) is present can be achieved only by thermal conversion, following the thermodynamic stability of the *E* form. The thermal $Z \rightarrow E$ isomerisation for unsubstituted azobenzene in homogeneous solution has an activation barrier of ~ 95 kJ mol^{-1}, thus is typically a rather slow process (thermal half-life in the order of tens of hours, at 25 °C).

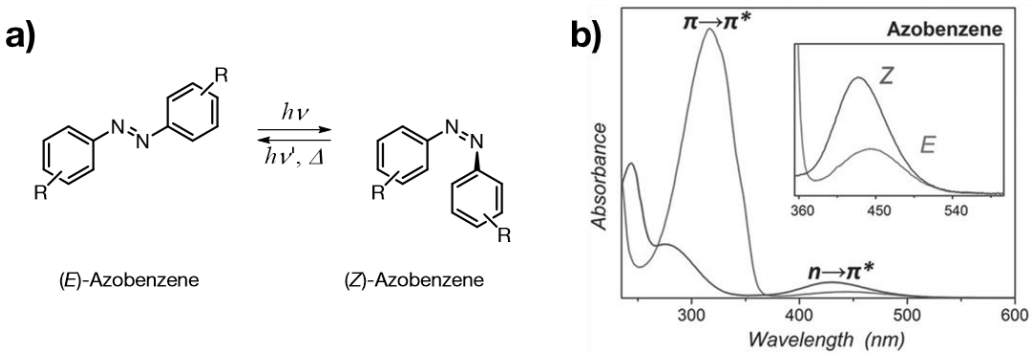

Figure 2. a) Schematic picture of the *E* – *Z* isomerisation of azobenzene derivatives. b) UV-Vis absorption spectra of azobenzene *E* and *Z* isomers in acetonitrile, adapted from Ref.[27]

Despite being widely studied, the mechanism of the apparently simple photoisomerisation reaction occurring on azobenzene is still subject of controversy. This is also due to the particularly short-lived character of the excited states of azobenzene (sub-picosecond timescale), and the complex mechanism for such reaction, following multiple possible pathways. This is evident from the fact that both *E* and *Z* azobenzene isomers undergo isomerisation following either $S_1 \leftarrow S_0$ and $S_2 \leftarrow S_0$ excitation, nevertheless the sum of the quantum yields for the two processes ($\Phi_{E\rightarrow Z}$ and $\Phi_{Z\rightarrow E}$) does not equal unity. Moreover, isomerisation occurs upon violation of Kasha's rule, as the quantum yield obtained upon excitation to the S_1 state is larger if compared to the same obtained upon exciting the molecule on S_2.[28] The quantum yield also depends on a number of external factors, such as solvent polarity and temperature. Several mechanisms of isomerisation over the central double bond on the diazo moiety have been proposed, being rotation, inversion, concerted inversion, and inversion-assisted rotation. The photoisomerisation thus can follow multiple pathways, depending on the external conditions, and the substitution pattern of the photochromic unit. For unsubstituted azobenzene in solution at room temperature for instance, isomerisation following π-π^* excitation shows $\Phi_{E\rightarrow Z}$ = 0.11 and $\Phi_{Z\rightarrow E}$ = 0.44 in n-hexane, while $\Phi_{E\rightarrow Z}$ = 0.15 and $\Phi_{Z\rightarrow E}$ = 0.35 in acetonitrile. For *n*-π^* excitation instead, $\Phi_{E\rightarrow Z}$ = 0.25 and $\Phi_{Z\rightarrow E}$ = 0.56 in n-hexane, while $\Phi_{E\rightarrow Z}$ = 0.31 and $\Phi_{Z\rightarrow E}$ = 0.46.[29] This suggests that viscosity and polarity may have an influence on the reaction mechanism. Moreover, upon embedding azobenzene in solid matrix, the isomerisation quantum yield shows a significant decrease. It is also important to state that azobenzene show no- or very low emission from their excited states, unless upon blocking the isomerisation (*e.g.* in solid at low temperature).

The general considerations mentioned above are valid for unsubstituted azobenzene, nevertheless such properties could largely change upon modifying its molecular backbone. The substitution pattern on the phenyl rings influences the electronic properties and the steric hindrance of the product, thus resulting in shifts in the position of the absorption bands, varying quantum yields, and importantly variation of the stability of the *Z* isomer with respect to the *E*, together with a modification of the activation energy barrier for the thermal isomerisation. Generally speaking, the introduction of substituents that do not have strong electronic influences (by mesomeric effect) do not substantially modify the properties of such compounds if compared to azobenzene derivatives. Therefore, the addition of alkyl, aryl, halide, carbonyl, amide, nitrile, ester and carboxylate groups, or nitro, 3-amino or 3-alkoxy moieties on the phenyl rings leads to azobenzenes having similar properties to the unsubstituted molecule. Thus,

excluding significant steric hindrance lowering the stability of *Z* isomer, their absorption bands, thermal isomerisation rate, as well as the quantum yields for photoisomerisation do not change substantially. On the contrary, addition of amino or hydroxyl groups in 2 or 4 position results in noticeable red shifts of the π-π^* transition which overlaps with the n-π^* (the entity of the red-shift depends on the degree of substitution on the aromatic backbone). Typically, also an increase of the photoisomerisation quantum yield occurs, which is also accompanied by a significant increase of the thermal isomerisation rate. The latter is induced by electron donating substituents, as they contribute in increasing the electron density of the π^* orbital, thus decreasing the energy barrier for such reaction.[30] Azobenzenes substituted in 2 and 4 position with hydroxyl groups are a peculiar example, as the presence of such moiety enables tautomerisation to the correspondant azohydrazone. The formation of strong hydrogen bonds in the *E* form, being intramolecular (for 2-hydroxy substitution), or intermolecular through dimerisation (for 4-hydroxy groups) results in largely increasing the rate for $Z \rightarrow E$ thermal isomerisation, occurring in the millisecond – second range.[31] Another important class of compounds is represented by the so-called push-pull azobenzenes: in such derivatives the two phenyl rings are substituted in 4 and 4' position with a strong electron donor and an electron acceptor group. This results in strongly lowering the energy of the π-π^* transition, which becomes nearly degenerate in energy with n-π^*, both occurring in the visible region. This usually occurs in addition with the appearance of charge-transfer bands arising from the electron transfer between electron-rich and electron-poor groups (*e.g.* anilino and nitro groups), also causing strong solvatochromism of such compounds. Push-pull azobenzenes are strongly coloured and have been widely used in industry as dyes. Such compounds are characterised by extremely fast thermal isomerisation rates due to the asymmetric electron distribution on the aromatic backbone: usually delocalisation of the electron lone pair of the electron-rich group leads to the formation of stable resonance structures in which the central double bond is ruptured, thus facilitating the rotation around it.[28]

Recently, a few breakthrough works over the synthesis of novel azobenzene derivatives have appeared in the literature. Following the aforementioned considerations about substitution on the azobenzene backbone, it is evident how the addition of groups having strong electronic effects (mostly electron donors) in *ortho* and *para* position on the phenyl rings allows for shifting the absorption spectra of the two isomers to the visible light range. The latter however is also accompanied with an increase of the thermal isomerisation rate, in most cases undesirable for the application of azobenzene-based switches as molecular actuators. The possibility of switching such compounds avoiding ultraviolet light is extremely appealing for using azobenzene-based switches in biological and materials sciences applications. It has been recently found that upon modifying the azobenzene backbone it is possible to obtain a split in the wavelength of the n-π^* bands of the *E* and *Z* isomers, resulting in transitions no longer overlapping, together with the stabilisation of the *Z* isomer. This allows both to address the two isomers with different wavelengths in the visible range, and to slow down the thermal $Z \rightarrow E$ reaction, thus to overcome the two main drawbacks from which azobenzene-based compounds suffer. Such function could be implemented following two main strategies: either by inducing a distortion on the typically planar *E* form, resulting in affecting the energy of its π and π^* molecular orbitals, or by influencing the energy level of the n orbitals, but without changing the conformation of the *E* isomer. In all cases, the substituents are anchored in 2-position (*ortho* substitution) with respect to the diazo moiety.[32] Distortion of the planarity of the *E* azobenzene

was accomplished by either inducing a strain bridging the two phenyl rings with a short linker (*e.g.* an ethylene bridge, Figure 3a),[33] or by introducing four methoxyl groups in *ortho* position, resulting in their repulsive interaction (Figure 3b).[34] In alternative, another important example of azobenzene compounds switchable with visible light and showing high photochromic performance (high *E-Z* photoconversion, slow rate for thermal *Z-E* reaction) was introduced by Bléger *et al.*: this class of compounds consists of azobenzenes substituted in the four *ortho* positions with fluorine atoms (Figure 3c).[32] Such compounds show the aforementioned characteristics without displaying noticeable distortion of the planarity of the *E* isomer, thus making them highly promising for their application as molecular actuators.

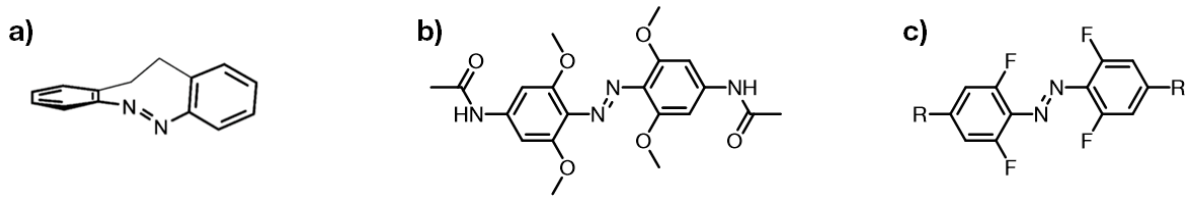

Figure 3. Azobenzenes modified in ortho-positions that show two-way isomerisation with visible light. a) Phenyl rings covalently bridged by ethylene linker, 5,6- dihydrodibenzo[c,g][1,2]diazocine, reported by Siewertsen et al.[33] b) Four ortho-methoxy substituents on the two phenyls, reported by Beharry et al.[34] c) ortho-Fluoroazobenzenes, reported by Bléger et al.[32]

Azobenzene is undoubtedly the most widely studied and applied class of photochromic compounds, mentioned in several thousands of publications and research reports, and their application in materials chemistry, or in biochemical research has been reviewed multiple times.[35] Although the change in the electronic properties between the *E* and *Z* isomers of azobenzene are limited, the isomerisation between the two is characterised by large conformational rearrangements, inducing significant changes over the free volume of the molecule. The *E* isomer is characterised by a nearly planar shape, while the *Z* has a more bulky character, as the isomer assumes a non-planar, kinked conformation. For azobenzene, electron diffraction data indicated that the two phenyl rings are tilted by about ~ 35° in the gas phase.[28] This conformational rearrangement thus also leads to a decrease in the end-to-end distance of the molecule.[36] Together with the shape, another substantial difference between the two isomers is represented by their polarity: upon conversion from the *E* to the *Z* isomer, their dipole moment goes from nearly zero, to about 3 Debye (such a change in polarity allowed for the first separation of the two isomers by Hartley, in 1937).[37] The aforementioned appealing properties, alongside with its photochemical robustness, and the ease of its chemical synthesis[35b, 36] explain the celebrity of azobenzene-based compounds among the known photoswitches, as they are particularly suitable as molecular-scale actuators. In order to exploit and/or amplify the shape variation of the switch to a greater length scale, it is vital to embed such unit in a conformationally rigid (macro)molecular scaffold.[38] Towards this end, typically a viable strategy consists of including them into rigid aromatic structures. However, such a solution could potentially prevent full, or even partial photochromism of the system, since electron delocalisation lowers the energy of the first excited state(s) precluding the access to the photoreaction pathway.[39] We will highlight here few notable examples of the use of azobenzene as light-activated switch.

1.1.1. Examples of application of azobenzenes to remote-control functions

One among the first and best known examples of azobenzene-based small-molecule actuator was given by the pioneering work of Shinkai *et al.*, in the 1980s, with the realisation of various crown ether derivatives bearing such light-triggered moiety.[40] An example that later became known as *molecular tweezers*. The working principle of the azacrown ethers and related compounds realised by the same researchers was based on the change in conformation of the molecule upon photoisomerisation: such a change results in the modification of the affinity of the macrocycles towards alkali metal and other organic cations, thus allowing to control the extraction of ions in organic solvents with the use of light. Since then, azobenzene has been extensively used to realise molecular devices which mechanical motion could be externally controlled, with various size and shapes, sometimes resembling macroscopic objects, such as the so-called *molecular scissors*, reported by Aida and coworkers in 2003.[41] In such a peculiar photoresponsive compound, an azobenzene unit is used to induce a phototriggered contracting-elongating motion, which is translated to a ferrocene moiety, acting as interlocking unit, but at the same time allowing for the free rotation of its cyclopentadienyl units, into an open-close motion of its termini, the "blades".

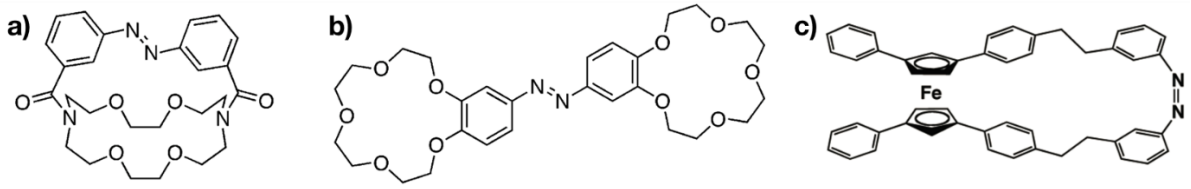

Figure 4. Early examples of light-activated molecular actuators. a) Photoresponsive azacrown ether.[40c] b) Molecular tweezers.[40a, 40b] c) Molecular scissors.[41]

In the aforementioned examples nevertheless, the azobenzene unit has been used only as a molecular switch, as its conformational rearrangements do not occur in a directional fashion. In order to realise artificial molecular motors capable to undergo unidirectional movements it is thus necessary to embed the azobenzene functional unit into more complex systems. In more recent work, azobenzene was also employed to realise molecular machines capable of performing directed molecular movements out of equilibrium conditions through energy and information ratcheting mechanisms. One example was given by Credi and colleagues, upon realising a pseudorotaxane containing an azobenzene unit embedded into a non-symmetric molecular axle (Figure 5).[42] The latter consists of three functional units, being the switch, an ammonium binding site for the macrocycle, and a bulky cyclopentyl pseudo-stopper. Where instead the macrocyclic ring is made by a 2,3-dinaphtho[24]crown-8 ether. In order for the threading-dethreading to occur through the pseudo-stopper positioned at one extremity of the axle, a relatively high activation energy barrier has to be overcome. In such a way, threading of the two components occurs through the azobenzene extremity residing in the *E* form. The working principle of such a system is based on the conformational change of the switch, allowing for the threading of the macrocycle through the molecular axle when the azobenzene resides in its *E* form, but destabilisation of the pseudorotaxane is induced by the isomerisation to the *Z* form. The isomerisation of the azobenzene unit in the *Z* form constitutes a high steric barrier

for the ring threading-dethreading through such extremity, and also destabilises the complex, thus resulting in dethreading of the macrocycle through the pseudo-stopper extremity. Being that the reversible *E*-*Z* isomerisation is induced in both ways by the same photons under steady irradiation (due to the overlap of the absorption spectra of the two isomers), the system can perform such a directionally controlled molecular motion in a repetitive fashion, being fuelled by light.

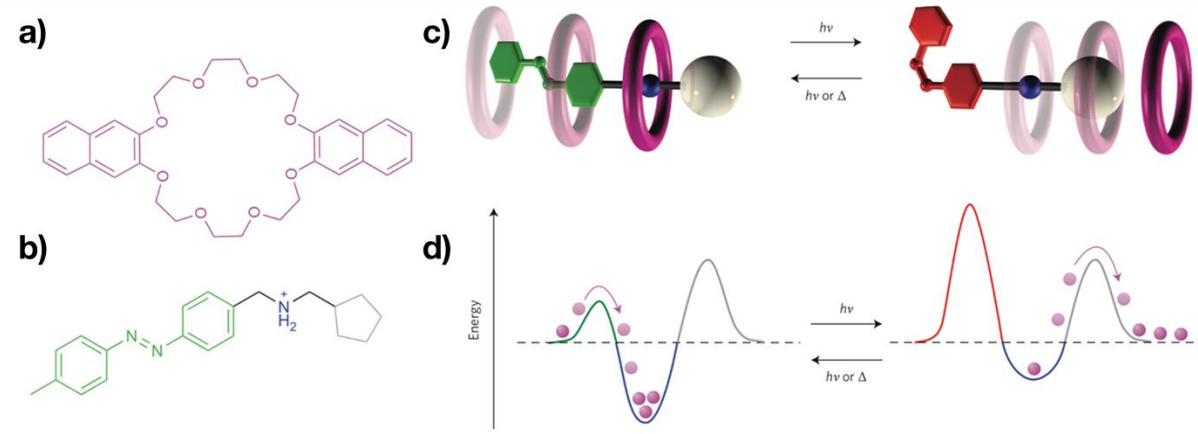

Figure 5. Light-driven supramolecular "pump" enabling the unidirectional threading-dethreading of a pseudorotaxane through the photoisomerisation of an azobenzene unit embedded in its axle. a) Structure formula of 2,3-dinaphtho[24]crown-8 ether. b) Structure formula of the molecular axle comprising an azobenzene unit at one end, a central ammonium moiety as recognition site for the crown ether macrocycle, and a methylcyclopentyl pseudo-stopper. c) Schematic picture of the light-powered directional threading-dethreading of the pseudorotaxane. d) Simplified potential energy diagram (free energy vs. ring-axle position) showing the working principle. Reproduced from Ref.[42]

Going from molecular-scale structural rearrangements to larger length scales, the isomerisation of azobenzene units can be exploited to induce conformational changes into larger objects. For instance, azobenzenes have been widely exploited to photocontrol the structure and function of biomolecules.[35b] Moreover, the modification of ion channels in neuronal cells with the use of such photoswitch has also proven the possibility of photo-controlling their activity.[43]

Azobenzene-based photochromic compounds have also been used to decorate the surface of nanoparticles of various nature, with the goal of imparting them light-responsive properties. The earliest and perhaps most notable examples are represented by noble metal, and especially gold nanoparticles. In most cases, the isomerisation of azobenzene is used to induce the nanoparticles to self-assemble, or aggregate in a reversible fashion.[44] In several reports, Klajn *et al.* reported reversible assembly (clustering) and disassembly of gold nanoparticles based on the large difference in dipole moment shown by the *E* and *Z* form of the photoswitch tethered to their surface. Being in all cases the higher molecular dipole moment of the *Z* form the cause of the emergence of dipole-dipole interactions, the latter driving the nanoparticles clustering. In an interesting research report, the dynamic assembly of nanoparticle aggregates has been achieved into well-ordered three-dimensional superstructures, either reversibly, or irreversibly (Figure 6a-b). This was made possible by judiciously playing with the concentration of azobenzene dithiol ligands on the surface of gold nanoparticles (diameter ≈ 5.6 nm) weakly bound with dodecylamine, thus on the interplay between dipole-dipole interactions and the formation of covalent bonds between the thiols bridging multiple nanoparticles.[45] In another example instead, gold nanoparticles with the same diameter were again functionalised with

mixed monolayers of dodecylamine and an (11-mercaptoundecanoxy)azobenzene, this time containing only one thiol functional group (Figure 6c-e). The nanoparticles in solution presented a reversible aggregation forming metastable supraspherical aggregates upon UV irradiation, causing also a red shift of the surface plasmon resonance band of the gold colloid. Interestingly, the nanoparticles could be dispersed in syndiotactic poly(methylmethacrylate) organogels and showed the same behaviour. The as-obtained films showed a bright colour which could be changed by UV light, thus demonstrating that such nanoparticles could be used as metastable inks for the realisation of self-erasable, rewritable materials.[46]

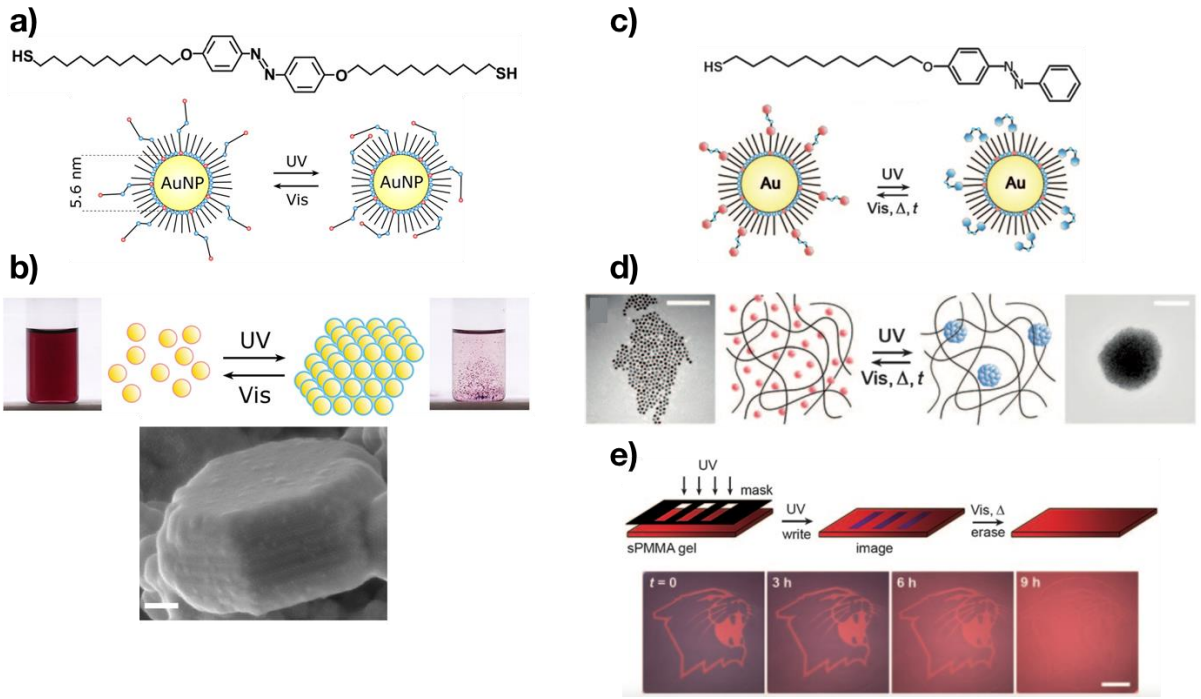

Figure 6. Gold nanoparticle aggregation can be controlled with light stimuli by functionalising their surface with azobenzene-containing stabilisers. a) Ordered supercrystals formed of gold nanoparticles can be obtained using mixed monolayers of 4,4'-bis(11-mercaptoundecanoxy)azobenzene and octadecylamine upon UV light irradiation. The reversibility of the formation of the ordered aggregates can be tuned by changing the concentration of the dithiol. b) At low dithiol surface concentration, aggregation/disgregation is reversible. SEM micrograph of a reversible crystal (scale bar 100 nm). If the dithiol concentration is increased, UV light irradiation leads to the irreversible formation of crystals. c, d) Gold nanoparticles functionalised with mixed monolayers of (11-mercaptoundecanoxy)azobenzene and octadecylamine form reversible, metastable spherical aggregates, also in organogel films (scale bar for the TEM images 100 nm). e) Images can be written into self-erasable nanoparticle-containing films by structured UV irradiation. Images reproduced from Ref.[45-46]

On the other hand, azobenzene shape variation makes it one of the principal candidates for the realisation of host-guest systems which guest uptake or release could be triggered with the use of light. In this regard, several works focussing on the synthesis of metal-organic materials going from coordination cages to metal-organic frameworks which cavity volume/hydrophobicity could be tuned by taking advantage of the different conformation of the two azobenzene *E* and *Z* isomers have been reported. This strategy opens great possibilities for their application in materials science. Metal-organic materials are discrete assemblies building up on the directionality of metal-ligand coordination using transition metal cations and organic ligands as building blocks: based on their geometry and connectivity, a vast library of nanostructures with different dimensionality could be made, going from "0D" polyhedra and coordination cages to three-dimensional coordination networks. The use of rigid organic building blocks enables to

realise discrete self-assembled systems possessing internal cavities that can be used to store small molecules, or also to perform catalysis in confined space. Metal-organic coordination cages for instance, could be used to store organic guest molecules due to hydrophobic interactions. In an example reported by Fujita and coworkers, spherical complexes with $M_{12}L_{24}$ stoichiometry showed to spontaneously self-assemble in solution, where M = Pd^{2+}, and L corresponds to a pyridine-based bent bridging ligand with attached an azobenzene pending group. Such a functional group allowed to obtain a supramolecular cavity containing 24 endohedral azobenzene groups. Upon mixing the complex with a hydrophobic guest (pyrene, or pyrene carboxaldehyde) in CH_3CN : H_2O = 1 : 1 mixture, it was shown that the former was capable of undergoing guest uptake occurring by hydrophobic interaction when azobenzene was residing in the *E* form, due to the low dipole moment of such isomer. UV light irradiation switching the endohedral azobenzene pendant groups to *Z* resulted in the release of pyrene guest, due to the lower affinity of the cavity for the latter. The system moreover showed to work in reversible fashion.[47]

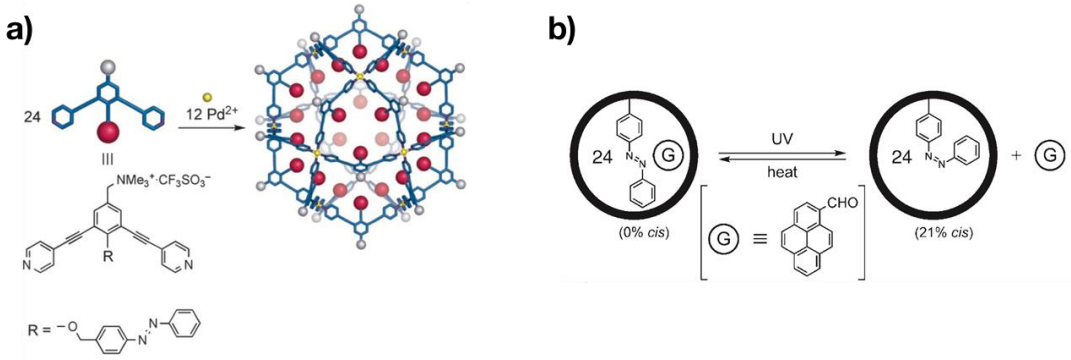

Figure 7. Self-assembled coordination cage containing 24 endohedral azobenzene units. a) Complex forming with $M_{12}L_{24}$ stoichiometry. b) The complex is able to uptake a hydrophobic guest in polar media (CH_3CN : H_2O = 1 : 1) due to the hydrophobic character of the cavity with the azobenzene units residing in *E* form. Upon UV irradiation, the guest is released (polar character of *Z* azobenzene), the system shows reversible behaviour upon thermal conversion of the pending group to the original *E* form. Reproduced from Ref.[47]

Going from 0D metal-organic polyhedra to 3D networks, metal-organic frameworks constitute an important class of crystalline materials that have been widely studied in the last decade, thanks to their structural and functional tunability. The principal interest of metal-organic frameworks (MOFs) is the possibility of building porous crystalline materials which internal cavities have uniform diameter and present extremely high internal surface areas, thus making them very promising for practical applications *e.g.* gas storage, separation/purification, or heterogeneous catalysis, to name a few. In the last few years some advances have been made in the realisation of photoswitchable metal-organic frameworks, enabling to photocontrol the aforementioned functionalities.[48] In this regard, the embedment of azobenzene within such porous materials represents a particularly promising route to induce structural modifications in the crystalline structure with light stimuli. This has proven possible following different strategies: in an early example reported by Yanai *et al.*, azobenzene has been included as a guest in a $[Zn_2(terephthalate)_2(triethylenediamine)]_n$ flexible porous coordination polymer, the latter not intrinsically photoresponsive.[49] In such example, the researchers demonstrated that the pore structure of the host material was efficiently deformed by the *E*-*Z* photo- and thermal isomerisation of the photochromic moiety: such drastic structural transformations showed to efficiently switch the adsorption behaviour towards guests, such as gaseous nitrogen. Going

further in this field, more complex examples of photoswitchable MOFs were given by including azobenzene as a pending group in the MOF structural units – the organic linkers. In such a way, the photoswitch can expose its extremity in the internal side of the cavity, in a similar fashion to what reported earlier for the coordination cage by Fujita and colleagues (Figure 7). Park *et al.* reported the first example of MOF including azobenzene in such fashion: a zinc carboxylate framework was made using 2-(phenyldiazenyl)terephthalate, which showed light-, and thermal induced reversible CO_2 adsorption behaviour.[50] The as-obtained material showed no disruption of the structural features upon repeated cycles, also due to the fact that azobenzene is included in the rigid organic framework and is free of moving inside the cavities of the material, thus potentially avoiding the fatigue that azobenzene photochromes could encounter when external constraints are applied. In another similar example, Brown *et al.* were able to realise a non-interpenetrated MOF containing azobenzene pending groups. The structure is based on the known MOF-74, with Mg nodes: such materials typically show porous structures having wide hexagonal monodimensional channels. In this example, the azobenzene pending groups in the channels determined a significant variation of the pore apertures, going from ca. 8.3 Å in the *E* form to ca. 10.3 Å in the *Z*.[51] Such large pores enabled to undergo reversible phototriggered guest release also for larger molecules, which was demonstrated with the luminescent dye propidium iodide. To date however, the MOF showing the largest photoinduced structural transformation was reported by Lyndon *et al*.[52] The researchers were able to synthesise a metal-organic framework including the photochromic units directly in the backbone of the material. The photoswitchable triply interpenetrated MOF [Zn(AzDC)(4,4'-BPE)$_{0.5}$] was realised using two different photoswitches as "pillars" of the porous coordination polymer, being azobenzene-4,4'-dicarboxylate (AzDC), and 1,2-bis(4-pyridyl)ethylene (4,4'-BPE). The effect resulting from light irradiation of this material is an apparent "squeezing", thus the framework upon shrinking is able of immediately expelling the guest molecules included inside the cavities. It is also interesting to note that the crystalline habit of such material appears to be stable upon irradiation, probably due to the triple interpenetration of the network.

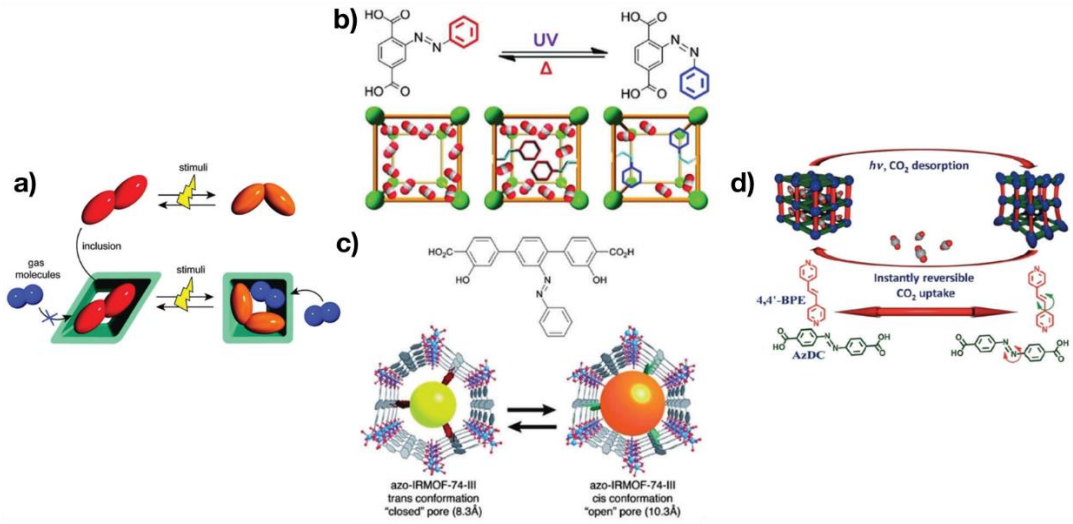

Figure 8. Examples of metal-organic frameworks (MOFs) including azobenzene switches allowing for photoactivated guest uptake/release. a) Azobenzene is included as guest in a porous coordination polymer not intrinsically photoresponsive. Conformational variation of the guest enables to induce a structural modification of the crystalline habit of the material. b, c) Azobenzene is included as pending group inside the MOF cavities, its E-Z isomerisation modifies the cavity volume. d) Photochromic units used as pillars of MOF crystals, inducing a light-triggered shrinkage of the network. Images reproduced from: a) Ref.[49] b) Ref.[50] c) Ref.[51] d) Ref.[52]

Importantly, azobenzene as molecular actuator could also be employed to tune the macroscopic properties of liquid crystalline materials: transduction of the molecular-scale movement given by the photoswitch to macroscopic motions is made possible by embedding the actuator in materials that show at the same time crystalline order and fluidic mobility. In the most notable examples, azobenzene photoswitches were used to induce macroscopic movements in liquid crystalline polymer films with the use of light, thus potentially enabling their use for the realisation of novel biomedical devices, soft robotics and morphing structures.[53] In a striking example reported by Ikeda and co-workers in 2003 for instance, the researchers showed the possibility of obtaining thin films of an azobenzene containing liquid-crystalline polymer that could be bent over a chosen direction using linearly polarised light.[54] Since then, several efforts have been devoted to obtaining systems that could achieve more complex motions, such as converting light-driven molecular events into work by their macroscopic movements, or also showing fast oscillatory behaviour. Recently, Iamsaard *et al.* designed a photoresponsive, azobenzene-containing liquid crystal having twist-nematic molecular organisation due to the inclusion of chiral dopants. Due to the twist in the liquid crystal, together with the film processing, they made possible to obtain macroscopic springs, loaded with the photoresponsive units. The photoisomerisation of the azobenzene showed to be amplified in a twisting motion associated to a local increase of disorder in the liquid crystal accompanied with anisotropic deformations. Hence, the as-obtained springs were capable to undergo complex movements such as winding, unwinding and helix inversion upon irradiation with UV light, and could be used to move macroscopic objects, therefore to perform mechanical work.[16c] In a more recent example, Gelebart *et al*. showed a striking photoactive liquid crystalline polymer system capable of performing wave-like oscillating movements fuelled by light energy upon including in the polymeric material azobenzene derivatives with fast $Z \rightarrow E$ thermal isomerisation rate. Such photoactive films were realised by playing with the alignment of the liquid crystalline polymer, fabricated in splay-aligned configuration, having homeotropic alignment on one side, and planar alignment on the other, thus providing the largest shape deformation possible on the films due to expansion and shrinkage on the two sides. Upon giving energy by constant UV irradiation, it was found that such films were capable of undergoing fast (in the ms – s range) millimetre-scale oscillatory movements, induced by the azobenzene photo- and thermal isomerisation occurring in the two verses. Interestingly, it was found that the oscillatory, wave-like movement of the films occurring when attaching their ends to a substrate was caused by its self-shadowing, generating feedback driving the waves. Remarkably, such a wave propagation could be used to move a self-propelled walking device powered by light, highlighting its potential application in light-driven locomotion and photomechanical energy harvesting.[16b]

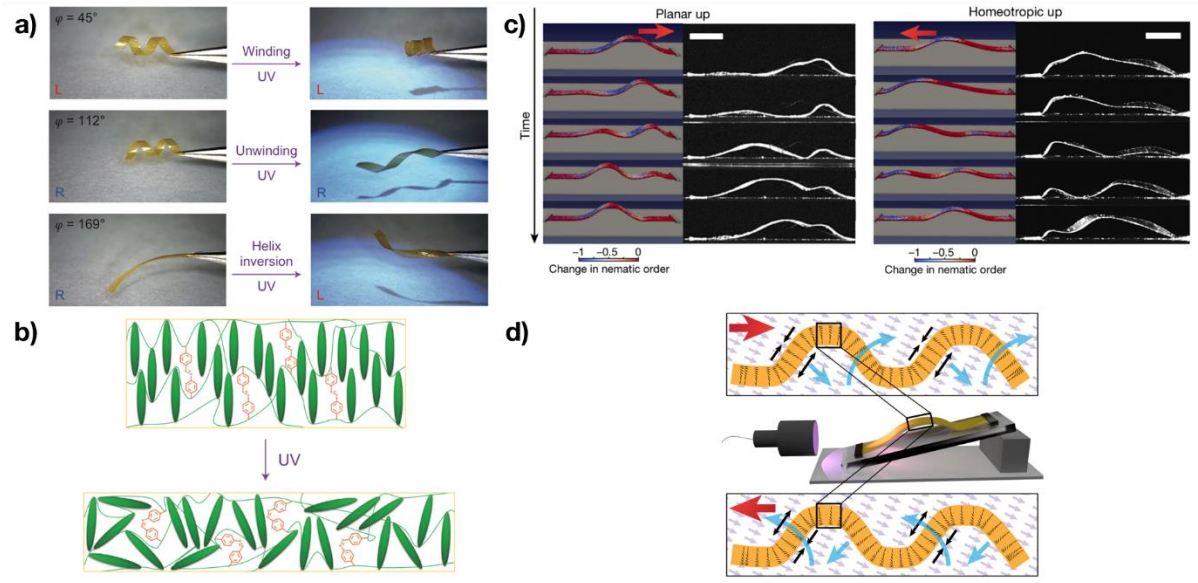

Figure 9. Embedding azobenzene in liquid crystalline polymeric films allows to realise macroscopic photoactuators performing complex motion, also doing mechanical work fuelled by light. a) Liquid crystalline polymer springs display winding, unwinding and helix inversion upon UV irradiation, depending on their initial shape and geometry. b) Schematic representation of the disorder induced in the nematic phase upon $E \rightarrow Z$ photoisomerisation. c) Photoactive liquid crystalline films undergoing continuous wave-like motions. Comparison between simulation (*left*), and experimental (*right*, black and white) data for planar-up and homeotropic-up films undergoing oscillating movements. d) Schematic representation of the system: the direction of the wave propagation depends on the direction of the film alignment. Figures a) and b) were reproduced from Ref.[16c], while c) and d) from Ref.[16b]

1.2. Diarylethene (DAE)

Among the vast class of photochromic molecules able to undergo reversible isomerisation between at least two states with photons of different wavelength, diarylethenes represent an important category for several reasons, and most importantly they feature thermal stability of both the forms accessible with light stimuli. Analogously as other categories of photoswitches, the two states accessible are characterised by drastically different physicochemical properties, allowing their use for engineering stimuli-responsive materials whose properties could be remotely controlled. Diarylethenes are characterised by a reversible photochemical 6π-electrocyclisation and –cycloreversion reaction occurring between the ring-open 1,3,5-hexatriene and the ring-closed 1,3-cyclohexadiene isomer. The reaction occurs according to the Woodward-Hoffmann principles of orbital symmetry conservation, therefore in disrotatory fashion when performed thermally, while in a conrotatory manner by photochemical excitation.[55] The thermal cyclisation normally has an endoergonic character since the 1,3,5-hexatriene core has a tricyclic structure, thus it occurs only photochemically. Being that typically the antiparallel and parallel conformer of the open isomer are energetically similar and their interconversion occurs in thermal equilibrium in solution, only a fraction (half) of the molecules in the open form can undergo the conrotatory photochemical cyclisation after excitation, thus resulting in a theoretical maximum quantum yield of 0.5 for the photocyclisation reaction

(Figure 10). Typically, quantum yields for ring-closure are in the range 0.1 – 0.5,[55] but may be higher in case there is an energetic preference for the antiparallel conformation in the ground state.[56] Since the large activation energy barrier for the thermal cyclisation and cycloreversion reactions of most diarylethenes, both their isomers are stable even at high temperatures.[55]

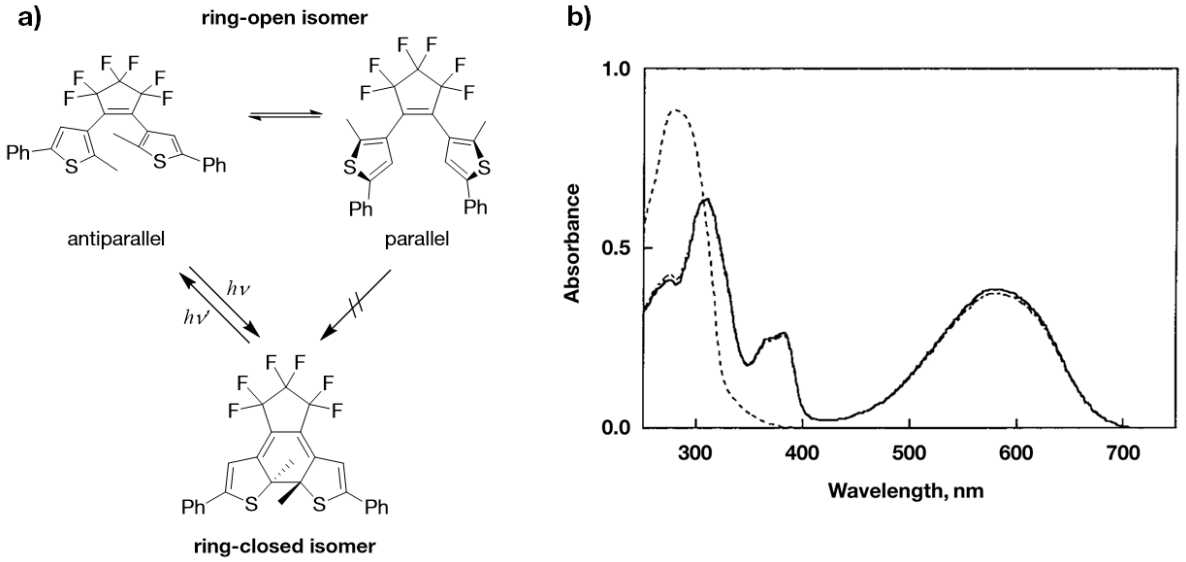

Figure 10. a) Scheme for the photochemical isomerisation of a prototype DAE. The reaction occurs by conrotatory cyclisation, therefore only from the antiparallel conformer. b) UV-Vis absorption spectra of the prototype DAE (c = 2.4 x 10^{-5} M in hexane): *dashed line*, ring-open isomer; *dotted line*, photostationary state obtained by UV (313 nm) irradiation; *black line*, ring-closed isomer. Figure b) was adapted from Ref.[57]

In such bi-stable organic compounds, the two isomers have dissimilar atom connectivity, hence they present a (small) change in conformation upon photoisomerisation. The most important difference between the open and the closed form concerns their conjugation: in case of the open-ring structure, conjugation is localised on the heteroaromatic rings, while in the closed isomer π-conjugation delocalises electrons over the whole backbone of the molecule, resulting in a lower HOMO-LUMO gap compared to its open counterpart. The first and most notable shift in the properties of the two isomers is their different absorption spectra. Typically, the open form of DAEs presents a strong absorption in the ultraviolet range of the electromagnetic spectrum (Figure 10), emerging from the presence of the two electronically decoupled, cross-conjugated heteroaromatic moieties. Upon photoisomerisation following UV light irradiation, a broad absorption band in the visible range is formed, related to the ring-closed DAE. The latter presenting its π-electrons delocalised over the whole molecular backbone. Due to the fact that both the isomers absorb in the ultraviolet range, generally a photostationary state (PSS) is formed, which composition depends on the reciprocal quantum yields of the forward and back reactions. Nevertheless, the most common diarylethene derivatives present a much lower quantum yield for the cycloreversion reaction, in most cases implying PSS with conversions to the ring-closed form above 90 %. On the contrary, upon visible light irradiation of the closed form, quantitative conversion to the open-ring isomer is observed, since the latter does not absorb at such wavelength.

Diarylethenes have seen their birth in the late 1980s upon serendipitous discovery by Irie and co-workers, whom soon recognised 1,2-dihetarylethenes as appealing thermally stable photochromes.[58] Since then, the group started to systematically develop the design of what

nowadays became one of the most employed photochromic units.[55, 59] A large corpus of research has been devoted to the discovery of the general structure-property relationships of this class of compounds: reviewing it does not constitute the focus of the present work, therefore only brief considerations over the most used structural units that show affinity with the work performed here will be given.

The term "diarylethene" is a general definition for stilbene derivatives, valid for all systems comprising two (hetero)aromatic rings bridged by an ethylene moiety. In general, it is useful to replace the ethylene unit with a cyclic moiety to avoid the $E \rightarrow Z$ isomerisation of the central double bond, which would hamper the desired photocyclisation reaction, representing a competitive excited state deactivation pathway. In principle, any cyclic structure possessing a double bond may be used as a bridge between the two hetaryl rings of a diarylethene. In this regard, the most used cyclic "bridging" units are the cyclopentene, perfluorocyclopentene, maleimide and maleic anhydride. Among them, undoubtedly the most widely employed is the perfluorocyclopentene bridge, since it typically allows to obtain both high switching efficiencies and acceptable photochemical stability.

Concerning the two rings providing the two double bonds of the 1,3,5-hexatriene unit, as previously mentioned the use of cyclic aromatic units ensures the endoergonic nature of the disrotatory cyclisation reaction, thus preventing the thermal pathway (thermal stability of both isomers). Together with this, it also gives rise to a π-electronic system which shows absorption in the near-UV range at reasonable wavelengths and with high extinction coefficients. The use of two 5-membered heteroaromatic rings with low stabilisation energy (such as furan or thiophene) generally allows the photochemical reaction to be reversible, and the two isomers to be thermally stable.[60] A variety of diarylethene derivatives having different hetaryl structures has been synthesised; however, furan and thiophene are by and large the most commonly used units, and especially the latter. Furthermore, the mode of connection between the heteroaromatic rings and the bridge strongly impacts the photochemical properties of DAEs. In case thiophene rings are used, if the connection with the bridging unit is made at the β-position of the hetaryl ring, the resulting diarylethene is called "normal type", while the ones with the hetaryl units connected at the α-position are named "inverse type". From now on we will refer to "normal type" diarylethene derivatives possessing thiophene hetaryl units, which will be called dithienylethene (DTE) photochromes.

Substituents of the heteroaromatic rings are also of crucial importance to establish the behaviour of DTEs. The substitution at the reactive carbon atoms (*i.e.* the two at which cyclisation occurs) is necessary to avoid irreversible oxidation of the ring-closed form resulting in subsequent aromatisation and formation of phenantrene analogues. This is therefore the principal reason for the presence of methyl groups in such position on the hetaryl rings. Other substituents could be used at those positions, nevertheless employing more bulky groups could result in the weakening of the C-C bond resulting from their steric hindrance, thus sometimes inducing (mostly) unwanted thermal reversibility to the closed isomer.[61] The use of substituents with an electron-donating character at those positions (*e.g.* methoxy groups) stabilises the closed-ring isomer, resulting in lower cycloreversion quantum yields.[62] On the contrary, the use of electron withdrawing moieties such as cyano groups favours the photochemical ring-opening reaction.[63] Also the substitution on the periphery of the heteroaromatic units could strongly impact the photochemical properties of DTEs. Concerning the latter, a large variety of

substituents has been used in the literature. As a general consideration, two different behaviours may be described. In first instance, the presence of strong electron accepting groups results in a general decrease of the thermal stability of the ring-closed form.[64] Conversely, the use of substituents leading to an enlargement of the π-conjugation of the ring-closed isomer yields a bathochromic shift of the absorption spectra of both forms. This on the one hand could potentially lead to the operation of DTEs with only visible light,[65] but on the other hand results in the stabilisation of the closed form, thus decreasing its cycloreversion quantum yield up to almost zero. In most cases however, it is desirable to decrease the quantum yield of the cycloreversion reaction, in order to obtain photostationary states showing a nearly quantitative conversion, which explains the reason why most DTEs present phenyl substituents on the periphery of the hetaryl rings. Substituents in such positions are also of fundamental importance as they provide anchoring points for implementing specific chemical functionalities to the photoswitches.

The mechanism of photoisomerisation of DTE derivatives has been thoroughly studied in the past decades, giving nowadays a detailed picture of their excited state properties.[59] Generally, upon excitation of the open-ring isomer, the closed form is generated within few picoseconds. This evidence, together with the temperature independence of the cyclisation quantum yield and the lifetime of the open-ring form, demonstrates the absence of barriers through the reaction pathway. Therefore, as previously mentioned, the quantum yield for the ring-closure reaction essentially depends only on the ratio between the antiparallel and parallel conformer in the ground state, as a conformational rearrangement cannot occur within the short lifetime of the excited state. Another consequence of the short lifetime of the excited state of the open-ring isomer is the substantial absence of radiative deactivation for such form. On the contrary, the photochemical ring-opening reaction is usually characterised by a much lower quantum yield compared to the cyclisation. This has been explained by observing that the depopulation of the excited state of the closed-ring isomer occurs through multiple pathways, including competitive non-radiative deactivation. In the case of the closed ring isomer moreover, the lifetime of the excited state as well as the cycloreversion quantum yield showed to be strongly temperature- and excitation wavelength-dependent, thus indicating the presence of an activation barrier on the potential energy surface of the excited state. Altogether with the widely investigated reaction pathway involving the singlet excited state of DTEs, such photochromic compounds were also found to undergo cyclisation through the triplet excited state. This could be induced for instance by the presence of heavy metal atom complexes, by excitation of their MLCT band, intersystem crossing and subsequent triplet energy transfer.[66] Population of the triplet state of the open-DTE could also be induced by intersystem crossing of the DTE itself,[66d] or by inter-[67] or intramolecular[68] sensitisation with an organic sensitiser. The triplet sensitisation pathway represents a very promising route towards the photoswitching of diarylethene derivatives, as, in alternative to the singlet photochemistry, it may be induced by irradiation with visible light, thus allowing to control the reactivity of DTEs in both ways avoiding ultraviolet light.

1.2.1. Examples of application of DTEs to remotely control functions

Among all, undoubtedly the most basic function that can be controlled by light stimuli, and falls directly under the definition of *photochromism* lies on the reversible change in colour occurring in such materials. DTE derivatives upon photoswitching from the ring-open to the ring-closed form undergo an alteration of their electronic energy levels resulting in a shift of their photophysical and redox properties. Alongside with the simple photochromism (open-DTE absorbs in the ultraviolet, while closed-DTE absorbs in the visible range of the electromagnetic spectrum, with a band that could be tuned between ~400 nm and ~700 nm depending on the molecular structure and its substitution pattern), DTEs could be used to perform a number of different functions according to the properties of their two states (*i.e.* different conformation and flexibility, delocalisation over the π-backbone, energy of the HOMO and LUMO molecular orbitals, energy of the excited states). Thanks to the superior photochromic properties of DTEs, such class of molecules is regarded as one of the most promising candidates for the construction of smart systems with remote-controllable functions, and wide academic interest has been dedicated to them in the last two decades.[55, 59] Generally, the strategies used to exploit DTEs and transduce their photochromism to a remotely controllable function fall within two main categories, the first based on their shape modulation, while the second is built upon the different electronic properties of the two stable forms. The former is however less employed, as the changes in shape and flexibility of the ring-open (o-DTE) and ring-closed (c-DTE) isomers is limited, compared to other photochromic units (*e.g.* azobenzene, *vide supra*).

Concerning the changes in molecular shape undergoing between o-DTE and c-DTE, the relatively limited conformational rearrangement occurring between the two forms remarkably allows DTEs to isomerise also within *single crystals*. In some cases, the mechanical stress experienced by the crystal can be translated to morphological changes of the crystalline habit, thus resulting in its shrinking, or bending. In such framework therefore, also DTE single crystals have been envisioned as potential photoactuators capable of converting light energy into mechanical work.[16a, 69]

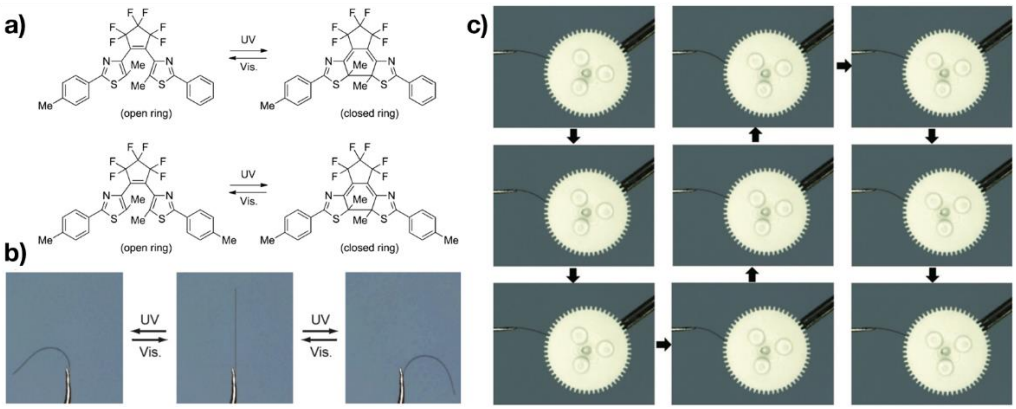

Figure 11. Single crystals of diarylethene derivatives may undergo photoinduced macroscopic shape variations. a) Diarylethene derivatives employed to make two-component mixed crystals, and their photochromism. b) Reversible bending (curling) of the rodlike two-component mixed crystal upon irradiation with UV light from the two sides. c) Gearwheel rotation operated by the rodlike crystal used as actuator, upon alternate illumination with UV and Vis light. Reproduced from Ref.[69b]

The variation in molecular flexibility between the open-ring and the ring-closed isomers has also shown to be applicable for the realisation of photoswitchable supramolecular systems. On the one hand, in the open-ring isomer the hetaryl fragments may rotate around the single bonds connecting them to the bridge, thus resulting in an equilibrium between the parallel and antiparallel conformer, meanwhile on the other hand the ring-closed form presents a planar shape, with a stiff character. Such a profound conformational change has been used to optically modulate the self-assembly of supramolecular systems in solution[70] and also on surfaces.[71] However, we will highlight here only few examples about supramolecular assemblies of diarylethenes on surfaces, being more relevant for the scope of the present work. The self-assembly on surfaces is also of particular interest, as the geometrical restrictions induced by 2D confinement could lead to the formation of chiral structures from achiral components, and this was shown also with achiral dithienylethene derivatives.[72] Concerning this, dithienylethenes (DTEs) have shown to be important systems for the study of the complex dynamics of surface-confined molecular self-assembly: in multiple experimental works performed by scanning tunnelling microscopy (STM) at the graphite-liquid interface, DTE derivatives have shown the possibility of giving rise to photoresponsive 2D self-assembled structures,[71] potentially allowing to tune the properties of the surface with light stimuli.[73] Interestingly, upon playing with the molecular design, Matsuda and coworkers showed that by tailoring the intermolecular interactions, the formation of surface-confined self-assemblies could occur following a cooperative behaviour. In such example, an "inverse type" DTE was used owning pending amide groups, together with long side alkyl chains (Figure 12).

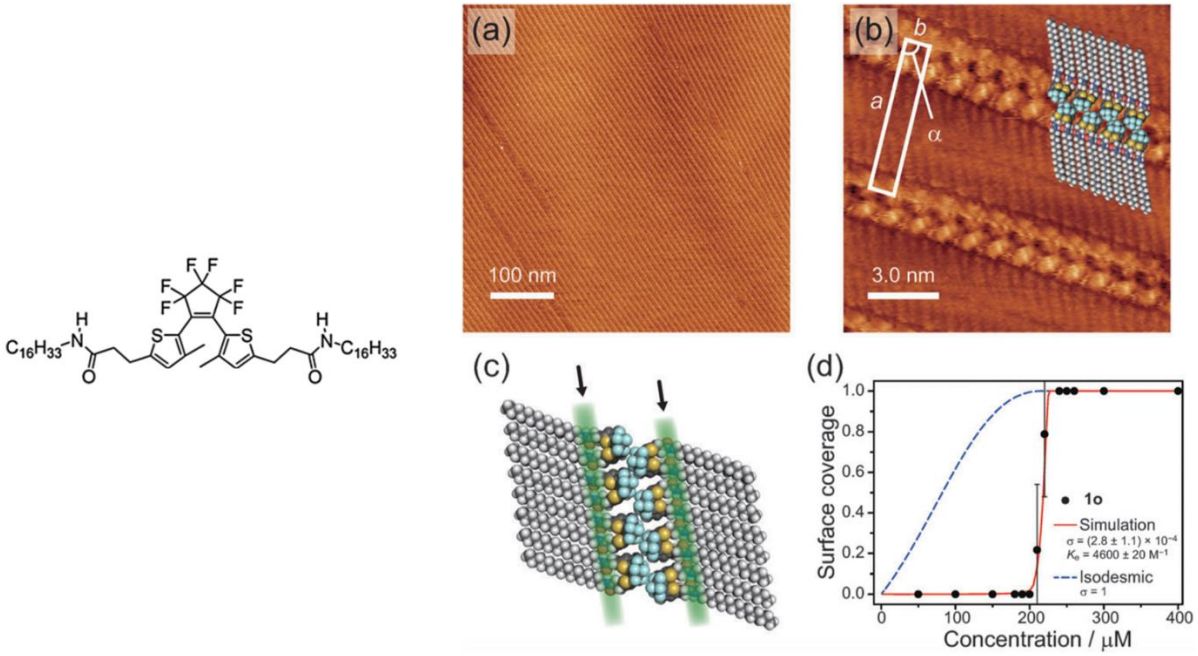

Figure 12. Cooperative 2D-confined self-assembly at the graphite-solution interface of "inverse type" DTE in the ring-open isomer, the system shows reversible ordering formation/disappearance upon in-situ irradiation. *Left*, Structure formula of the "inverse type" DTE in the open-ring isomer. *Right*, a) STM image of the ordering of the open-ring form. b) High resolution image. c) Molecular model of the assembly, showing the hydrogen bond network (green stripes). d) Concentration dependence of the fractional coverage of the open isomer. The red curve shows the best-fit curve for the theoretical model simulation assuming a cooperative behaviour. The dashed line denotes the simulation assuming an isodesmic model. Reproduced from Ref.[71b]

This substitution pattern allows the formation of stable self-assemblies at the graphite-solution interface due to the formation of intermolecular hydrogen bonding together with van der Waals

interactions between the surface and the long side alkyl chains. Interestingly, the assemblies formed by the open-ring isomer were seen to abruptly disappear upon *in-situ* irradiation, sign of the fact that the closed isomer was not capable to self-assemble in such conditions due to its conformation. Moreover, the abrupt formation/disruption of the surface-confined supramolecular structure upon varying the open-DTE concentration was seen related to the occurrence of cooperative aggregation on the surface. The emergence of the latter was demonstrated by studying the surface coverage upon varying the concentration of the open-DTE derivative and reproducing the experimental data with a model based on Langmuir-type adsorption, introducing two ordering formation processes with different equilibrium constants for nucleation and elongation (Figure 12).[71b]

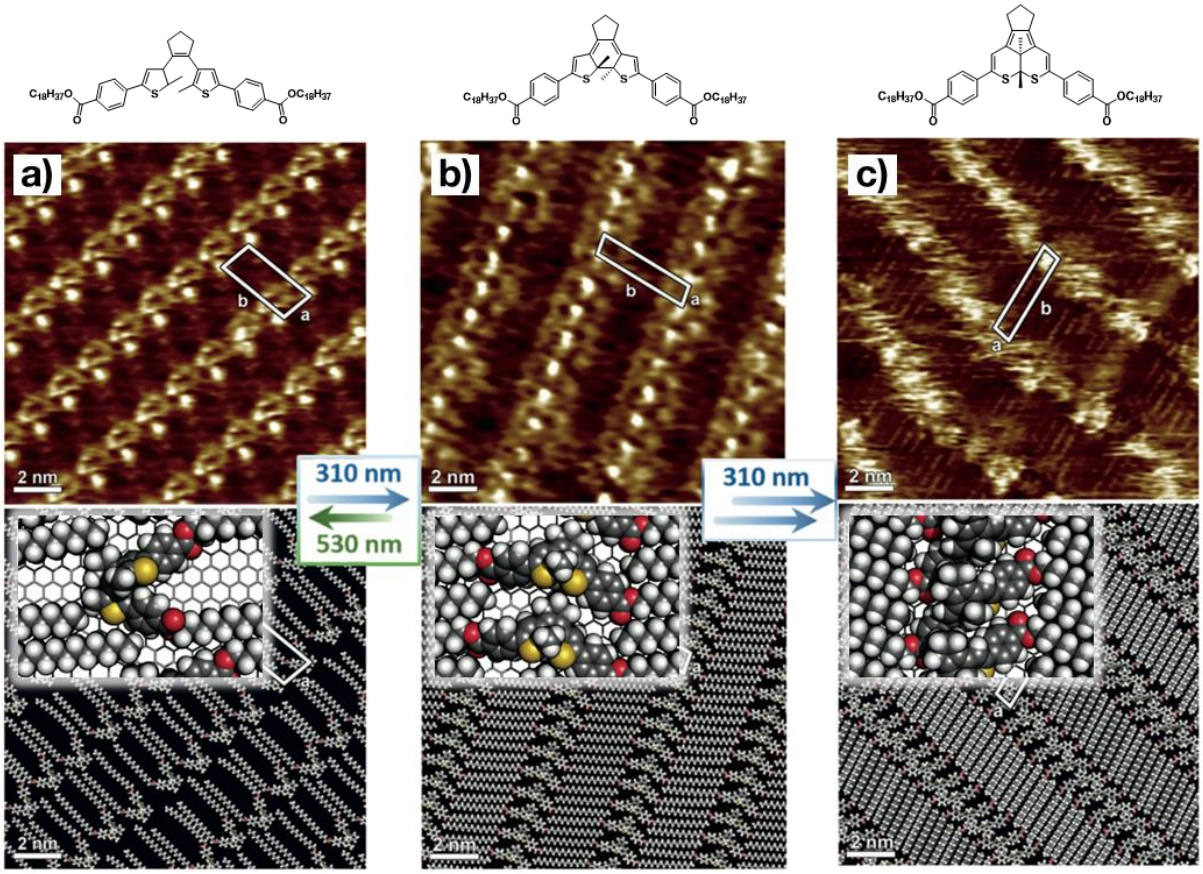

Figure 13. Surface-confined self-assemblies of a "normal type" DTE isomers visualised by STM at the HOPG-1-phenyloctane solution interface. *Top*, structure formulae; *middle*, STM images of monolayers of DTE; *bottom*, molecular packing models obtained from molecular mechanics simulations, with magnified structures (*inset*). a) Open-ring DTE isomer; b) closed-ring DTE isomer; c) annulated polycyclic DTE by-product. Reproduced from Ref.[71a]

Immediately after, Bonacchi *et al.* reported for the first time the interconversion between the self-assemblies of multiple states of DTE-based switches, evidencing submolecularly resolved patterns of a "normal type" DTE derivative in both the ring-open, ring-closed isomers, but also visualising the formation of the irreversible by-product of DTE cyclisation reaction by STM at the graphite-liquid interface. The interconversion between the assemblies formed by the different isomers was obtained by either *in-situ* and *ex-situ* irradiation. In such work, it was also shown that the annulated by-product shows a competitive adsorption behaviour with the closed-ring reversible isomer: it thus resulted that the self-assemblies of the former are thermodynamically preferred.

In further works reported by the group of Matsuda with "inverse type" DTEs, the researchers found that the self-assembly processes followed isodesmic or cooperative adsorption depending on the use of sidegroups allowing for weak or strong intermolecular interactions, respectively.[71d] Further works done in the same group were based on the STM investigation on the self-assembly of "normal type" DTE derivatives at the graphite-solution interface. The researchers could, analogously as reported by Bonacchi *et al.*, demonstrate that the formation of self-assembled surface-confined structures occurred for both the open, and closed-ring isomers, together with the irreversible by-product of the photochemical reaction. A quantitative analysis on the cooperativity of the formation of 2D assemblies of the three isomers showed that such an ordering phenomenon occurred alternatively with isodesmic, or highly cooperative processes depending on the shape of each. Moreover, also a mixing-induced cooperativity was visualised, as the presence of the isomer showing cooperative assembly together with the one assembling following an isodesmic model induced cooperativity into the formation of molecular ordering of the latter.[71e] Additionally, in a more recent work done by the same group, it was found that the racemic mixtures of (chiral) closed-ring DTE isomers were capable of forming molecular orderings with different 2D chirality, the latter being the result of the relatively small structural differences of the enantiomers.[71g] The precise control of cooperativity in surface-confined self-assembly represents an important instrument for gaining a deeper understanding over the complex phenomenon of molecular ordering on solid surfaces.

As previously mentioned, the isomerisation of DTE yields profound changes over the π-electronic system of the molecule, resulting in the variation of its molecular orbitals energy, together with the shift in energy of the ground and excited states of the two isomers. Such differences are responsible for the high interest that has been devoted in the last two decades towards the development of highly efficient and fatigue-resistant switches for their applications in opto-electronic devices,[2, 17, 74] smart materials,[75] or also for gating chemical reactions.[20, 76] Especially, the thermodynamic stability of the two isomers of DTE makes such photoswitches particularly promising for their application in the field of optical memories,[2, 55, 59] since the information written with a light stimulus can be retained.

Another interesting aspect regarding the modification of the π-electronic backbone following isomerisation concerns the possibility to reversibly couple or decouple electronically the two extremities of the switch. This strategy could be applied on the one hand to optically gate chemical reactions, by coupling electron donor or electron withdrawing substituent groups with other chemical functionalities present on the DTE. Recently it was demonstrated that the reactivity or the catalytic activity of certain functional groups can be modulated with light.[20, 76-77] The variation of the electronic delocalisation over the molecular backbone was also applied for completely different purposes (*e.g.* in molecular electronics), as DTEs could be used as photoactivated molecular junctions. This is based on the principle that the two isomers present different electrical conductance, thus can be used as switchable bridges for molecular junctions, being sandwiched between nano-scaled metallic conductors such as nanoparticle networks,[78] or covalently bonded between graphene sheets, to name a few.[74a]

Furthermore, as stated previously, the different structure of the π-backbone of the two isomers implies a shift in the energy of HOMO and LUMO molecular orbitals together with their energy levels. This could be employed to gate energy- or electron transfer phenomena within molecular or supramolecular architectures. In such a way, these photoswitches work as light-

triggered modulators, able to quench a selected excited state located on a chemical species close in space only when the switch resides in one of its two stable forms (usually the c-DTE following its reduced energy gap). This strategy has been used for instance to control photoinduced electron-transfer reactions on complex multicomponent systems,[79] or to quench the excited states of triplet sensitisers,[80], but above all it has been widely employed to modulate the light emission of luminophores connected to the photochromic switch (*vide infra*).[59] The latter strategy opened the doors to the application of DTEs in in highly attractive research fields such as all-optical information storage[81] and superresolution optical microscopy.[82] Importantly, DTEs have been widely employed to build light-controllable organic electronic devices, in combination with organic semiconductors.[2, 74b] The shift in energy of their HOMO and LUMO molecular orbitals for instance allowed for optically tuning the charge trapping in organic semiconductors, thus enabling to make organic thin film transistors (OTFTs) which could work as optically rewritable memory elements.[2, 17a]

1.3. Spiropyran

Spiropyran is a peculiar class of photoswitches, whose photochemical behaviour is also characterised by a pericyclic reaction. Spiropyrans, and closely related spirooxazines are capable to undergo a reversible photochemical cleavage of the C-O bond in the closed-ring spiropyran form to yield a ring-open form called merocyanine. Such a molecule consists of an indoline and a chromene moiety bound through a spiro junction and oriented perpendicularly to one another. A vast number of spiropyran and spirooxazine derivatives have been synthesised and studied since the discovery of such family of compounds. Among all, the most widely employed is the so-called nitrospiropyran, being a spiropyran derivative possessing a nitro group as substituent in 4-position with respect to the oxygen atom of the chromene moiety. The presence of such an electron withdrawing group enables to stabilise the ring-open form. From now on, we will therefore refer to spiropyrans as both the isomers of nitrospiropyran derivatives. The primary difference between the two isomers, analogously as all other photochromic compounds is the difference in their absorption spectra, following the changes over their π-electronic system occurring upon isomerisation. The mechanism of 1,6-electrocyclisation constitutes the basis of the photo- and thermochromic behaviour of such class of molecules, capable of converting between a colourless spirocyclic isomer to a deeply coloured merocyanine.[83] Contrarily from DTE switches, the reactions allowing for the interconversion between the ring-closed, colourless spiropyran (SP) and the ring-open merocyanine (MC) form could occur either thermally, at the ground state, or by deactivation of an electronically excited state following a photochemical pathway. In both cases, the rate-controlling stage of the isomerisation reaction is the cleavage of the C-O bond in the 2H-pyran ring, and is stabilised by following *Z-E* isomerisation around the spiro- and pyran-bridging double bonds. It thus follows that the MC form may exist as several *E*/*Z* isomers obtained by rotation around those. Nevertheless, due to the low thermal stability of the conformation obtained with the central *Z* double bond, only the form(s) showing

the central double bond in *E* are observed at room temperature, and in most cases the thermally most stable isomer is the so-called *TTC* form (Figure 14).[84]

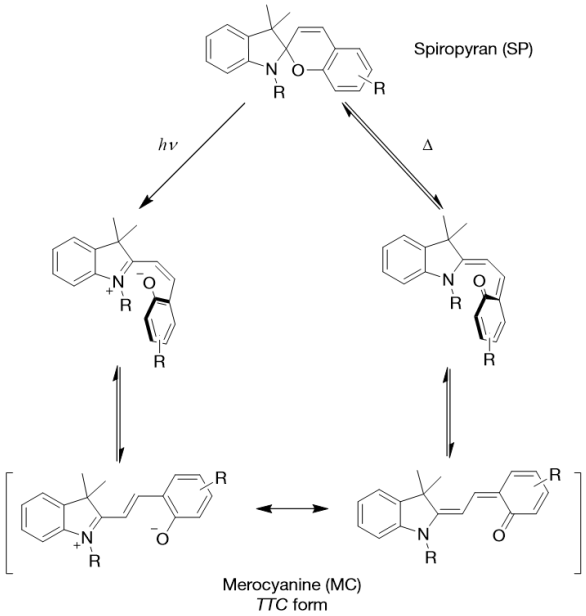

Figure 14. Simplified mechanism of photochemical (*left*) and thermal (*right*) isomerisation pathways for spiropyran derivatives.

In nonpolar solvent solution, spiropyran derivatives exist in the ring-closed isomer, nevertheless thermal ring-opening reaction could occur by increasing the polarity of the environment. Such thermal equilibrium does not depend only on polarity, but also on the solution concentration, as MC form has strong tendency to aggregation (by forming either H- and J-aggregates) resulting in its stabilisation. Thus, it is important to state that the isomerisation reaction occurs in thermal equilibrium conditions, which position strongly depends on the external conditions, which is a factor that should be kept in mind when employing such photochrome for specific applications (*e.g.* when anchoring it to a surface). The ring-closed SP isomer presents two most intense transitions in the ultraviolet range, being the one located at $\lambda_{max} \approx 270 - 300$ nm relative to the π-π^* transition of the indoline moiety, while the one occurring at $\lambda_{max} \approx 320 - 350$ nm corresponding to the chromene unit.[85] Importantly, the ring-opening reaction could also occur by means of photochemical stimuli, upon UV irradiation of the SP isomer ($\lambda = 365$ nm). Ring-opening occurring by either heterolytic C-O bond cleavage, or as 6π electrocyclic reaction, lead to the zwitterionic or quinoidal MC forms, respectively, being the two resonance structures. The relative contribution of the two resonance forms depends on the environment, as non-polar media would stabilise the quinoidal form, and *vice versa* would occur in polar media. The MC has a planar structure, characterised by an extended π-conjugated system. It thus results intensely coloured, since its broad absorption band in the visible spectrum, located at $\lambda_{max} \approx 550 - 600$ in non-polar environment. Following from the presence of the two resonance structures, the MC isomer presents a strong solvatochromism: in apolar media, the stabilisation of the quinoidal structure results in a decrease of the energy gap between the ground and excited states, resulting in a batochromic shift of its absorption band, phenomenon named negative solvatochromism.[85] Additionally, the merocyanine form on the contrary of the ring-closed spiropyran presents a strong emission band upon its excitation in the visible range, with a maximum located at $\lambda_{max} \approx 650$ nm.

The first step of the photochromic reaction in spiropyran derivatives involves the cleavage of the C-O bond upon deactivation of the excited state. For nitrospiropyrans, the ring-opening through C-O bond cleavage occurs in the triplet excited state.[83] Electronic excitation is followed by intersystem crossing to a short lived triplet state of the ring-closed isomer SP; the bond cleavage is followed by the formation of the "perpendicular", *Z* merocyanine form (Figure 14, centre) in the triplet state, in equilibrium with the triplet of the *E* isomer. At this stage, de-excitation occurs by quenching of the triplet state with molecular oxygen, followed by the thermal equilibria for the isomerisation around the double bonds of the MC to obtain the most stable *TTC* isomer. The presence of the nitro- group on nitrospiropyrans has important effects on their photochromism (together with the stabilisation of the MC in the ground state) as it both enhances the quantum yield for the SP → MC reaction (0.7 – 0.9 in apolar solvents[83]), increasing the quantum yield of intersystem crossing. The latter nevertheless could be a detrimental factor for the durability of the photochrome, as the quenching of the triplet excited state in non-deaerated solution results in the generation of singlet molecular oxygen, and thus degradation of the photochromes via oxidation.

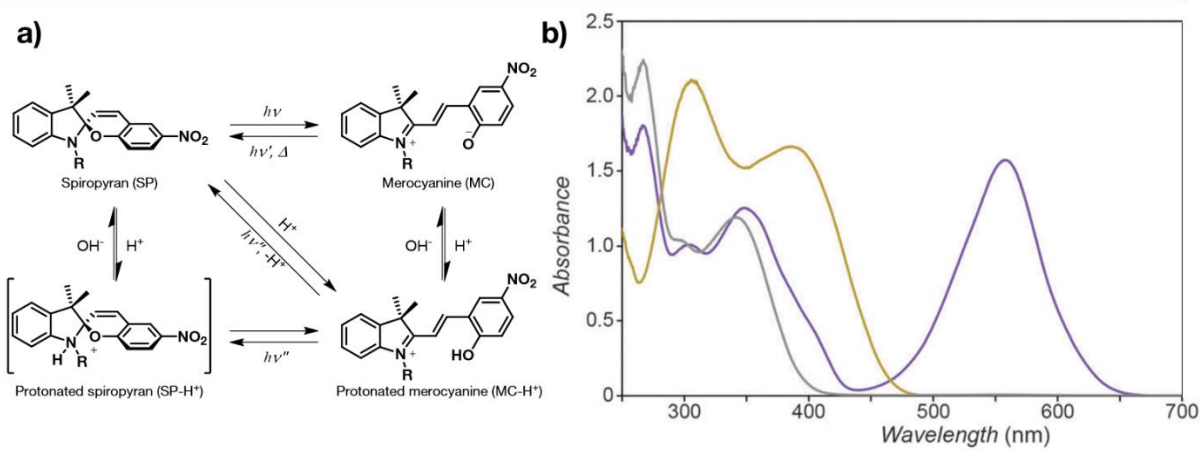

Figure 15. a) Schematic picture of the thermal and photochemical isomerisation of nitrospiropyrans, including acidochromism. b) UV-Vis absorption spectra of the prototype nitrospiropyran 1',3',3'-trimethyl-6-nitrospiro[chromene-2,2'-indoline] in acetonitrile (c = 2.3 x 10^{-4} M). *Grey trace*, no irradiation. *Purple trace*, UV PSS (λ = 365 nm). *Yellow trace*, addition of 20 eq. of HCl. Figure b) reproduced from Ref.[85]

Such a photoswitch is highly appealing because of the markedly different physicochemical properties of the two isomers. Most importantly, the formation of a charge-separated species in the MC is the reason for its interesting large variation of molecular dipole moment upon photoisomerisation from the ring-closed neutral spiropyran (SP) form to the open, metastable zwitterionic isomer merocyanine (MC).[86] It has been shown that the molecular dipole moment of SP lies in the range of $\mu \approx 4$ - 6 D, while for the MC this is largely increased to $\mu \approx 14$ - 18 D. Moreover, upon isomerisation such molecule shows consistent conformational changes, as SP displays a more bulky character if compared to the planar, rigid MC. As previously said, the merocyanine isomer, on the contrary of its ring-closed isomer is also conjugated, therefore planar, intensely coloured ($\lambda_{max} \approx$ 550-600 nm) and fluorescent ($\lambda_{em,\ max} \approx$ 650 nm). The open merocyanine form is nevertheless metastable and shows fast thermal cycloreversion reaction to the closed form when in diluted solution at room temperature (in apolar solvents). Moreover, such peculiar photochromic architecture is not only sensitive towards photochemical stimuli, as the merocyanine isomer is also significantly more basic than SP. Protonation of MC results in

the formation of its conjugated acid MCH^+, which has a distinctive absorption spectrum, different from SP and MC, having a band located at $\lambda_{max} \approx 400$ nm. Protonation of the hydroxyl group of the open merocyanine form leads to its stabilisation, resulting in strong acidochromism.[84] For nitrospiropyran derivatives, the MCH^+ has a rather acidic character, with a $pK_a \approx 2.25$, being the phenoxide anion stabilised by the 4-nitro group.[85] Finally, the merocyanine form has also higher affinity towards different chemical species such as other zwitterions and metal cations.[85] Following these large variations in the physicochemical properties of SP and MC, together with their responsiveness to multiple stimuli (*i.e.* photochromism, thermochromism, acidochromism, solvatochromism), nitrospiropyrans have been widely applied to realise stimuli-responsive materials.[53, 85]

1.3.1. Examples of application of spiropyrans to remotely control functions

Spiropyran-based photochromic units have been widely used to control the stability of colloidal dispersions upon decorating nanoparticles on their surface with monolayers containing such switch.[87] This is typically achieved thanks to the dissimilar physicochemical properties of the two isomers SP and MC. The non-polar character of the ring-closed SP isomer is in contrast with the highly polar, open-ring MC form. The reversible dispersion-flocculation phenomenon on the one hand is due to the fact that the SP form stabilises the dispersion in apolar solvents, while on the other hand the MC isomer in such environment has a strong tendency to associate into aggregates with a stack-like arrangement, the latter driven by dipole-dipole and π-π stacking interactions. In apolar solvents, without addition of acid excess the thermodynamically stable SP form can be photochemically converted to MC by ultraviolet irradiation ($\lambda \approx 365$ nm), while the reverse ring-closure reaction is promoted by visible light ($\lambda > 500$ nm). Notably, due to the known large two-photon cross section of SP and MC,[88] the photochromic reactions can also be driven by two-photon excitation in the vis-NIR range.[87c] Spiropyrans could also be used to trigger the assembly/disassembly of gold nanoparticles that were not grafted with such photoswitch. In an example reported by Kundu *et al.*,[89] non-photoresponsive gold nanoparticles functionalised with ligands exposing COOH moieties were dispersed in methanol with the presence of strong acids. It was found that upon addition of spiropyran and subsequent formation of protonated merocyanine form, the event was followed by nanoparticle aggregation. Such molecule allowed to control by light stimuli the release of H^+ in solution, event which was followed by reversible dispersion/aggregation of the colloid. Analogously, this was obtained also in PEG gels and their films showed to be reversibly photorewritable.

In few literature examples, plasmonic systems have been combined with spiropyran-based photochromes, and the appearance of exciton-plasmon coupling effects was observed upon inducing the SP → MC isomerisation,[3b, 90] in some cases also in the ultrastrong coupling regime.[3a]

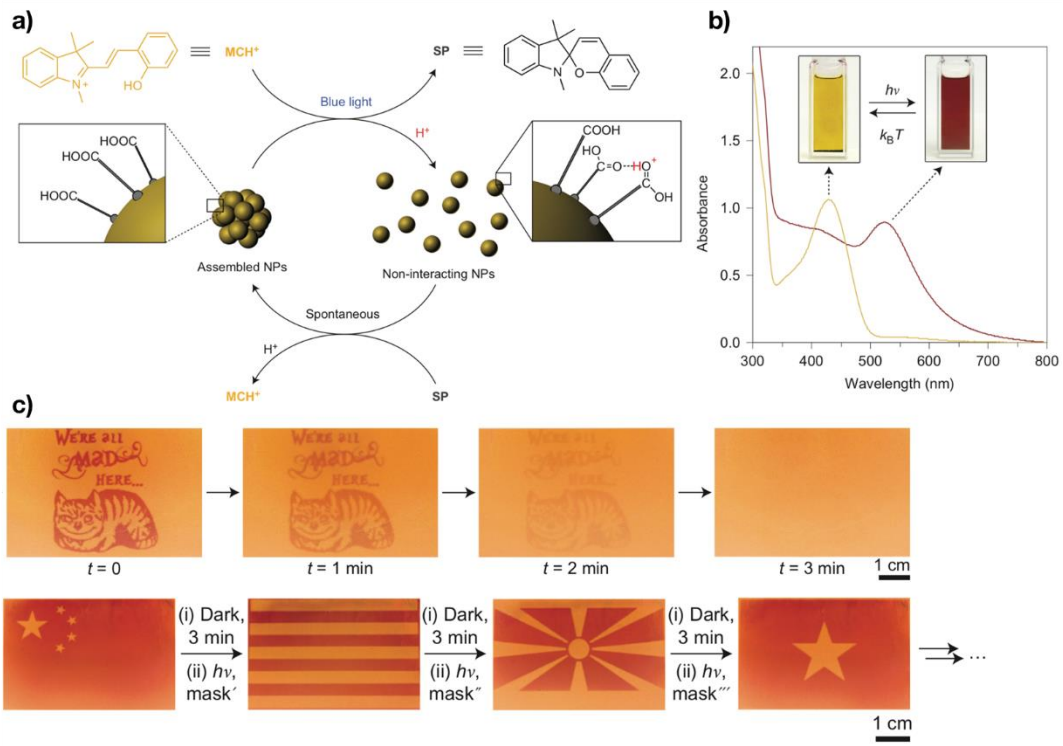

Figure 16. a) Schematic picture of the light-driven reversible (dis)assembly of COOH-functionalised AuNPs by photoacid effect. b) UV-Vis absorption spectra and photographs of: *red*, AuNPs dispersions in MeOH, showing the characteristic surface plasmon resonance band of the gold colloid; *yellow*, aggregated AuNP precipitate, absorption band related to MCH^+. c) Photographs of disappearing images with time, obtained by structural illumination of a PEG gel containing AuNPs and spiropyran derivative. Reproduced from Ref.[89]

2. Multi-photochromic systems

Recently, with the aim of increasing the complexity of the molecular-scale events attainable with synthetic molecular systems, an increasing interest has been devoted to the integration of more than one photochromic unit within one single molecule, or more broadly speaking "object". Such strategy is seen highly appealing since it could potentially enable to obtain a system switchable between 2^n states, where *n* is equal to the number of *distinguishable* photochromic units, in contrast to a simple photochromic compound, which is typically a binary "on/off" switch, thus it could allow to outrun the typical bistability of standard molecular switches.[91] The aims of such a challenge are multiple: firstly, it results obvious to understand how a system containing multiple and fully functional switching units would return a more highly contrasted photoresponse as a result of the conversion between the initial *A* to the *B* form of each switch. This system will be conceptually analogous to its traditional single-switch counterpart if the various photoproducts are not distinguishable from one another, nevertheless showing more promising properties from the applicative point of view, as the contrast between the initial state and the one obtained in photostationary conditions would be increased. Secondly, as previously mentioned, a multiphotochromic switch could also allow its conversion from an initial *A* state, to an ensemble of several *B*, *C*, *D*, *etc.* photoproducts, thus, if the latter are distinguishable as they show remarkably different properties, this approach could provide access to more states, therefore to more complex phenomena in comparison with a simple photoswitch. Going further, in certain cases the interaction between the photochromic units will result in the appearance of emerging properties that are not shown by the single photoswitches, thus providing a *synergistic effect* between the photochromes as, for instance, in a biphotochromic molecule comprising two units that can be converted each between an *A* to a *B* state, the interaction between the *B* units will result in the occurrence of a *C* state.[92] Ultimately, undoubtedly the most highly appealing challenge in the development of multiphotochromic architectures consists in the inclusion of (individually addressable) switches with different nature within the same compound, in order to realise a functional system which could be selectively switched between multiple states in orthogonal fashion, thus with a wavelength-selective control.[4a, 93]

Conceptually speaking, the idea of combining multiple photoswitches in intermolecular fashion may appear a simple operation, nevertheless its practical realisation is complicated by several factors. Realising multi-photochromic systems in which all the possible isomeric states are individually addressable showed to be a challenging task, since the successful isomerisation of the photochromic units could be hampered by several factors, *e.g.* energy transfer between the different subunits, or electron delocalisation on the whole molecular backbone. Therefore, in recent years several theoretical and experimental studies have been performed in order to rationalise the optical properties of multiphotochromic systems, and to determine the main structural parameters determining their photochromic performance, with the aim to realise "intelligent" architectures, featuring each single unit being "aware" of the state of the others, thus to obtain supramolecular systems which properties do not only correspond to the sum of each part. Among these, the role of the bridging unit between the photoswitches has been regarded as of main importance, and in particular a reduction of the electronic communication

between the switches, but also their spatial separation were seen fundamental to preserve their photochromism.[39, 91, 94]

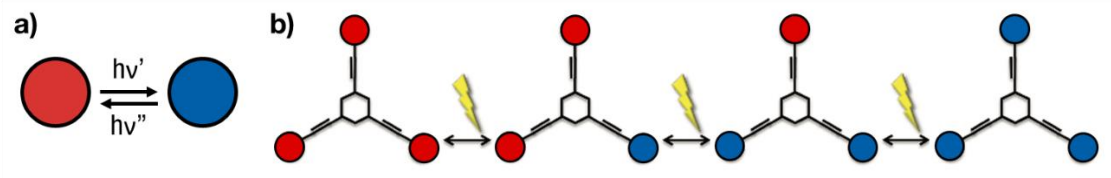

Figure 17. a) Sketch of a binary photoswitch. b) Simplified scheme of multi-photochromic system.[91b]

Central importance in the properties and performance of multi-photochromic systems is undoubtedly held by the linker between the functional units, as this determines the entity of the through-bond, and trough-space interaction between them. Two simple -yet prototypical- examples of systems containing multiple photoswitches highlighting the importance of their chemical connection were given recently by Credi *et al.*[39a] and Hecht *et al.*[39b] with bis(azobenzene) derivatives. Those systems showed that in order to retain good photochromic performance it is crucial to decouple electronically the switches, as in the opposite case the extended π-conjugation would lead to a dramatic decrease photoreactivity of the systems, demonstrated by both low photoisomerisation quantum yields and fraction of photoproduct at the photostationary state(s).

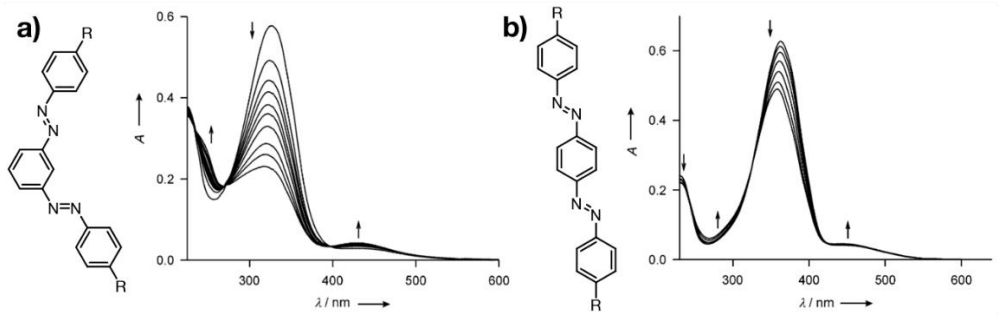

Figure 18. a) Bis(azobenzene) compound realised by connecting the chromophores in 1,3-position on a central benzene ring, showing electronic decoupling of the photochromic units, the UV-Vis absorption spectral variation highlights the independent behaviour of each switch by the appearance of isosbestic points and a large conversion at the PSS. b) Bis(azobenzene) characterised by 1,4-substitution pattern. The conjugation between yields limited photochromic performance. Reproduced from Ref.[39a]

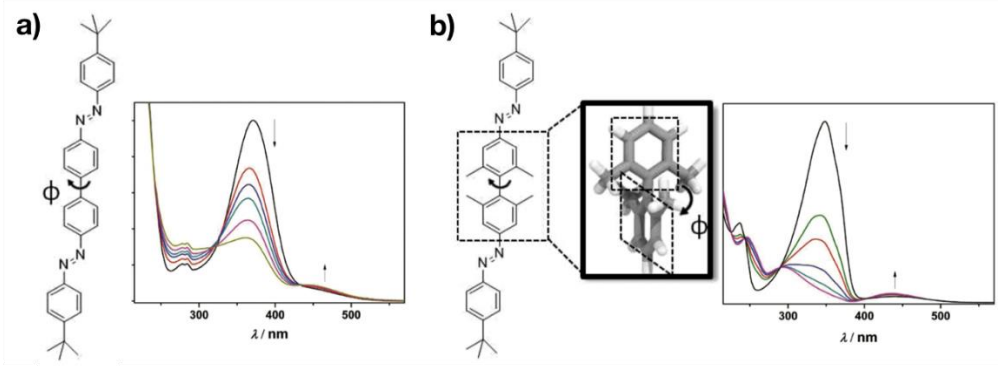

Figure 19. Bis(azobenzene) derivatives obtained by increasing the dihedral angle (Φ) of the central covalent bond connecting the photochromic units. a) $\Phi \approx 37$ °, showing partial electronic delocalisation over the π-electronic backbone, yielding limited photochromism. b) $\Phi \approx 90$ °, forced by the sterical hindrance of the α-methyl substituents with respect to the connecting bond; electronic decoupling results in good photochromic performance, with ca. 95 % of the *Z,Z* isomer at the PSS. Reproduced from Ref.[39b]

In principle, the synthesis of fully functional molecular and supramolecular systems integrating more than one photochromic unit within the same backbone should allow to individually address each state by irradiation with light at different wavelength, if the isomers of each photochrome have distinct spectral features (multicolour photochromism). Nevertheless, the development of orthogonally-responsive systems is still in an embryonal phase.[4, 93] Conversely, if all the photochromes in the molecular backbone are equivalent, one could obtain as a result a more highly contrasted photoresponse.[95] The implementation of multiple switches in the same covalent scaffold showed to be a not trivial task, since in order to guarantee the photoactivity of all units, interchromophore interactions such as conjugation or energy transfer must be avoided.[9la, 94] So far, the main achievements in the field have been made towards the synthesis of multiphotochromic units bearing equivalent photochromes, not individually addressable. However, the inclusion of multiple photochromic units within the same compound has shown to be useful to increase the contrast in the overall photoresponse of the system, thus making such molecular devices more appealing for their application in the field of optical memories and photoactivated fluorescent switches. We already discussed on how multi-photochromic systems are sensitive to electronic delocalisation in π-conjugated system, being the presence of the latter detrimental to the desired photoisomerisation reaction. This is particularly delicate for systems containing multiple diarylethene (DTE) units,[96] as complete closure is usually inhibited by the occurrence of intramolecular energy transfer between o-DTE and c-DTE fragments, thus preventing full conversion to all-closed state.[9l] Indeed, the choice of a suitable bridging unit between the switches is key towards the realisation of systems showing suitably large conversions.[97] Photochromism is generally prevented when the switches are embedded into a large π-conjugated system, following the emergence of low-lying excited state manifolds which usually do not lead to the photoreaction pathway. Multi-DTE systems have been extensively investigated,[9la] by examining the role of bridges of various nature, including for instance alkynyl,[98] arenyl,[97] or silyl[99] moieties and metal complexes[100] as spacers.

3. Surface-confined self-assembly

On-surface self-assembly is an intriguing phenomenon involving the physi- or chemisorption of molecular species on solid surfaces: key for the formation of structures presenting order on the molecular scale is the reversibility of the interaction between the adsorbate and the surface involved. This adsorption process takes advantage of supramolecular chemistry and intermolecular interactions allowing to form 2D crystalline monolayer structures under chemical equilibrium conditions (or in a kinetically trapped state), which topology is the result of a subtle balance between a large number of factors, being intermolecular interactions and molecule-substrate adsorption of first and foremost importance.

In recent years, scanning tunnelling microscopy (STM) has been widely used as a powerful tool to study molecular systems, following its unparalleled ability to achieve sub-molecular scale resolution in real space. The assembly of suitably designed molecular species into periodically ordered structures on the surface of an electrically conductive, crystalline substrate has been investigated by STM either in ultrahigh vacuum (UHV) conditions, or at the interface between the substrate and a solution.[101] The latter experimental technique literally allowed to visualise the phenomenon of molecular self-assembly driven by noncovalent interactions.[102] Recently, also several examples of covalently bonded bidimensional structures such as covalent-organic frameworks (COFs), or 2D polymers were widely investigated with such technique.[103] Especially STM at the solid-liquid interface allowed to achieve a detailed insight into the phenomenon of molecular self-assembly on crystalline substrates such as Au(111), or on the basal plane of highly ordered pyrolytic graphite (HOPG). Such an experimental technique, allowing to investigate the formation of 2D crystalline assemblies (residing on global or local minima of the Gibbs free energy landscape) at the interface between the substrate and the supernatant solution literally enables to visualise supramolecular chemistry at surfaces, and is of particular interest for the study of host-guest, or stimuli responsive systems.[71a, 71b, 71e, 104]

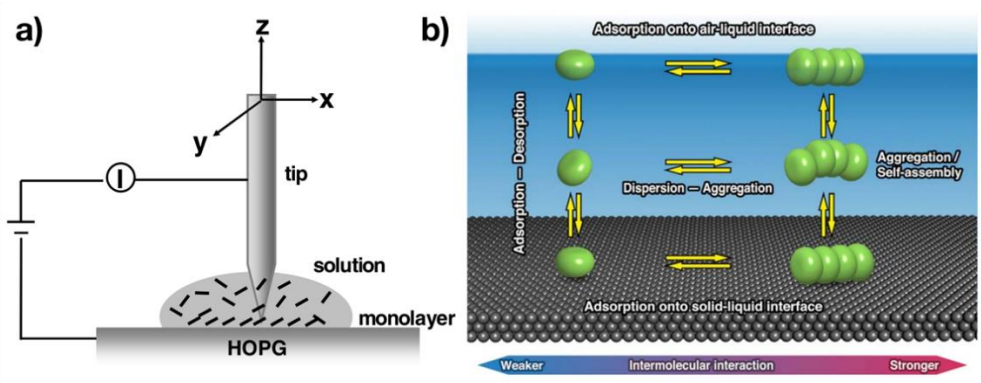

Figure 20. a) Scheme of the experimental set-up for performing STM at the graphite (HOPG)-liquid interface. b) Schematic picture of the chemical equilibria occurring in homogeneous phase and at the various interfaces. Picture a) and b) reprinted from Ref.[105] and Ref.[106], respectively.

In the past years, numerous studies have been performed on the self-assembly of rigid aromatic carboxylic acids in two-dimensional crystalline structures, with the use of STM at the interface between graphite and their solutions.[5b, 107] The study of simple di- and tricarboxylic acids such as isophthalic, terephthalic and trimesic acid showed their propensity to form periodic

structures held together by noncovalent supramolecular interactions such as hydrogen bonding. Taking advantage of the directionality of such noncovalent interaction, the self-assembled structure morphology was seen to depend on the reciprocal position of the carboxyl groups on the molecular backbone, and the integration of an increasing number of carboxyl moieties was seen to lead to their bidimensional assembly into lattices with intriguing complexity and symmetry features.

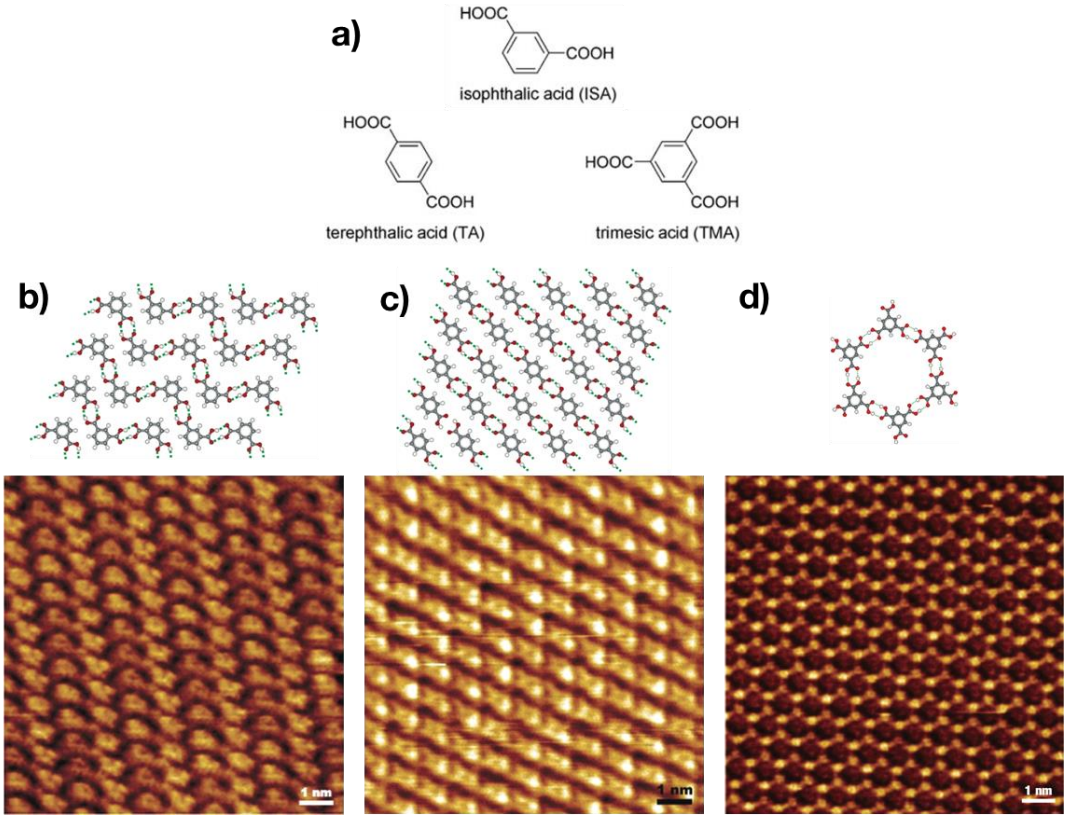

Figure 21. a) Structure formulae of isophthalic, terephthalic and trimesic acid. b) Isophthalic acid monolayer on HOPG, showing the characteristic zigzag arrangement, due to the presence of hydrogen bonds. bottom, STM topography; top, molecular mechanics simulation. c) Terephthalic acid monolayer on HOPG, showing hydrogen bonded linear chains. *bottom*, STM topography; *top*, molecular mechanics simulation. d) Trimesic acid monolayer on HOPG, forming hydrogen bonded hexagonal networks, *bottom*, STM topography; *top*, molecular mechanics simulation. Figure b-d) taken from Ref.[107a] and Ref.[5b], respectively.

Trimesic acid (1,3,5-tricarboxylic acid) represents the most prototypical and widely studied example of C_3-symmetric building block for the construction of H-bonded supramolecular networks. Several studies performed with STM either in UHV and at the solid-liquid interface showed its tendency to form hexagonal honeycomb structures, which symmetry is of great interest for the realisation of nanoporous networks.[108] Lackinger *et al.* studied the self-assembly of C_3-symmetric carboxylic acids on HOPG (using heptanoic, octanoic or nonanoic acid as solvents) with increasingly large aromatic cores, showing that it was possible to obtain large area crystalline domains of hexagonally packed molecules with progressively larger "cavities", compared to trimesic acid. The experiments showed that the main intermolecular interaction allowing the formation of such monolayers was the formation of 2-fold cyclic O-H···O hydrogen bonds between the terminal carboxylic acid moieties.[5b] The geometry of such ideal hydrogen bonding pattern yields the strongest possible intermolecular interaction between two carboxylic acid moieties.

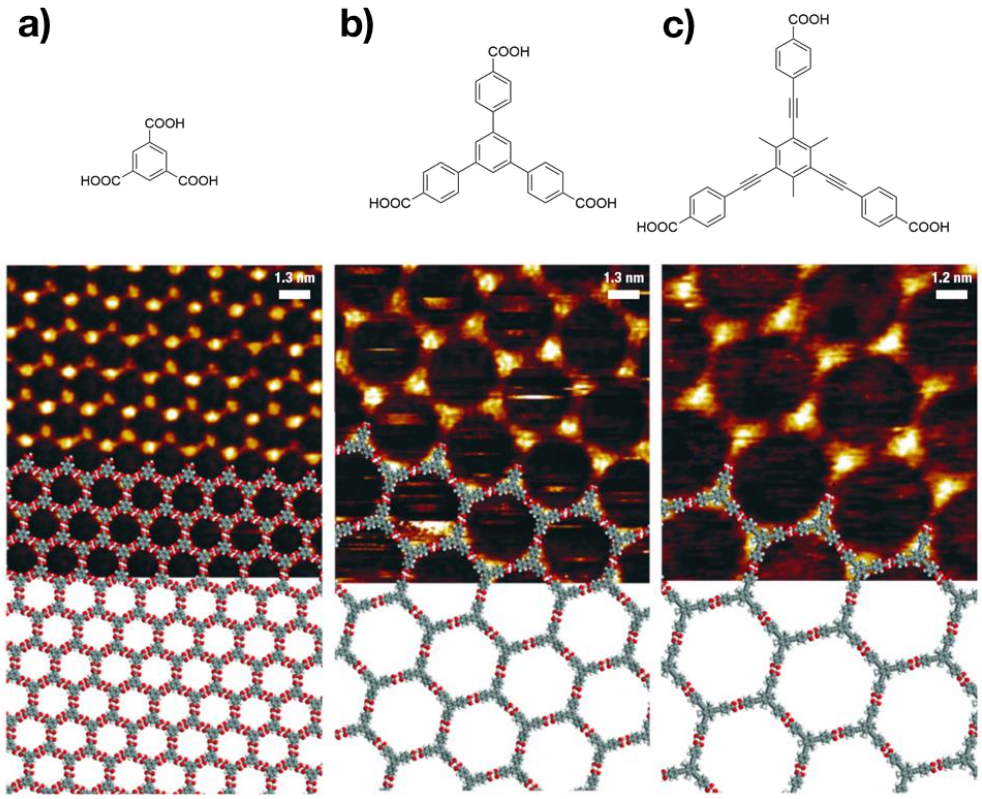

Figure 22. C_3 symmetric aromatic tricarboxylic acids giving rise to isostructural networks at the graphite-nonanoic acid solution interface. The formation of hexagonal structures is due to the intermolecular interactions dominated by hydrogen bonding (formation of carboxylic acid dimers). a) *top*, Trimesic acid structure formula; *centre*, STM topograph with superimposed model of the molecular arrangement. b) *top*, Structure formula of 1,3,5-benzenetribenzoic acid; *centre*, STM topograph with superimposed model of the molecular arrangement. c) *top*, Structure formula of 1,3,5-tri(4-carboxyphenylethynyl)-2,4,6-trimethylbenzene; *centre*, STM topograph with superimposed model of the molecular arrangement. Reproduced from Ref.[5b]

Nonetheless, the driving force for the formation of such self-assembled supramolecular systems on the surface of crystalline substrates is the result of a complex interplay between anisotropic intermolecular interactions (*e.g.* hydrogen bonds), and isotropic van der Waals forces between the molecule and the substrate, together with the contribute of solvation, since the crystalline monolayer is in thermodynamic equilibrium with the supernatant solution (or alternatively in a kinetically trapped state).[109] Following the known tendency in Nature to avoid energetically unfavourable voids when forming crystalline structures, the question if the aforementioned nanoporous 2D honeycomb geometry could be retained upon further increase of the building block size arose.[110] Further experimental work corroborated by molecular mechanics simulations done on the larger carboxylic acid 1,3,5,-tris[4'-carboxy(1,1'-biphenyl-4-yl)]benzene (TCBPB) showed the occurrence of three polymorphs in the 2D crystalline packing on HOPG, with the exclusion of the aforementioned, "ideal" hexagonal, honeycomb lattice (Figure 23). The appearance of multiple hydrogen bonding patterns included the observation of weaker C-H···O hydrogen bonds together with simple O-H···O ones. The experimental evidence was explained by *in silico* estimation of the thermodynamics of the self-assembly of TCBPB on graphite, showing that the "ideal" honeycomb shaped pattern was less thermodynamically stable compared to the polymorphs experimentally visualised. The studies evidenced that the molecule-substrate interaction for the formation of the densely packed monolayers experimentally shown has a larger contribution in the overall adsorption free energy compared

to the stabilisation followed by forming the "ideal" 2-fold cyclic O-H···O hydrogen bonds between the terminal carboxylic acid moieties.

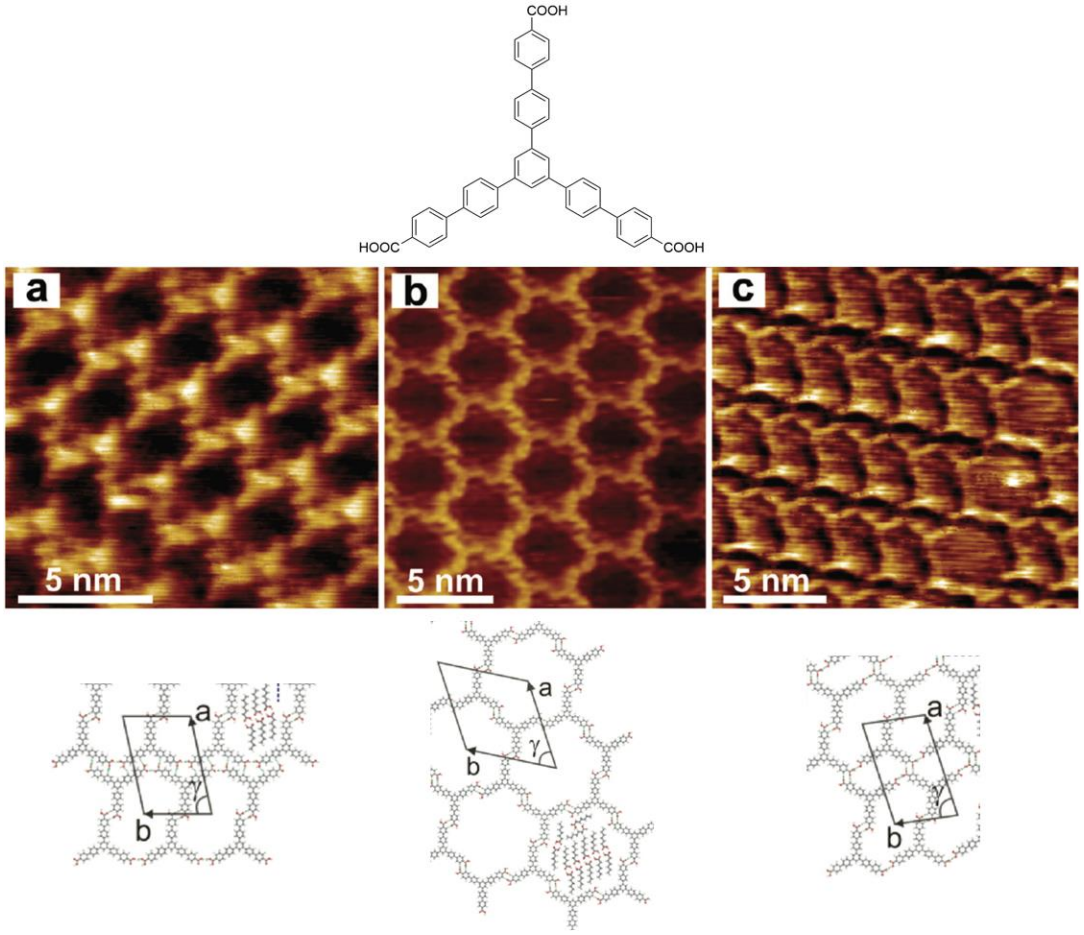

Figure 23. *Top*, structure formula of 1,3,5,-tris[4'-carboxy(1,1'-biphenyl-4-yl)]benzene (TCBPB). *Middle*, STM topography of the TCBPB monolayers at the HOPG-heptanoic acid solution interface. *Bottom*, molecular packing models. a) Oblique-I polymorph. b) Displaced chickenwire polymorph. c) Oblique-II polymorph. Adapted from Ref.[110]

Investigation on the isomerisation of azobenzene with STM has always been an appealing task for surface scientists,[111] nevertheless visualisation of the *Z* isomer at the solid-liquid interface between graphite and its solution showed to be particularly challenging following its non-planar, kinked geometry, which yields unfavourable van der Waals interactions with the underlying surface.[112] Therefore, the use of several artifices such as suitable functional groups, or system geometries allowing the self-assembly of both *E* and *Z* isomers on graphite have demonstrated to be effective, but sometimes making their visualisation a cumbersome task.[73, 112] In a first example, De Feyter *et al.* studied the dynamic assembly of an azobenzene-containing photochromic molecule characterised by the presence of long alkyl chains and an isophthalic acid unit 5-[ω-(4′-dodecyloxy-4-azobenzenexy)dodecyloxy]isophthalic acid. The studies showed that it was possible to obtain monolayers containing the *Z* isomer of the molecule with codeposition of solvent molecules only by *ex-situ* irradiation, also highlighting the lower stabilities of such domains with respect to the regions containing monolayers of the *E* isomer.[113] Interestingly, Shen *et al.* succeeded in demonstrating the isomerisation of a photochromic system containing multiple azobenzene units in the same molecular backbone by observing the transition between various isomeric forms of photoswitchable macrocyles with STM at the solid-

liquid interface (Figure 24). The photoswitchable architecture consisted of a flexible macrocyclic architecture containing four azobenzene units, which isomerisation led to large conformational rearrangements. In such examples, a host-guest complex made by a four azobenzene-containing flexible macrocycle and 1,3,5-tris(10-Carboxydecyloxy)-benzene (TCDB) showed to form large area, self-assembled 2D crystalline domains at the interface between HOPG and their solution in heptanoic acid. UV-light irradiation of the aforementioned co-assemblies positively led to the observation of various domains with different morphology, demonstrating that the photoinduced conformational change of the macrocycle was effective in modifying the order of the system, moreover further studies were performed with the use of a guest, showing the possibility to perform a light-induced guest release.[114] In a few recent examples, De Feyter and colleagues demonstrated that alkoxylated dehydrobenzo[12]annulene derivatives constitute excellent molecular building blocks to realise two-dimensional porous patterns at the liquid-solid interface, which could be used to perform host-guest chemistry in two-dimensional space.[104b] They discovered that appending azobenzene moieties to such structures could enable to reversibly modify the size of the nanopores of the network, allowing to release co-adsorbed guest molecules.[73]

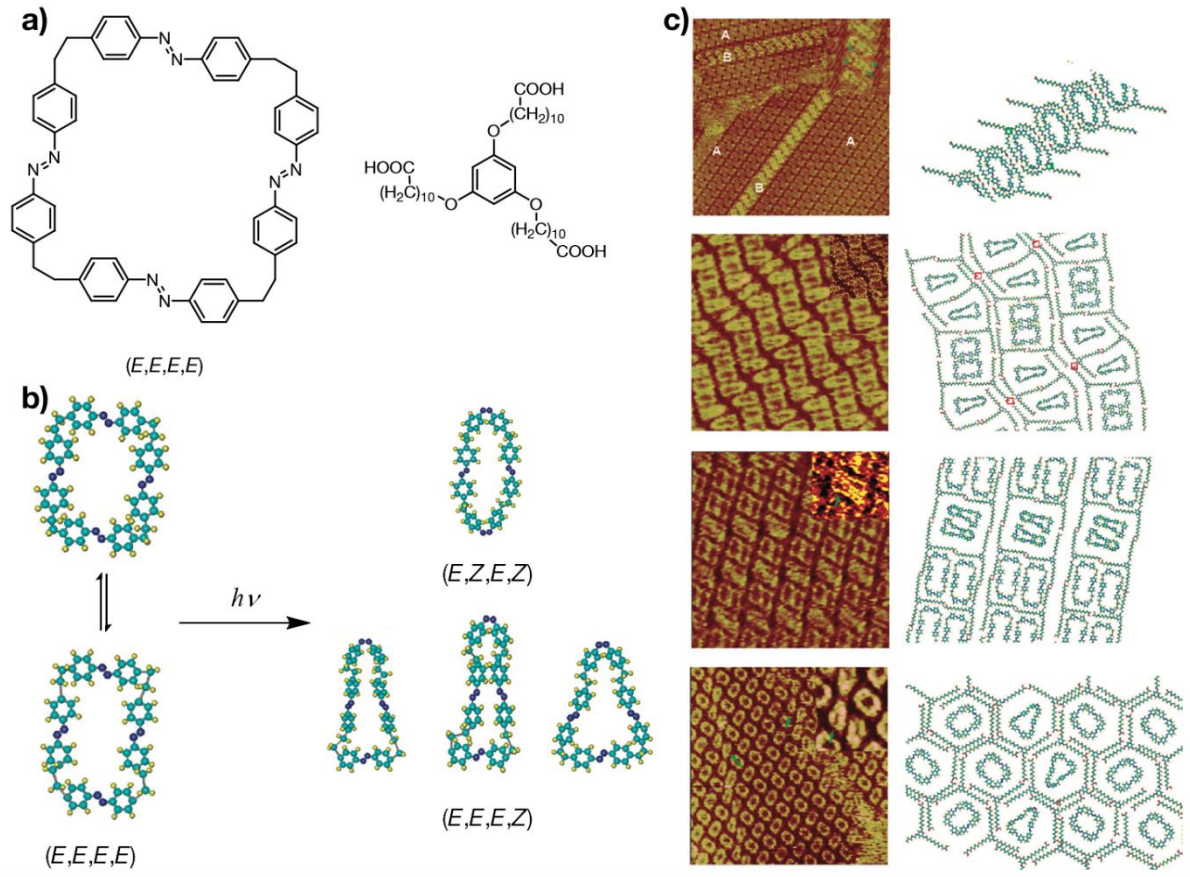

Figure 24. a) Structure formulae of tetra-azobenzene macrocycle and 1,3,5-tris(10-Carboxydecyloxy)-benzene (TCDB) giving rise to co-adsorption in host-guest complexes. b) Molecular models of the conformational isomers, together with the photoisomers observed by STM. c) STM topographs at the HOPG-heptanoic acid solution interface and attributed molecular models of the bi-component system, which morphology is modified by photoisomerisation of the tetra-azobenzene macrocycle. Adapted from Ref.[114a]

4. Photoswitchable fluorophores

Attaining optically-triggered modulation of the luminescence of a molecule or metal complex in reversible fashion is extremely appealing for their application as all-optical memory elements,[81b, 81c, 81e] or as photoswitchable probes in superresolution microscopy.[115] Since in this field the main emissive derivatives emit by means of fluorescence, we will from now on only focus on the latter phenomenon. Diarylethenes in this context represent the ideal photoswitchable unit, thanks to their high fatigue resistance and thermal stability of the two forms, allowing to perform several switching cycles and to retain the information written by light stimuli. Fluorescent photoswitchable molecules may be generally classified in two main classes: inherently fluorescent switches, having one of the two states showing emissive properties, or (supra)molecular systems consisting of a fluorophore coupled with a photochromic unit capable of quenching the fluorophore emission in one of its two states. Although inherently fluorescent switches, and especially diarylethenes, result convenient thanks to their simple synthesis and high contrast between the two states, their main drawback consists on the fact that the emission process is in competition with the photochromic reaction. Thus, a practical approach to overcome the latter problem consists in the combination of bright fluorophores and photochromes in the same molecular backbone. The most common strategy lies on the use of fluorophores in combination with diarylethenes: the emission quenching of the former could be obtained by either Förster resonance energy transfer (FRET), or photo-induced electron transfer. Modulation of the absorption properties or the oxidation/reduction potentials of the diarylethene unit upon its isomerisation are the cause for the emission switching.[116] For such application, high contrast between the ON- and OFF-states, reversibility and cyclability are factors of crucial importance.

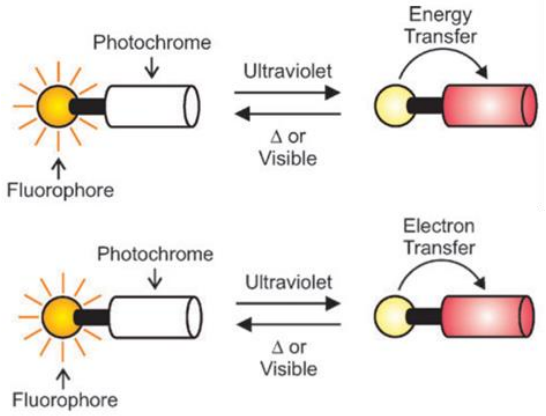

Figure 25. Schematic illustration of a photoswitchable dye realised by coupling a fluorophore with a photochromic unit. Reprinted from Ref.[117]

The latter properties depend primarily on the chemical robustness of the photoswitch towards side reactions and/or decomposition, together with the resistance of the emissive unit towards bleaching. The use of DTE photochromes in such case is highly promising, seen their superior fatigue resistance with respect to other classes of photochromic compounds. Conversely, achieving high contrast in the modulation of the emission of a luminophore is generally complicated by two main factors: non-quantitative conversion of the photochromic unit(s) upon

achieving the photostationary state (PSS), and low (or generally below unit) quantum efficiency of the luminescence quenching process. These two drawbacks could be overcome with a conceptually simple strategy: increasing the amount of switchable (quencher) units surrounding the luminophore. Pioneering work was done by the group of Irie, with the design of an anthracene emissive core surrounded by two DTE residues:[118] such a compound showed a remarkable difference between the fluorescence emission quantum yield of the all-open-DTE form (Φ_{fl} = 0.83) and the isolated closed-DTE form (Φ_{fl} < 0.001), nevertheless the latter was obtained by purification and the photoproduct was assigned to the form with only one ring-closed DTE unit. Moreover, the contrast showed to be low at the photostationary state following the low conversion to the closed-DTE form. The appearance of such a low conversion was ascribed to the inclusion of the photochromic units in the extended π-conjugated system. Another conjugated multi-DTE-fluorophore was reported by the group of Müllen, also in such case leading to low contrast due to limited photochromism of DTEs.[119] Notably, a promising multi-DTE system enabling to achieve an excellent ON-OFF contrast upon switching the photochromes at the photostationary state was recently reported by Li *et al.*, in which they realised a dyad composed by a perylenemonoimide fluorophore bearing up to three DTEs attached via a non-conjugated linker.[95a] In such work, three perylenemonoimide (PMI) dyes were synthesised, bearing either one, two or three DTE units, and their photophysical and photochromic properties were compared. The presence of up to three photochromes in the open form showed the absence of any perturbation of the original emission of the fluorophore, while in the derivative bearing three DTE units, closure of the latter induced an extremely high fluorescence quenching ratio, compared to the bis- and mono(DTE) derivatives. Such excellent properties allowed to realise all-optical transistors and to use the dye for super-resolution fluorescence imaging. This system, thanks to the robustness and large fluorescence quantum yield of the emissive core, together with the presence of several, non-electronically interacting DTEs successfully showed that with such a simple strategy it is possible to achieve switchable fluorophores with extremely high ON/OFF ratio.

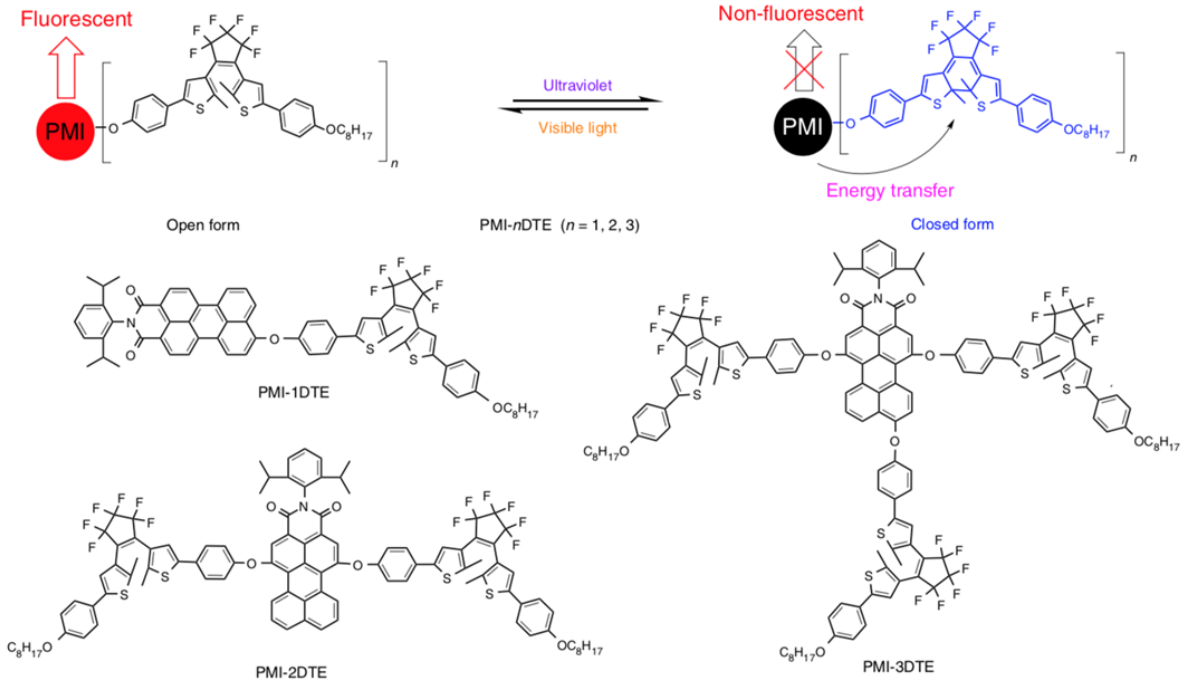

Figure 26. Perylenemonoimide (PMI) derivatives modified with up to three DTEs. Adapted from Ref.[95a]

5. Gold nanomaterials

In the realm of nanoscience and nanotechnology, the field of nanomaterials engineering, and especially the synthetic methods enabling the generation of tailored structures with bottom-up approaches hold a position of primary importance, since they allow us to bridge the gap between molecular chemistry and bulk solids. Materials that have dimensions in the range of tens of nanometres show the appearance of exotic properties if compared to their macroscopic counterparts, and such properties strongly depend on the size, shape, structure and composition of the nanomaterial.[120] Those peculiarities emerging from nanoscale confinement and surface effects drove in the last decades a tremendous interest in the development of synthetic strategies enabling to tailor nanomaterials with a high control over their size, shape and composition. The enormous growth of such field allowed not only to reach a wide knowledge over the synthesis of a vast library of nanomaterials, but also to unravel the complex physics resulting from *e.g.* the electron confinement by nanocrystals with low dimensionality.[121] Although the use of gold and silver colloids is widespread since the antiquity for the fabrication of stained glass and ceramics, the early discoveries done by Faraday,[122] and later Mie and Zsigmondy,[123] opened the way to this extremely appealing field. Nowadays, noble metal nanoparticles, and especially gold nanoparticles represent the most widely studied and applied example of nanomaterial fabricated with bottom-up approaches, being such field still active, particularly towards the synthesis of novel nanocrystals having unparalleled shape, size and properties. Noble metal nanoparticles bearing plasmonic properties, thanks to their ability to concentrate the electromagnetic field of light into their immediate surroundings, are currently investigated and already applied in a broad spectrum of technological fields,[124] such as nanomedicine and diagnostics,[125] energy harvesting and photovoltaic devices[126] and plasmonic metamaterials,[127] to name a few.

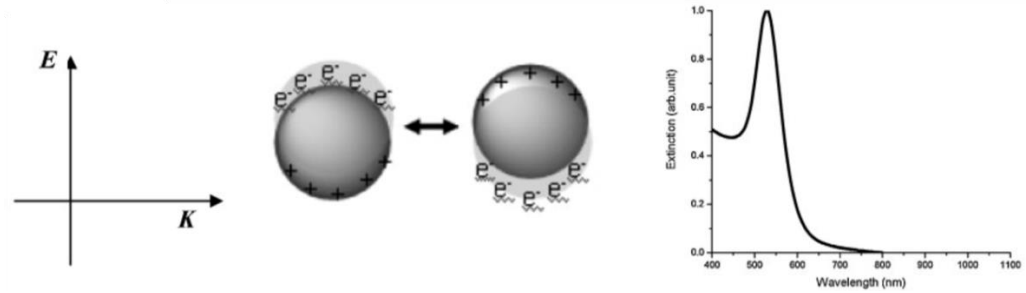

Figure 27. Schematic representation of the interaction of polarised electromagnetic radiation with noble metal (gold) nanospheres. The incident oscillating electric field (*E*) propagating along a direction (*K*) induces a coherent oscillation of the conduction band electrons with respect to the metallic core. The resulting dipolar oscillation is resonant with the incoming electromagnetic radiation at a specific frequency depending of particle size and shape. For gold nanospheres with diameter lower than 20 nm this corresponds to light in the visible range ($\lambda \approx 520$ nm). Reproduced from Ref.[128]

The main reason for the wide interest that has been devoted to noble metal nanoparticles lies on the localised surface plasmon resonance (SPR) effect which these nanostructures are subject to. The SPR has origin upon the excitation of the coherent motion of the surface conduction band electrons of a nanoparticle by an incident electromagnetic field. Classically, the electrical field of an incoming light wave induces polarisation of the electrons with respect to the largely heavier ionic core of the nanocrystal (with spherical shape). This results in a net charge variation at the surface of the nanoparticle which acts as restoring force, thus, in the simplest case

returning an in-phase oscillating motion of the electrons. Their optical properties (extinction) originate from the absorption (and scattering) of the incident radiation when the frequency of its electromagnetic field is in resonance with the coherent oscillation of the conduction band electrons.[120a] The frequency and linewidth of the SPR depends on the dielectric function of the metal, as well as the on the dielectric environment, together with the size and shape of the nanocrystal. For nanospheres this effect can be theoretically described by Mie theory, providing an analytical description of the SPR in terms of a multipole expansion; for nanospheres with a diameter below one tenth the excitation light wavelength ($d \leq 20$ nm), only the dipole term has to be taken into account, leading to the following expression for the extinction cross section (σ):

$$\sigma = \frac{18\,\pi\,V\,\varepsilon_m^{\frac{3}{2}}}{\lambda}\,\frac{\varepsilon_2}{(\varepsilon_1+2\varepsilon_m)^2+\varepsilon_2{}^2} \qquad (2.1)$$

where V is the nanoparticle volume, λ the wavelength, ε_m the dielectric constant of the medium, and $\varepsilon_1 + i\varepsilon_2$ is the complex dielectric function of the metal. The resonance condition is met when $\varepsilon_1 = -2\varepsilon_m$, which occurs in the visible for gold and silver nanospheres.[129] In the dipolar approximation, the SPR has no dependence on the diameter of the nanosphere, but only on the dielectric functions of the dielectric medium and the metal. However, these conditions do not apply for larger nanospheres, as the contribution from higher multipoles becomes important; in such case, a red shift and broadening of the SPR is evident. The SPR broadening is due to the different peak wavelengths of higher order multipoles together with the radiative damping of the resonance related to the increase of the scattering cross section.

The bottom-up synthesis of noble metal nanoparticles as nanocrystals is accomplished by means of colloidal chemistry routes, and their surface passivation is crucial for stabilising the nanomaterial, thus to prevent their aggregation and the subsequent loss of nanometre-scale structural features. The use of a specific capping agent for the highly reactive faces of the nanoparticles is key for any synthetic method, since in most cases the nanometre-sized colloid is produced by reduction of a metal salt precursor: the choice of a specific stabiliser will play a fundamental role in the nucleation and growth of the nanocrystals, the latter phenomena determining the final shape and dimension of the colloid. For gold nanoparticles for instance, citrate has been one of the most popular stabilising agents, acting also as the reducing agent for gold (III) salts in the so-called Turkevich method, the latter being still widely employed for the synthesis of 20-150 nm spherical gold nanoparticles bearing a (physisorbed) loose ligand shell.[130] Concerning stabilisers not forming covalent bonds with the metal atoms, surfactants are also widely used, as the reduction of the metal salts within a micellar microenvironment would act as a template yielding nanocrystals with peculiar morphology (*vide infra*). Over the past years countless examples of noble metal nanoparticles functionalisation with various ligands have been reported.[121, 131] Various binding moieties have been used to graft organic ligands to the metal nanoparticles, with the dual purpose of stabilising the nanometre-sized colloid and imparting to it novel functionalities.[121] After the breakthrough reported by Brust *et al.*, among the ligands used to stabilise the metallic nanocrystals, the most frequently used has been the thiol group.[132] The use of thiol moiety is motivated by its high affinity towards the formation of covalent bonds with noble metals. Moreover, thiol chemistry and its reactivity towards gold is well-established.[133] The use of thiol-based stabilising agents thus enables to give a specific chemical functionality to the gold nanocrystals.

Recently, increasing interest has been focussed on anisotropic nanoparticles, being the presence of asymmetric axes the origin of additional physicochemical properties. Among them, perhaps the most appealing characteristics reside on the peculiar optical response of such materials (*e.g.* multiple localised surface plasmon resonances),[128] but also in their catalytic activity.[134] One other reason is the possibility of obtaining their self-assembly, or self-organisation into highly ordered supercrystals made of aligned particles due to their peculiar shape.[135] The high tunability of the localised surface plasmon resonance bands in the whole visible spectrum makes gold and silver nanorods highly appealing for their use as optical antennas. The highly concentrated electromagnetic field in the immediate surroundings of the nanocrystals can lead to the enhancement of several phenomena such as excitation, radiative emission, two-photon absorption, Raman scattering, to name a few. Especially the latter has been widely exploited for sensing applications, due to the Surface-Enhanced Raman Scattering effect (SERS), allowing the detection even of single molecules in their proximity.[136] As optical antennas, generally gold and silver nanorods have the highest performances, nevertheless more attention has been focussed on the former. On the other hand, silver nanostructures show the highest enhancement factors, though such materials are more prone to oxidation.

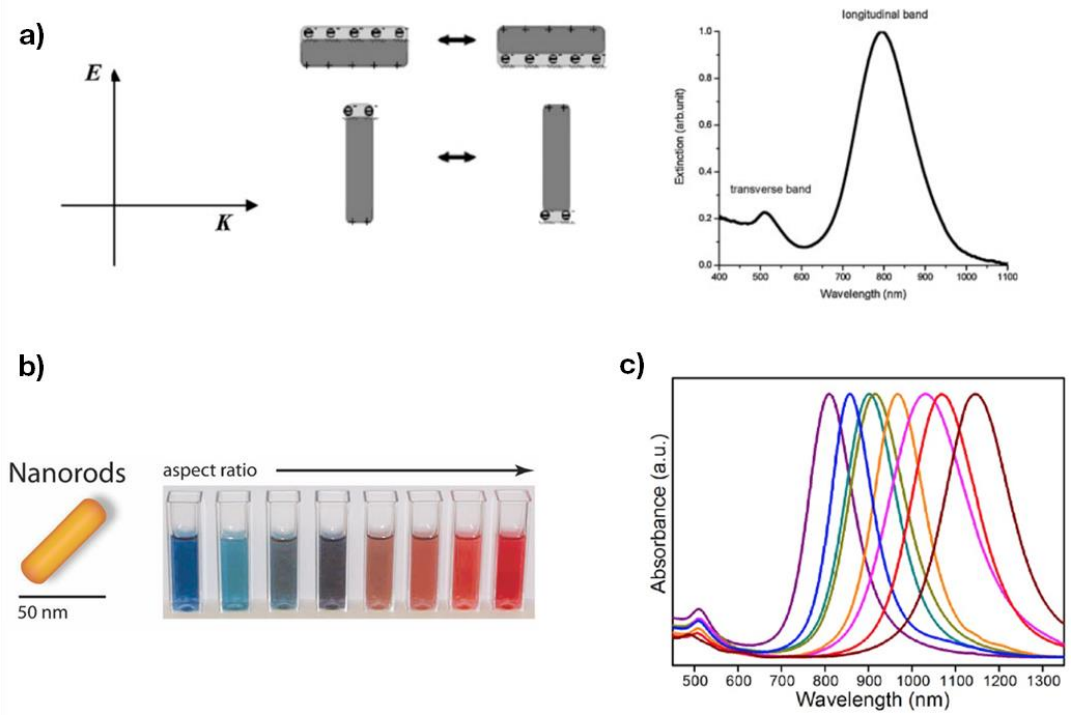

Figure 28. Schematic representation of the interaction of polarised electromagnetic radiation with noble metal (gold) nanorods. Gold nanorods show two SPR bands, being the strong longitudinal SPR band (LSPR) corresponding to the electron oscillation along the long axis, and a weaker transverse band (TSPR) corresponding to the electron movement along the short axis. b) Visual appearance of colloidal dispersions of gold nanorods of increasing aspect ratio. c) Normalised extinction spectra of gold nanorods: as the aspect ratio increases, the corresponding LSPR band is red-shifted. Figure a), b), c) adapted from Ref.[128, 137] respectively.

Gold nanorods are among the most widely studied nanoparticles presenting surface plasmon resonance properties. Such peculiar gold colloids in most cases are cylindrical nanostructures, with diameters in the 10 – 20 nm range, and 20 – 150 nm length. The main reason for their broad scientific interest lies on the fact that the wavelength and intensity of their spectral features can be tuned over a wide range of the visible and near-infrared spectrum by varying their dimensions. They display peculiar extinction spectra, showing the presence of two bands

corresponding to the localised surface plasmon resonance along their length, called longitudinal SPR (LSPR), and across their diameter, called transverse SPR (TSPR). Their extinction spectra cannot be analytically described by Mie theory, though qualitatively can be approximated with Gans theory, an extension of the Mie theory for spheroidal nanoparticles. Gans theory allows to account for a depolarisation factor along each axis of the spheroid: upon increasing the aspect ratio, the longitudinal surface plasmon resonance mode along the semimajor axis of the spheroid red shifts, and the transverse along the semiminor axis blue shifts. Nevertheless, the approximations made by Gans theory are valid only in limited cases, leading to only qualitative agreement. In order to accurately calculate the LSPR and TSPR band positions, it is necessary to use numerical methods such as discrete dipole approximation (DDA). The latter method represents the nanoparticle as a cubic array of polarisable points and calculates the extinction cross sections basing on the induced dipoles.[138] The energy of the TSPR does not depend on particle size and aspect ratio, and similarly to spherical gold nanoparticles with radius between 10-20 nm it occurs around $\lambda \approx 520$ nm wavelength. On the contrary, the longitudinal surface plasmon resonance band (LSPR) occurs at lower energy, and red shifts upon increasing the aspect ratio of the rod-shaped particle. The SPR features of gold nanorods strongly depend also on their shape, hence their description must take into account the morphology of the endcap, as structures having flat ends, or "dumbbell" shaped endcaps typically display large shifts if compared to the ones having hemispherical extremities.[129] For the sake of clarity, in the present work we will discuss only about cylindrical AuNR having hemispherical endcaps.

Another interesting feature of metallic nanostructures is the sensitivity of their SPR to the dielectric environment. As stated previously, the surface plasmon resonance is originated by coherent oscillations of the surface conduction electrons coupled with an external optical field at the interface between metal and dielectric. Surface plasmon resonances are thus highly sensitive towards variations of the local refractive index in the close proximity of the metal-dielectric interfaces, and a change in the refractive index is associated to a shift of the peak position in the extinction (or scattering) spectrum of the nanostructure. Such a phenomenon renders the structures supporting SPR an important building block for optical sensing, as they can be used to detect even small refractive index changes: nowadays, sensors based on SPR are widely studied and employed also in commercial applications for the detection of chemical and biological species.[139] The localised surface plasmon resonance features of silver and gold nanoparticles in the visible-NIR spectrum generally undergo a red-shift upon increasing the refractive index of the surrounding medium, and such tight dependence is the basis of localised plasmon resonance spectroscopy.[140] It has also been shown that anisotropic gold nanostructures (such as nanorods) show a higher refractive index sensitivity compared to spherical gold nanoparticles.[7, 141]

Chapter 3.

METHODS

The scope of the present chapter is to give an overview on the experimental techniques used for the characterisation of the systems based on photochromic compounds developed in this thesis. At the end of the chapter the synthetic methodology used for synthesising the single-crystalline gold nanorods (AuNR) employed in Chapter 6 will be also discussed. A brief introduction over the theoretical concepts underlying the methods used will be given, together with the explanation on the instrumental configurations, while at the end of each section details on the experimental conditions employed will be indicated. Firstly, the chapter will focus on a general overview over molecular spectroscopy, starting from electronic spectroscopy: steady state absorption and emission, and time-resolved emission. The methods used to determine photoreaction and photoluminescence quantum yields will be also discussed. Subsequently, vibrational spectroscopy, especially Raman spectroscopy will be briefly addressed, with particular attention on surface enhanced Raman scattering (SERS). Furthermore, the focus will be moved towards mass spectrometry, describing ion-mobility mass spectrometry. Then, the microscopy techniques employed in the present work will be discussed: scanning electron microscopy and scanning tunnelling microscopy, with particular attention on the latter, as it represents one of the principal techniques used for our investigations.

1. Electronic spectroscopy, basic aspects of photochemistry

Photochromic derivatives are molecular building blocks which upon reversible isomerisation are accompanied by a change in their absorption and emission spectra, resulting from an alteration of the chromophore system. Such isomerisation is induced in at least one direction by electromagnetic radiation (ultraviolet or visible light).[142] The various isomeric forms of such compounds are characterised by different molecular conformations, atom connectivity and π-conjugation, thus leading to the variation of their main physicochemical properties, such as shape, molecular flexibility, dipole moment and energy of their ground and

excited states. Therefore, electronic spectroscopy represents the primary tool to investigate the outcome of the photo- and thermal reactions characterising this class of compounds.

In virtue of the wave-particle duality, electromagnetic radiation can be regarded not only as radiant energy propagating in space as a sinusoidal wave (according to Maxwell's theory), but also as a stream of photons, quanta of energy depending on the frequency of the electromagnetic wave associated, following the equation $E = h\,v$. Following from the same principle, any microscopic physical system exists in multiple quantised energy levels: a transition between such levels is allowed only by applying quanta of energy corresponding to the energetic difference between such states. Atoms and molecules can indeed be regarded as microscopic systems whose energy levels are quantised, and the interaction of photons or electromagnetic radiation with those could result in their transition to a higher energy state (excited state). For molecular systems, thanks to the fact that the motions of electrons and nuclei occur on different timescales following from their difference in mass, transitions involving electronic or nuclear coordinates will require vastly different energy to occur. Therefore, the absorption of photons having suitable energy will result in the promotion of a given molecule to a rotationally, vibrationally or electronically excited state. Upon absorption of a photon with energy (hν) falling typically in the ultraviolet or visible range of the electromagnetic spectrum, a given molecular system (A) is promoted to an electronically excited state (*A), reaction which can be indicated in the general form $A + h\nu \rightarrow {}^*A$. A molecular system in the electronically excited state (*A) in virtue of its excess energy has distinctive properties and has to be regarded as a different chemical species in comparison to the same in the ground state (A). A molecule upon interaction with a photon can give rise to a number of unimolecular processes which, in case they do not lead to chemical modification of its structure, can be indicated as *photophysical processes*, and can be approximately schematised with the so-called Perrin-Jablonski diagram (Figure 29).

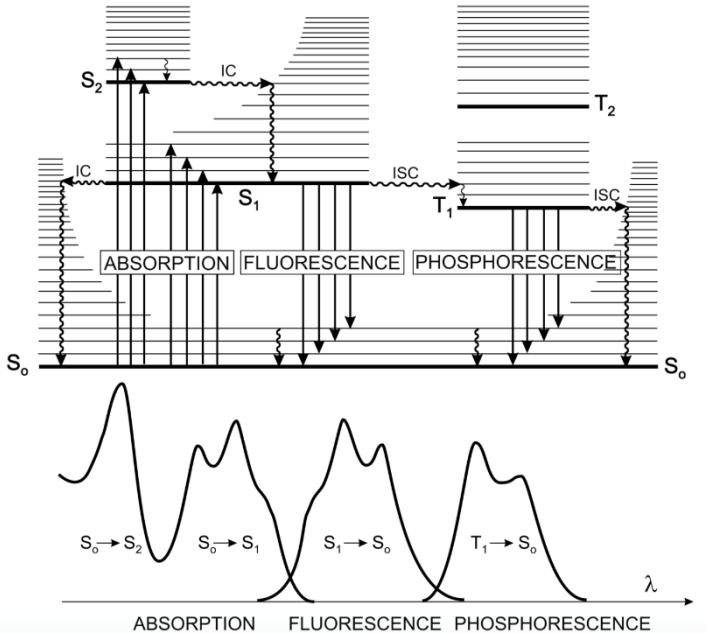

Figure 29. *Top*, Simplified state diagram (Perrin-Jablonski diagram) indicating molecular states and photophysical processes occurring on a typical organic molecule. The radiative transitions are indicated with full arrows, while radiationless transitions with wavy arrows. *Bottom*, General scheme indicating the position and shape of the corresponding electronic absorption and emission spectra. Reproduced from Ref.[143]

Light absorption typically occurs when *one* photon of suitable energy interacts with *one* molecule, with a timescale of ~10^{-15} s; since the vast majority of organic molecules have a closed shell electron configuration, their ground state is a singlet, and is indicated as S_0. Because of the orthogonality of spin wavefunctions, any transition occurring from states with different spin multiplicity is *spin-forbidden*, therefore absorption of light with suitable energy will lead to the population of a singlet excited state ($S_{1, \ldots, n}$*). According to the Franck-Condon principle, electronic excitation is a fast ($\approx 10^{-16} - 10^{-15}$ s) vertical process, following from the fact that electronic motion occurs on a much faster timescale if compared to the nuclei. Henceforth, if the vertical excitation leads to a vibrationally "hot" excited state $*S_{1, \ldots, n}$, a relaxation over the nuclear coordinates will occur, leading to the zero vibrational level of such excited state. The latter process is called vibrational relaxation ($\approx 10^{-12} - 10^{-10}$ s), and since deactivation of electronically excited states occurs on longer timescales, with good approximation one could state that all relevant photophysical and photochemical processes occur from thermally equilibrated excited states.

From electronically excited states, intramolecular deactivation to the ground state could occur following three principal (unimolecular) mechanisms: radiationless deactivation, radiative deactivation, or alternatively by undergoing chemical reactions. In the former two cases, the compound will be restored in its initial state, while on the latter the product will be a different (meta)stable chemical species. A radiationless deactivation occurs without emission of electromagnetic radiation: the overall mechanism is the result of a two-step process, being the former an *isoenergetic* conversion from the (vibrationally ground) electronically excited state to a vibrationally "hot" lower energy electronic state. The latter consists of the vibrational relaxation to the resulting zero vibrational level of such state. The radiationless deactivation itself only consists of the horizontal, isoenergetic process, while the vibrational relaxation is its consequence. The probability of such transition is given by Fermi's Golden Rule and depends on the overlap between the vibrational component of the wavefunctions of the two states, hence it will be case-dependent, but generally decreases exponentially with the energy gap between the two electronic states (energy gap law). A radiationless deactivation could occur not only between states of the same spin multiplicity (internal conversion, IC, $\approx 10^{-11} - 10^{-9}$ s), but also resulting in the population of a state with different spin multiplicity (intersystem crossing, ISC, $\approx 10^{-10} - 10^{-8}$ s). The latter phenomenon is *spin-forbidden*, therefore has low probability to occur, nevertheless especially in systems containing heavy atoms the spin selection rule is overcame by spin-orbit coupling. Radiative deactivation on the contrary will result in the population of the ground state with the emission of photons. In the case of *spontaneous emission*, it will occur with the emission of *one* photon $*A \rightarrow A + h\nu$. Radiative deactivation could occur between states with the same, or also different spin multiplicity. In the former case, which on common organic molecules will occur from a singlet excited state to the (singlet) ground state is called fluorescence. While, in case the spin multiplicity is varied upon transition, it is called phosphorescence. It is important to note that such phenomena occur on largely different timescales: fluorescence is a *spin-allowed* transition hence a typically fast process (excited state lifetime $\tau \approx 10^{-10} - 10^{-7}$ s), while on the contrary phosphorescence is *spin-forbidden* resulting in the emission occurring on longer timescales ($\tau \approx 10^{-6} - 1$ s). The energy difference between the lowest energy absorption band and the emission is called Stokes shift and is due to vibrational relaxation to the vibrationally ground states of the electronic levels involved in the transition. In the vast majority of cases, the

aforementioned radiative processes are the result of the deactivation of the lowest electronic excited state of a given multiplicity (Kasha's rule), as direct consequence of the energy gap law.[144] This concept is valid also for most of chemical reactions occurring from excited states; it follows the fact that usually the high-lying electronic excited states have lower difference in energy compared to the gap between the lowest excited and the ground state, hence internal conversion occurs on faster timescale than their radiative deactivation to the ground state.

It is important to point out that all the aforementioned processes are unimolecular, hence they follow first order kinetic laws. One therefore can define the rate of each deactivation process (k_j), and supposing that the deactivation of an excited state is the result of three processes in competition, being radiationless deactivation (k_{nr}), radiative deactivation (k_{em}) and photoreaction (k_r) for instance, the lifetime of the excited state *A is indicated as follows:

$$\tau(\,^*A) = \frac{1}{k_{nr} + k_{em} + k_r} = \frac{1}{\sum_j k_j} \tag{3.1}$$

Each photophysical and photochemical process characterised by a rate constant k_i, being the result of the competition between several phenomena could be characterised by its efficiency (η_i):

$$\eta_i = \frac{k_i}{\sum_j k_j} = k_i\,\tau(\,^*A) \tag{3.2}$$

The *quantum yield* Φ_i of a given photophysical of photochemical process equals to the ratio of the number of molecules undergoing such process divided by the numbers of photons absorbed by the reactant. Hence, if the process of interest follows from the deactivation of excited state *A (with efficiency η_i), and such level is populated by subsequent processes, each one with efficiency η_j, the quantum yield is defined by:

$$\phi_i = \prod_n \eta_n \tag{3.3}$$

where η_n represent the efficiency of each step involved in the process.[145]

Deactivation of the electronic excited state of one chemical species (*A) in fluid solution could occur not only following unimolecular pathways, but also by collisions with other chemical species, called quenchers. In such a way, the deactivation follows a second order kinetic law, depending on the concentration of the quencher (B). The reaction results in a transfer of excitation energy or of electrons to the second chemical species: in the first case (3.4), the product of the reaction will be the quencher in an electronically excited state, while in the second case it will result in the reciprocal oxidation and reduction of the two species (3.5 and 3.6).

$$^*A + B \rightarrow A + \,^*B \tag{3.4}$$

$$^*A + B \rightarrow A^+ + B^- \tag{3.5}$$

$$^*A + B \rightarrow A^- + B^+ \tag{3.6}$$

If one defines τ_0 as the lifetime of the excited state of the species *A in absence of quencher, as eq. 3.1:

$$\tau_0 = \frac{1}{k_{nr} + k_{em} + k_r} \tag{3.1}$$

The lifetime τ of species *A in presence of quencher B will then correspond to:

$$\tau = \frac{1}{k_{nr} + k_{em} + k_r + k_q[B]} \quad (3.7)$$

where k_q is the quenching rate constant. Dividing the two latter equations will give the Stern-Volmer equation (3.8):

$$\frac{\tau_0}{\tau} = 1 + k_q \tau_0 [B] \quad (3.8)$$

By looking at the latter equation, a first observation becomes evident: since such bimolecular process is limited by diffusion in solution (collisional deactivation), the rate constant for quenching can have a maximum value of $k_q \approx 10^{10}$ M^{-1} s^{-1}. Also, in solution conditions, the concentration of the quencher is most likely lower than [B] $\approx 10^{-2}$ M, hence it follows that in order to observe collisional deactivation, the excited state lifetime must be long-lived ($\tau \geq 10^{-9}$ s).

The advancement of science in the field of synthetic and supramolecular chemistry recently led to the realisation of complex multicomponent systems made up of multiple functional units kept together by covalent, or non-covalent interactions. Also multi-chromophoric species including several photoactive moieties within the same covalent backbone can be regarded as supramolecular species, if each chromophore retains the same photophysical properties of the isolated species. Hence, if their excited states are localised on the single components and not on the overall molecular backbone.[145] In such case, in multicomponent systems, energy and electron transfer can occur as intramolecular processes, following first order kinetics, without being limited by diffusion in solution.

1.1. UV-Visible absorption spectroscopy

As mentioned in the previous paragraphs, absorption of a photon with suitable energy in the ultraviolet and visible region of the electromagnetic spectrum will result in the promotion of such molecule to an electronically excited state. It follows that upon irradiation with a continuous spectrum of electromagnetic radiation comprised between 190 – 1100 nm, one could observe the attenuation of light at the wavelengths associated to the energy of the main electronic transitions occurring on the substance analysed. The transmittance (T) will be given by the ratio between the incident light (I_0) and the transmitted light (I) passing through a sample:

$$T = I/I_0 \quad (3.9)$$

while the absorbance:

$$A = -log_{10}\, T \quad (3.10)$$

Therefore, absorbance could be measured using a double beam spectrophotometer, by measuring at each wavelength the intensity difference of monochromatic light between the analysis beam (I) and the reference beam (I_0). In the case of measurements in solution, the sample and reference (the latter usually consisting of pure solvent) solutions are contained within matched optically transparent and chemically inert vessels (quartz cuvettes).

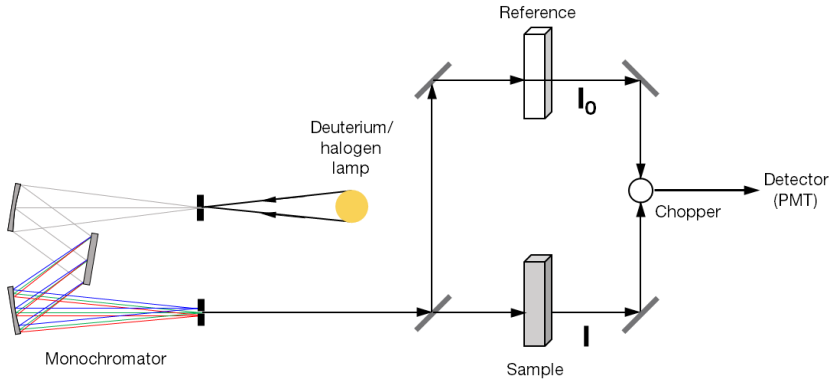

Figure 30. Simplified instrumental scheme of a double beam spectrophotometer.

Considering a thin layer of solution with thickness dx containing n absorbing molecules per unit volume, and each chromophore having a certain absorption cross-section σ, the variation of light intensity dI absorbed through dx is given by the relationship:

$$\frac{dI}{dx} = I\sigma n \tag{3.11}$$

Upon integration of the rearranged equation applying the boundary conditions: $I = I_0$ at $x = 0$, one obtains the Beer-Lambert law:

$$A = -log\frac{I}{I_0} = \varepsilon\, c\, l \tag{3.12}$$

where ε is the molar extinction coefficient expressed in L mol^{-1} cm^{-1}, c is the concentration expressed in mol L^{-1} and l is the optical path length, expressed in cm. Here it is important to note that such relationship is a limit law: the absorbance varies linearly with the analyte concentration only in the case of highly dilute, homogeneous solutions. Moreover, such linear variation could not be respected also in case of aggregation of the analyte, or its association with other chemical species. Light scattering must also be taken into account in case of non-homogeneous dispersions, since could lead to the observation of artifacts: the optical density relative to this phenomenon is proportional to $1/\lambda^4$, according to Rayleigh scattering.

The instruments employed to perform the work described here were a Jasco V-670 and a Jasco V-650 spectrophotometers. Both the instruments are double beam, single monochromator spectrophotometers equipped with two light sources, deuterium ($\lambda \approx$ 190-380 nm) and halogen ($\lambda \approx$ 380 - ~2000 nm) lamps. The Jasco V-670 is equipped with two detectors, being one a photomultiplier tube (PMT) for measurements in the UV-Vis range ($\lambda \approx$ 190-850 nm), and a Peltier-cooled PbS detector allowing to perform measurements in the NIR range ($\lambda \approx$ 850-~2000 nm). The Jasco V-650 is analogous, but not equipped with the NIR detector, hence allowing only measurements in the UV-Vis range. For temperature-dependent measurements, the latter instrument was used, equipped with a custom-built Peltier thermostatted cuvette holder

(ThorLabs). The UV-Vis-NIR Jasco V-670 spectrophotometer was used to characterise the anisotropic gold nanocrystals described in chapter 6. While, for the remaining experimental work the Jasco V-650 was employed, situated in a dark room equipped with safe red lights in order to exclude external light irradiation as a source of error in our measurements on photochromic compounds. In all cases, spectroscopy grade solvents (Uvasol, Merck), in matched quartz cuvettes (Suprasil – Hellma) were used for the measurements.

1.2. Steady state emission spectroscopy

As previously evidenced, depopulation of an electronically excited state could occur through a radiative pathway, hence leading to the luminescence of the chemical species under investigation. The spectral distribution of the light emitted throughout such process could be examined by steady-state emission spectroscopy, using a common laboratory equipment such as a spectrofluorimeter. An emission spectrum is collected by measuring the wavelength distribution of the emitted light from a sample upon excitation at a single wavelength, while an excitation spectrum can be collected by monitoring the emitted light at fixed wavelength while sweeping the wavelength of the excitation light. In standard spectrofluorometric measurements in solution, the emitted radiation is collected at *right-angle geometry*, hence at 90° from the excitation beam in order to minimise the amount of light coming from the latter reaching the detector. On the contrary of absorbance, a physical quantity which can be expressed in an absolute scale, light intensity measured by a fluorimeter is an observable which depends on several instrumental factors and on the sample properties, therefore it must be expressed in arbitrary units, and/or on a relative scale in case of experiments performed in comparable conditions. Luminescence intensity depends on the instrument used and on its configuration: the first cause of this instrumental factor is the non-constant intensity of the excitation light over the whole electromagnetic spectrum. This comes from both the fact that the lamp used has a peculiar spectral output due to its nature (Xe discharge lamp), and that for a monochromator light transmission efficiency is wavelength-dependent: such defect could be overcome by measuring the intensity of light coming out from the excitation monochromator with a reference detector. Moreover, the apparent overall luminescence intensity measured is influenced by the wavelength-dependent response of the detector, which could be subtracted knowing its response curve. Numerous artifacts could also come from the light-sample interaction and the configuration of the latter with respect to the incident and emitted light beams. These include for instance the appearance of spurious bands in the excitation and emission spectra not coming from the luminescence of the substance examined, and could be due by several phenomena, such as elastic light scattering (Rayleigh- or Tyndall scattering, with the latter especially visible in non-perfectly homogeneous samples), Raman scattering (mostly from the solvent in solution measurements), or higher-order harmonic bands, intrinsic defect of the monochromators based on diffraction gratings (the latter could be overcome using suitable cut-off filters). It must also be stated that emission (and excitation) spectra could be distorted by re-absorption of the emitted light, especially in case luminophore has low Stokes shift. Moreover, light intensity could be also decreased by a geometric factor, due by the fact that the emitted light is collected at the centre of a spectrofluorometric cuvette, hence the excitation light could be fully absorbed

prior to reach the centre of the cell. Both these two issues enlighten the importance of working at low analyte concentration for quantitative measurements.

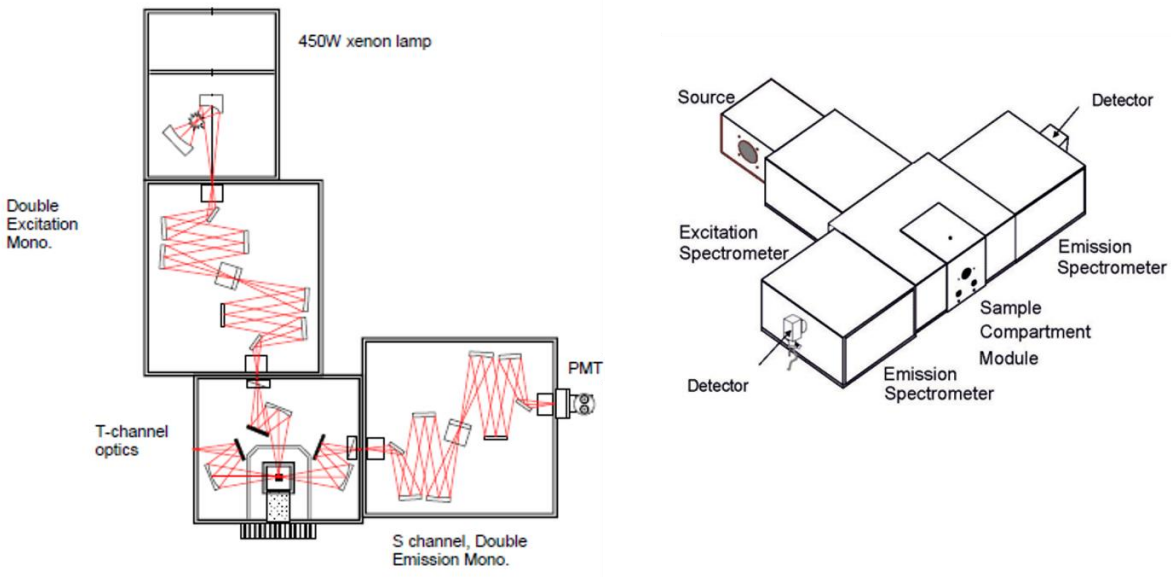

Figure 31. Internal layout and scheme illustrating the T-configuration of a modular fluorimeter Fluorolog FL3-22 (Horiba Jobin-Yvon) (Copyright www.horiba.com).

In the present work, steady-state emission measurements have been performed on the tetra-DTE porphyrins studied in chapter 5. For such purpose, two different spectrofluorometers have been used: an Agilent Cary Eclipse and a Horiba Jobin Yvon Fluorolog FL3-22. The Agilent Cary Eclipse is equipped with a 80 Hz pulsed xenon arc excitation lamp, single excitation and emission monochromators and a Hamamatsu R928 photomultiplier tube (PMT). The Horiba Jobin Yvon Fluorolog FL3-22 instead has a 450 W Xe arc excitation lamp, double excitation and emission monochromators and a PPD picosecond single photon counting detector (Horiba). The latter instrument gives also the possibility to measure corrected spectra in *ratio mode*. Routine measurements were performed on the Cary Eclipse, while higher resolution spectra with the latter, especially in case of samples displaying high absorbance at the emission wavelength. The studies were performed in spectroscopy grade solvents, using 1 cm or 3 mm optical path length Suprasil quartz cuvettes (Hellma), at low concentration, to keep the absorbance at the excitation wavelength lower than 0.1 in order to avoid reabsorption of the emitted light.

1.2.1. Photoluminescence quantum yield

The quantum yield of a radiative decay process (Φ_{em}) occurring from a luminescent compound is defined as the ratio between the number of emitted photons from such process and the number of absorbed photons by the luminophore. From an experimental point of view, the absolute determination of the photons emitted from an emissive species is not feasible with standard laboratory instruments, as already discussed. Among the possible sources of error in

the quantification of the amount of photons emitted, one could include polarization effects, refractive index effects, reabsorption and reemission effects, internal reflection effects, and the spectral sensitivity of the detection system.[146] A number of procedures to determine photoluminescence quantum yields have been developed, which rely on absolute, or relative methods. Among the absolute methods for instance, the Vavilov,[147] and the Weber and Teale[148] are based on the calibration of the excitation light using a solid scatterer, or a dispersion of it in liquid. Also photothermal methods are available,[149] detecting the amount of energy that is lost by non-radiative deactivation of a luminophore, nevertheless they generally require the assumption that no photochemical reaction occurs as part of the nonradiative processes. Another important and easily applied method consists in the use of integrating spheres for evaluating absolute photoluminescence quantum yields. The use of such set-up allows to collect all the emitted photons from a sample and to easily relate them with the number of absorbed photons. In such a way, the effects of polarization, scattering and different refractive index at the interfaces are ruled out.[150] Nevertheless, the use of such absolute methods involves complicated data treatment, and/or non-common experimental setups. On the contrary, the most commonly used and simple method to determine photoluminescence quantum yields in solution consists in the comparison with standard luminophores having known quantum yield (relative method). Such experiments are performed with the use of a common spectrophotometer and a fluorimeter. The emission quantum yield (Φ_{em}) is determined by comparing the integrated emission spectrum (over the whole wavelength range) of the sample with the same of a reference compound taken under identical experimental conditions:

$$\Phi_{em} = \Phi_{em,R} \frac{S}{S_R} \frac{A_R}{A} \frac{n^2}{n_R^2} \tag{3.13}$$

where $\Phi_{em,R}$ is the emission quantum yield of the reference compound, S the integrated emission intensity of the sample, S_R the integrated emission intensity of the reference compound, A the absorbance of the sample at the excitation wavelength, A_R the absorbance of the reference at the excitation wavelength, n and n_R are respectively the refractive indices of the solvents used for the sample and the reference.

It should be stated that in this expression it is assumed that the sample and reference are excited at the same wavelength, and the measured quantum yield obtained is only as accurate as the certainty of the quantum yield of the fluorescence standard. Moreover, the concentration of the solutions used must be kept low, with an absorbance of the excitation light lower than 0.1 (or better 0.05) in order to minimise the inner filter effects.

Within the present work, luminescence quantum yields have been measured on the tetra-DTE porphyrins described in chapter 5, in order to evaluate the extent of their fluorescence switching. For this purpose, the measurements were carried out by comparison with a standard compound with known quantum yield. Free base tetraphenylporphyrin (H_2TPP, Sigma–Aldrich) in toluene was used, which has $\Phi_R = 0.10$.[151] The measurements were performed upon excitation of the tetra-DTE porphyrin derivatives at the isosbestic points (429 and 430 nm, respectively) of their absorption spectra upon DTE isomerization, in order to rule out any change in the absorption of the excitation light. Concentration was kept low, in order to have $A_{\lambda exc} < 0.05$.

1.3. Time-resolved emission spectroscopy

In case of radiative deactivation of an electronic excited state, the temporal characteristics of the emission from such state could be measured by time-resolved techniques, thus recording the emission intensity as a function of time. By doing so, it is possible to determine the decay of the excited state population, therefore the lifetime of an excited state. By defining an excited species *A, the decay of the concentration of such species can be described as:

$$\frac{d[\,^*A]}{dt} = (k_{nr} + k_{em} + k_r)[\,^*A] \tag{3.14}$$

When observing the light emitted by a luminophore, the intensity of radiation is measured over time, the latter being proportional to the concentration of the excited species:

$$I(t) = I_0\, e^{-\frac{t}{\tau}} \tag{3.15}$$

where I_0 is the intensity at time 0, the lifetime τ the inverse of the total decay rate according to eq. 3.1. Hence the lifetime of an emissive excited state can be calculated from the slope of a plot of $\log I(t)$ vs. t.

Several methods to perform such experiments exist, including single flash, gated sampling, single photon counting and phase shift, being among them the most universal and commonly used the single photon counting technique. The principle of such methodology, commonly called *time correlated single photon counting* (TCSPC) relies on the fact that emission of a single photon from an assembly of luminophores is a random process: from repeated, periodic excitation of their luminescence and the possibility of detecting and precisely timing single photons coming from the sample it is possible to reconstruct the time-profile (or waveform) of the decay of its emission. In other words, each photon emitted from the sample is collected and labelled as the time difference between its arrival and the excitation pulse: a wide number of similar events is collected and binned in the same way, thus building a histogram that would have the same shape of a time decay curve of light emission observed after an infinitely short excitation light pulse. This occurs if one condition applies: a lower amount of emitted photons must be detected per excitation pulse, in other words if the probability of recording more than one photon per cycle is low.

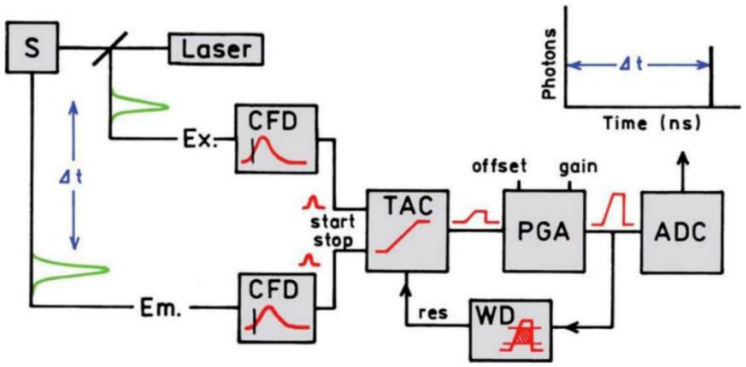

Figure 32. Scheme of the electronics in a TCSPC instrumental set-up: Laser indicates the pulsed excitation source, S the sample, CFD states for constant function discriminator, TAC time-amplitude converter, PGA programmable gain amplifier, ADC analog-to-digital converter, WD window discriminator. Reproduced from ref. [152].

Each measurement cycle starts with a short excitation pulse, which is split into the excitation light sent to the sample and a signal sent to the electronics, specifically to a constant function discriminator (CFD), a device allowing to time precisely the event. Such signal is interpreted as start event (t_0) by a time-to-amplitude converter (TAC). A second (stop) signal at time t is collected by detection of a single photon emitted by the sample, and analogously passed through a CFD for its timing. The TAC module generates a voltage linearly proportional to the time elapsed between the excitation t_0 and the emission t events. Such voltage is then amplified by a programmable gain amplifier (PGA, if needed) and converted to a numerical value by an analog-to-digital converter (ADC). In the electronics, also a window discriminator (WD) is present, allowing to discard the events giving rise to voltages outside of a given range, in order to reduce false readings. The single photon emitted from the sample is therefore converted to a digital Δt value: such electronics therefore act as a "stopwatch" for single photon events. Those are then digitally processed as channels of a histogram reporting the number of events occurred, each at their time delay: upon repeating such cycle a large amount of times with a pulsed source, it is possible to reconstruct the luminescence time decay as a statistical time distribution.

In order to perform correctly TCSPC measurements, it is of crucial importance to limit the amount of emitted photons reaching the detector, and specifically to detect less than one photon per excitation pulse (typically 1-10 photons per 100 excitation pulses). This requirement is originated from the capability of the available electronic systems to record only the first photon emitted per each cycle. On the contrary, in case the amount of photons per excitation cycle is greater than one, such system would record only the first photons reaching the detector (most likely event), thus underestimating the events occurring on a longer timescale. The resulting histogram would be distorted to shorter times, by an effect called *pulse pile-up*. Another crucial factor to take into account about these measurements is the instrument response function (IRF), being the response of the instrument to a sample with *zero* lifetime. The latter is intrinsic to the fast timing electronics and the instrument detector, and also influenced by the pulsewidth of the excitation source. The IRF could be measured by monitoring the excitation light, substituting a highly scattering dispersion (usually colloidal silica) to the luminescent sample, and must be convoluted with the luminescence decay in order to correctly fit the lifetime data.

The quality of the fit made on the experimental data is assessed by visual inspection of the deviations between the calculated and measured values, weighted by the standard deviations of each measurement. For a good fit the deviations are random, thus indicating that the only difference is given by random error. For multi-exponential decays, it is commonly assumed that the intensity decay over time corresponds as the sum of monoexponential decays:

$$I(t) = \sum_{n}^{i=1} a_i \, e^{-\frac{t}{\tau_i}} \tag{3.16}$$

where τ_i are the lifetime values, and a_i the amplitude of each component at t_0, the latter are commonly expressed as percentage (and discarded when below 3%).

Within the present work, TCSPC measurements were performed in chapter 5 to measure the excited state lifetime of tetra-DTE porphyrins. The experiments were made on a Horiba Jobin Yvon Fluorolog FL3-22 fluorometer equipped with a FluoroHub A+TCSPC controller and a PPD picosecond single photon counting detector. Excitation was performed using NanoLED LED light sources (pulse width ≤ 1.3 ns), using λ_{exc} = 590 nm and λ_{exc} = 560 nm. The excitation pulse

profile was deconvoluted by measuring the instrument response function using a scattering dispersion of colloidal silica (Ludox, Sigma–Aldrich) in water.

2. Light irradiation – photoisomerisation studies

Various light sources were used to perform stepwise irradiation of the compounds and materials characterised within the present work. In all solution studies, the experiments were performed in a dark room to avoid interference with environmental light. The solutions contained within standard 10x10 mm, 3 mL quartz cuvettes were thoroughly stirred to guarantee homogeneous irradiation. A manual shutter was used to control the irradiation time. The light sources used were selected according to their emission spectra for each photochromic moiety. For the study of azobenzene derivatives reported in chapter 4, ultraviolet and visible light irradiation was performed with optical fibre-coupled LEDs (ThorLabs): for UV light λ_{max} = 367 nm, FWHM = 9 nm, for Vis light λ_{max} = 454 nm, FWHM = 20 nm, equipped with collimating lenses to ensure a parallel orientation of the emitted light. In case of diarylethene derivatives, UV irradiation was performed with either: 312 nm mercury vapour lamp (λ_{max} = 312 nm, FWHM ≈ 40 nm, Herolab GmbH), 315 nm LED (λ_{max} = 315 nm, FWHM = 10 nm, Roithner GmbH), while Vis light irradiation was performed either with a 150 W halogen lamp and a green filter (λ_{max} = 530 nm, FWHM = 80 nm, Edmund Optics), or an optical fibre-coupled LED (λ_{max} = 550 nm, FWHM = 30 nm ThorLabs). Conversely, for spiropyran derivatives, the λ_{max} = 367 nm and λ_{max} = 550 nm optical fibre-coupled LEDs discussed previously were used.

In case of *in-situ* irradiation while performing scanning tunnelling microscopy on the azobenzene derivatives reported in chapter 4, the aforementioned LEDs (ThorLabs) were used: for UV light λ_{max} = 367 nm, FWHM = 9 nm, for Vis light λ_{max} = 454 nm, FWHM = 20 nm, by directly placing the terminus of an optical fibre at ~ 1.5 cm from the substrate covered with a solution of the photochromic moieties. Light irradiation was also performed on solid-supported samples: in the case of tetra-DTE porphyrins described in chapter 5, the compounds were deposited as thin films on glass substrates upon blending with high molecular weight polystyrene and spin-coating. Light irradiation was then performed using the 312 nm mercury lamp and 150 W halogen lamp with green filter previously described. Alternatively, in order to record positive and negative fluorescent patterns, structured illumination was accomplished using a confocal laser scanning microscope (Zeiss LSM 710 confocal microscope system, 10x magnification objective). For ultraviolet irradiation, a UV continuous wave (CW) laser was used (λ = 355 nm). For visible irradiation, we could not accomplish the experiments with a green laser due to instrumental limitations, but the λ = 405 nm CW laser showed to be effective as Vis light source for switching the diarylethene derivatives. For studying the photoswitching of spiropyran derivatives coating gold nanorods by means of surface enhanced Raman scattering (SERS) described in chapter 6, a dispersion of the gold nanocrystals was deposited on glass slides by drop-casting prior to their analysis with a custom-built confocal Raman microscope set-up. The

measurements were performed in the laboratory of Prof. H. Uji-I (Katholieke Universitat Leuven), in collaboration with Dr. S. Toyouchi. UV-light irradiation on the samples was performed upon irradiation of the whole sample with a λ_{max} = 367 nm LED (ThorLabs). Conversely, visible light and two-photon NIR irradiation on the samples were performed with laser sources, focussing the beam on the sample using the microscope optics, through an objective lens (60x, N.A. 1.25 PlanFluor, Nikon). For visible light, a continuous wave (CW) λ = 532 nm diode laser (Cobolt Samba TM 532nm) was used, while two-photon irradiation was accomplished with a Ti:sapphire laser tuned at λ = 780 nm and λ = 1040 nm, giving 120 fs (linearly polarised) pulses at 80 MHz repetition rate (Maitai SP, SpectraPhysics). The laser power was controlled by neutral density filters.

2.1. Photoisomerisation quantum yields

Photochromic compounds are substances capable of undergoing reversible isomerisation between (at least) two states, being the reaction in at least one direction driven by light. In the most simple case, a photoswitch can be interconverted between *A* and *B* states using two photochemical stimuli, with the following reaction scheme:

$$A \underset{\Phi_{BA}}{\overset{\Phi_{AB}}{\rightleftharpoons}} B \tag{3.17}$$

with each isomer having a specific absorption spectrum. For monochromatic irradiation, one can define Φ_{AB} or Φ_{BA} as photoisomerisation quantum yield in the two verses, respectively. The concentration of the two species will vary until a photostationary state (PSS) is reached, with the reciprocal concentration of *A* and *B* depending on their molar absorption coefficients at the irradiation wavelength ε_A and ε_B, respectively:

$$[A]\varepsilon_A\Phi_{AB} = [B]\varepsilon_B\Phi_{BA} \tag{3.18}$$

In general, the quantum yield of a photochemical reaction (Φ_r) can be defined as the ratio between the number of reactant *R* molecules consumed (or of product formed) divided by the amount of *absorbed* photons per unit time:

$$\phi_r = -\frac{dn(R)/dt}{q_{abs}} \tag{3.19}$$

where *n(R)* is the number of molecules of reactant consumed, and q_{abs} the photon flux absorbed by *R*.

A photoreaction quantum yield can thus be determined by monitoring the variation in concentration of the reactant or of the product over the irradiation time with (almost) monochromatic light. In the case of photochromic compounds, the reaction can be monitored by UV-Vis absorption spectroscopy, since their isomers absorb in different spectral ranges and one can operate at wavelengths at which the molar absorption coefficient of one species is negligible compared to the other.

The quantum yield definition is expressed in differential terms, hence its integration is required to obtain such quantity.

The photon flux absorbed by *R* is a fraction of the incident photon flux, the latter obviously dependent on the irradiation source used. Supposing that the radiation is absorbed only by the species *R*, and that its molar absorption coefficient is constant over the whole irradiation wavelength range in case of non-monochromatic irradiation, one can express the decrease in light intensity (I_{abs}) with respect to the incident light (I_0) through the optical path l via the Lambert-Beer law:

$$I_{abs} = I_0 - I_l = I_0(1 - 10^{-A}) \tag{3.20}$$

where *A* is the absorbance of *R* at the irradiation wavelength. By defining the incident photon flux as q_{in}, commonly expressed in Einstein min^{-1}, and in virtue of eq. 3.12, one can define the absorbed photon flux as:

$$q_{abs} = q_{in}\,(1 - 10^{-\varepsilon\,[R]\,l}) \tag{3.21}$$

with ε the molar absorption coefficient of *R* at the irradiation wavelength expressed in L mol^{-1} cm^{-1}, *[R]* the concentration of the reactant (mol L^{-1}) and *l* the optical path (cm).

It results:

$$-\frac{dn(R)}{dt} = \phi_r\, q_{in}\,(1 - 10^{-\varepsilon\,[R]\,l}) \tag{3.22}$$

Following from the fact that the reactant concentration changes over irradiation time, also the absorbed photon flux varies, hence making exact integration of such differential equation not always feasible. Nevertheless, it is possible to work in suitable conditions allowing approximate solutions. The most used is called *initial slope method*, and is performed upon monitoring the reaction at low conversions (< 10 %), since in this case two simplifying assumptions can be made: the variation of absorbance at the irradiation wavelength is small and appears linear, hence the absorbed light fraction at each step of the photoirradiation $(f_{ab})_m$ can be calculated using the following relation:

$$(f_{ab})_m = \frac{(1 - 10^{-A_0}) + (1 - 10^{-A_t})}{2} \tag{3.23}$$

where A_0 and A_t correspond to the absorbance (at λ_{irr}) at instants t = 0 and t, respectively. Moreover, the amount of product *P* formed is small and its absorption can be neglected, being its absorption coefficient much smaller than the one of the reagent *R* ($\varepsilon_P << \varepsilon_R$): in such a way, the light-induced back reaction can be neglected. With such approximation, by supposing that at the beginning of the reaction only the reactant *R* is present, the equation is obtained:

$$\phi_r \approx \frac{([R]_0 - [R]_t)}{t}\,\frac{V}{q_{in}\,(f_{ab})_m} \tag{3.24}$$

2.1.1. Actinometry

The molar incident photon flux, quantity which depends on the spectral irradiance of the light source used, can be measured by actinometry.[153] A chemical actinometer is realised with a reference compound undergoing an established photochemical reaction with known quantum yield: upon monitoring the concentration variation after repeated light irradiation one could obtain the desired quantity in the experimental conditions used. In most cases the latter is conveniently performed with UV-Vis absorption spectroscopy. Several standard substances are used as actinometers, depending on the spectral range of the irradiation source needed. The most widely used compounds for such practice are azobenzene ($230 < \lambda_{irr} < 450$ nm),[154] potassium ferrioxalate ($220 < \lambda_{irr} < 550$ nm)[155] and Aberchrome 670 ($450 < \lambda_{irr} < 600$ nm).[156]

Throughout the experiments performed within this work, potassium ferrioxalate has been chosen as standard, since its high reliability in the wavelength range of our interest ($230 < \lambda_{irr} < 450$ nm)[153] for measuring the $E \rightarrow Z$ and $Z \rightarrow E$ photoreaction quantum yields of the azobenzene-based compounds described in chapter 4. The so-called potassium ferrioxalate actinometer is based on the photoreduction of Potassium tris(oxalato)ferrate(III) trihydrate, $[K_3Fe(C_2O_4)_3]\cdot 3H_2O$, following the reactions:

$$Fe(C_2O_4)_3^{3-} \xrightarrow{h\nu} Fe^{2+} + C_2O_4^{\cdot -} + 2\,C_2O_4^{2-} \tag{3.25}$$

$$Fe(C_2O_4)_3^{3-} + C_2O_4^{\cdot -} \rightarrow Fe^{2+} + 2\,CO_2 + 3\,C_2O_4^{2-} \tag{3.26}$$

Hence, it follows that from one mole of reactant, two moles of product, Fe^{2+} ions are produced. The evolution of the reaction is controlled upon adding a phenantroline buffer after the irradiation, thus monitoring the formation of the coloured complex $Fe(phen)_3^{2+}$ (λ_{max} = 510 nm, ε = 11100 L mol^{-1} cm^{-1}): the photoreaction can be easily followed by UV-Vis absorption spectroscopy. The quantum yields for such reaction are available in the literature for a wide range of irradiation wavelengths, and for several experimental conditions. One particular advantage for the use of such technique is the little quantum yield variation for different irradiation wavelengths in the UV, thus enabling to measure with confidence the photon flux with non-monochromatic irradiation light.

In our case, ferrioxalate actinometry was used in its "micro-version", under conditions of total absorption, and for low conversions.[157] The common procedure involves the irradiation of multiple 2.5 mL samples $[K_3Fe(C_2O_4)_3]\cdot 3H_2O$ (0.15 M in 0.05 M H_2SO_4) in a cuvette for various time intervals, and subsequent addition of 0.417 mL of 1,10-phenantroline buffer (0.1 % w/w in 0.5 M H_2SO_4, 1.6 M CH_3COONa). Thus, by monitoring the absorbance variation at 510 nm ($\Delta A_{510\ nm}$), one can determine the incident photon flux (in Einstein min^{-1}):

$$q_{in} = \frac{\Delta A_{510\,nm}}{\Delta t} \frac{V}{l\,\varepsilon_{510\,nm}\,\phi} \tag{3.27}$$

where Δt is the irradiation time expressed in minutes, V is the final volume of the solution (L), l the optical path length of the cuvette (cm), $\varepsilon_{510\ nm}$ is the extinction coefficient of the tris-phenantroline complex (l mol^{-1} cm^{-1}) and Φ the quantum yield at a given wavelength. We used Φ = 1.21 for irradiation at $\lambda_{max} \approx 365$ nm, while Φ = 1.12 for irradiation at $\lambda_{max} \approx 450$ nm.

3. Raman spectroscopy and SERS

Vibrational spectroscopy constitutes another principal investigation tool for the study of photochromic molecules, since it allows to access detailed chemical and structural information on the basis of their specific vibrational fingerprint. Therefore it could be used as an alternative method to probe the various isomers of photochromic derivatives, especially if those are located at interfaces (therefore no longer in the bulk), or their properties cannot be determined by conventional electronic spectroscopy. Among the available vibrational spectroscopy techniques, Raman spectroscopy is of particular interest, providing great chemical specificity and especially because in particular conditions thanks to the surface enhanced Raman scattering phenomenon (SERS), the Raman signals could be enhanced, therefore allowing to perform spectroscopic measurements up to the single molecule level.

Raman spectroscopy allows to study the inelastic scattering of light. Such phenomenon is induced by excitation of matter with photons having an energy not necessarily leading to an electronic excitation of the compound involved. Such photons, often leading to a "virtual state", and not to an electronically excited state induce a dipole in the molecule analysed, which yields inelastic scattering, hence the scattered light has a different energy than the incident photon used to produce the excitation. Stokes scattering occurs when the inelastically scattered photon has lower energy than the incident one, with the difference in energy corresponding to one or more quanta of vibrational energy, hence leaving such molecule in a vibrationally excited state. On the contrary, anti-Stokes scattering is observed when the scattered photon has higher energy than the exciting one in view of the fact that the molecule originally resided in a non-zero vibrational level prior to excitation. It follows that in equilibrium conditions the intensity of the anti-Stokes Raman bands depends on the population of the vibrationally excited states (given by Boltzmann distribution).

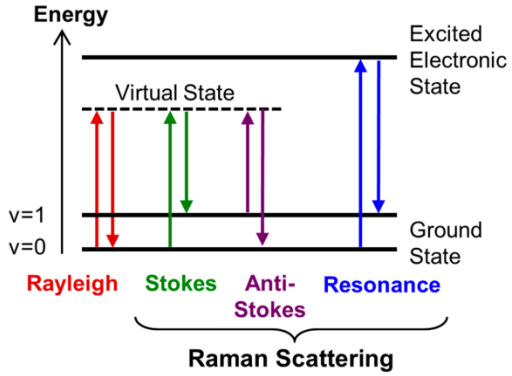

Figure 33. Simplified energy diagram showing the transitions involved in Rayleigh, Raman and resonance Raman scattering. Reproduced from Ref. [158]

In light of the brief description given above, it is simple to understand how the analysis of inelastically scattered light could give detailed chemical information, nevertheless such phenomenon normally has extremely low probability to occur. Several methods exist allowing to enhance the Raman scattering signal: by performing resonance Raman for instance, it is possible to achieve signal enhancements in the order of ~10^2 – 10^6.[159] However, thanks to the early discoveries made in the 1970s regarding the enhancement of Raman signal of molecules

adsorbed on rough coinage metal electrodes,[160] the field of surface enhanced Raman scattering (SERS) became widely studied, and nowadays is universally accepted as a powerful analytical technique allowing to obtain information down to the single molecule level.[158-159] The SERS effect is generally observed when the analyte is in proximity of nanostructured metal surfaces, and especially noble metal surfaces, being linked to the presence of localised surface plasmon resonance (SPR). The presence of SERS effect could give enhancements of several orders of magnitude to the Raman signal displayed by a molecule, and its source could be ascribed to two principal mechanisms: the electromagnetic enhancement (EM) and the chemical enhancement (CE). The first mechanism could be easily explained, since the intensity of Raman scattering (I) is directly proportional to the square of the induced molecular dipole moment (μ_{ind}):

$$I \propto {\mu_{ind}}^2 \tag{3.28}$$

while the latter is in turn the product of the Raman polarisability (α) and the magnitude of the incident electromagnetic field (E):

$$\mu_{ind} = \alpha E \tag{3.29}$$

If the molecule is in proximity of a nanostructured metal surface giving rise to LSPR, as a consequence of the excitation of the latter, in such regions the electromagnetic field is greatly enhanced, especially when the excitation light is in resonance with the LSPR band. This phenomenon could give rise to signal enhancements of up to ~10^{10}, especially in hotspots made by the contacts of two or more metal nanoparticles.[158] The chemical enhancement mechanism instead, is of lower intensity (~10 – 10^2) and is thought to come from the modification of the Raman polarisability tensor resulting from the adsorption of the molecule(s), and also from charge transfer phenomena occurring between the molecule(s) and the substrate. The signal enhancement factor (EF) can be quantified as the ratio between the SERS signal and the normal Raman signal displayed by the analyte:

$$EF = \frac{I_{SERS}/N_{SERS}}{I/N} \tag{3.30}$$

where I_{SERS} and I are the intensity of the SERS, and of the normal Raman signals, respectively, while N_{SERS} and N the number of molecules giving rise to SERS and normal Raman, respectively. SERS could give rise to EF up to ~10^{14}, allowing to obtain Raman spectra of single molecules.

It is worth to mention that since the Raman scattering enhancement is originated by the excitation of LSPR modes on metal nanostructures, the latter could be obtained using a wide variety of noble metal structures having features with dimensions lower than the wavelength of visible light: not only metal nanoparticles could be used for this purpose, but also scanning probe microscopy (SPM) tips, for example. The use of the latter gave rise to the so-called tip-enhanced Raman spectroscopy (TERS), allowing to couple the power of SPM of performing sub-nanometer scale manipulation and imaging together with the possibility of obtaining spectroscopic information at the single- (or few-) molecule level.[158]

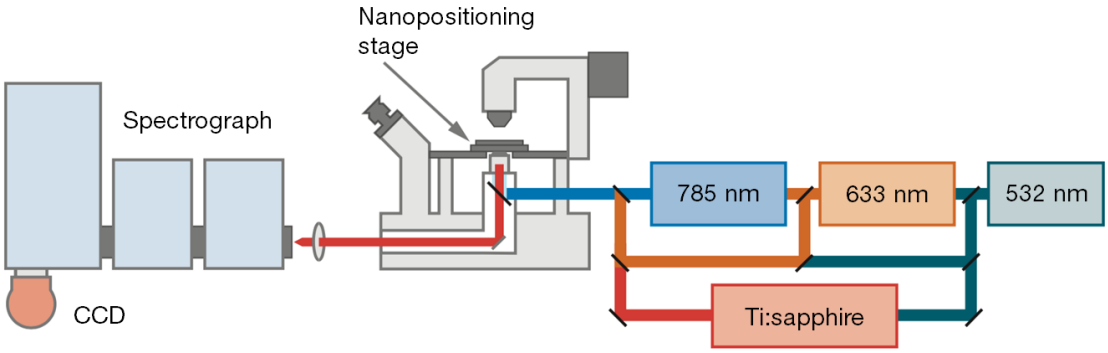

Figure 34. Simplified scheme of the experimental set up used for Raman spectroscopy in an inverted microscope, in epi-illumination geometry. Adapted from Ref.[140]

The Raman (SERS) measurements reported within this work have been performed to investigate the isomerisation of spiropyran derivatives adsorbed on anisotropic gold nanocrystals (nanorods, AuNR) described in chapter 6. The experiments have been performed in collaboration with the group of Prof. H. Uji-I, by Dr. S. Toyouchi (Katholieke Universitat Leuven), using a custom-built Raman microscope setup. The samples were prepared by drop-casting the spiropyran-coated AuNR dispersions in THF on previously cleaned glass microscope cover slides. The Raman spectroscopy setup was based on an inverted microscope (Nikon TiU) equipped with a piezoelectric stage (P517.3CL, Physik Instrument). AuNR aggregates were located by dark field illumination: white light from a halogen lamp was focussed on the sample through a dark field condenser (Nikon TI-DF, dry, N.A. 0.95-0.80). Laser excitation and collection of scattered light from the sample were performed using an objective lens (60x, N.A. 1.25 PlanFluor, Nikon) and passed through a confocal pinhole (100 µm diameter). Spectra were recorded using a charge-coupled device (CCD) camera (DU920P, Andor) operated at -85 °C equipped with a spectrograph (iHR320, Horiba), dichroic mirrors and longpass optical filters were used in order to reject the excitation laser light. Excitation was performed either with a continuous wave (CW) 532 nm diode laser (Cobolt Samba TM 532nm), a CW 632.8 nm He-Ne laser (1145P, JDSU), or a CW 785 nm diode laser. The laser power was controlled by neutral density filters.

4. Ion-mobility mass spectrometry (IMMS)

As stated previously, in most cases the isomerisation of photochromic compounds is studied by means of electronic or vibrational spectroscopy, techniques allowing to give qualitative and quantitative information on the photoreaction progression and the PSSs. NMR spectroscopy is also a frequently used technique for this purpose. Nevertheless, all these techniques fail when the (multiple) states of a photochromic compound have the same spectroscopic signature, or are chemically equivalent. In case of photoswitchable derivatives undergoing large conformational rearrangements upon isomerisation (*e.g.* azobenzene), the use of techniques capable of distinguishing between isomers (or conformers) by their different shape in the gas phase such as ion-mobility mass spectrometry is achieving wider acceptance.[161]

The Ion-mobility technique combined with mass spectrometry represents nowadays a well-established analytical tool, allowing to provide deep insight into molecular structure in the gas-phase. Ion mobility was pioneered between the 1950s and 1960s,[162] and since then has experienced a tremendous growth, being nowadays present in several commercial instruments available on the market.[163] Ion mobility mass spectrometry (IMMS) allows to separate mixtures of ions having the same mass over charge ratio (m/z) on the basis of their three-dimensional shape in the gas phase. With IMMS it is possible to experimentally determine the latter by monitoring the mobility of an ion under the influence of an external electric field, in presence of a gas with which the analyte experiences collisions. The shape resulting from the conformation of an ion in the gas phase is translated into an experimentally observable quantity called collisional cross section (CCS). Ion-mobility adds an extra "dimension" to mass spectrometry analysis, enabling to discriminate not only between ions with different mass and m/z but also on the basis of their physical shape. Commonly, in a mass spectrometer equipped for performing ion-mobility separation a drift cell filled with a buffer gas (He or N_2) is fitted between the ionisation source and the mass analyser/detector. IMMS measures the time the ion takes to migrate through the drift cell in the presence of an electric field. Traditionally, in the first IM spectrometers available the drift cell was the so-called drift tube (DTIM), in which the applied electric field is homogeneous, by applying a constant potential gradient along the tube: in such conditions the CCS (Ω) can be directly determined on the basis of the fact that the number of low-energy collisions between an ion and the neutral buffer gas molecules (or ions) is proportional to the ion size. Hence, the experimentally measured drift time (t_d), is directly proportional to the CCS (Ω) *via* the Mason-Schamp equation:[164]

$$\Omega = \frac{\sqrt{18\pi}}{16}\frac{ze}{\sqrt{k_b T}}\sqrt{\frac{1}{m_I}+\frac{1}{m_N}}\frac{760}{P}\frac{T}{273.2}\frac{1}{N}\frac{t_D\,E}{L} \qquad (3.31)$$

where z is the charge of the ion i having mass m_I, e the elementary charge, k_b the Boltzmann constant, T the temperature, P the pressure of the buffer gas with mass m_N and density number N at standard temperature in the drift cell of length L. The reciprocal of the sum between the masses of the collision partners can be also expressed as the reduced mass ($1/\mu = 1/m_I + 1/m_N$).

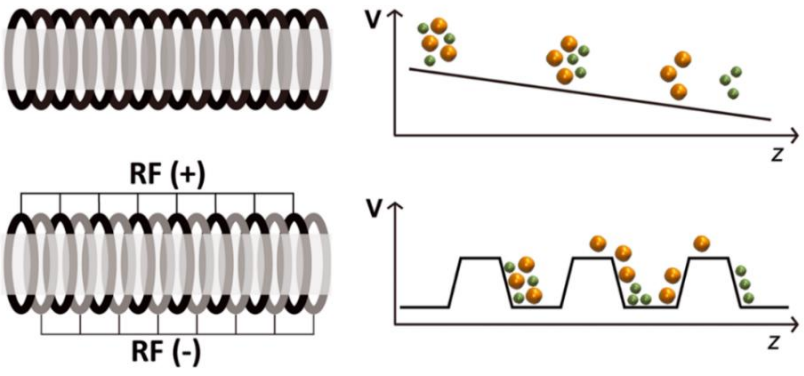

Figure 35. Simplified scheme of the drift cell working principle in the two most common IMMS systems available. The cell is filled with a buffer gas, and the ions migrating under the influence of an external electric field experience collisions with the gas atoms (or molecules), hence they are separated according to their shape. *Top*, drift tube system (DTIM), a constant and homogeneous potential difference is applied through the focussing rings of the drift tube. *Bottom*, travelling wave system (TWIMMS), the ions are radiofrequency confined, and a direct current voltage wave travelling to the exit of the trap is applied. Reproduced from Ref. [164]

Nevertheless, on most modern commercially available IMMS mass spectrometers the ion mobility separation is based on a different technology, called travelling wave ion mobility (TWIMMS). Travelling wave cells are stacked ring ion guides enabling radiofrequency confinement of the ions, with in addition a direct current voltage wave travelling to the exit of the trap. Such systems typically allow to obtain a higher resolution separation than DTIM-based ones: like in DTIMMS, ions with higher mobility exit the TWIMMS cell earlier than ions with lower ones. However, analytical equations describing the ion movement are complicated to obtain because of the non-linearity of the electric field, and its variation in both time and space. In such instruments, the linear relationship between CCS (Ω) and the drift time (t_D) is no longer valid, and current mathematical models substitute it with the non-linear relationship:

$$\Omega = \frac{\sqrt{18\pi}}{16} \frac{ze}{\sqrt{k_b T}} \frac{1}{\sqrt{\mu}} \frac{760}{P} \frac{T}{273.2} \frac{1}{N} A\, {t_D}^B \tag{3.32}$$

where A and B depend on instrumental parameters. For simplicity, the latter could be rewritten including all the experimental parameters in the factor A':

$$\Omega = \frac{z}{\sqrt{\mu}} A'\, {t_D}^B \tag{3.33}$$

It is now evident that the CCS values could be obtained by first measuring A' and B values through calibration with known analytes. The calibrant ions of known CCS must be used according their charge states and CCS ranges, being similar to the analyte.[165]

In fact, for practical reasons the drift time (t_D) is not directly measured, but rather the *arrival time* (t_A), depending also of the transfer of the ion from the end of the drift cell to the detector (dead time, t_0).

$$t_A = t_D + t_0 \tag{3.34}$$

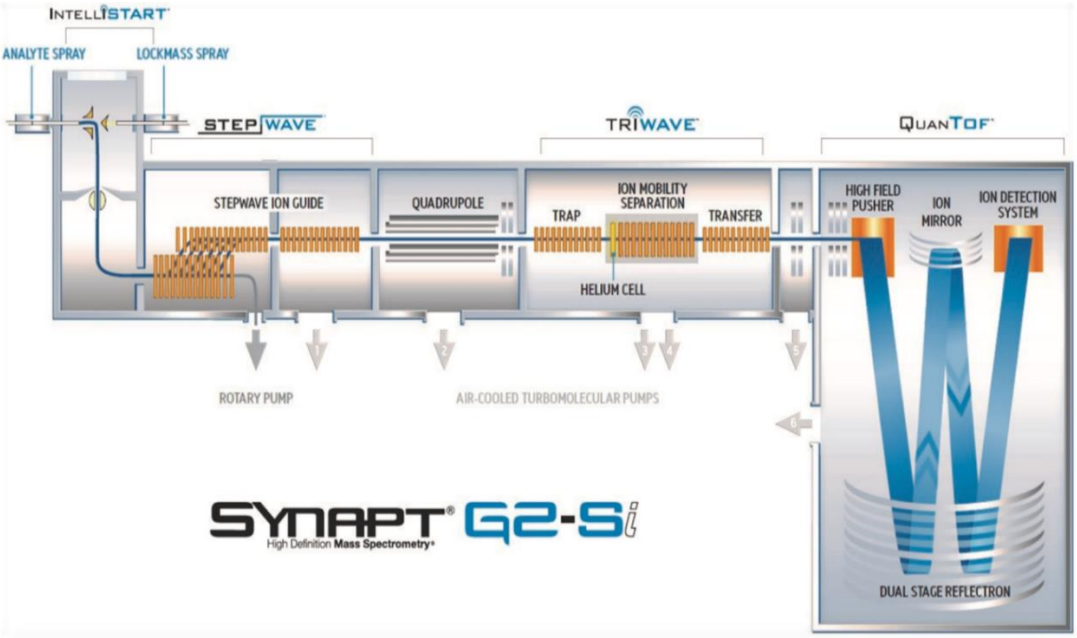

Figure 36. Scheme of the commercial TWIMMS system (Synapt G2-Si, Waters UK) employed for our studies. (Copyright www.waters.com)

IMMS measurements were performed within the present work to study the isomerisation of star-shaped azobenzene systems described in chapter 4. The experiments were performed in collaboration with Q. Duez and Dr. J. De Winter in the group of Prof. P. Gerbaux (Université de Mons), on a Synapt G2-Si (Waters, UK). The instrument is equipped with a travelling wave ion-mobility separation cell (TWIMMS), preceded and followed by an ion trap and a transfer cell respectively. In the three units, the electric field is varied by applying a DC voltage travelling wave, and in each the wave and amplitude are user-tunable (so-called Tri-wave setup). Trap and transfer cells are filled with argon, while the drift cell with nitrogen, and preceded with a RF-only cell containing helium. The Tri-wave section is preceded by a quadrupole mass analyser, allowing to select the ions on the basis of their m/z if needed. A high resolution time-of-flight (TOF) mass spectrometer is finally employed. The instrument is equipped with an electrospray ionisation source (ESI), used in negative mode. Collisional cross section data were obtained through calibration using polyalanine as standard.[165-166] The IMMS measurements were either obtained by direct infusion of the analyte solution in the ESI source, or by previously separating the mixtures with an HPLC setup (Acquity UPLC, Waters UK). The solutions were injected into the HPLC and separated on a reversed phase column (Phenomenex, C18, 5 μm, 150 x 4 mm) by eluting solvent gradients of 95-5 % formic acid 0.1% (v/v) in water / 5-95 % acetonitrile.

5. Scanning electron microscopy (SEM)

Scanning electron microscopy is one of the most widely used microscopy techniques following from its versatility: such method allows to perform microstructure morphology and chemical composition analyses on a wide variety of samples, spanning from inorganic materials to biological specimens. Electron microscopy allows to obtain morphological (and compositional) information with higher lateral resolution compared to optical microscopy, and follows from the use of electrons accelerated at high energies, which can be focussed beyond the diffraction limit of (visible) light. Image formation is related to the acquisition of signals resulting from the interaction between the electron beam and the specimen, and could be divided into two main categories, inelastic and elastic interactions. The basis of a scanning electron microscope is the use of a tightly focussed electron beam as a probe: by moving such probe on a raster on the sample and associating each point of the sample with a point on a screen, it is possible to reconstruct a topographic image of the specimen, without using image-forming lenses.

In a SEM instrument, the electron beam is produced by an electron gun: multiple electron sources could be used for SEM, working on different electron emission phenomena, such as thermoionic emission, field emission, and Schottky emission. Traditionally, thermoionic sources are the most widely used, especially thanks to the low-cost and the low required working vacuum. Nevertheless, they provide several disadvantages, especially for high-resolution application, such as large electron energy spread, source size and low brightness. These defects are overcome with field-emission guns (FEG). A FEG source consists of a single crystal tungsten wire with sharp tip (curvature radius ~ 100 nm): electron emission is produced by applying a bias of few kilovolts between the tip and the first acceleration anode. Field emission occurs

through quantum tunnelling. FEG sources (also called cold-cathode electron guns) typically have two acceleration anodes to create an electron beam with small source size, *e.g.* 3-4 orders of magnitude lower than for a thermoionic gun. However, the "image" of the electron source must be demagnified in order to produce a narrow probe on the surface of the specimen. Multiple electron lenses are used to perform such task, and the specific design depends on the instrument configuration used. However, the simplest example could be schematised as follows: the divergent electron beam produced by the source is converged and collimated using an electromagnetic condenser lens, generally followed by an aperture below the focal point of the electron beam. The subsequently diverging beam is then focussed using objective lenses into the probe point at the specimen surface down to the required spot size (in the range of 1 – 100 nm). The spot size is chosen by varying the width of the aperture placed between the condenser and the focussing lenses. The electron spot, "probe" is then scanned on the sample using deflection coils within the electron optics of the system. The as-described part containing the electron optics of a SEM is usually called "electron column", and is kept in ultra-high vacuum ($P \leq 10^{-7}$ Pa), in order to avoid scattering of electrons by the air.

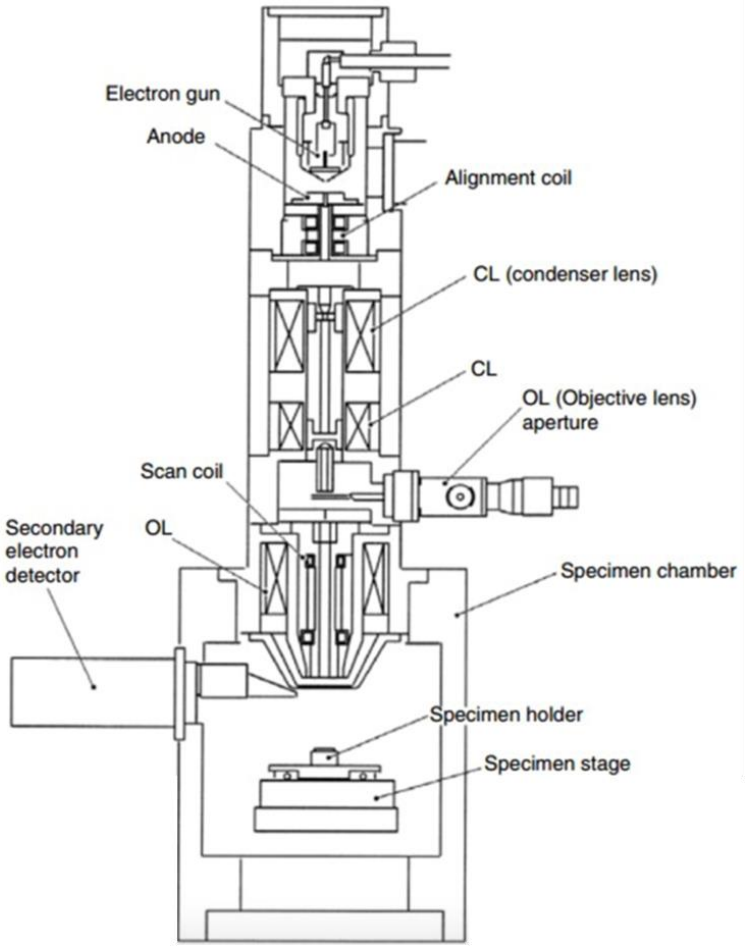

Figure 37. Schematic diagram of a scanning electron microscope. CL stands for condenser lens, while OL for objective lens. Reproduced from Ref.[167]

The specimen and the detectors are contained within a chamber which internal pressure could be varied depending on the sample nature and the desired resolution, spanning from high vacuum ($P \leq 10^{-4}$ Pa) up to atmospheric pressure. The latter is the so-called "environmental SEM" (ESEM), inevitably yielding to lower resolution imaging. ESEM is performed by saturating the

sample chamber with water vapour, used to allow the non-conducting sample to discharge. Such a technique could be utilised to image electrically insulating samples, or specimens which in virtue of their water content could not be kept in high vacuum (*e.g.* biological samples).

The interaction between the high-energy "probe" electrons and the sample could result in multiple phenomena which could be divided into two major categories: elastic interactions and inelastic interactions. Elastic scattering is the result of the deflection of the incident electron by the atomic nuclei of the specimen, or by outer electrons with similar energy. The resulting scattered electrons are called backscattered electrons (BSE), have relatively high energy (negligible energy loss), and their total scattering angle is greater than 90°. BSEs can be generated by a single- or multiple scattering events, and the volume of their production generally increases with the accelerating voltage of the electron beam, while their production yield increases with the atomic number of the atom of the specimen. On the contrary, secondary electrons (SE) are yielded from inelastic scattering, being electrons ejected from the k-shell of the specimen atoms following collisions with the primary beam. The latter have commonly low energies (< 50 eV) and are typically generated close to the sample surface (5 – 50 nm).

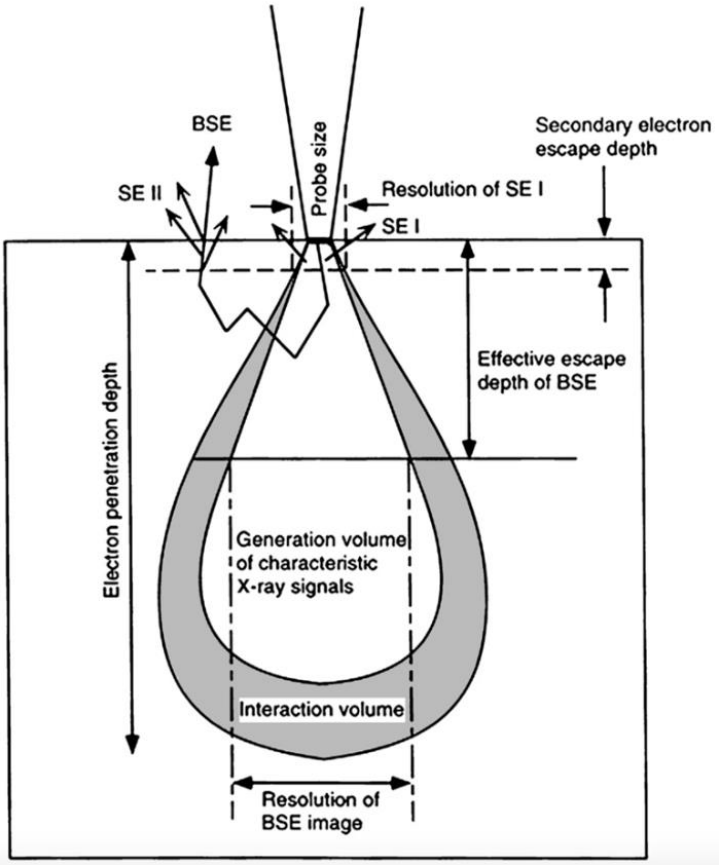

Figure 38. Schematic representation of the signals generated by electron-sample interaction in SEM. SE I are secondary electrons produced by a single scattering event (direct interaction between the analysis beam and sample), SE II are secondary electrons produced from multiple scattering events. BSE are backscattered electrons. Reproduced from Ref. [168]

BSE and especially SE are the two most common signals used to perform topographic analyses. BSE could be collected by a detector placed normally to the surface following their high scattering angle, and typically solid state diodes placed close to the source electron beam are used for such purpose. Secondary electrons are produced with a higher angle distribution and

have lower energy: typically Everhart-Thornley detectors are used for such purpose. The latter consist of a scintillator surrounded by a Faraday cage, connected to a photomultiplier: thus, after being hit by an electron a light signal is produced, which is consequently transduced to an electrical signal. By selecting the voltage applied to the Faraday cage one could select the type of electrons entering the detector, being either the BSEs or the SEs. In summary, a SEM image consists of a false colour map which contrast is given by the intensity of the BSE or SE signal observed upon raster scanning of the sample, which is directly related to its morphology and composition.

Within this thesis, scanning electron microscopy was employed to characterise the morphology of the gold nanorods (AuNR) described in chapter 6. All the measurements reported here were performed with a Quanta FEG 250 (FEI), equipped with a cold cathode field emission gun. Images were recorded on conductive samples prepared by drop-casting AuNR dispersions on p-doped silicon substrates, operating the microscope in high vacuum, using 2-3 nm spot size and 20-30 kV acceleration voltages. AuNR morphology and particle size statistics were determined using ImageJ software.

6. Scanning tunnelling microscopy (STM)

Scanning tunnelling microscopy, the firstborn among the scanning probe microscopies,[169] still represents today one of, or probably the most powerful yet inexpensive technique for obtaining topographic (and spectroscopic) information with sub-molecular scale resolution, in *real space*. Contrarily from other surface characterisation techniques based on diffraction of incident radiation, in suitable conditions STM allows to probe objects or structures not possessing translational symmetry, therefore enabling to visualise and manipulate also single molecules or disordered monolayers.[170] STM can be employed to image atomically flat crystals and physi- and chemisorbed monolayers on their surface under various environmental conditions, spanning from ultra-high vacuum to liquid and in a wide range of temperatures, thus making it a precious instrument to study molecular-scale phenomena such as self-assembly or even chemical reactivity in two dimensions.[102a, 171]

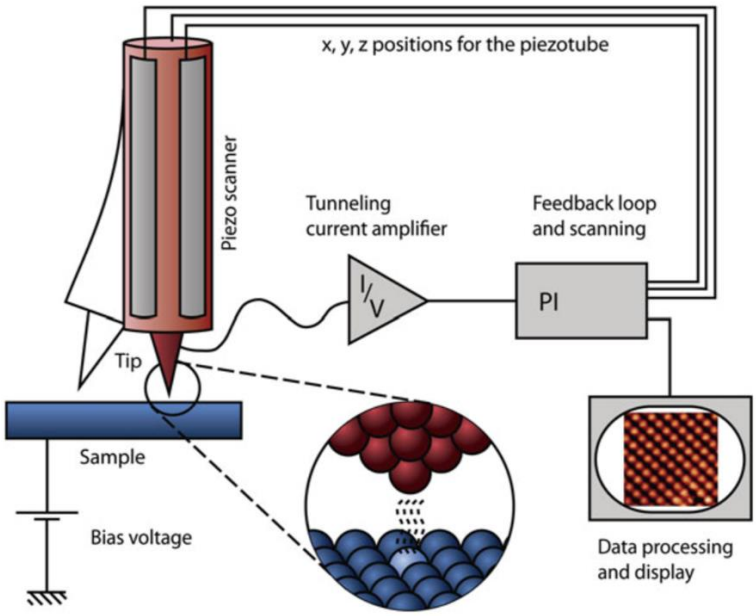

Figure 39. Schematic representation of a STM setup. The heart of a scanning tunnelling microscope is the tip-sample tunnelling junction: a sharp metallic probe is kept at low distance (few Å) from a conducting sample, while applying an external bias between the two. A resulting current, function of the tip distance, position, bias and electronic structure of the sample can be used for imaging purposes. Mapping of the sample with sub-molecular scale resolution is accomplished by raster scanning over its surface using a piezoelectric actuator. The motion is controlled by feedback electronics. Reproduced from Ref.[172]

The working principle of STM relies on the electron tunnelling effect occurring between an electrically conductive sample and a sharp, virtually monoatomic metallic tip as a probe. An STM can in fact probe the number of filled or unfilled energy states near to the Fermi level of tip and sample: rather than directly measuring the topography of a sample, it gives a surface with constant tunnelling probability. Electron tunnelling is observed upon applying a bias between tip and sample, by keeping their distance extremely short (few Å), thus resulting in an observable tunnelling current. Such current is a function of tip distance, position, bias applied and electronic structure of the sample, which could be expressed as its local density of states (LDOS). Such information could be used for imaging purposes, achievable by monitoring the tunnelling

current upon raster scanning the sample surface. The current measured point-by-point upon scanning could be used to reconstruct a contrast map of the *electron density* of the specimen.

Piezoelectric ceramics undergo a geometric strain proportional to an applied electric field: such materials are used to build actuators which movement can be precisely controlled by applying an external voltage. Piezoelectric actuators having subnanometer range resolution are used to control the tip-sample position, while the scanning motion is governed by feedback electronics. STM imaging can be performed by scanning the sample with two operating modes: *constant height mode*, and *constant current mode*. In *constant height mode*, the line scan is performed by keeping the probe at a fixed height above the sample, recording the current measured at each point: the current signal thus represents the dataset employed to generate the image of the sample. Conversely, in *constant current mode* a line scan is accomplished upon setting a current *setpoint* to the feedback electronics controlling the scanner: the system in such case varies the tip-sample distance in order to keep the current value set unvaried. Thus, a map is reconstructed with the height of the tip recorded at each point of the raster scan. The *constant height mode* allows to perform faster scanning with usually higher lateral resolution, since it does not require the feedback loop to re-adjust the tip-sample distance at each point. Nevertheless, it has limited applicability: for instance, if the surface has features higher than the set scan height, the tip will crash, modifying its- (and the sample) geometry. Furthermore, on a practical point of view it is complicated to keep the vertical height of the tip stable against thermal drift and external vibrations: hence, it is normally not utilised in instruments working at room temperature and ambient pressure.

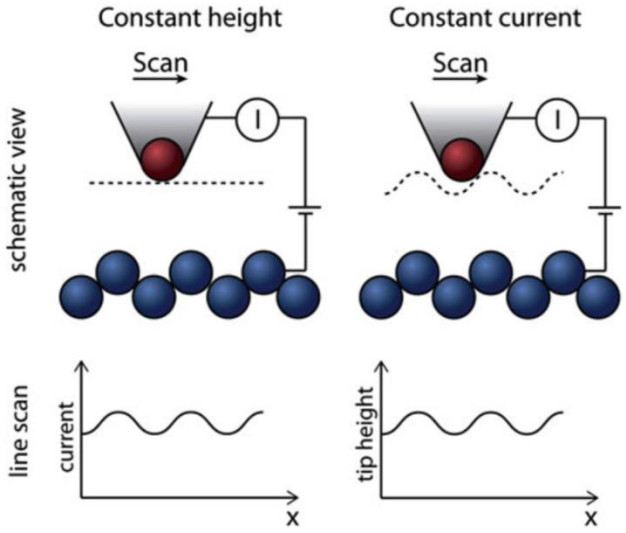

Figure 40. Scheme of the scanning modes used for STM imaging. Reproduced from Ref.[172]

The tunnelling effect is a purely quantum mechanical phenomenon: it occurs when electrons move through a barrier which could not be classically overcome. Electrons, in virtue of the wave-matter duality can be considered as waves, and as such they have non-zero probability to tunnel through the gap if such barrier is thin enough. For tunnelling in vacuum through a unidimensional barrier (time-independent case), the phenomenon could be modelled by solving the stationary Schrödinger equation:

$$\left(\frac{\hbar^2}{2m_e}\Delta + \mathrm{V(r)}\right)\Psi = E\,\Psi \tag{3.35}$$

where m_e is the electron mass, and $V(r)$ is the potential describing the barrier with height Φ and width x, and E the energy of the electron. The exact solution can be found by expressing Ψ as plane waves for the three regions: 1, tip; 2, vacuum; 3, sample.

$$\Psi_1 = e^{ikx} + A\, e^{-ikx}$$

$$\Psi_2 = B\, e^{i\kappa x} + C\, e^{-i\kappa x}$$

$$\Psi_3 = D\, e^{ikx}$$

$$\text{with } k = \frac{\sqrt{2m_eE}}{\hbar} \text{ and } \kappa = \frac{\sqrt{2m_e(\Phi - E)}}{\hbar} \tag{3.36}$$

The A, B, C, D coefficients can be determined by setting equal the amplitude and first derivatives of the wavefunctions at the boundaries. The transmission coefficient (T) can then be defined by comparing the wavefunctions on both sides of the barrier (1 and 3):

$$T = \frac{|\Psi_1|^2}{|\Psi_3|^2} = \frac{A^2}{D^2} = \left[\left(\frac{k^2+\kappa^2}{2k\kappa}\right)^2 \sinh(\kappa x)\right]^{-1} \tag{3.37}$$

The latter may be simplified by assuming a high barrier potential compared to the energy of the electron $\Phi >> E$, hence $\kappa x >> 1$.

$$T \approx \frac{16k^2\kappa^2}{(k^2+\kappa^2)^2}\, e^{-2\kappa x} \tag{3.38}$$

The number of tunnelling electrons (the tunnelling current, I) is linearly proportional to the transmission coefficient T, which depends exponentially on the length of the barrier x:

$$I \propto T \propto e^{-2\kappa x} \tag{3.39}$$

The latter relation clearly evidences the exponential dependency of the tunnelling current with the tip-sample distance, which is the reason, in first approximation, of the high vertical resolution of such scanning probe technique.

However, a more realistic model taking account of the three-dimensionality of the system and the electronic structure of tip and sample exists, being introduced by Tersoff and Hamann in the 1980s.[173] Such model is derived from the treatment of the tunnelling effect through a three-dimensional barrier by the perturbative theory (Bardeen).[174] Describing the tip and the sample with the wavefunctions Ψ_μ and Ψ_ν, respectively, and the tunnelling matrix $M_{\mu,\nu}$ representing the overlap between them, the tunnelling current for a general geometry could be written with the following expression:

$$I = \frac{2\pi e}{\hbar}\sum_{\mu,\nu} f(E_\mu)[1 - f(E_\nu + eV)]\left|M_{\mu,\nu}\right|^2 \delta(E_\mu - E_\nu) \tag{3.40}$$

where $f(E)$ is the Fermi-Dirac distribution function, E_μ, E_ν the energies of the states of sample and tip, and V the applied bias voltage. In the limit of low temperature and voltages, the term $[1 - f(E_\nu + eV)]$ can be approximated with a step function, leading to the approximated expression:

$$I = \frac{2\pi}{\hbar} e^2 V \sum_{\mu,\nu}\left|M_{\mu,\nu}\right|^2 \delta(E_\mu - E_F)\delta(E_\nu - E_F) \tag{3.41}$$

with E_F being the Fermi energy of sample and tip.

The equation could be resolved by approximately describing the sample as a wavefunction parallel to its surface (Bloch's theorem), which in vacuum decays exponentially on the perpendicular direction. The tip is modelled as spherical s-wavefunction at the point closest to the sample, while the rest is arbitrary. By assuming that the work function of tip and sample is equal, it is possible to obtain the following expression used to define the tunnelling current:

$$I = 32\ \frac{\pi^2}{\hbar k^4} e^2 V \Phi^2 R^2 e^{2kR} \frac{1}{V_{tip}} \sum_{\mu,\nu} |\Psi_\nu(\overrightarrow{r_0})|^2\ \delta(E_\mu - E_F)\delta(E_\nu - E_F) \tag{3.42}$$

where k is the inverse decay length for the wavefunctions in vacuum, as defined in (3.34), R the tip radius, V_{tip} the normalisation volume of the tip, the centre of the tip is at $\overrightarrow{r_0}$.

The local density of states (LDOS) of tip (μ) and sample (ν) can also be defined:

$$\rho_\mu(E) = \frac{1}{V_{tip}} \sum_\mu \delta(E_\mu - E_F) \tag{3.43}$$

$$\rho_\nu(E, \vec{r}_0) = \sum_\nu |\Psi_\nu(\overrightarrow{r_0})|^2 \delta(E_\nu - E_F) \tag{3.44}$$

Hence, the final expression for the tunnelling current becomes:

$$I \propto V \rho_\mu(E) \rho_\nu(E, \vec{r}_0) \tag{3.45}$$

where V is the applied bias voltage. Thus, the current depends on the LDOS of the sample at the position of the tip $\overrightarrow{r_0}$ at the Fermi energy E_F, demonstrating that by STM it is the LDOS of the sample being imaged, rather than its topography.

In case of molecular adsorbates located between the tip and the substrate, the tunnelling current is proportional to the density of states of the adsorbate/substrate system. The image contrast of the adsorbate depends on the perturbation it induces to the local density of states of the substrate, since the observed tunnelling current is the result of the overlap between the states of the two. It follows that the image obtained contains information on the symmetry of the molecular orbitals of the adsorbates, together with the location of their adsorption site on the substrate. Nevertheless, one has to keep in mind that the adsorbate electronic levels are pinned with respect to the substrate Fermi level: when a molecule is physisorbed on a surface, the energy of its molecular orbitals are shifted with respect to the case where there are no interactions. The same happens to the electronic states of the substrate, although this shift is lower.[175] This is to state that STM does not provide exact topographic information over the adsorbate layers on a substrate, but is the result of the hybridisation of the states of the two: therefore the broadening or the depletion of the electron density of a molecular adsorbate also depends on the adsorption mechanism (*e.g.* the electronic interaction between molecule and substrate).

In order to perform STM imaging, it is necessary to use highly sharp metal tips, having a curvature radius lower than few tens of nanometers. Nearly the totality of the current measured in the tunnelling junction is transported through the tip apex (atom). This allows to obtain lateral resolutions of ~ 1 Å, together with the high vertical resolution mentioned previously. STM tips are fabricated by cutting or etching a metal wire, being tungsten (W), or a platinum-iridium alloy (Pt/Ir) the most commonly used. Tips are made by mechanically cutting the metal wire, or alternatively by electrochemical etching, the latter technique allowing to obtain sharper and

more uniform tip shapes. Electrochemical etching nevertheless yields probes covered by an oxide layer which removal is necessary for effective measurements, and is intrinsically slower than mechanical cutting. For measurements performed in air or in liquid Pt/Ir is the material of choice following its chemical stability.

STM imaging can be performed in a vast variety of environmental conditions, spanning from ultra-high vacuum to liquids. One key condition that has to be respected is the minimisation of faradaic and capacitive currents, hence to work in a dielectric environment. This is obviously obtained in vacuum conditions, but for other media it is necessary to use *e.g.* liquids with low dielectric constant. For instance, to perform STM studies at the solid-liquid interface, low dielectric solvents such as 1-phenyloctane, n-tetradecane, 1-octanol, heptanoic-, octanoic- or nonanoic acid, and 1,2,4-trichlorobenzene (TCB) must be used. The other requirement for such solvents is their low volatility in order to avoid changes in solute concentration within the measurements timescale. On the other hand, when working in water, or high dielectric constant media, the use of an insulated tip and an additional electrode is necessary (reference electrode), such setup is called electrochemical STM, but will not be the object of our work.

Within this thesis STM was used to study the self-assembly of tris(azobenzene) star-shaped scaffolds at the solid-liquid interface between heptanoic acid and highly ordered pyrolytic graphite (HOPG), described in chapter 4. Investigation on the self-assembly of the star-shaped molecules was performed by STM at ambient pressure and room temperature, using freshly cleaved highly ordered pyrolytic graphite (HOPG) as substrate. The experiments were performed using a Veeco Multimode III (Bruker) equipped with a STM head and a 1 µm-range piezoelectric scanner (A-Piezo, Veeco), working in constant current mode. STM tips were mechanically cut from a Pt/Ir (80 : 20) wire (0.25 mm diameter, Goodfellow). Self-assembly was studied at the solid-liquid interface between HOPG and a supernatant solution (1-heptanoic acid, Sigma Aldrich), by applying 4 µL of the latter on the substrate, after having checked the integrity of substrate and tip by visualising the graphite lattice. The raw STM data was processed using a dedicated image processing software (SPIP, Image Metrology), by means of flattening and subtraction of a 2-degree polynomial background. The images were corrected from drift by calibration with the underlying graphite lattice. Unit cell parameters were obtained by Fourier analysis.

7. Gold nanorods (AuNR) synthesis

Among the colloidal metal nanoparticles with nonspherical symmetry, gold nanorods (AuNR) probably represent the first and most successful example synthesised by a chemical bottom up approach.[128, 176] Due to their striking optical properties, a great deal of efforts has been spent in recent years to develop synthetic methods enabling to obtain AuNR with high yield and size/shape selectivity. Several routes have been proposed, going from top down approaches used to obtain nanostructures directly on surfaces, to several bottom up methods yielding colloidal dispersions of rod-shaped nanocrystals, all aiming to narrow size and aspect ratio distributions as principal target. The latter methods are usually preferable, since they allow to obtain the material in large amounts, following facile and inexpensive experimental strategies.

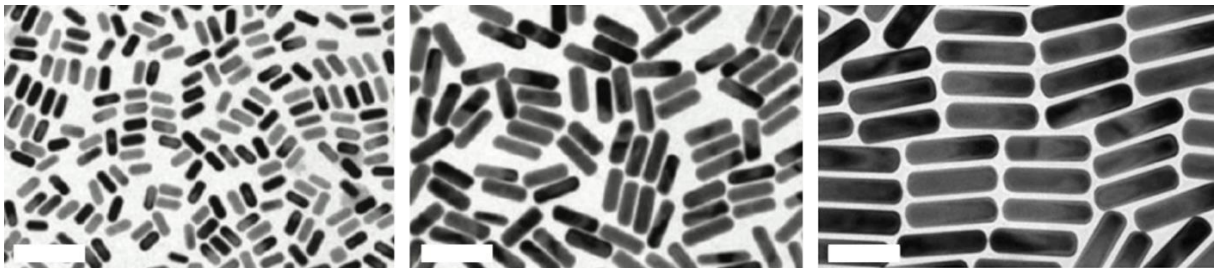

Figure 41. TEM micrographs of samples taken from colloidal dispersions of CTAB-stabilised AuNRs synthesised by seed-mediated growth in water. *Left*, rods synthesised using sodium salicylate as additive, showing an average diameter of 14 ± 1 nm and 36 ± 3 nm length, reproduced from Ref.[177] *Centre*, rods synthesised using 5-bromosalicylic acid as additive, showing an average diameter of 22 ± 1 nm and 64 ± 5 nm length, reproduced from Ref.[177] *Right*, rods synthesised using sodium oleate as additive, showing an average diameter of 35 ± 2 nm and 125 ± 7 nm length, reproduced from Ref.[137b] All scale bars represent 100 nm.

In all cases, the bottom up synthesis of gold colloids is performed by the reduction of Au(III) salts in presence of agents capable to stabilise the dispersion, method known since the pioneering work of Faraday first,[122] and later Zsigmondy.[123b] These early discoveries greatly boosted the research in such field, nevertheless processes allowing the realisation of anisotropic gold colloids did not appear before the 1990s.[178] The common idea is to use a template to direct the particle growth in a specific direction: first syntheses of gold rod-shaped particles were performed by electrochemical reduction of gold either in nanoporous materials,[179] or by using rod-inducing reverse micelles.[180] Among the bottom-up strategies, the seed-mediated growth is undoubtedly the most popular and widely applied, thanks to the facile and inexpensive experimental procedure, and its flexibility allowing to obtain high quality colloidal dispersions with a wide variety of size and aspect ratios. Although such method was first employed for the formation of *anisometric gold colloids* in 1989,[178] the AuNR seeded growth in colloidal dispersion was developed from the first experiments done by Jana *et al.* in 2001.[176]

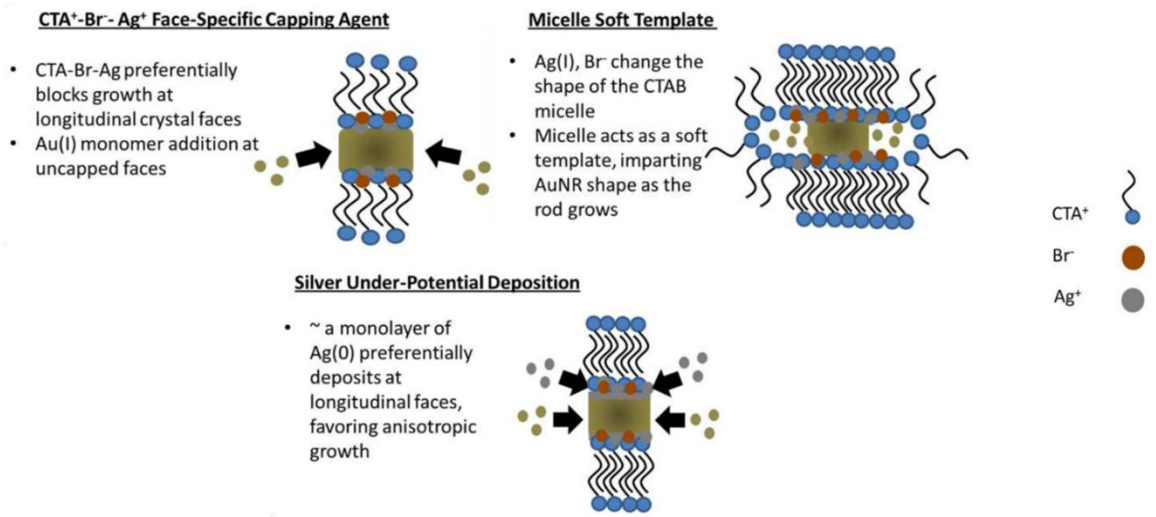

Figure 42. Proposed mechanisms for the anisotropic growth of AuNRs. The presence of Ag(I) ions is fundamental for the growth of AuNRs, nevertheless their role is still under debate. Reproduced from Ref. [181]

The AuNR seed-mediated growth is based on the reduction of Au(III) chloride within cetyltrimethylammonium bromide (CTAB) micelles by a weak reducing agent (usually ascorbic acid), catalysed by small "seed" spherical gold nanoparticles. The methods that are still used nowadays are based on a two-step process, consisting in the preparation of the seed nanospheres, and their addition to a growth solution where the rod-shaped particles are produced. The resulting particle shape is mainly due by the particular choice of CTAB as surfactant, since it is known to form bilayer, cylinder-shaped micelles in water, at suitable concentration,[182] but also to act as crystal face-specific capping agent, allowing the growth of nanocrystals on preferential crystal axes. The AuNR synthesis process is the result of a complex multi-step mechanism, and the exact reason for such anisotropic crystal growth is still being under debate, however a general picture is accepted and will be summarised here.[183] The seed nanoparticles consist of small diameter gold nanospheres (≤ 5 nm) prepared by the reduction of tetrachloroauric acid $HAuCl_4$ with a strong reductant (most commonly sodium borohydride, $NaBH_4$), in presence of CTAB as stabiliser. Particular care has to be taken in consuming all the reductant used in this step prior to add the seed to the growth solution. The reason for this precaution comes from the fact that perhaps the most important aspect of the seeded growth method is the use of a weak reducing agent. The latter must not be able to reduce the gold ions to Au(0) in absence of the seed particles, which surface act as catalyst, otherwise no anisotropic growth would occur. The use of CTAB is also fundamental for two main reasons: the bromide counterions exchange the chloride ones in the tetrachloroaurate $AuCl_4^-$ anion, yielding to the complex $AuBr_4^-$, and the latter forms ion pairs with the tetraalkylammonium cationic head of the surfactant CTA^+. Both the ligand exchange and the formation of the ion pairs lead to a shift of the gold ions redox potential (cathodic shift).[184] In such conditions, in the growth solution the following equilibrium reaction is pushed towards the comproportionation:

$$Au^{3+} + 2\,Au^0 \rightleftharpoons 3\,Au^+ \tag{3.46}$$

resulting in Au(I) being the most stable oxidation state in the growth solution. As previously mentioned, particular care has to be taken in order to use a reducing agent enabling to perform the reaction only in presence of the seed spherical nanoparticles. Upon addition of the

reductant, which most commonly is ascorbic acid, all the Au(III) ions are reduced to Au(I), but the reduction does not proceed until the addition of the seed. In case the reductant used is ascorbic acid, another important precaution must be taken in order to control the pH, following its pH-dependent reduction potential. The pH can be varied in order to modulate the growth, but must be kept under pH ~ 9, otherwise in basic conditions the ascorbic acid will be high enough to reduce Au(I) into Au(0) even in the absence of seeds. Once the seed nanoparticles are added to the growth solution, slow AuNR growth takes place, process which requires several hours to reach its completion. The temperature is generally kept slightly above room temperature (30 °C): high enough in order to guarantee complete CTAB solubility, but at the same time avoiding high temperatures is desirable, since it allows to slow down the reduction, hence achieving a narrower size distribution.

In order to successfully synthesise single crystal AuNRs, also the use as silver ions (Ag^+, usually as $AgNO_3$) in the growth solution is required. The role of Ag^+ ions in AuNR seeded growth is still not clear, since three mechanisms of its action have been postulated, but no experimental agreement was found yet. As indicated in Figure 42,[181] silver ions could have multiple roles: in one case, the metal could form the complex $Ag[BrCTA]_2$, which could act as a side-specific capping agent by blocking the growth on the longitudinal axis, thus allowing Au(I) reduction only on the ends. Another hypothesis stands on the fact that Ag^+ modifies the shape of the micelle, the latter acting as a soft template for anisotropic growth. Alternatively, another proposed mechanism consists on the underpotential deposition of Ag(0) as monolayer on the short crystal facets. Although not clearly explained yet, it has been shown that the presence of silver ions is necessary for the synthesis of single crystal AuNRs.

Importantly, also the use of additives, or co-surfactants for fine tuning the AuNR aspect ratio and their monodispersity has to be mentioned.[137b, 177] As a general mechanism, it has been proposed that such additives intercalate in the CTAB micelle bilayer modifying its shape, or resulting in an increase of its stiffness, thus varying the template for AuNR growth. In such context, the most successful compounds used were on the one hand small aromatic additives, derivatives of salicylic acid, while on the other hand sodium oleate was used as long-chain co-surfactant.

In the present context, AuNRs have been synthesised as CTAB-stabilised colloidal dispersions in water. The anisotropic nanoparticles were used as a starting material in order to study their surface functionalisation with photochromic thiols described in chapter 6. Single crystalline AuNRs with different size and aspect ratio have been synthesised following the procedures reported by Murray *et al.* Utilising sodium salicylate, 5-bromodsalycilic acid,[177] or sodium oleate[137b] respectively we were able to obtain good quality AuNR colloidal dispersions with increasing aspect ratio. Following from the satisfying size and shape distributions shown by the colloidal dispersions obtained, no further shape-selective purification step *e.g.* by centrifugation,[185] or depletion forces[186] was needed. The as-synthesised AuNR colloidal dispersions could be directly stored in the dark at room temperature, and showed excellent stability over long periods of time.

7.1. AuNR functionalisation with thiolate-based self-assembled monolayers (SAMs).

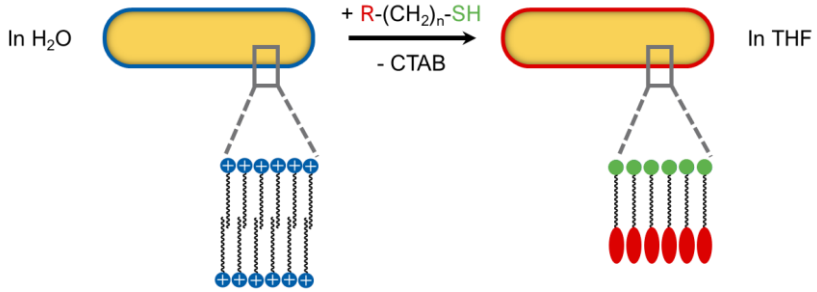

Figure 43. Schematic representation of the ligand exchange. AuNR are synthesised as colloidal dispersions in water, stabilised by bilayer micelles of the cationic surfactant CTAB: the latter is removed by chemisorption of organic thiols as monolayers on the AuNR surface.

Surface functionalisation of AuNRs colloidal dispersions synthesised by seed mediated growth methods is a fundamental step for their application, going from biology to materials chemistry.[187] As-synthesised single crystal AuNRs are stabilised in water by micelles formed by a double layer of the cationic surfactant CTAB, which is not chemically bound to the surface of the gold colloid. Although adding chemical functionalities through electrostatic interactions between the bilayer cationic micelle and negatively charged polyelectrolytes (layer-by-layer approach – LbL) was proposed as a viable strategy,[188] covalent functionalisation is the most widely employed method for tuning AuNR properties. In case of stabilisation by CTAB micelles, the stabiliser is not surface-bound, thus it is in constant dynamic exchange between the solution and the AuNR surface. CTAB acts as surface-capping agent in water, when its concentration is highly above the critical micellar concentration (CMC ≈ 0.9 – 1.0 mM). If these two conditions are not satisfied (*e.g.* different solvents, low surfactant concentration) irreversible aggregation occurs, resulting in the loss of the original nanocrystal shape and dimensions. On the other hand, covalent functionalisation by chemisorption of the nanocrystals surface with chemical groups having high affinity for coinage metals allows, at least in principle, to stabilise the nanocrystals preventing their irreversible aggregation in a variety of different environments, without the need of working in presence of high surfactant concentrations. Chemisorption is attained by exploiting the widely known affinity of thiols for gold and noble metals in general. Thiolate-terminated organic molecules form self-assembled monolayers (SAM) on metallic surfaces upon chemisorption and subsequent re-organisation to form highly ordered one-molecule-thick layers passivating the metal.[133] In case of spherical gold nanoparticles, consolidated and widely employed methods for their direct synthesis as thiol-stabilised colloidal dispersions are available,[132a] nevertheless this is not the case for anisotropic structures such as gold nanorods. The synthesis of thiolate-functionalised AuNRs therefore requires to replace the surface-capping CTAB with organic thiol monolayers as a further preparation step.

Several efforts have been made in the past to develop reliable strategies for the exchange reaction of CTAB with organic thiols, avoiding any morphological variation of the nanocrystal habit. Such strategy relies on the exposure of the nanocrystals to highly affine thiols upon disruption of the original CTAB micelle coating, thus exposing their highly reactive facets towards Au-S bond formation. To date many attempts have been performed following literature,

by either phase transfer methods, allowing the functionalisation at the interface between aqueous and organic phases[189] or in a one-phase approach, by addition of the thiol in a (water miscible) solvent to a CTAB-stabilised AuNR dispersion in water, allowing micelle break-up.[187b] The latter, most frequently used, is based on the assumption that polar, water miscible solvents such as ethanol (or THF) affect the critical micellar concentration of cetyltrimethylammonium bromide surfactant, used as stabiliser for the nanoparticles.[187b] As a result, adding ethanol to a water-CTAB dispersion of colloidal nanocrystals would lead to the disruption of the micelle and consequent irreversible aggregation and precipitation of the particles, if the process is performed in absence of a ligand able to stabilise them. On the contrary, using a concentrated solution of the desired organic thiol would lead to AuNR stabilisation following the formation of a SAM on their surface.

For the work described within this thesis, CTAB-stabilised AuNRs with different aspect ratio have been functionalised with a photochromic organothiol derivative, as described in chapter 6. Control experiments have also been performed with commercial, non-photochromic thiols having alkyl chains with similar length. The procedure used, adapted from methods in the literature,[187a, 187b] involved multiple centrifugation rounds of the as-synthesised AuNR dispersions in order to reduce the CTAB concentration to the minimum amount required for keeping the dispersion stable. In all cases, centrifugal precipitation of AuNRs is performed twice, upon discarding the surnatant and re-suspending the precipitate in water. The final AuNR dispersion in water, ten times more concentrated than the initial suspension, is flash-added to a thoroughly stirred solution (5 mM) of the desired thiol in either ethanol or THF, depending its solubility. Thiol oxidation by reaction with atmospheric oxygen is avoided upon degassing the mixture and working under inert gas atmosphere. The mixture is allowed stirring for at least 24 hours at room temperature. The product is finally purified from traces of unreacted thiol, residual CTAB, additives and metal salts by multiple centrifugation cycles initially with 1 : 1 = H_2O : THF mixtures, and later with pure organic solvent until the surnatant reaches a clear, colourless aspect.

Chapter 4.

ELECTRONIC DECOUPLING IN RIGID MULTI(AZOBENZENE) SWITCHES:

An Insight into their Multi-Photochromism and Self-Assembly Properties[1]

The main focus of the work described within the present chapter lies on the study of novel azobenzene-based photochromic derivatives containing up to three switches within the same molecular backbone. Such molecules were realised as promising building blocks for the generation of light-responsive materials, such as 2D and 3D metal-organic materials and covalent-organic frameworks, as well as to study their self-assembly in hydrogen-bonded networks.[5, 110, 190] The molecular scaffolds studied here consist of rigid, star-shaped cores, being their geometry dictated by the presence of an aromatic backbone and by the photochromic units branching from a central, 1,3,5-trisubstituted benzene ring. Such a substitution pattern results in the arms being reciprocally in *meta*- position, thus lowering the conjugation of the multi-chromophoric systems. A detailed study over the multi-photochromism of the tris(azobenzene) derivative has been performed with multiple analytical techniques, by comparison with bis(azobenzene) and mono(azobenzene) model compounds. The latter two were designed by progressively substituting the diazene-1,2-diyl groups with ethyn-1,2-diyl units, thus yielding similar, yet non-photoresponsive branches. The self-assembly of our tris(azobenzene) derivative in 2D networks on graphite surface has been studied by scanning tunnelling microscopy, corroborated by molecular modelling. The exploration of the dynamic self-assembly of such systems into ordered supramolecular architectures allowed to identify patterns resulting from multiple isomers, thereby demonstrating that the multi-photochromism is retained when the molecules are confined in two-dimensions.

1. INTRODUCTION

Azobenzene represents the most well studied class of photochromic compounds: its celebrity is mainly due by the large conformational rearrangements occurring upon its isomerisation,

[1] Large parts of this section have been, or will be published: - Galanti, A.; Diez-Cabanes, V.; Santoro, J.; Valášek, M.; Minoia, A.; Mayor, M.; Cornil, J.; Samorì, P. Electronic Decoupling in C_3-Symmetrical Light-Responsive Tris(Azobenzene) Scaffolds: Self-Assembly and Multiphotochromism. *J. Am. Chem. Soc.*, **2018**, *140*, 16062-16070; - Galanti, A.; Santoro, J.; Mannancherry, R.; Duez, Q.; Diez-Cabanes, V.; Valášek, M; De Winter, J.; Cornil, J; Gerbaux, P.; Mayor, M.; Samorì, P. *in preparation*.

making azobenzene particularly suitable as molecular-scale actuators. In order to exploit and/or amplify the shape variation of the switch to a greater length scale, it is vital to embed such unit in a conformationally rigid molecular scaffold.[38] Towards this end, typically a viable strategy consists of including them into rigid aromatic structures. However, such a solution could potentially prevent full, or even partial photochromism of the system, since electron delocalisation lowers the energy of the first excited state(s) precluding the access to the photoreaction pathway.[39] Systematic research work was performed in order to find the ideal substitution pattern allowing the coexistence of structural rigidity and satisfying photoswitching extent: in this framework however, little was done on systems containing more than one photochromic unit.[191] It is worth pointing out that the electronic decoupling between the photochromes is indeed a necessary goal in order to preserve the photoactivity of multichromophoric systems.[38-39, 192] In particular, star-shaped multi-azobenzene systems were realised by mutual chromophore connection to non-planar,[191a, 193] or to quasi-planar[191b-d] cores. However, the isomerisation behaviour of the individual switches has been characterised only to a partial extent by means of ^{1}H-NMR spectroscopy and in the case of mutual connection via a central amine linker the undesirable presence of electronic delocalisation between the chromophores was observed.[191a]

Recent research reports brought our interest to C_3-symmetrical aromatic systems, since as a result of their shape, rigidity and high planarity, they have been successfully exploited as organic ligands for supramolecular coordination complexes and metal-organic frameworks.[5a, 5c, 190, 194] On the other hand, the study of the self-assembly of rigid aromatic molecules in two-dimensional crystalline structures with the use of STM at the interface between graphite and their solutions has been a hot topic for surface scientists in the last decade.[102a, 195] Such a technique enabled to visualise and to study in detail the subtle interplay between the noncovalent interactions giving rise to peculiar 2D crystalline assemblies in thermodynamic equilibrium with the supernatant solution.[196] Hydrogen bonding received particular interest, due to the directional character of such interaction. Trimesic acid (1,3,5-tricarboxylic acid) represents the most prototypical and widely studied example of C_3-symmetric building block for the construction of H-bonded supramolecular networks, since its tendency to form hexagonal honeycomb structures, which symmetry is of great interest for the realisation of nanoporous networks.[108] Nevertheless, the study of increasingly larger C_3-symmetrical building blocks showed that above a certain limit the "ideal" honeycomb shaped pattern was less thermodynamically stable compared to other polymorphs experimentally visualised.[110] This experimental evidence emerged from the fact that the driving force for the formation of such self-assembled supramolecular systems is the result of the enthalpic balance between anisotropic intermolecular interactions (*e.g.* hydrogen bonds), and isotropic van der Waals forces between the molecule and the substrate, together with the contribute of solvation, since the crystalline monolayer is in thermodynamic equilibrium with the solution overhead.[109] The study of even larger aromatic systems showing such symmetry, and the possibility to add a photoresponsive character to these assemblies further motivated our research.

Investigation on the azobenzene-based switches by STM has always been an appealing task for surface scientists,[111, 197] albeit the visualisation of the *Z* isomer at the solid-liquid interface has always posed problems because of its non-planar, kinked geometry, which yields unfavourable van der Waals interactions with the underlying substrate surface.[112] Therefore, the

use of several artifices such as the decoration of the photoswitchable derivatives with ad-hoc functional groups, or molecular geometries enabling the self-assembly of both *E* and *Z* isomers on graphite have demonstrated to be effective, although sometimes making their visualisation a cumbersome task.[73, 112-113] Solid-liquid interface STM imaging of various isomers of a photochromic system containing multiple azobenzene units in the same molecular backbone was achieved by embedding the switches in a host-guest network.[114] Such a finding suggests that the isomerisation of multi-photochromic systems could be also monitored in mono-component ultrathin films by attaining an exquisite control over the interplay between intermolecular and interfacial interactions via an ad-hoc molecular design. In this regard, a rigid scaffold possessing C_3 symmetry around a central benzene core appears ideal to address the key question of electronic decoupling on the isomerization of multi(azobenzene) systems.

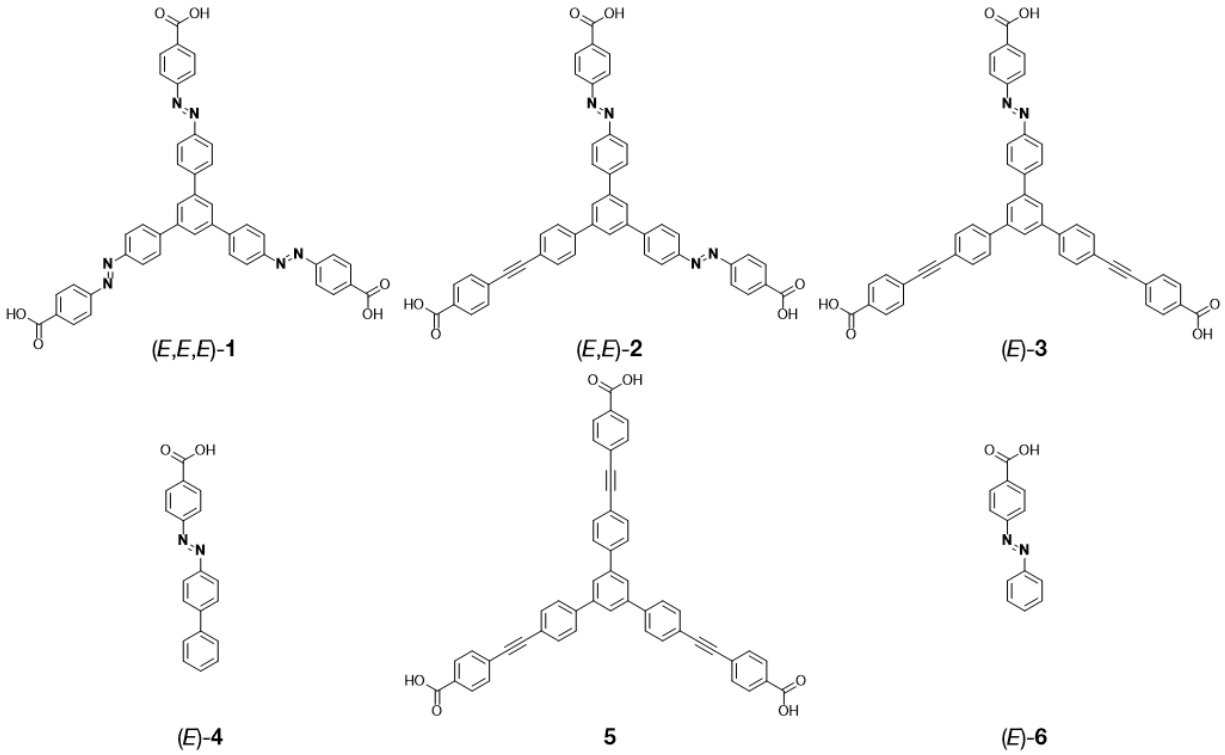

Figure 44. Chemical structures of the compounds described within the present chapter.

The photoswitches **1**, **2** and **3** studied here were designed in order to include the following structural features: (i) a significant conformational rigidity determined by the use of aromatic units, (ii) a central 1,3,5-trisubstituted benzene ring, which dictates the peculiar geometry of this class of molecules; (iii) up to three azobenzene (azo) moieties which can respond to light stimuli; (iv) the carboxylic acid-terminated azobenzene arms to enable the use of intermolecular H-bonding for controlling the self-assembly. The work described here is divided into two main parts.

On the one hand, the attention has been focussed on the characterisation of the photochromic behaviour of tris(azobenzene) **1**, in comparison with its bis(azo) and mono(azo) derivatives (**2** and **3**, respectively). As reference compounds we have also investigated the linear mono(azobenzene) molecule **4** and the commercially available 4-(phenylazo)benzoic acid **6**. For the sake of comparison, also the non-photoresponsive derivative **5** exposing three ethyn-1,2-diyl arms has been examined. To gain a comprehensive insight, detailed investigation on the

photophysical properties and photoisomerisation quantum yields performed by UV-Vis absorption spectroscopy have been combined to high performance liquid chromatography (HPLC) and ion-mobility mass spectrometry (IMMS) to bestow information onto the photogenerated isomer mixtures. Both HPLC and IMMS were used to separate the four possible (*E*,*E*,*E*), (*E*,*E*,*Z*), (*E*,*Z*,*Z*) and (*Z*,*Z*,*Z*) isomers of **1** upon UV light irradiation. HPLC was employed to determine the composition of the photostationary states (PSS) and to probe the $Z \rightarrow E$ thermal isomerisation kinetics: by studying the temporal evolution of the isomer mixture we could directly prove the independent kinetic behaviour of each azobenzene unit embedded within the same molecular scaffold. Moreover, IMMS provided unambiguous evidence for the large difference in shape of the aforementioned isomers,[161, 198] as a result of their structural rigidity. Our investigation suggested that it is possible to realise relatively small rigid molecules having efficient, fully independent photochromic units by simply connecting them in *meta*- position on a central trisubstituted benzene ring. Upon $E \rightarrow Z$ isomerisation the various isomers of compounds **1**-**3** show different shape, as evidenced by the change in the collisional cross section (CCS) of their ions, a quantity that is directly correlated to the volume occupied by a molecule in the gas phase. These evidences given by ion mobility mass spectrometry represent also the first investigation conducted on a multi-photochromic compound with such technique. Furthermore, we could also show that the separated *Z* isomer(s) of **1** could be thermally converted to the thermodynamically stable all-(*E*) within the mass spectrometer by collisional heating in the gas phase.

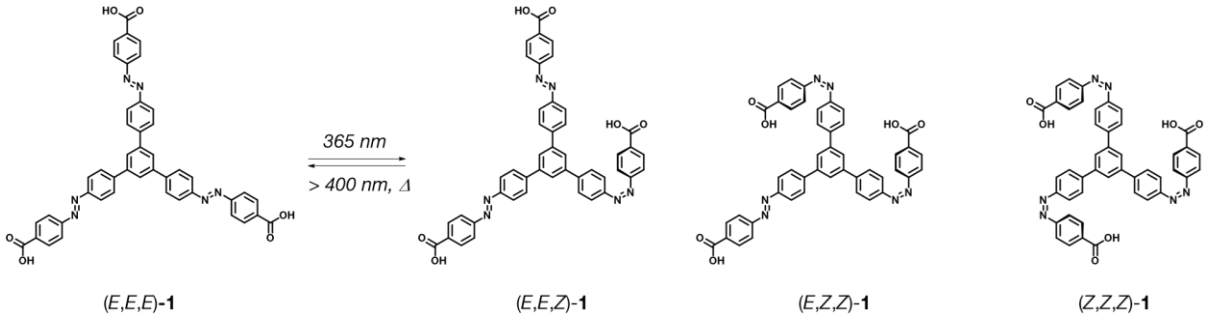

Figure 45. Schematic picture of the isomerisation of tris(azobenzene) **1**.

On the other hand, we have performed thorough investigation by means of STM on the molecular self-assembly of our tris(azobenzene) **1**. The photoswitch **1** evidenced the formation of dynamic 2D crystalline assemblies on highly ordered pyrolytic graphite (HOPG). The experiments offered an in-depth insight into the responsive nature of the supramolecular assemblies of molecule **1** when *in-situ* irradiated with ultraviolet and visible light. The subtle interpretation of sub-molecularly resolved patterns was achieved with the aid of Molecular Mechanics/ Dynamics (MM/MD) simulations. In order to demonstrate that the dynamic self-assembly upon light irradiation at different wavelengths is due to the isomerisation of the three azobenzene moieties, we have extended our study to an analogue molecule **5** in which the diazene-1,2-diyl groups have been substituted with ethyn-1,2-diyl units, thus suppressing the photochromic nature of the system.

2. METHODS

2.1. Photochemical characterisation

All the experiments in solution were performed using air-equilibrated spectroscopy grade DMSO and THF (Merck Millipore). UV-Vis absorption spectra were recorded at room temperature with a Jasco V650 spectrophotometer, in matched quartz Suprasil cuvettes (Hellma) with 1.0 cm optical path. Ultraviolet and visible light irradiation was performed with optical fibre-coupled LEDs (ThorLabs): for UV light λ_{max} = 367 nm, FWHM = 9 nm, for Vis light λ_{max} = 454 nm, FWHM = 20 nm. All irradiation experiments were performed upon thorough stirring of the solution in a closed spectrophotometric cell. The number of incident photons ($q_{p, in}$) were calculated by ferrioxalate actinometry.[153, 157] For λ_{irr} = 367 nm, $q_{p, in}$ = 2.0 x 10^{-7} Einstein min^{-1}; for λ_{irr} = 454 nm, $q_{p, in}$ = 2.7 x 10^{-8} Einstein min^{-1}. The $E \rightarrow Z$ isomerisation quantum yields (LED λ_{irr} = 367 nm) were determined upon monitoring the decrease in absorbance of the maximum π-π* absorption band of the (*E*)-azobenzene unit, starting from a non-irradiated solution of the compound in DMSO (**1**-**3** c = 2.0 x 10^{-5} M, **4** c = 6.0 x 10^{-5} M, **6** c = 7.8 x 10^{-5} M) with a slight base excess (NaOH in H_2O, **1**-**3** 6.0 eq., **4**, **6** 2.0 eq.) to ensure their complete solubilisation. Vice versa, the $Z \rightarrow E$ isomerisation quantum yields (LED λ_{irr} = 454 nm) were determined upon monitoring the increase of the π-π* absorption band of the (*E*)-azobenzene unit starting from the UV photostationary state. The quantum yields were determined at low conversion by extrapolation at t = 0, and taking into account the fraction of light transmitted at the irradiation wavelength. The estimated error on the quantum yields is ± 10 %. In order to further validate our procedure, the UV-induced quantum yield for azobenzene $E \rightarrow Z$ isomerisation in acetonitrile solution was measured in our experimental conditions, and resulted equal to values found in the literature ($\Phi \approx 0.14$).[39a]

The qualitative absorption spectra of the individual isomers of **1**-**3** were determined upon their separation via HPLC (Accela HPLC, reversed phase C_{18} Hypersil GOLD column, 50 × 2.1 mm, 1.9 µm, - Thermo Fisher Scientific), elution by solvent gradients of 5 – 95 % CH_3CN / 95 – 5 % H_2O with 0.1% (vol.) trifluoroacetic acid (pH ≈ 2), by injecting a pre-irradiated solution to the UV PSS (in DMSO). Separation of the isomers by chromatography was followed by checking their UV-Vis absorption spectra using the photodiode array detector, upon integration of the absorption spectra in the 200-650 nm wavelength range. The qualitative absorption spectra of the individual isomers of **1**-**3** were normalised at the wavelength of their UV isosbestic point determined by UV-Vis absorption spectroscopy of the mixture.

Quantification of the isomeric composition of the UV (LED λ_{irr} = 367 nm) and Vis (LED λ_{irr} = 454 nm) photostationary states was performed in collaboration with Q. Duez, Dr. J. De Winter and Prof. P. Gerbaux (Université de Mons). It was accomplished via HPLC separation (Waters Acquity UPLC, reversed phase column Phenomenex, C18, 5 μm, 150 x 4 mm), elution by solvent gradients of 5 – 95 % CH_3CN / 95 – 5 % H_2O with 0.1% (vol.) formic acid, and detection of the compounds with a mass spectrometer (Synapt G2-Si, Waters) equipped with an ESI source (negative mode). In order to accurately quantify the isomeric composition of the mixtures, the

chromatograms were integrated over all the ionic species generated for each compound, thus each isomer fraction was calculated as the sum of the area of its chromatographic peak measured for each ionic species detected for the compound divided by the sum of all the peaks area measured in the same way. The above procedure was used in order to rule out the possible different ionisation efficiencies of the various isomers.

2.2. Kinetical study of the *Z* → *E* thermal isomerisation

The thermal *Z* → *E* isomerisation for compounds **1**-**3** was followed via HPLC after bringing the mixture at the UV photostationary state (λ_{irr} = 365 ± 2 nm, high pressure Xe lamp, wavelength selected with a monochromator - FEI Polichrome V), by monitoring the isomer distribution over time upon continuous sampling of the solution (10 µL aliquots) kept at constant temperature (25, 30, 35, and 40 °C).The experiments have been performed thanks to a collaboration with R. Mannancherry and Prof. M. Mayor (University of Basel), whom are greatly acknowledged for data collection and treatment. A Shimadzu LC-20AD HPLC set-up equipped with a photodiode array UV/Vis detector (Shimadzu SPD-M20A VP, λ= 200-600 nm), a column oven Shimadzu CTO-20AC, and a reverse phase column BDS HYPERSIL C18, 5 µm, 250 x 3 mm; Thermo Scientific was used. Elution was performed with solvent gradients of 70 – 90 % CH_3CN (+ 0.1% v HCOOH) / 30 – 10 % H_2O (+ 0.1% v HCOOH). The chromatograms of **1**-**3** were integrated at the wavelength of their UV isosbestic point determined by UV-Vis absorption spectroscopy of the mixture.

The thermal *Z* → *E* isomerisation for compound **4** was followed by UV-Vis absorption spectroscopy after bringing the mixture at the UV photostationary state (LED, λ_{irr} = 367 nm), by monitoring the increase in absorbance of the maximum π-π* absorption band of the (*E*)-azobenzene unit over time keeping the solution at constant temperature (25, 30, 35, and 40 °C). The solution was maintained at constant temperature inside the spectrophotometer chamber using a custom-built Peltier set-up (Thorlabs).

2.3. Ion-mobility mass spectrometry (IMMS)

The experiments were performed in collaboration with Q. Duez and Dr. J. De Winter and Prof. P. Gerbaux (Université de Mons), whom are greatly acknowledged. The measurements were done on a hybrid quadrupole (Q)–traveling wave (T-wave) ion mobility (TWIMMS)–time-of-flight (TOF) mass spectrometer (Synapt G2-Si, Waters, U.K.) equipped with an ESI source (negative mode). The sample solutions were injected in the instrument by either direct infusion, or by using a HPLC set-up (mentioned previously) to separate the isomers of **1** prior to analysis. Typical ion-source conditions were capillary voltage 3.1 kV, sampling cone 40 V, source offset 80 V, source temperature 150 °C, and desolvation temperature 300 °C. This mass spectrometer was used for the recording of ESI full-scan mass spectra, and for the ion-mobility experiments. The trap and transfer cells were filled with argon, whereas the IMMS cell was filled with nitrogen.

A small RF-only cell filled with helium was fitted between the trap and the IMMS cell. Collisional energy may be applied to the trap (trap CE) and to the transfer (transfer CE) to fragment (or in the present case to "heat") ions before and after ion-mobility separation. The energy-resolved collisional activation experiments were performed on single isomers of **1** by previously selecting them with HPLC. Mass-selected ions were subjected to collisions with increased kinetic energies in the trap cell and subsequently separated and analysed by IMMS. We worked at low trap CE in order to avoid collision-induced fragmentation of the ions. Collisional cross-section data were obtained by following a calibration protocol with polyalanine as a calibrant.[165-166]

2.4. Scanning tunnelling microscopy

Investigation on the self-assembly of **1** and **5** was performed by STM at ambient pressure and room temperature, using freshly cleaved highly ordered pyrolytic graphite (HOPG) as substrate. The experiments were performed using a Veeco Multimode III (Bruker) equipped with a STM head and a 1 μm-range piezoelectric scanner (A-Piezo, Veeco), working in constant current mode. STM tips were mechanically cut from a Pt/Ir (80 : 20) wire (0.25 mm diameter, Goodfellow). Self-assembly was studied at the solid-liquid interface between HOPG and a supernatant solution (1-heptanoic acid, Sigma Aldrich), by applying 4 μL of the latter on the substrate, after having checked the integrity of substrate and tip by visualising the graphite lattice. The raw STM data was processed using a dedicated image processing software (SPIP, Image Metrology), by means of flattening and subtraction of a 2-degree polynomial background. The images were corrected from drift by calibration with the underlying graphite lattice. Unit cell parameters were obtained by Fourier analysis.

STM experiments at the solid-liquid interface were performed at an initial c = 10 μM concentration of **1** (all-(*E*)-) prior to irradiation) and **5** solutions in 1-heptanoic acid, freshly prepared by dilution of a mother solution in THF. The use of lower concentrations did not lead to the observation of ordered structures, meanwhile increasing the concentration in most cases yielded fuzzy contrast, probably due to the formation of an additional disordered ad-layer on the crystalline (*E*,*E*,*E*)-**1** monolayer. Also the use of different chain length fatty acids as solvent, such as 1-octanoic or 1-nonanoic acid did not lead to the observation of different crystalline structures of (*E*,*E*,*E*)-**1**, contrarily with what was displayed by smaller, C_3-symmetric tricarboxylic acids.[108c]

In order to verify whether the switching of **1** occurred when the molecules are adsorbed on the HOPG surface, we have also performed a qualitative study of the self-assembly of **1** at the solid-air interface (*e.g.* in absence of solution on the substrate). The samples showing continuous monolayers of (*E*,*E*,*E*)-**1** with domains having areas of ~ 200 – 400 nm^2 were prepared by spin-coating. A freshly cleaved HOPG substrate was covered with a 50 μL drop of a (non-irradiated) ~ 10^{-5} M solution of (*E*,*E*,*E*)-**1** and spun for 30 s at 2000 rpm. The procedure was repeated twice, with the precaution of avoiding environmental light during the sample preparation. Scanning was performed without addition of liquids on the sample.

Ultraviolet and visible light irradiation experiments were performed *in situ*, by irradiating the solution on the substrate after having verified the supramolecular packing of **1** and **5** prior to light irradiation. The experimental set-up to perform UV (LED, λ_{max} = 367 nm) and Vis (LED, λ_{max} = 454 nm) irradiation involved the use of an optical fibre, which terminus was placed at ~ 1.5 cm from the substrate.

2.5. TD-DFT modelling

TD-DFT calculations were performed by V. Diez-Cabanez and Prof. J. Cornil at the Université de Mons, whom are greatly acknowledged. DFT calculations have been performed on the various isomers of **1**-**3**, using the Gaussian 09 package. Geometry optimizations were carried out with the B3LYP functional and a 6-31G(d) basis set. Time-Dependent DFT (TD-DFT) calculations were performed to simulate the absorption spectra and assess the nature of the relevant electronic excited states, using the same functional and basis set, without consideration of the solvent effects.

2.6. Theoretical simulation by molecular mechanics/dynamics of the STM data

Molecular Mechanics/Dynamics (MM/MD) simulations were performed by V. Diez-Cabanez, Dr. A. Minoia and Prof. J. Cornil at the Université de Mons, whom are greatly acknowledged. The software employed was Materials Studio 7.0 package.[199] In order to have a good geometrical description of the four isomers of **1** adsorbed on graphite, geometries optimised by DFT were taken as benchmark. Following such methodology, the various isomers of **1** adsorbed on a finite graphene sheet were optimised at the ωB97XD/6-31G(d) level.[200] This functional was chosen based on its good description of the van der Waals interactions.[201] The resulting geometries were compared with those obtained by optimisation at the molecular MM level for the same system using the standard Dreiding force field.[202] In order to improve the agreement between the two sets of data, the force field description of the torsional profiles associated to the dihedral angles θ_1 and θ_2 (Figure 46) has been modified to match the dihedral scans obtained by DFT at the B3LYP/6-31G(d) level. Since the resulting geometries for the (*Z*)-azobenzene fragments after this modification show noticeable differences with the DFT structures, two harmonic restraints have been introduced: (i) one applied to the dihedral θ_1 centred at 15° with a magnitude equal to k_1 = 100 kcal/mol/rad^2 and (ii) another applied to the H-H distance marked as d_2 centred at 3.7 Å with a magnitude of k_2 = 25 kcal/mol/Å^2. Doing so, the resulting geometry is similar to that obtained at DFT level.

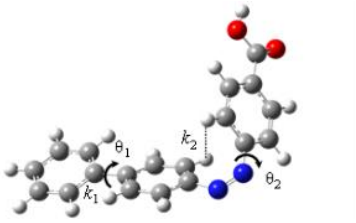

Figure 46. Optimised (*Z*)-azobenzene fragment of **1** at the ωB97XD/6-31G(d) level together with the representation of the modified dihedral angles θ_1 and θ_2 and introduced restraints k_1 and k_2.

An orthorhombic simulation box and Periodic Boundary Conditions (PBC) were used to depict the structural packing on the graphene substrate. The unit cell is formed by 144 molecules and the lateral dimensions were chosen in order to avoid interactions with their images by leaving a lateral vacuum of 30 Å. The graphene layer upon which the monolayers are modelled has been considered as an infinite rigid body to reduce the computational cost. The simulations have been conducted in vacuum and at T=100 K in the NVT ensemble (constant Number of particles, Volume, and Temperature). The Velocity Scale thermostat has been used to control the temperature. The atomic charges were calculated by the Gasteiger method.[203] This approach is validated by the fact that this method reproduces the same trends in the atomic charges compared to DFT calculations. Atom based summation method was used to describe the non-bonded interactions with a cut-off distance of 12.5 Å. The resulting unit cell was first optimised at the molecular MM level. The optimised unit cell was then used as the starting point for a quenched simulation (MM/MD). The quenched run (MM/MD) was carried for 25 ps and frames were saved every fs. The geometries were extracted each 500 steps, dealing in a total of 50 geometries per quench. The most stable geometry was taken as starting point for a new quench. This process has been repeated until the energy difference between the starting and the most stable geometry of the quench is low (< 5 kcal/mol).

The adsorption energy (E_{ads}) has been computed as the average adsorption energy of an individual **1** molecule on the graphite surface, following eq. 4.1:

$$E_{ads} = \frac{E_{tot} - E_{Gr} - E_{\mathbf{1}}}{n} \qquad (4.1)$$

with E_{tot} the total energy of the system, E_{Gr} the energy of the graphite layer, $E_{\mathbf{1}}$ the energy of the monolayer of **1** and n the number of **1** molecules that form the assembly. In our case we have taken n = 24. The binding energy (BE) has been considered as the average interaction energy between the molecules **1** in the assembly following eq. 4.2:

$$BE = \frac{E_{\mathbf{1}} - \sum_{i=1}^{n} E_i}{n} \qquad (4.2)$$

with E_i the individual energy of the individual molecules that form the monolayer. As in the last case we considered a representative assembly made of 24 molecules.

3. RESULTS AND DISCUSSION

3.1. Synthesis

With the exception of the commercial product **6**, compounds **1**-**5** have been synthesised in the group of Prof. M. Mayor in Karlsruhe Institute of Technology (KIT), by J. Santoro and Dr. M. Valášek, whom are greatly acknowledged. A schematic picture of their syntheses is given here for illustrative purposes. The detailed description of the synthesis of **1** and **5** is reported elsewhere. In practice, the strategy used for the synthesis of the two key moieties present in compounds **1**-**5**, being the photoresponsive diphenyldiazene- and the non-photochromic diphenylethynyl- moieties consists in using *Mills* reaction of aromatic amine with nitroso compound to generate the former, and a sequence of *Sonogashira* coupling and *Miyaura* borylation reactions for the latter. Both unsymmetrical derivatives **2-3** were stepwise assembled using Pd catalysed *Suzuki* cross-coupling protocol between a three-directional core (*e.g.* 1,3,5-tribromobenzene) and the corresponding arm moieties. A similar sequence of reactions was used for the preparation of the linear azobenzene derivative **4**, made via *Mills* reaction of a 4-nitrosobenzoate derivative with 4-aminobiphenyl, the latter made by *Suzuki* cross-coupling.

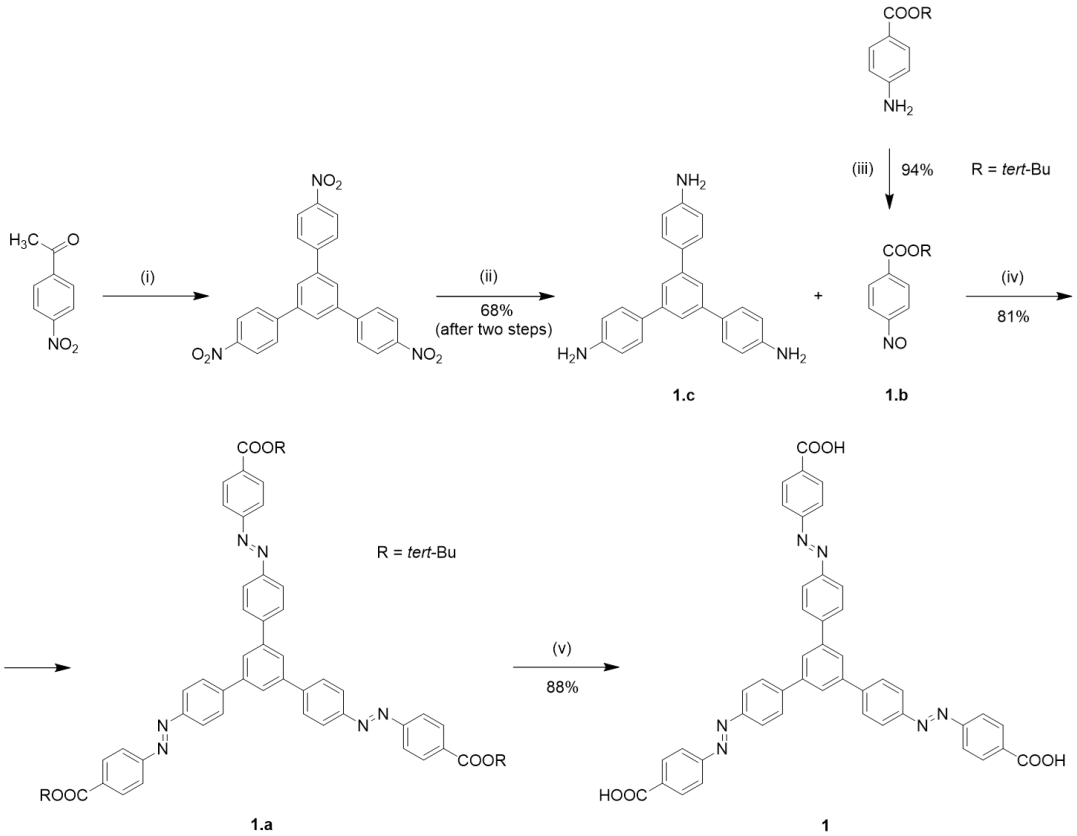

Scheme 1. Synthesis scheme of **1**. Reagents and conditions: (i) $SiCl_4$, EtOH; (ii) Pd/C, $N_2H_4{\cdot}H_2O$; (iii) Oxone®, CH_2Cl_2, H_2O; (iv), AcOH, RT; (v) TFA, CH_2Cl_2.

The synthetic strategy used for the preparation of star-shaped azobenzene (*E*,*E*,*E*)-**1** is outlined in Scheme 1. The required C_3- symmetric 1,3,5-tris(4'-aminophenyl)benzene **1.c** was prepared in two reaction steps according to the published procedure, starting from the condensation of 4-

nitroacetophenone to 1,3,5-tris(4'-nitrophenyl)benzene and its subsequent reduction.[204] Star-shaped azobenzene **1.a** was assembled via the Mills reaction from 1,3,5-tris(4'-aminophenyl)benzene **1.c** and corresponding tert-butyl-4-nitrosobenzoate **1.b**, prepared by oxidation of tert-butyl-4-aminobenzoate with Oxone®. Final hydrolysis of tert-butyl ester **1.a** was performed using trifluoroacetic acid (TFA) in dichloromethane.

Star-shaped azobenzene derivatives **2** and **3** were obtained via palladium catalysed Suzuki cross-coupling reaction of non–photoractive tolane arm (**5.a**) with the corresponding azobenzene moiety (**2.b** and **3.b**). The synthetic strategy used for the preparation of tolane building block **5.a** is displayed in Scheme 2. Commercially available 4-iodobenzoic acid was esterified to the corresponding *tert*-butyl ester **5.e** according to a published procedure.[205] Synthesis of the first building block started with 4-*tert*-butyl-iodobenzoate **5.e**, which was coupled with an excess of trimethylsilylacetylene to afford trimethylsilyl protected derivative **5.d** in quantitative yield. Subsequent cleavage of trimethylsilyl protecting group under basic conditions, using *tert*-BuOH as the solvent in order to avoid transesterification side reaction, provided **5.c** quantitatively. Synthesis of tolane derivative **5.b** was accomplished by Sonogashira coupling of derivative **5.c** with 1-bromo-4-iodobenzene at low temperature to chemoselectively replace only iodo group. Subsequent Miyaura borylation of **5.b** provided the desired pinacol boronic ester **5.a**.

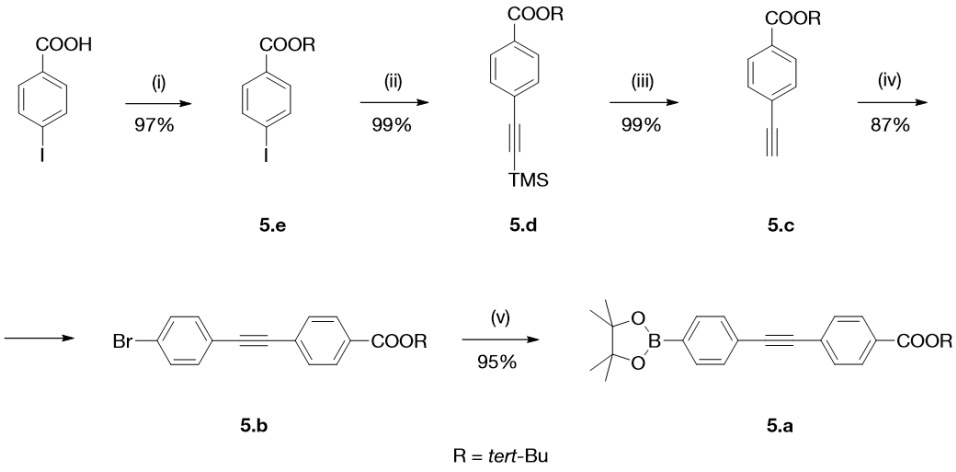

Scheme 2. Synthesis of **5.a**. Reagents and conditions: (i) $SOCl_2$, DMF, 70 °C; KOtBu, THF, RT. (ii) trimethylsilylacetylene, $Pd(PPh_3)_2Cl_2$, CuI, Et_3N, RT. (iii) Cs_2CO_3, tert-BuOH, 45 °C. (iv) 1-bromo-4-iodobenzene, $Pd(PPh_3)Cl_2$, CuI, Et_3N, 0 °C. (v) bis(pinacolato)diboron, AcOK, $Pd(dppf)Cl_2$, dioxane, 90 °C.

The synthetic pathway for the preparation of star-shaped di(azobenzene) derivative **2** is outlined in Scheme 3. 5'-Bromo-[1,1':3',1''-terphenyl]-4,4''-diamine core **2.c** was obtained via a Suzuki cross-coupling reaction between the commercially available 1,3,5-tribromobenzene and 4-aminophenylboronic acid pinacol ester. The photoresponsive building block **2.b** was prepared via the Mills reaction of amino derivative **2.c** with corresponding *tert*-butyl-4-nitrosobenzoate **1.b** (see above). With both building blocks **5.a** and **2.b** in hand, star-shaped *tert*-butyl ester **2.a** was assembled via a Suzuki cross-coupling reaction. Final acid-catalyzed hydrolysis of *tert*-butyl ester **2.a** provided the desired bis(azobenzene) **2**.

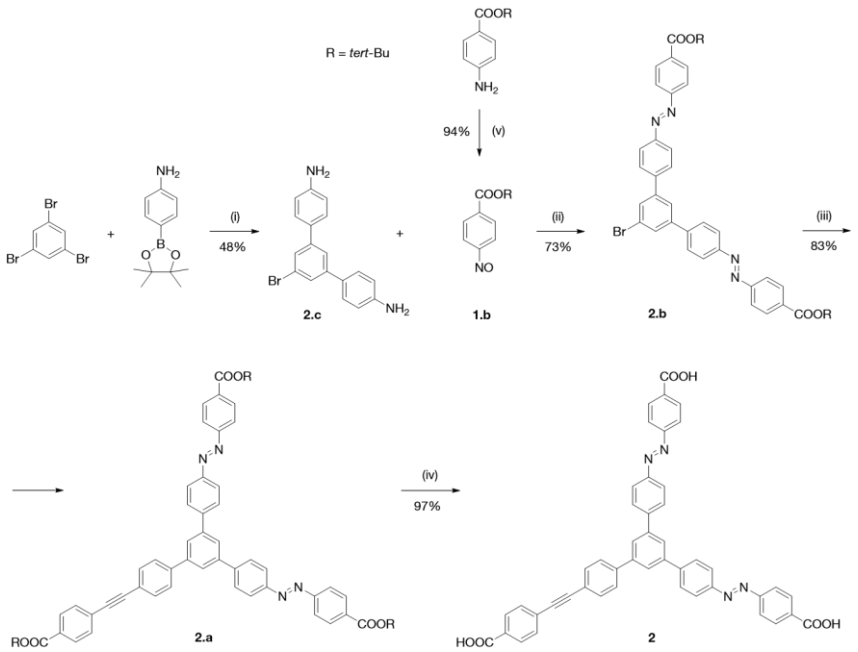

Scheme 3. Synthetic strategy towards star-shaped bis(azobenzene) **2**. Reagents and conditions: (i) $Pd(PPh_3)_4$, K_2CO_3, H_2O, toluene, 95 °C; (ii) AcOH, RT; (iii) compound **5.a**, $Pd(dppf)Cl_2$, K_2PO_4, H_2O, dioxane, 90 °C; (iv) CH_2Cl_2, TFA, RT; (v) CH_2Cl_2, Oxone®, H_2O, RT.

The synthetic strategy used for the preparation of **3** is shown in Scheme 4. 4-Amino-3',5'-dibromobiphenyl **3.c** was obtained via a Suzuki cross-coupling reaction of the commercially available 1,3,5-tribromobenzene with 4-aminophenylboronic acid pinacol ester. The photoresponsive moiety in the building block **3.b** was introduced via Mills reaction of intermediate **3.c** and corresponding *tert*-butyl-4-nitrosobenzoate **1.b**. With both building blocks **5.a** and **3.b** in hand, *tert*-butyl ester **3.a** was assembled via a Suzuki cross-coupling reaction. Final acid-catalyzed hydrolysis of *tert*-butyl ester **3.a** provided the desired star-shaped mono(azobenzene) **3**.

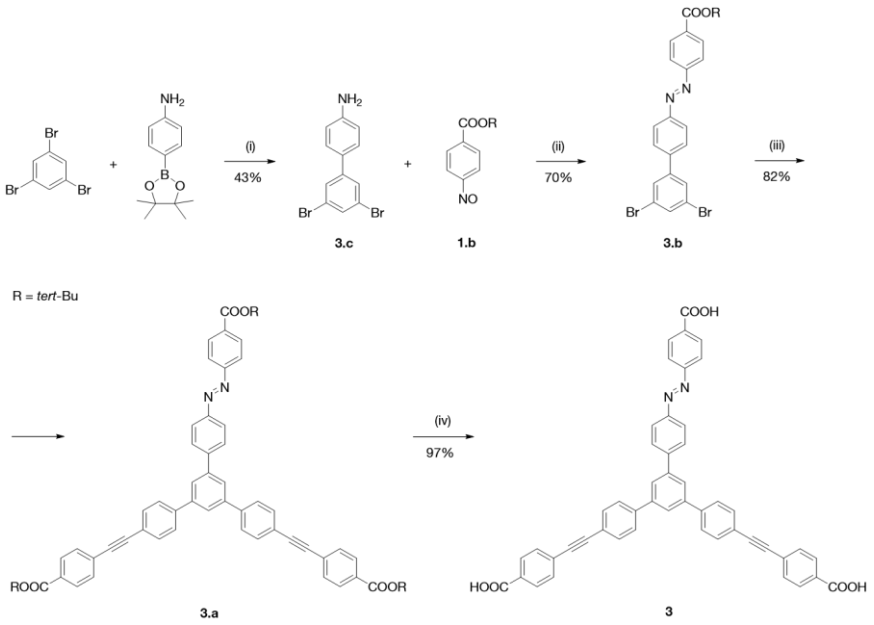

Scheme 4. Synthetic strategy towards star-shaped mono(azobenzene) **3**. Reagents and conditions: (i) $Pd(PPh_3)_4$, K_2CO_3, H_2O, toluene, 95 °C; (ii) AcOH, RT; (iii) compound **5.a**, $Pd(dppf)Cl_2$, K_2PO_4, H_2O, dioxane, 90 °C; (iv) CH_2Cl_2, TFA, RT.

The synthetic strategy used for the preparation of **4** is displayed in Scheme 5. The synthesis started with a Suzuki cross-coupling reaction of 4-bromoaniline and phenylboronic acid, which provided 4-aminobiphenyl **4.b**. The photoresponsive derivative **4.a** was assembled via Mills reaction of amine **4.b** with corresponding *tert*-butyl-4-nitrosobenzoate **1.b**. Final acid-catalysed hydrolysis of **4.a** provided the desired azobenzene **4** quantitatively.

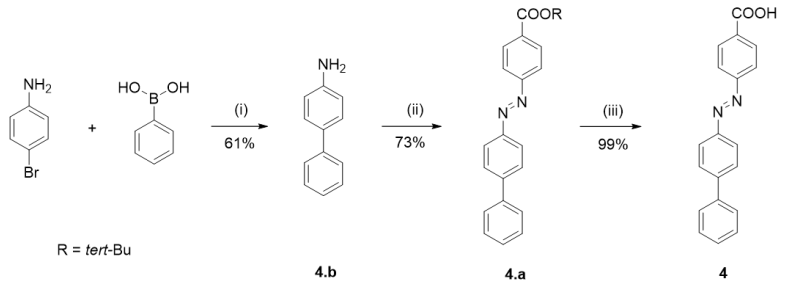

Scheme 5. Synthetic strategy towards azobenzene derivative **4**. Reagents and conditions: (i) $Pd(PPh_3)_4$, K_2CO_3, H_2O, dioxane, 90 °C; (ii) compound **1.b**, AcOH, RT; (iii) CH_2Cl_2, TFA, RT.

The synthesis of 1,3,5-tris{4'[(4''-carboxyphenyl)ethynyl]phenyl}benzene **5** is displayed in Scheme 6. This synthetic approach is based on the assembly of two building blocks **5.e** and **5.g** via a Sonogashira cross-coupling reaction. The synthesis of 1,3,5-tris[4′-(ethynyl)phenyl]benzene **5.g**, the first building block, started from the commercially available 1,3,5-tris(4-bromophenyl)benzene, which was coupled with an excess of trimethylsilylacetylene to afford trimethylsilyl protected acetylene derivative **5.h**. Subsequent cleavage of trimethylsilyl protecting group under basic conditions provided **5.g**. tert-Butyl-4-iodobenzoate **5.e** was synthesized according to a published procedure (see above).[205] With both building blocks **5.g** and **5.e** in hand, 1,3,5-tris{4′[4′′(tert-butoxycarbonyl)phenylethynyl]phenyl}benzene **5.f** was assembled via a Sonogashira-type coupling reaction.

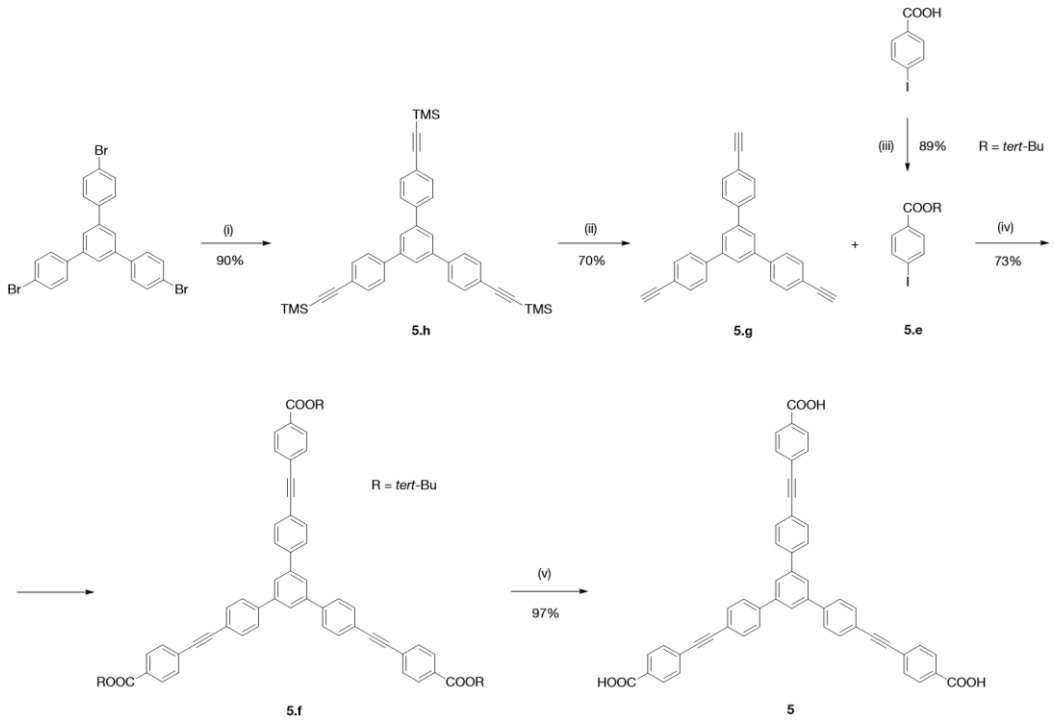

Scheme 6. Synthetic scheme of **5**. Reagents and conditions: (i) ethynyltrimethylsilane, $Pd(PPh_3)_2Cl_2$, CuI, Et_3N, 65°C; (ii) K_2CO_3, MeOH/THF, RT; (iii) 1. $SOCl_2$, 70°C, 2. KOtBu, THF, RT; (iv) $Pd(PPh_3)_2Cl_2$, CuI, Et_3N, RT; (v) TFA, CH_2Cl_2.

3.2. Photophysical and photochemical properties

In a first instance, the photophysical properties of compounds **1**-**6**, and their switching in solution have been investigated by absorption spectroscopy in DMSO with the addition of a base excess to ensure their complete solubilisation. The solvent environment and the presence of a base to deprotonate the carboxylate moieties have been chosen according to preliminary experiments made on **1**, enlightening its highest solubility in such conditions.

3.2.1. Absorption spectra of all-(*E*) isomers

The UV-Vis absorption spectra (Figure 47) of all-(*E*) tris(azobenzene) compound (**1**) and its star-shaped bis(azo) (**2**) and mono(azo) (**3**) derivatives exhibit the two characteristic transitions related to azobenzene chromophores (Azo), consisting in a higher energy band due to the π-π^* transition and a lower energy n-π^* transition. For **1**-**3** the absorption maxima are located at *ca.* 370 nm for the π-π^* and *ca*. 455 nm for the n-π^*. When compared to the linear, single Azo chromophore 4-[[4'-(4-phenyl)phenyl]diazenyl]benzoic acid **4**, a slight (*ca*. 10 nm) bathochromic shift is observed, together with an intensity increase (if compared to the absorption spectrum of **4** reported in ε multiplied by a factor 3, Figure 47) and a partial broadening evidences that partial conjugation occurs between the arms of **1**-**3** despite the *meta* substitution, as previously reported on similar star-shaped systems.[206] Compounds **2**-**3** display one additional absorption band for a transition located in the UV region (ca. 320 nm). This can be ascribed to the 4-(phenylethynyl)-1,1'-biphenyl chromophore unit (PE), as shown by comparison with the C_3-symmetrical non-photochromic derivative **5**. Despite the occurrence of partial conjugation between the chromophores in our star-shaped systems cannot be neglected, an additive behaviour of the absorption spectra of the single chromophores is evident. This appears clear by observing the ε values of the most intense transitions of Azo and PE units (Table 1), enlightening that the transitions are substantially localised on each chromophoric unit. Additionally, the maxima of Azo-centred transitions are constant between **1**, **2** and **3**. By comparison, the model single arm Azo chromophore **4** reveals that the λ_{max} related to the π-π^* transition is located at ca. 360 nm, largely red shifted if compared with the known position of the same band for azobenzene (ca. 315 nm[36a]) and 4-(phenylazo)benzoic acid **6** (ca. 335 nm). Such a red shift can therefore be attributed to the extension of the conjugated system including one additional phenyl unit in *para*-position with respect to the azobenzene moiety, rather than by inclusion of the Azo chromophore in the π-extended **1**, **2**, and **3** systems.

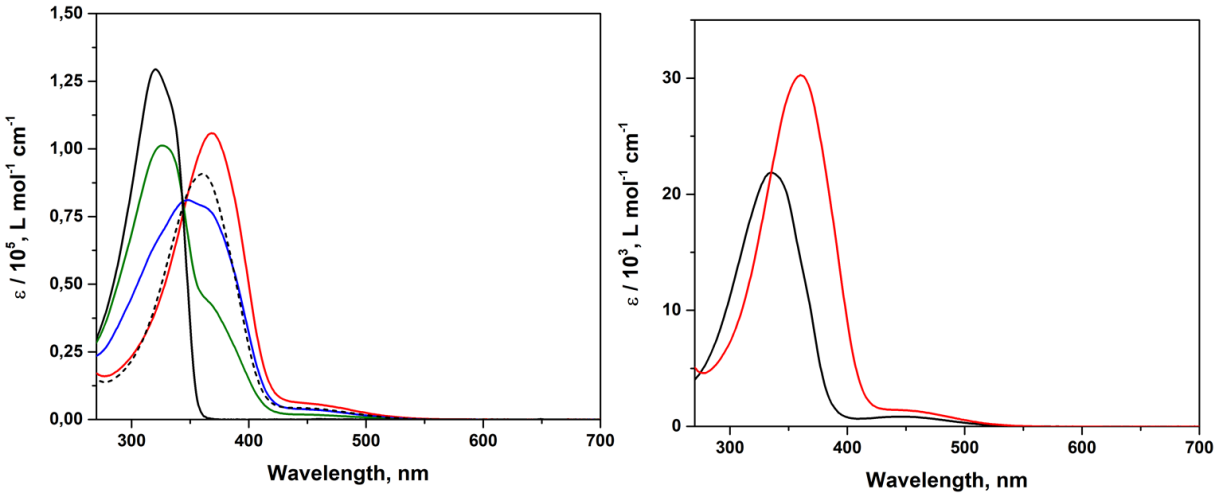

Figure 47. UV-Vis absorption spectra of all-(*E*)-**1**-**4**, (E)-**6** and **5** in DMSO with base excess, no irradiation. *Left*, comparative absorption spectra of **1**-**5**: (*E,E,E*)-**1** (+6.0 eq. NaOH) *full red line*, (*E,E*)-**2** (+6.0 eq. NaOH) *full blue line*, (*E*)-**3** (+6.0 eq. NaOH) *full green line*, **5** (+6.0 eq. NaOH) *full black line*, (*E*)-**4** (+2.0 eq. NaOH) multiplied by three *black dashed line*. *Right*, comparative absorption spectra of (*E*)-**4** and (*E*)-**6**: (*E*)-**4** (+2.0 eq. NaOH) *full red line*, (*E*)-**6** (+2.0 eq. NaOH) *full black line*.

3.2.2. Photoisomerisation of 1-4 and 6

The photoisomerisation of compounds **1**-**4** and **6** was studied upon irradiation with UV (λ_{max} = 367 nm) and Vis (λ_{max} = 451 nm). UV Irradiation of the aforementioned compounds in DMSO solution showed spectral variations typical for $E \rightarrow Z$ isomerisation of azobenzene derivatives (Figure 48-49), with a progressive decrease of the absorbance in the (*E*)-Azo π-π^* region, accompanied by an increase of the absorbance in the higher energy UV region, together with the same variation in the visible range. Both the evidences are related to a decrease in concentration of the (*E*)-isomer(s) accompanied by an obvious increase of the (*Z*) ones upon reaching a photostationary state (UV – PSS). The initial spectral features were seen to recover partially upon subsequent Vis irradiation reaching another PSS (Vis – PSS), while complete recovery was encountered only by storing the solution in the dark over several days. It is crucial to note for all compounds, especially for tris(azobenzene) **1** and bis(azobenzene) **2**, the presence of clear isosbestic points throughout both $E \rightarrow Z$ and $Z \rightarrow E$ photoconversions, which provide unambiguous evidence for the absence of inter-chromophore interactions.

Preliminary experiments showed the impossibility of characterising the photochemical reaction by means of ^{1}H-NMR, since no distinctive peaks related to the photoproducts appeared, in comparison to non-irradiated solutions. Conversely, the composition of UV – and Vis – PSS was characterised by HPLC: thanks to the known difference in molecular dipole moment between the *E* and *Z* isomers of azobenzenes, all the possible isomeric forms of **1**-**3** could be separated. Thus, the experiments could prove the formation of all the expected isomers for the multi-azobenzene compounds (qualitative absorption spectra in Figure 48-49 *insets*). Qualitative absorption spectra were obtained with the photodiode array spectrophotometer integrated in our HPLC setup (arbitrary units), and were normalised at the wavelength of the isosbestic point measured by UV-Vis (Figure 48, *inset* 315 nm for **1**, Figure 49, *insets* 321 nm for **2** and 322 nm for **3**).

Table 1. Photochemical characterisation of compounds **1-6** in air-equilibrated DMSO (+ exc. NaOH) at 298 K.

	λ_{max} all-(*E*) isomer [nm] (ε / 10^3 [L mol^{-1} cm^{-1}])			$\Phi_{E\rightarrow Z}$ (x 10^2)[a]		$\Phi_{Z\rightarrow E}$ (x 10^2)[b]		UV – PSS composition [%][c]	Vis – PSS composition [%][c]
	π-π* PE	π-π* Azo	n-π* Azo	Overall[d]	Single Azo[e]	Overall[d]	Single Azo[e]		
1	-	370 (110)	455 (5.7)	3.3	8.8	28	77	55 (*Z*,*Z*,*Z*) 27 (*E*,*Z*,*Z*) 13 (*E*,*E*,*Z*) 5 (*E*,*E*,*E*)	9 (*Z*,*Z*,*Z*) 17 (*E*,*Z*,*Z*) 30 (*E*,*E*,*Z*) 44 (*E*,*E*,*E*)
2	320 (65)	370 (77)	455 (3.7)	4.5	9.5	47	98	61 (*Z*,*Z*) 29 (*E*,*Z*) 10 (*E*,*E*)	13 (*Z*,*Z*) 32 (*E*,*Z*) 55 (*E*,*E*)
3	320 (100)	370 (42)	455 (1.8)	9.1		100		73 (*Z*) 27 (*E*)	32 (*Z*) 68 (*E*)
5	320 (130)	-	-	-		-			
4	-	360 (30)	455 (1.4)	9.6		88		~ 99 (*Z*) 1 (*E*)	
6	-	335 (21)	450 (0.8)	11		70			

[a]UV π-π* irradiation, λ_{irr} = 367 nm (FWHM = 9 nm). [b]Vis n-π* irradiation, λ_{irr} = 454 nm (FWHM = 20 nm). [c]Determined by HPLC-MS. [d]Overall isomerisation quantum yield, calculated using the ε of the compounds. [e]Isomerisation quantum yield of the single chromophore unit, calculated using the ε of mono(azobenzene) compound 4.

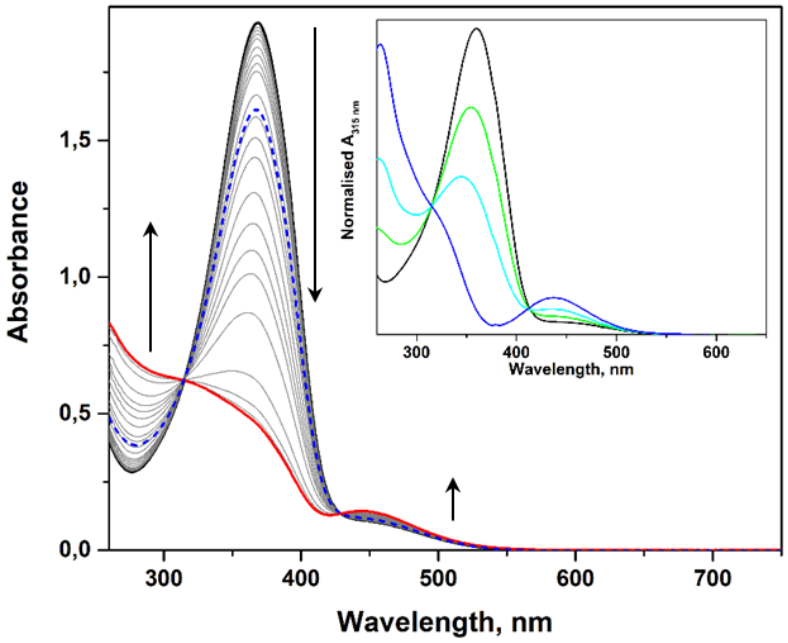

Figure 48. UV-Vis spectral variation of the star-shaped compound **1** upon UV irradiation in DMSO with base excess: *black line*, no irradiation, *red line* UV PSS, *blue dotted line* Vis PSS. c = 2.0 x 10^{-5} M (+ 6.0 eq. NaOH) *inset*, absorption spectra of the single isomers recorded upon HPLC separation *black line* (*E*,*E*,*E*)-**1** isomer, *green line* (*E*,*E*,*Z*)-**1** isomer, *light blue line* (*E*,*Z*,*Z*)-**1** isomer, *dark blue line* (*Z*,*Z*,*Z*)-**1** isomer,

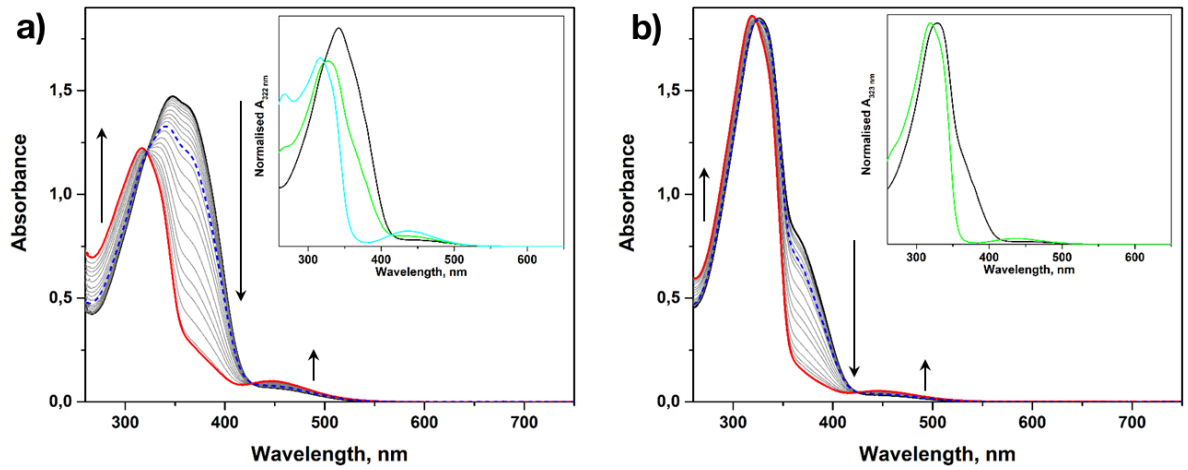

Figure 49. UV-Vis spectral variation of the star-shaped compounds **2**-**3** upon UV irradiation in DMSO with base excess: *black line*, no irradiation, *red line* UV PSS, *blue dotted line* Vis PSS. a) Compound **2**, c = 2.0 x 10^{-5} M (+ 6.0 eq. NaOH) *inset*, *black line* (*E*,*E*)-**2** isomer, *green line* (*E*,*Z*)-**2** isomer, *light blue line* (*Z*,*Z*)-**2** isomer, b) **3**, c = 2.0 x 10^{-5} M (+ 6.0 eq. NaOH) *inset*, *black line* (*E*)-**3** isomer, *green line* (*Z*)-**3** isomer.

The absorption spectra of single isomers obtained by HPLC are also nicely comparable with the simulated spectra by TD-DFT (Figure 53, courtesy of V. Diez-Cabanes, Université de Mons). Quantification of the composition of the photostationary state(s) was performed in collaboration with Q. Duez, Dr. J. De Winter and Prof. P. Gerbaux (Université de Mons) using a HPLC-MS set-up (Table 1, Figure 51-52). The mass spectrometer used employed an electrospray ionisation (ESI) source, and the instrument was set in negative mode (detecting anions), in order to measure the signal due by the anions produced by deprotonation of the carboxylate moieties present in **1**-**4**. The chromatograms were integrated on all the anionic species generated by compounds **1**-**4**, in order to rule out any effect related to differences in ionisation efficiency, thus to avoid systematic errors in the quantification of the isomeric composition of PSSs. It is worth noting that for both the tris(azobenzene) **1**, and the bis(azobenzene) **2** derivatives it is possible to reach a (*Z*)-rich UV – PSS (95% and 90% overall *Z* content for **1** and **2**, respectively), while for **3** the UV PSS contains ca. 70 % of the (*Z*)-isomer (Table 1). For the linear model compound **4** conversely, by irradiation at the wavelength used the isomerisation is quantitative (*Z*-content ca. 99 %).

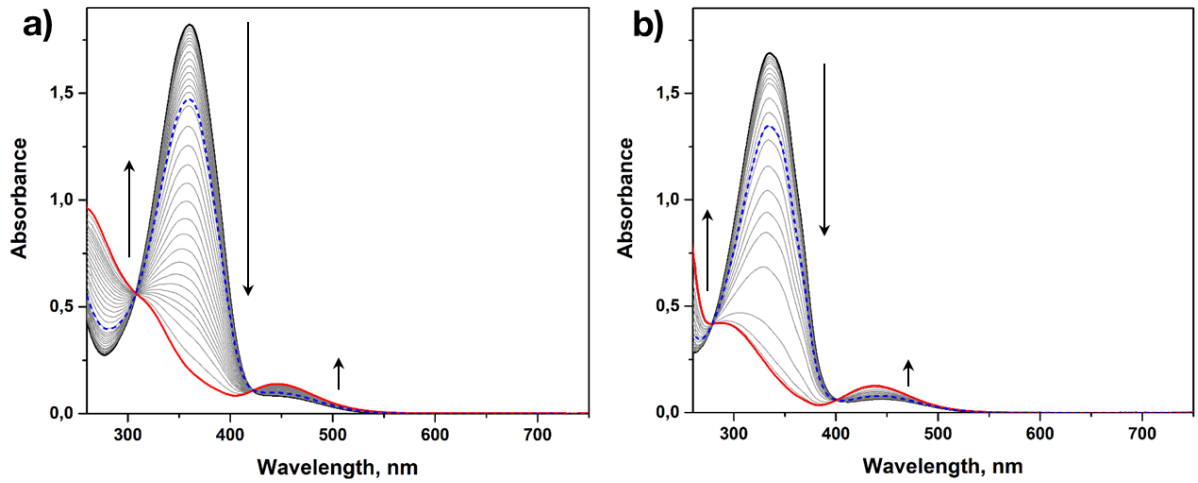

Figure 50. UV-Vis spectral variation of the linear azobenzene carboxylic acids **4** and **6** upon UV irradiation in DMSO with base excess: *black line*, no irradiation, *red line* UV PSS, *blue dotted line* Vis PSS. a) Compound **4**, c = 6.0 x 10-5 M (+ 2.0 eq. NaOH). b) 4-phenylazo benzoic acid **6**, c = 7.8 x 10-5 M (+ 2.0 eq. NaOH)

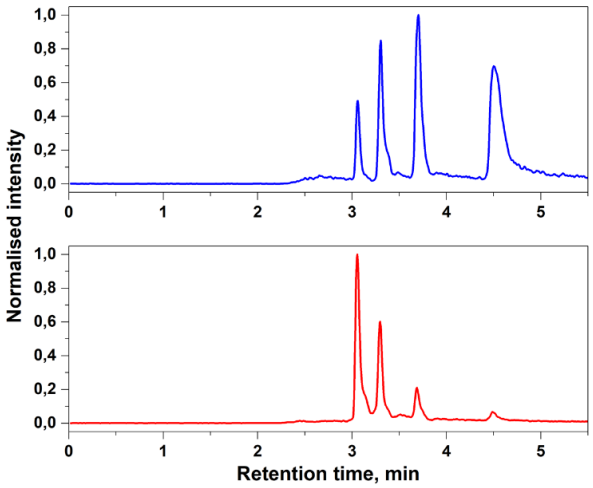

Figure 51. Isomeric composition of UV PSS (*red line*) and Vis PSS (*blue line*) for compound **1** determined by HPLC-MS. Chromatograms integrated at $[M\text{-}H^+]^-$ m/z = 749.2. Peak at 3 min 5 s retention time corresponds to (*Z*,*Z*,*Z*)-**1**, 3 min 20 s (*Z*,*Z*,*E*)-**1**, 3 min 40 s (*Z*,*E*,*E*)-**1**, 4 min 30 s (*E*,*E*,*E*)-**1**.

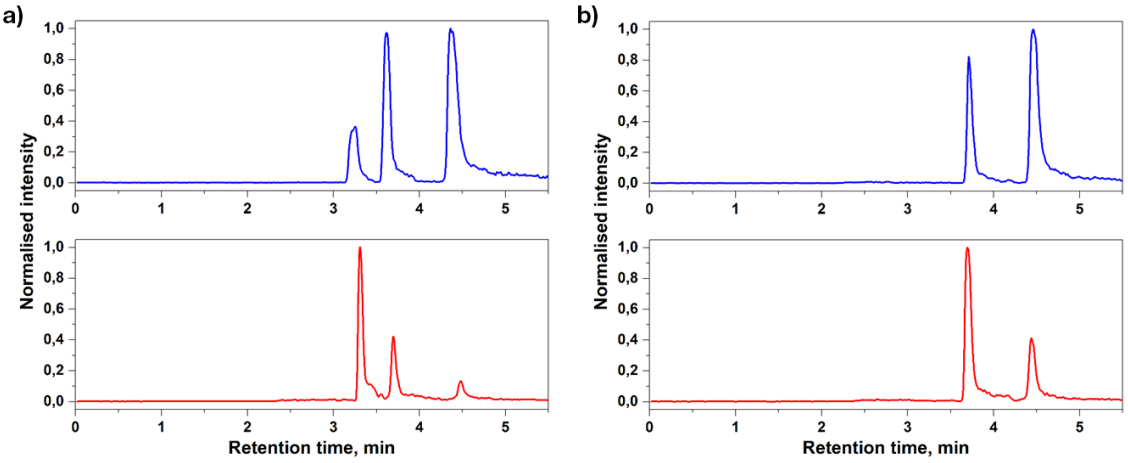

Figure 52. Isomeric composition of UV PSS (*red line*) and Vis PSS (*blue line*) determined by HPLC-MS. a) Compound **2** chromatograms integrated at $[M\text{-}H^+]^-$ m/z = 745.2. Peak at 3 min 20 s retention time corresponds to (*Z*,*Z*)-**2**, 3 min 40 s (*Z*,*E*)-**2**, 4 min 30 s (*E*,*E*)-**2**. b) Compound **3** chromatograms integrated at $[M\text{-}H^+]^-$ m/z = 741.2. Peak at 3 min 40 s retention time corresponds to (*Z*)-**3**, 4 min 30 s (*E*)-**3**.

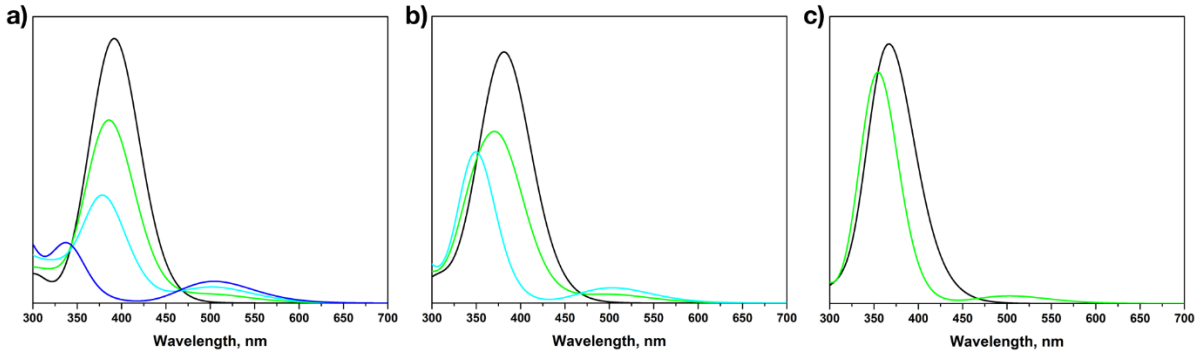

Figure 53. Calculated UV-Vis absorption spectra of **1**-**3** by TD-DFT. a) Compound **1**, *black line*, (*E*,*E*,*E*)-**1**, *green line*, (*E*,*E*,*Z*)-**1**, *light blue line*, (*E*,*Z*,*Z*)-**1**, *blue line*, (*Z*,*Z*,*Z*)-**1**. b) Compound **2**, *black line*, (*E*,*E*)-**2**, *green line*, (*E*,*Z*)-**2**, *light blue line*, (*Z*,*Z*)-**2**. a) Compound **3**, *black line*, (*E*)-**3**, *green line*, (*Z*)-**3.**

The efficiency of $E \rightarrow Z$ and $Z \rightarrow E$ photoreactions was estimated by evaluating their quantum yields (Φ). Isomerisation quantum yields were determined by monitoring the variation in concentration of the reactant (all-*E*- isomer) over the irradiation time by UV-Vis absorption spectroscopy, with the so-called *initial slope method*, and is performed upon following the reaction at low conversions (< 10 %). The values given in Table 1 and indicated as *overall* Φ were calculated by using the ε of each compound, therefore they refer to the quantum yield of isomerisation of all azobenzene units within each molecular scaffold, while the *single Azo* Φ values were calculated using the ε of the mono(azobenzene) "arm" **4**, and provide a comparative estimation over the isomerisation quantum yield of the single photochrome.[207] Generally, it may be seen erroneous to utilise the ε of a different compound to calculate photoreaction quantum yields with this procedure: nevertheless, here the experiments were performed to extract a comparative parameter to evaluate the compounds characterised *within this work*. Such a procedure was seen particularly suitable with **1**-**3**, following the additivity of the ε values of each chromophore (Table 1). Similar results could however be obtained by dividing the ε of the Azo chromophore by the number of azobenzenes contained within each molecule (*e.g.* dividing by three and by two the ε of **1** and **2** respectively). It is particularly interesting to benchmark the *single Azo* Φ of star-shaped compounds **1**-**3** with standard azobenzene derivatives, since it is generally known that conjugation between the chromophores drastically lowers the photoreaction efficiency.[39a] We will take azobenzene as benchmark, showing for $E \rightarrow Z$ isomerisation $\Phi \approx 0.14 - 0.15$ in polar solvents ($\lambda_{irr} \approx 345$ nm):[39a, 153] compared to it, 4-(phenylazo)benzoic acid **6** shows a slightly lower value ($\Phi \approx 0.11$), presumably due to the presence of the electron-withdrawing carboxyl moiety in *para*-position with respect to the chromophore, as reported in the literature.[207] Extension of the π-conjugated backbone in **4** is accompanied by an almost negligible reduction ($\Phi \approx 0.10$) of efficiency for the process, while interestingly for the star-shaped mono(azobenzene) derivative **3** $\Phi \approx 0.09$ and for both multi-azobenzene scaffolds **2** and **1** the *single Azo* Φ exhibit the same value. Conversely, for $Z \rightarrow E$ photoreaction induced by Vis irradiation, the quantum yields result even higher than azobenzene ($\Phi \approx 0.63$, $\lambda_{irr} \approx 436$ nm) itself.[208] However, the values obtained from these experiments are expected to display a higher uncertainty, since the concentration of the (*E*)-isomer(s) in the initial conditions (UV – PSS) was not zero.[209] The results showed here evidence that upon embedding azobenzene photochromes into such large, and at least partially π-conjugated rigid backbones as **1**-**3**, does not result in a sensible disruption of the photoreactivity of the system. The latter is a further evidence of the successful electronic disconnection provided by the *meta*- substitution pattern on the central benzene ring of our structures.

Ultimately, in order to clearly demonstrate the photochemical robustness of compound **1**, we have performed a test over 10 photoswitching cycles, which showed negligible degradation of its photochromic activity (Figure 54). Additionally, a blank experiment was performed in order to confirm the absence of photoreactivity of **5** by UV-Vis absorption spectroscopy (Figure 55).

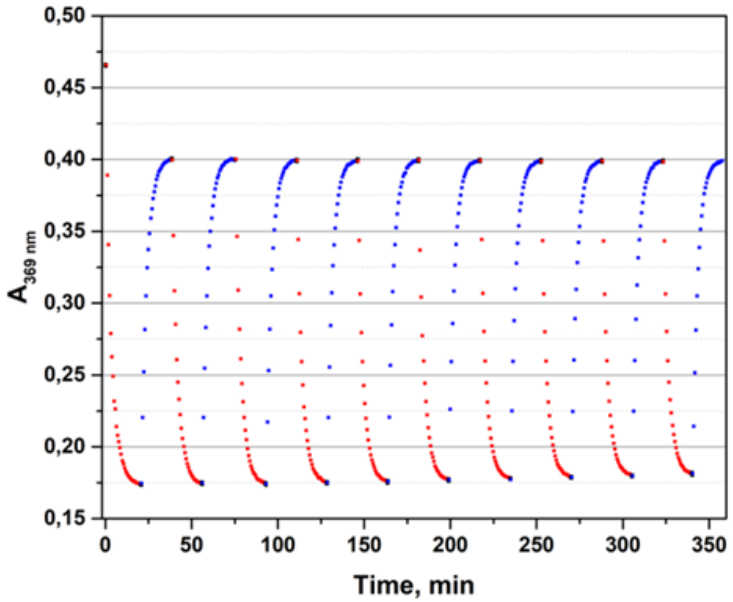

Figure 54. UV-Vis spectral variation of **1** upon multiple irradiation cycles. Plot of the absorbance variation over time, observed at λ_{max} for π-π* absorption band of **1** (in DMSO, c = 5.0×10^{-6} M) upon irradiation with: *red squares* UV light ($P_d \approx 1.5$ mW cm^{-2}), *blue squares* Vis light ($P_d \approx 1.5$ mW cm^{-2}).

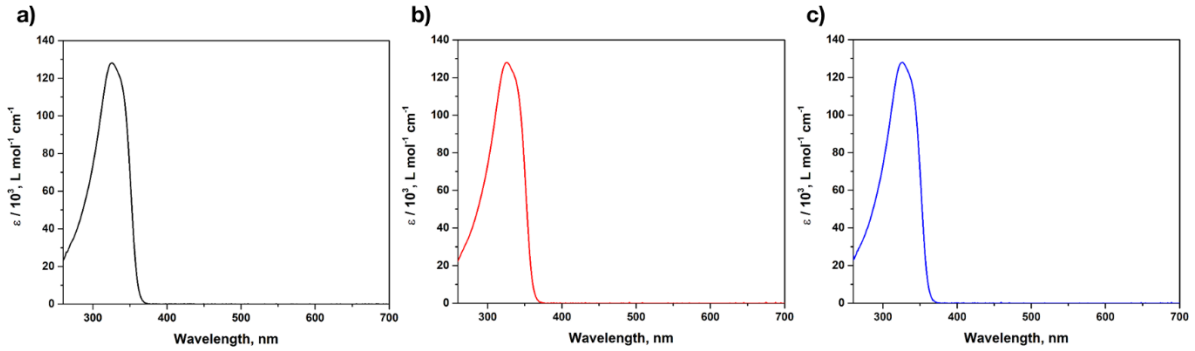

Figure 55. UV-Vis spectra of **5** in DMSO (c = 1.0×10^{-5} M). a) no light irradiation. b) after 22 minutes UV irradiation ($P_d \approx 1.5$ mW cm^{-2}). c) after subsequent 19 minutes Vis irradiation ($P_d \approx 1.5$ mW cm^{-2}).

3.3. Kinetics of Z → E thermal isomerisation[2]

The *Z* → *E* thermal reaction for **1**-**3** was followed by HPLC in order to monitor the population of each isomer starting from the UV – PSS over time. This experimental procedure enabled us to further demonstrate that the single azobenzene units of compounds **1**-**2** are electronically decoupled from one another. In order to make a useful comparison, the thermal back-isomerisation of **4** was studied by UV-Vis absorption spectroscopy. Multi-azobenzene compounds are known to undergo isomerisation from the all-(*Z*) to the all-(*E*) forms via the

[2] Experiments performed by R. Mannancherry, Prof. M. Mayor (University of Basel).

mixed (*Z*,*E*) isomers, and the reaction mechanism could be treated as a consecutive and irreversible cascade reaction where isomerisation of the single azobenzene units is a first order process.[39b, 210]

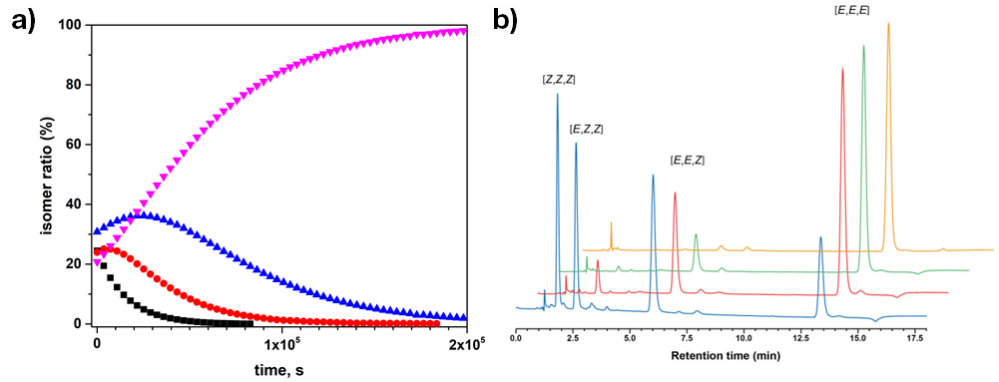

Figure 56. a) Time profiles at T = 40 °C for the thermal *Z* → *E* isomerisation of **1** starting from the photostationary state obtained upon irradiation at 365 nm in DMSO/CH_3CN, monitored by HPLC by integrating the UV absorption at 290 nm. (*Z*,*Z*,*Z*)-**1** (*black squares*), (*Z*,*Z*,*E*)-**1** (*red dots*), (*Z*,*E*,*E*)-**1** (*blue triangle*), (*E*,*E*,*E*)-**1** (*pink triangles*). b) Chromatograms of **1** recorded upon heating at T = 40 °C at various time intervals: *blue line* recorded at PSS 365 nm, *red line* after 17 h, *green line* after 29 h, *orange line* after 55 h.

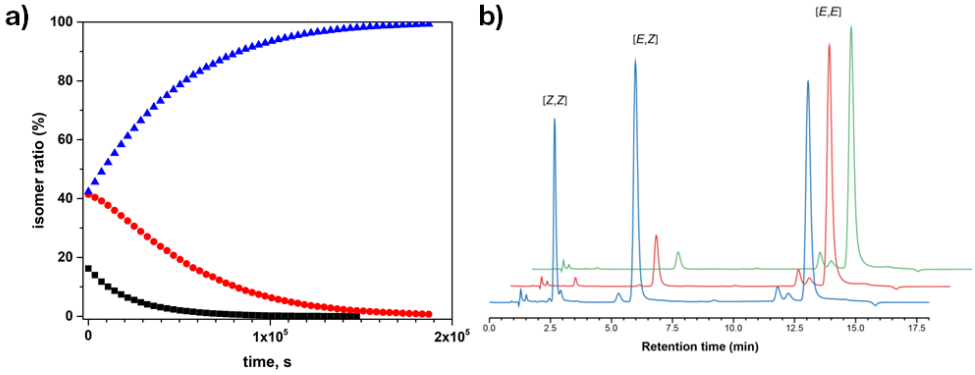

Figure 57. a) Time profiles at T = 40 °C for the thermal *Z* → *E* isomerisation of **2** starting from the photostationary state obtained upon irradiation at 365 nm in DMSO/CH_3CN, monitored by HPLC by integrating the UV absorption at 280 nm. (*Z*,*Z*)-**2** (*black squares*), (*Z*,*E*)-**2** (*red dots*), (*E*,*E*)-**2** (*blue triangles*). b) Chromatograms recorded upon heating **2** at T = 40 °C at various time intervals: *blue line* recorded at PSS 365 nm, *red line* after 17 h, *green line* after 29 h.

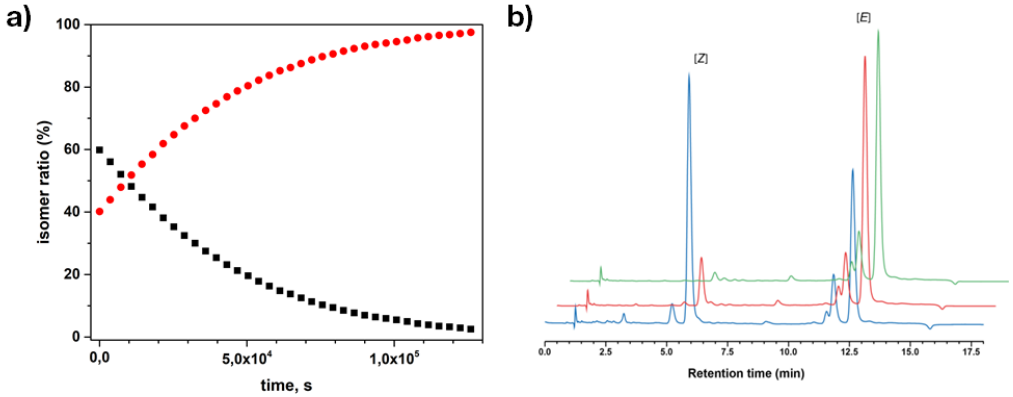

Figure 58. a) Time profiles at T = 40 °C for the thermal *Z* → *E* isomerisation of **3** starting from the photostationary state obtained upon irradiation at 365 nm in DMSO/CH_3CN, monitored by HPLC, by integrating the UV absorption at 285 nm. (*Z*)-**3** (*black squares*), (*E*)-**3** (*red dots*). Chromatograms recorded upon heating **3** at T = 40 °C at various time intervals: *blue line* recorded at PSS 365 nm, *red line* after 17 h, *green line* after 36 h.

Upon plotting the isomer fraction over time, we could fit the evolution curves with the kinetic equations presented here (eqs. 4.4, 4.5, 4.6), thus obtaining the reaction rates for each azobenzene unit (Table 2). Generally, the isomerisation $[A] \rightarrow [B]$ of an azobenzene unit can be described as a first order reaction (eq. 4.4), while the second and third $[B] \rightarrow [C]$ and $[C] \rightarrow [D]$ by assuming a pseudo-first order cascade process (equation 4.5 and 4.6):

For tris(azobenzene) compound **1**:

$[A]$ = (*Z*,*Z*,*Z*)-**1**; $[B]$ = (*Z*,*Z*,*E*)-**1**; $[C]$ = (*Z*,*E*,*E*)-**1**; $[D]$ = (*E*,*E*,*E*)-**1**

For bis(azo) compound **2**:

$[A]$ = (*Z*,*Z*)-**2**; $[B]$ = (*Z*,*E*)-**2**; $[C]$ = (*E*,*E*)-**2**; $[D] = 0$

For mono(azobenzene) compounds **3** and **4**:

$[A]$ = (*Z*); $[B]$ = (*E*); $[C] = 0$; $[D] = 0$.

$$[A] \overset{k_1}{\rightarrow} [B] \overset{k_2}{\rightarrow} [C] \overset{k_3}{\rightarrow} [D] \tag{4.3}$$

$$[A] = [A]_0 \, e^{-k_1 t} \tag{4.4}$$

$$[B] = \frac{[A]_0 \, k_1}{k_2 - k_1} \left[e^{-k_1 t} - e^{-k_2 t}\right] + [B]_0 \, e^{-k_2 t} \tag{4.5}$$

$$[C] = [A]_0 \, k_1 \, k_2 \left[\frac{e^{-k_1 t}}{(k_2-k_1)(k_3-k_1)} - \frac{e^{-k_2 t}}{(k_2-k_1)(k_3-k_2)} + \frac{e^{-k_3 t}}{(k_3-k_1)(k_3-k_2)}\right] + \frac{[B]_0 \, k_2}{k_3 - k_2} \left[e^{-k_2 t} - e^{-k_3 t}\right] + [C]_0 \, e^{-k_3 t} \tag{4.6}$$

where k_1, k_2 and k_3 are the isomerisation rates, $[A]_0$, $[B]_0$, $[C]_0$ and $[D]_0$ the initial concentrations, and t the time. The experimental data together with their fitting can be found in Appendix I.

The $k_{n\,=\,1,2,3}$ values can be used to determine the free Gibbs energy of isomerisation $\Delta G^{\neq}_{n(T)}$ by rearranging the Eyring equation:

$$\Delta G^{\neq}_{n(T)} = -RTln\left(\frac{hk_n}{k_B T}\right) \tag{4.7}$$

where k_n is the obtained kinetic rate constants, k_B the Boltzmann constant (k_B = 1.380662 x 10^{-23} J K^{-1}), h the Planck's constant (h = 6.626176 x 10^{-34} J s), R the universal gas constant (R = 8.31446 J K^{-1} mol^{-1}) and T the measured temperature. Finally, plotting $\ln(k_{n\,=\,1,2,3})$ vs. $1/T$ (Arrhenius plot) and $\ln(k_{n\,=\,1,2,3})/T$ vs. $1/T$ (Eyring plot) gives the activation energy parameters, by linearisation of Arrhenius (4.8) and Eyring (4.9) equations, respectively.

$$k_n = Ae^{-\frac{Ean}{RT}} \tag{4.8}$$

$$k_n = \frac{k_B T}{h} e^{\frac{-\Delta H^{\neq}_n + T\Delta S^{\neq}_n}{RT}} \tag{4.9}$$

Table 2. Rate constants for the thermal *Z* → *E* isomerisation of compounds **1**-**4**.[a].

	298 K			303 K			308 K			313 K		
	$\|k_1\|$, s^{-1}	$\|k_2\|$, s^{-1}	k_3, s^{-1}	$\|k_1\|$, s^{-1}	$\|k_2\|$, s^{-1}	k_3, s^{-1}	$\|k_1\|$, s^{-1}	$\|k_2\|$, s^{-1}	k_3, s^{-1}	$\|k_1\|$, s^{-1}	$\|k_2\|$, s^{-1}	k_3, s^{-1}
1	3.8 x 10^{-6}	3.7 x 10^{-6}	3.9 x 10^{-6}	5.9 x 10^{-6}	6.3 x 10^{-6}	7.5 x 10^{-6}	1.1 x 10^{-5}	1.2 x 10^{-5}	1.3 x 10^{-5}	2.1 x 10^{-5}	2.2 x 10^{-5}	2.3 x 10^{-5}
2	-	3.5 x 10^{-6}	4.2 x 10^{-6}	-	7.4 x 10^{-6}	7.2 x 10^{-6}	-	1.3 x 10^{-5}	1.3 x 10^{-5}	-	2.1 X 10^{-5}	2.4 x 10^{-5}
3	-	-	5.4 x 10^{-6}	-	-	7.0 x 10^{-6}	-	-	1.3 x 10^{-5}	-	-	2.2 x 10^{-5}
4[b]	-	-	1.1 x 10^{-5}	-	-	1.8 x 10^{-5}	-	-	3.6 x 10^{-5}	-	-	6.0 x 10^{-5}

[a]Parameters with appendix x_1 refer to (*Z*,*Z*,*Z*)-**1** → (*Z*,*Z*,*E*)-**1** isomerisation, while the ones with x_2 to (*Z*,*Z*,*E*)-**1** → (*Z*,*E*,*E*)-**1** and (*Z*,*Z*)-**1** → (*Z*,*E*)-**1** and x_3 to (*Z*,*E*,*E*)-**1** → (*E*,*E*,*E*)-**1**, (*Z*,*E*)-**1** → (*E*,*E*)-**1** and (*Z*)-**3**-**4** → (*E*)-**3**-**4**. The normalised rate constants $|k_1|$ and $|k_2|$ were divided by three or two in order to account for the statistical character of the (*Z*,*Z*,*Z*)-**1** → (*Z*,*Z*,*E*)-**1**, or (*Z*,*Z*,*E*)-**1** → (*Z*,*E*,*E*)-**1** and (*Z*,*Z*)-**1** → (*Z*,*E*)-**1** isomerisations, respectively. [b]Determined by UV-Vis absorption spectroscopy.

Table 3. Kinetic data for the thermal *Z* → *E* isomerisation of compounds **1**-**4**.[a]

	k^b, s^{-1}			$\Delta G^{\neq}$ [b], kJ mol^{-1}			$\Delta H^{\neq}$, kJ mol^{-1}			$\Delta S^{\neq}$, J mol^{-1}			$\Delta E_a^{\neq}$, kJ mol^{-1}		
	$\|k_1\|$	$\|k_2\|$	k_3	$\|\Delta G_1^{\neq}\|$	$\|\Delta G_2^{\neq}\|$	$\Delta G_3^{\neq}$	$\|\Delta H_1^{\neq}\|$	$\|\Delta H_2^{\neq}\|$	$\Delta H_3^{\neq}$	$\|\Delta S_1^{\neq}\|$	$\|\Delta S_2^{\neq}\|$	$\Delta S_3^{\neq}$	$\|\Delta E_{a1}^{\neq}\|$	$\|\Delta E_{a2}^{\neq}\|$	$\Delta E_{a3}^{\neq}$
1	3.8 x 10^{-6}	3.7 x 10^{-6}	3.9 x 10^{-6}	104	104	104	88	89	88	-55	-52	-52	90	91	91
2	-	3.5 x 10^{-6}	4.2 x 10^{-6}	-	104	104	-	90	88	-	-48	-54	-	92	90
3	-	-	5.4 x 10^{-6}	-	-	103	-	-	74	-	-	-99	-	-	76
4[c]	-	-	1.1 x 10^{-5}	-	-	102	-	-	86	-	-	-52	-	-	88

[a]Parameters with appendix x_1 refer to (*Z*,*Z*,*Z*)-**1** → (*E*,*Z*,*Z*)-**1** isomerisation, while the ones with x_2 to (*E*,*Z*,*Z*)-**1** → (*E*,*E*,*Z*)-**1** and (*Z*,*Z*)-**2** → (*E*,*Z*)-**2** and x_3 to (*E*,*E*,*Z*)-**1** → (*E*,*E*,*E*)-**1**, (*E*,*Z*)-**2** → (*E*,*E*)-**2** and (*Z*)-**3**-**4** → (*E*)-**3**-**4**. The normalised rate constants $|k_1|$ and $|k_2|$ were divided by three or two in order to account for the statistical character of the (*Z*,*Z*,*Z*)-**1** → (*E*,*Z*,*Z*)-**1**, (*E*,*Z*,*Z*)-**1** → (*E*,*E*,*Z*)-**1** and (*Z*,*Z*)-**2** → (*E*,*Z*)-**2** isomerisations, respectively. [b]At 298 K. [c]Determined by UV-Vis absorption spectroscopy.

The activation energy parameters for the thermal isomerisation were determined by Eyring analysis (Table 3). The experimental data together with their fitting can be found in Appendix I. Thanks to such evidences we could prove that for our tris(azobenzene) system **1** the mechanism of the thermal reaction follows the expected pseudo-first order cascade reaction: (*Z*,*Z*,*Z*)-**1** → (*E*,*Z*,*Z*)-**1** → (*E*,*E*,*Z*)-**1** → (*E*,*E*,*E*)-**1**. The bis(azobenzene) **2**: (*Z*,*Z*)-**2** → (*E*,*Z*)-**2** → (*E*,*E*)-**2** exhibits equivalent behaviour. For such cascade reactions, it is necessary to account for the statistical character of the first reaction(s), since the first isomerisation could occur on three equivalent azobenzene units for **1**, and on two for molecule **2**. In our case, the normalised rate constant $|k_1|$ for the (*Z*,*Z*,*Z*)-**1** → (*E*,*Z*,*Z*)-**1** reaction was divided by three. Thus, the normalised rate constant $|k_2|$ accounting for (*E*,*Z*,*Z*)-**1** → (*E*,*E*,*Z*)-**1** and (*Z*,*Z*)-**2** → (*E*,*Z*)-**2** reactions was divided by two. It is worth mentioning that, for both the tris(azobenzene) (**1**) and bis(azobenzene) (**2**) the thermal isomerisation rate constants are substantially analogous, thus indicating that the azobenzene

units do not influence one another, being electronically and geometrically decoupled and showing the absence of cooperative effects. Although geometrical decoupling was seen rather obvious, being the azobenzene units reciprocally connected by a central rigid benzene ring, complete electronic decoupling could not be postulated only on the basis of the electronic spectra of compounds **1**-**3** (see above). Those in fact enlighten the occurrence of partial (even though limited) π-conjugation between the azobenzene chromophores when embedded in the π-extended star-shaped system, if compared to **4**. Indeed, the examination of the activation energy parameters for the thermal $Z \rightarrow E$ isomerization obtained under dark revealed that all the azobenzene units in compounds **1** and **2** display the same kinetic behaviour, while in the case of star-shaped mono(azobenzene) **3**, a small but not substantial lowering of the activation free energy is visible. However, we impute experimental error being most likely the cause of such observation. Reference compound **4** instead shows slightly faster thermal isomerisation, if compared to the star-shaped compounds **1**-**3** (Table 3). The values are however within the same order of magnitude and are comparable with similar rigid azobenzene and bis(azobenzene) derivatives found in the literature. [13a] Here it is visible how the mild electron-withdrawing character of the carboxylic group in *para*-position with respect to the azobenzene moiety does not sensibly lower the activation energy for the thermal isomerisation, as this is a known effect for stronger electron acceptor groups by mesomeric effect (*e.g.* nitro $-NO_2$ or cyano –CN).[2ll]

3.4. Ion-mobility mass spectrometry (IMMS)[3]

The conformational rigidity of compounds **1**-**3**, combined with their satisfactory photochromism resulting from electronic decoupling of the switches grafted to the central benzene core motivated us to study their shape variation resulting from the E – Z isomerisation of their photochromic units. We used ion-mobility mass spectrometry (IMMS) to discriminate the different molecular configurations of the various isomers of **1**-**3**, since this technique may help resolving mixtures of isomeric ions based only on the difference in their collisional cross section (CCS), a property which is directly related to their gaseous ions geometries.[16la] With such experimental technique, ions drift under the influence of an electric field and undergo collisions with a buffer gas. The ions drift time across the mobility cell is associated to the probability of collision with the buffer gas, hence to the ions CCS. Nevertheless, compared to the conventional methods, ionized species are mandatory for conducting IMMS experiments. For the present study, compounds **1**-**3** bearing carboxylic acid functional groups can be readily deprotonated upon Electrospray Ionization (ESI) in negative ion mode. The mass spectra obtained upon ESI of our star-shaped azobenzene derivatives **1**-**3** present intense signals, with the most intense peak corresponding to the mono-deprotonated species: [**1** $-H^+]^-$ m/z = 749.2, [**2** $-H^+]^-$ m/z = 745.2 and [**3** $-H^+]^-$ m/z = 741.2 (Figure 59).

[3] Experiments performed in collaboration with Q. Duez, Dr. J. De Winter, Prof. P. Gerbaux (Université de Mons)

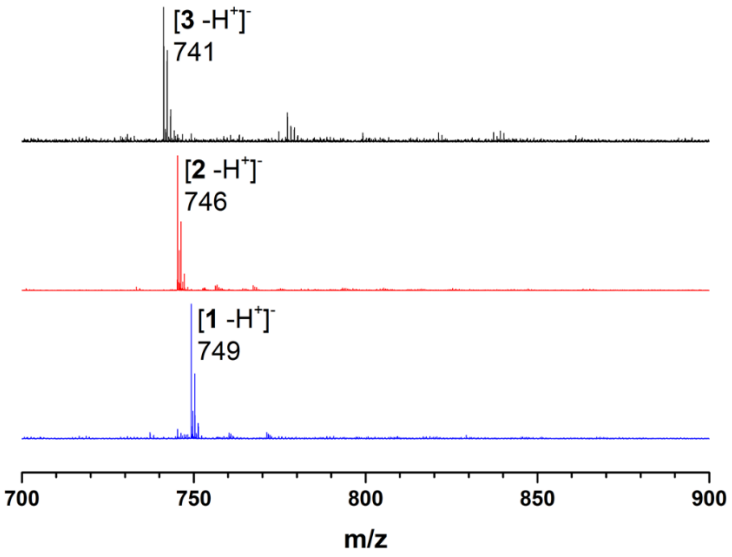

Figure 59. ESI-MS (negative mode) analysis of solutions (10^{-5} M) of **1** (*bottom*), **2** (*middle*) and **3** (*top*) in THF.

Multiply-charged ions are also detected but, for our discussion, we will only focus on the singly charged ions. When subjected to ion mobility, the singly charged ions, [**1** -H^+]$^-$, [**2** -H^+]$^-$ and [**3** -H^+]$^-$ from non-irradiated solutions, are all characterized by single Arrival Time Distributions (ATD) associated to the all-(*E*) species. Conversely, the analysis of UV light-irradiated solutions (UV – PSS) evidenced the appearance of additional ATD signals at lower drift times (Figure 60). The latter observation clearly enlightens that the UV-generated configurations present lower CCS compared to the less compact all-*E* isomers. Furthermore, it is worth mentioning that for each molecular photoswitch, the number of ATD signals detected after irradiation correspond to the number of different configurations, with four, three and two peaks being resolved for respectively **1**, **2** and **3.** The ATD are then used to calculate the experimental collisional cross section, *i.e.* CCS, by applying a calibration procedure (see Methods and Chapter 3, section 4). Again, the CCS values confirm that the *E* to *Z* isomerization induces the compaction of the ion structures with, for instance, CCS drastically decreasing from 269 to 187 $Å^2$ when passing from the (*E*,*E*,*E*)-**1** to the (*Z*,*Z*,*Z*)-**1** configurations. Interestingly, as a reference experiment IMMS performed on UV-irradiated solutions of the reference linear azobenzene **4** did not lead to the observation of new peaks in the IMMS chromatograms, indicating that the large molecular shape rearrangement detectable with such technique is uniquely due to the their embedment into a large and rigid π-conjugated scaffold.

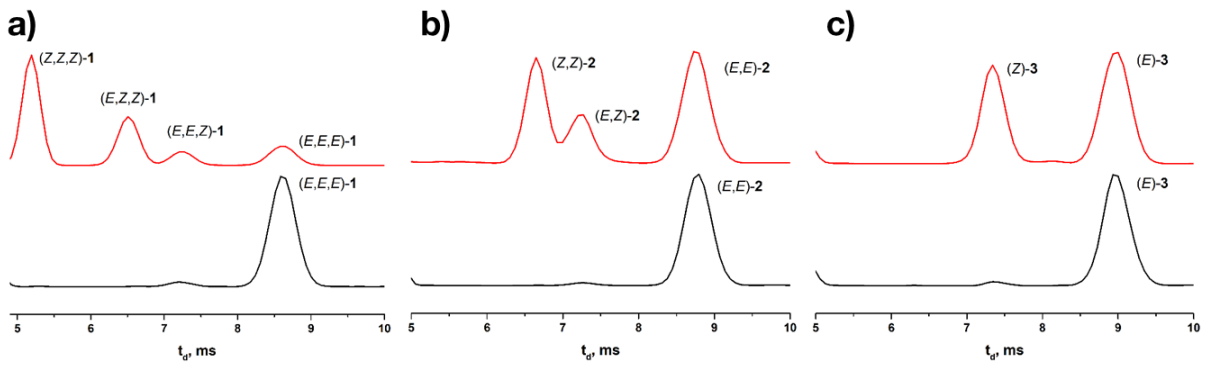

Figure 60. IMMS experiments on compounds **1-3** upon UV light irradiation in solution. Arrival time distributions (ATD) recorded for: a) tris-azobenzene **1**, b) bis-azobenzene **2** and c) mono-azobenzene **3**. *Black line* no light irradiation, *red line* UV PSS.

Table 4. Experimental collisional cross section (CCS) values of the various isomers of **1-3** determined by IMMS.

	CCS (Å^2)		**CCS** (Å^2)		**CCS** (Å^2)
(*E*,*E*,*E*)-**1**	269	(*E*,*E*)-**2**	273	(*E*)-**3**	277
(*E*,*E*,*Z*)-**1**	237	(*E*,*Z*)-**2**	239	(*Z*)-**3**	241
(*E*,*Z*,*Z*)-**1**	220	(*Z*,*Z*)-**2**	224		
(*Z*,*Z*,*Z*)-**1**	187				

IMMS was used also to monitor the stepwise photoisomerisation of **1**: the technique was used to follow the light-induced process upon on-line irradiation of a DMSO solution with continuous infusion in the ESI source (Figure 61). The ATDs show the gradual appearance of the aforementioned photogenerated peaks relative to the (*E*,*E*,*Z*)-**1**, (*E*,*Z*,*Z*)-**1** and (*Z*,*Z*,*Z*)-**1**, until the UV – PSS is reached. Interestingly, upon integration of the peaks obtained for the four isomers at the UV – PSS we measured the following apparent isomeric ratio: 63 % (*Z*,*Z*,*Z*)-**1**, 30 % (*E*,*Z*,*Z*)-**1**, 3 % (*E*,*E*,*Z*)-**1**, 4 % (*E*,*E*,*E*)-**1.** The comparison with the similar results obtained by HPLC-MS (Table 1) reveals that the mobility diagrams overestimate the amount of (*Z*,*Z*,*Z*)-**1** with respect to the (*E*,*E*,*Z*)-**1**. The discrepancy between the IMS and HPLC-MS data (Table 1) comes from the fact that for the IMMS data we only monitor the singly charged ions that are merged with all differently charged states for the HPLC experiments.

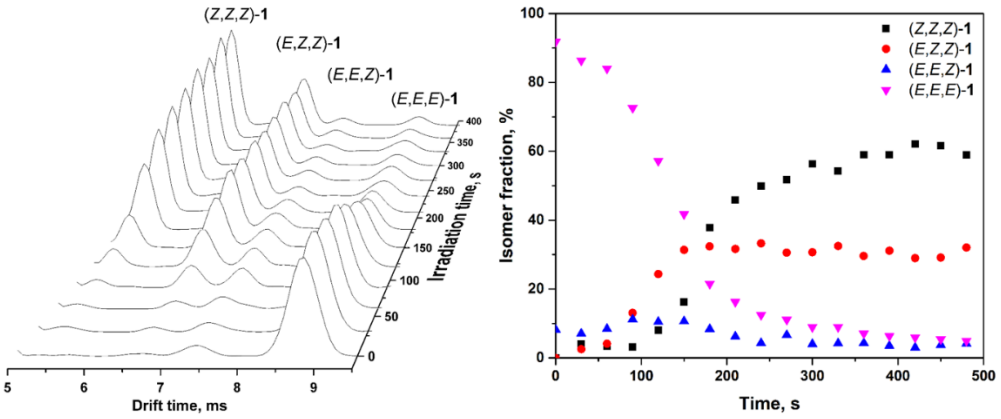

Figure 61. Photoisomerisation of **1** followed by IMMS. A solution of **1** was irradiated with UV light upon continuous IMMS separation. *Left*, temporal evolution of the IMMS traces. *Right*, isomer fraction over time determined by integration of the IMMS peaks.

Furthermore, we investigated the possibility to induce the in-flight $Z \rightarrow E$ isomerisation of azobenzene ions by collisional activation prior to their separation by ion-mobility.[16la] In this case, we employed an HPLC set-up to separate the four isomers prior to injection in the mass spectrometer and performed the aforementioned experiments on the isolated photogenerated Z isomers of **1**. Such an experiment benefits from the great versatility of ion manipulations offered by the Waters Synapt G2-Si mass spectrometer. Indeed, after HPLC separation of the (*Z*,*Z*,*Z*)-**1** isomer and the preparation of the gas phase ions upon ESI(-), the molecular anions ($[\mathbf{1}\text{-}H^+]^-$ at m/z 749.2) are mass-selected with the quadrupole mass selector.). The ions are then subjected to collisional heating (collisional activation) in the trap cell prior to the ion mobility separation by gradually increasing their kinetic energy (Figure 62). It is worth noting that we only used low voltages (U_{tr}) to induce isomerization while avoiding ion decomposition. At low U_{tr} (4 V), only the signature of the (*Z*,*Z*,*Z*)-**1** ions is detected upon IMMS, demonstrating the successful isolation of the corresponding molecule by HPLC separation. This also reveals that no isomerisation is induced in source or in the ion transfer regions in our experimental conditions.

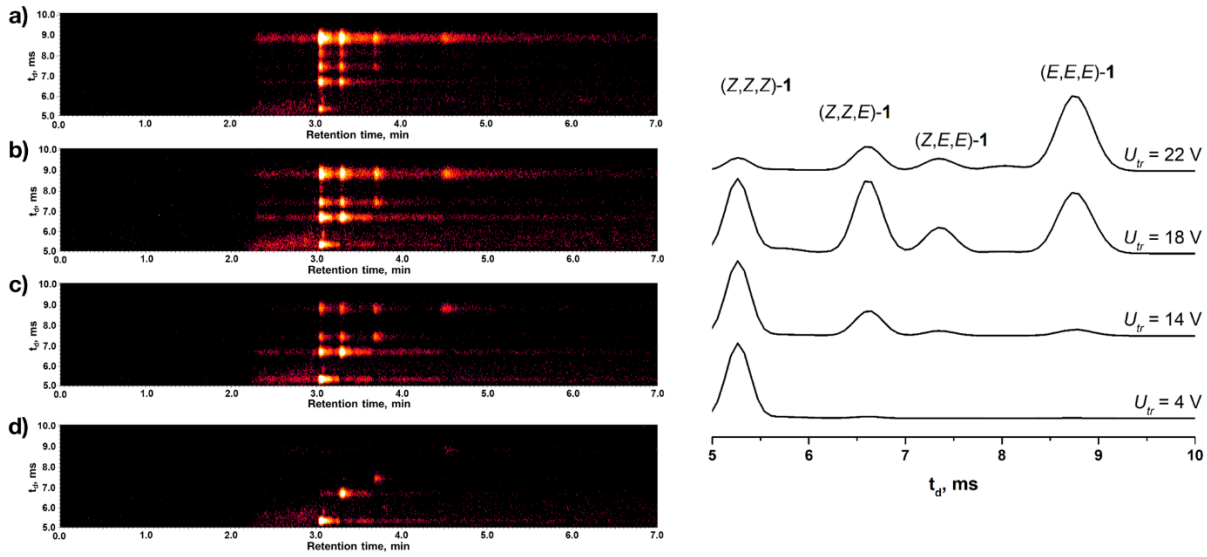

Figure 62. Collisionally induced $Z \rightarrow E$ isomerisation of (*Z*,*Z*,*Z*)-**1** ions. *Left panel*, 2D IMMS/HPLC traces of **1** irradiated with UV light (UV PSS) in DMSO solution (+ NaOH exc.) at different collision energies (U_{tr}). Chromatograms integrated at $[M\text{-}H^+]^-$ m/z = 749.2. Peak at 3 min 5 s retention time corresponds to (*Z*,*Z*,*Z*)-**1**, 3 min 20 s (*Z*,*Z*,*E*)-**1**, 3 min 40 s (*Z*,*E*,*E*)-**1**, 4 min 30 s (*E*,*E*,*E*)-**1**. d) trace recorded at U_{tr} = 4 V, c) trace recorded at U_{tr} = 14 V, b) trace recorded at U_{tr} = 18 V and a) trace recorded at U_{tr} = 22 V showing the occurrence of thermal Z → E isomerisation. Right panel, IM traces plotted for the (HPLC) chromatographic peak at 3 min 5 s corresponding to (*Z*,*Z*,*Z*)-**1**.

Upon progressive increase of the U_{tr}, additional signals are detected upon IMMS and are of course related to the progressive appearance of the *E* isomers. Interestingly, the successive appearance of the (*E*,*Z*,*Z*)-**1**, (*E*,*E*,*Z*)-1 and finally (*E*,*E*,*E*)-**1** isomers also reveals that the thermal isomerization of the (*Z*,*Z*,*Z*)-**1** ions is a stepwise process. These experimental evidences suggest that upon collisional activation, in analogous fashion as heating, it is possible to increase the rate of the thermal $Z \rightarrow E$ isomerisation of azobenzenes, thus to generate the more thermodynamically stable *E* isomer(s) within the timescale of their residence in the Trap Cell (μs) prior to the ion mobility separation.

3.5. Investigation on the self-assembly of 1 and 5 on graphite (HOPG)

The compelling properties of our tris(azobenzene) photoswitch **1**, including its rigidity, the large shape variation and the presence of carboxylic acid pendant groups enabling intermolecular H-bonding motivated us to study by STM their self-assembly on graphite. Our experiments showed that **1** forms ordered monolayers; the assemblies in addition exhibited peculiar light response. We focussed most of our attentions to the study of the self-assembly at the solid-liquid interface, thus on the monolayers forming on graphite at the equilibrium with their overlying solution. We relied on the photoresponsive character of such assemblies after the thorough investigation performed on the photochemical properties of **1** in solution. Following from the high amount of photogenerated (*Z*)-isomers of **1** upon UV irradiation, we expected that such a variation of the solution composition would have led to the assembly of different isomers at the interface between graphite and the solution, as this is generally observed for photochromic derivatives.[7la, 113] In order to fully understand the experimental data obtained by the STM experiments and to confirm the assignment of the molecular packings of the various isomers of **1**, we have also simulated the assembly by Molecular Dynamics.[4] Furthermore, blank experiments with the non-photochromic derivative **5** were performed, proving the role of the isomerisation of azobenzenes in **1** towards the variation of the assembly. Nevertheless, the observation of a light-induced variation of the molecular assembly could not answer the question whether the isomerisation of **1** could occur also when adsorbed on the graphite surface. In order to explore the aforementioned phenomenon, we performed additional qualitative STM experiments at the solid-air interface (*e.g.* without solution between the STM tip and the sample) by depositing **1** using a standard spin-coating method. The films formed showed the appearance of ordered monolayers that retained a photoresponsive character, thus demonstrating that the photoisomerisation of **1** could occur also when this is adsorbed on graphite.

Initially, we targeted at investigating the self-assembly of all-(*E*)-**1** in the dark at the interface between its solution in 1-heptanoic acid (c = 10 μM) and highly ordered pyrolytic graphite (HOPG). Towards this end, to make sure that all three azobenzenes moieties of molecule **1** were in their all-(*E*) state, we applied to the surface a drop of a non-irradiated solution of **1**, in order to benefit from the thermodynamic stability of (*E*)-azobenzene isomer. The STM images recorded *in-situ* display a tightly packed 2D crystalline lamellar structure consisting of (*E*,*E*,*E*)-**1** arranged in a zig-zag fashion (Figure 63, Figure 66a). The structure observed displays a unit cell: a = 4.1 ± 0.2 nm, b = 3.0 ± 0.3 nm, α = 41 ± 5 ° with an area A = 8.7 ± 0.3 nm^2, each containing two molecules. A careful image analysis revealed the absence of polymorphs of such a crystalline packing, also upon varying the concentration of **1** solution used for the experiments: 10 μM was found to be the optimal value for attaining higher spatial resolution (for details see Methods). The total absence of the ideal "honeycomb network" H-bonded pattern which should arise from the formation of the intermolecular 2-fold cyclic O-H···O bonding between carboxylic groups is not surprising. This consideration comes from the large dimension of the rigid aromatic core of **1**, in line with the reported tendency of large C_3-symmetric tricarboxylic acids to form more

[4] The theoretical studies were performed by V. Diez-Cabanes, Dr. A. Minoia and J. Cornil (Université de Mons).

densely packed structures.[110] The reason for this evidence was explained by the higher adsorption energy contribution obtained by forming a more densely packed crystal with a non-ideal H-bonding pattern compared to the corresponding "ideal" honeycomb structure expected from the generation of the two-fold H-bonding dimers, leading to a looser crystalline structure. In other words, the most prominent term driving the assembly is not associated to intermolecular interactions, but rather to the molecule--substrate adsorption energy per unit area, thus yielding the "tightest" assembly and not the "ideal" H-binding motif.[110] In order to confirm the assignment of the molecular packing given by experimental data, we simulated the assembly of (*E*,*E*,*E*)-**1** by Molecular Dynamics (MD), which yielded an average unit cell: a = 4.3 nm, b = 2.8 nm, α = 41 °, with two molecules per unit cell (Figure 66b). The result obtained by MD simulations matches very well the experimental values obtained by STM, therefore confirming the validity of our model. The azobenzene units in molecule **1** present a kink in the CNNC bond, it thus follows that upon the adsorption of **1** on the HOPG surface the resulting structures could show two isomers of the compound, together with the possibility of the emergence of their chirality. Nevertheless, from the images obtained, we could not attain the level of detail needed to neither assign unambiguously which specific isomer the crystalline domains belonged to, nor to comment about the chirality of the 2D structures.

Interestingly, the *in-situ* photoirradiation of a solution of (*E*,*E*,*E*)-**1** with ultraviolet light is generally accompanied with a loss of ordered crystalline packing, indicating a decrease in concentration of the (*E*,*E*,*E*)-**1** isomer. The general disappearance of the initial packing was seen logical knowing the lower stability of the azobenzene *Z*-isomer when adsorbed on a surface, due to its non-planar geometry.[112] Surprisingly, in such a situation it was also possible to visualise domains of **1** displaying a periodical assembly (Figure 63). From our interpretation, each domain is composed by one isomer: (*E*,*Z*,*Z*)-**1** and (*E*,*E*,*Z*)-**1**.

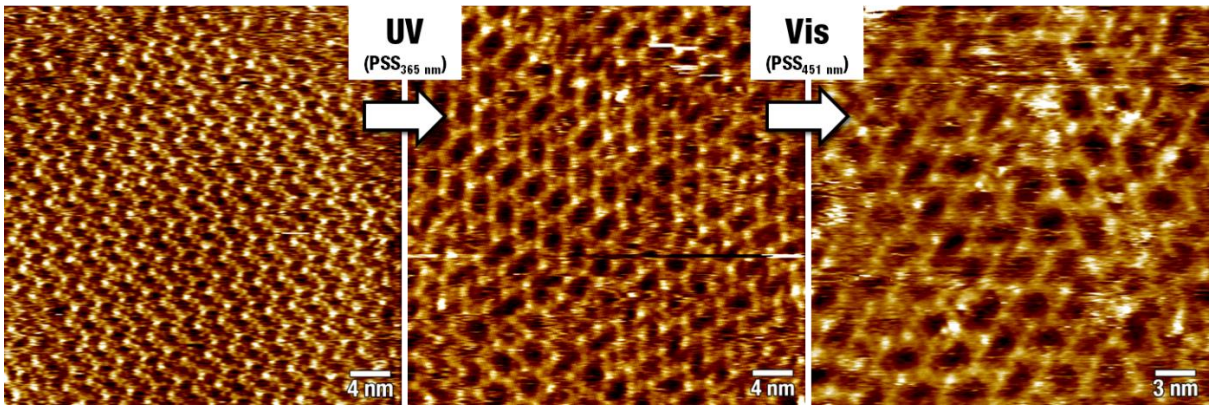

Figure 63. STM images of **1** recorded at the interface between an HOPG substrate and a 10 μM solution of **1** in 1-heptanoic acid. *Left*, no light irradiation (average tunnelling current (I_T) = 30 pA, tip bias voltage (V_T) = +800 mV). *Centre*, *in-situ* UV (λ_{max} = 365 nm) light irradiation (I_T = 30 pA, V_T = +800 mV). *Right*, subsequent in-situ Vis (λ_{max} = 451 nm) light irradiation (I_T = 20 pA, V_T = +800 mV).

As a blank experiment, the same study was also performed on the non-photochromic compound **5**, displaying a similar geometry to (*E*,*E*,*E*)-**1**, but having tolane moieties instead of azobenzenes in each of the three "arms". Compound **5** was found to self-assemble in a crystalline structure with the same symmetry displayed by (*E*,*E*,*E*)-**1** (Figure 64). Such structure is characterised by the following unit cell: a = 4.2 ± 0.2 nm, b = 2.9 ± 0.1 nm, α = 46 ± 1 ° with an area A = 8.8 ± 0.4 nm^2, each containing two molecules. The parameters are substantially unvaried when compared

with (*E*,*E*,*E*)-**1**, within experimental error. A blank test performed by irradiating **5** solutions *in-situ* with both UV and visible light did not lead to any perceivable variation in the supramolecular packing.

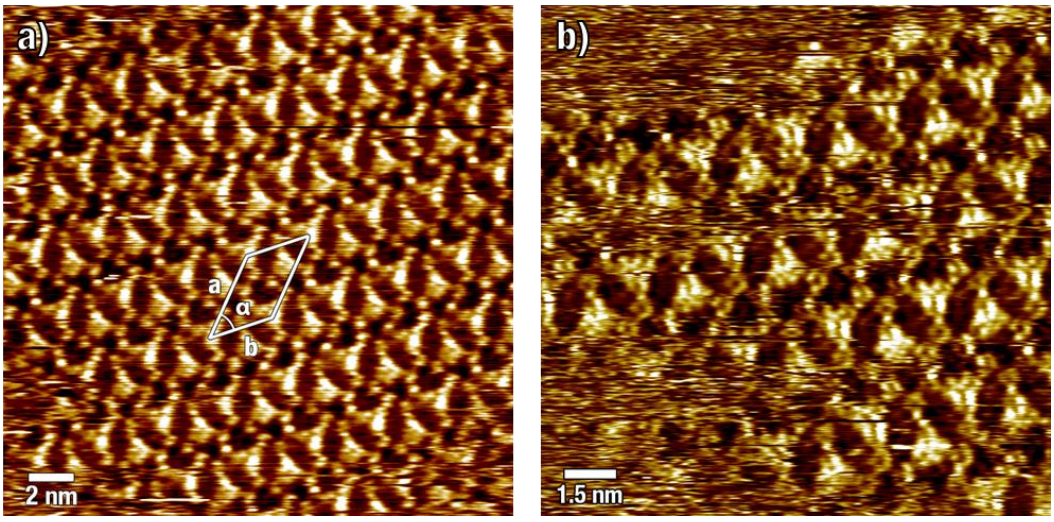

Figure 64. STM images of **5** at the solid-liquid interface between highly ordered pyrolytic graphite (HOPG) and a **5** (c = 10 μM solution in 1-heptanoic acid). a) I_T = 20 pA, V_T = +800 mV. b) I_T = 20 pA, V_T = +800 mV. Images recorded without irradiation.

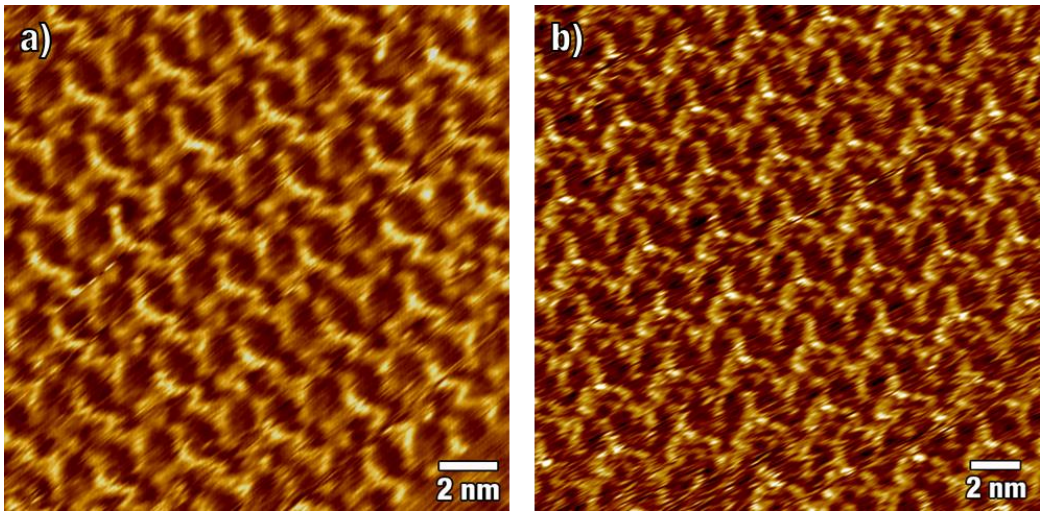

Figure 65. STM images of **5** at the solid/liquid interface between highly ordered pyrolytic graphite (HOPG) and a **5** (c = 10 μM) solution in 1-heptanoic acid. a) image obtained after 15 minutes in-situ UV irradiation, I_T = 20 pA, V_T = +800 mV. b) image obtained after subsequent *in-situ* Vis irradiation for 15 minutes, I_T = 20 pA, V_T = +800 mV.

As previously mentioned, upon *in-situ* UV- and Vis-irradiation of **1** it was possible to visualise ordered domains showing a different supramolecular packing compared to the situation seen without light irradiation (*e.g.* only (*E*,*E*,*E*)-**1** isomer, see Figure 63). Namely, we could assign the composition of such ordered domains to the two isomers (*E*,*E*,*Z*)-**1** and (*E*,*Z*,*Z*)-**1**, but we could not visualise (*Z*,*Z*,*Z*)-**1**. For (*E*,*Z*,*Z*)-**1**, the estimated unit cell parameters are the following: a = 7.6 nm, b = 2.7 nm, α = 69 ° with an area A = 20 nm^2, each containing four molecules (Figure 66c). Conversely, for (*E*,*E*,*Z*)-**1** we estimate the following unit cell: a = 4.0 nm, b = 3.3 nm, α = 55 ° with an area A = 11 nm^2, each containing two molecules (Figure 66e). Both assemblies display notably different geometry and unit cell parameters compared to (*E*,*E*,*E*)-**1** and **5**. Moreover, their stability appears lower compared to the one of the (*E*,*E*,*E*)-**1**, being evidenced by the smaller size

of the ordered domains, and the sometimes fuzzy contrast visible in the STM images. Interestingly it was not possible to visualise the formation of ordered domains formed by (*Z*,*Z*,*Z*)-**1**; this observation can be ascribed to the non-planar conformation of the three (*Z*)-azobenzene units, lowering the energy of adsorption of the molecules on the basal plane of graphite and hence providing unfavourable geometry for stabilisation via H-bonding with neighbouring molecules. Upon subsequent visible light irradiation, a radical change in the supramolecular assembly was evidenced, yielding a scenario in which the only ordered domains monitored at the interface were those containing (*E*,*E*,*Z*)-**1** (as mentioned above, Figure 63, Figure 66e).

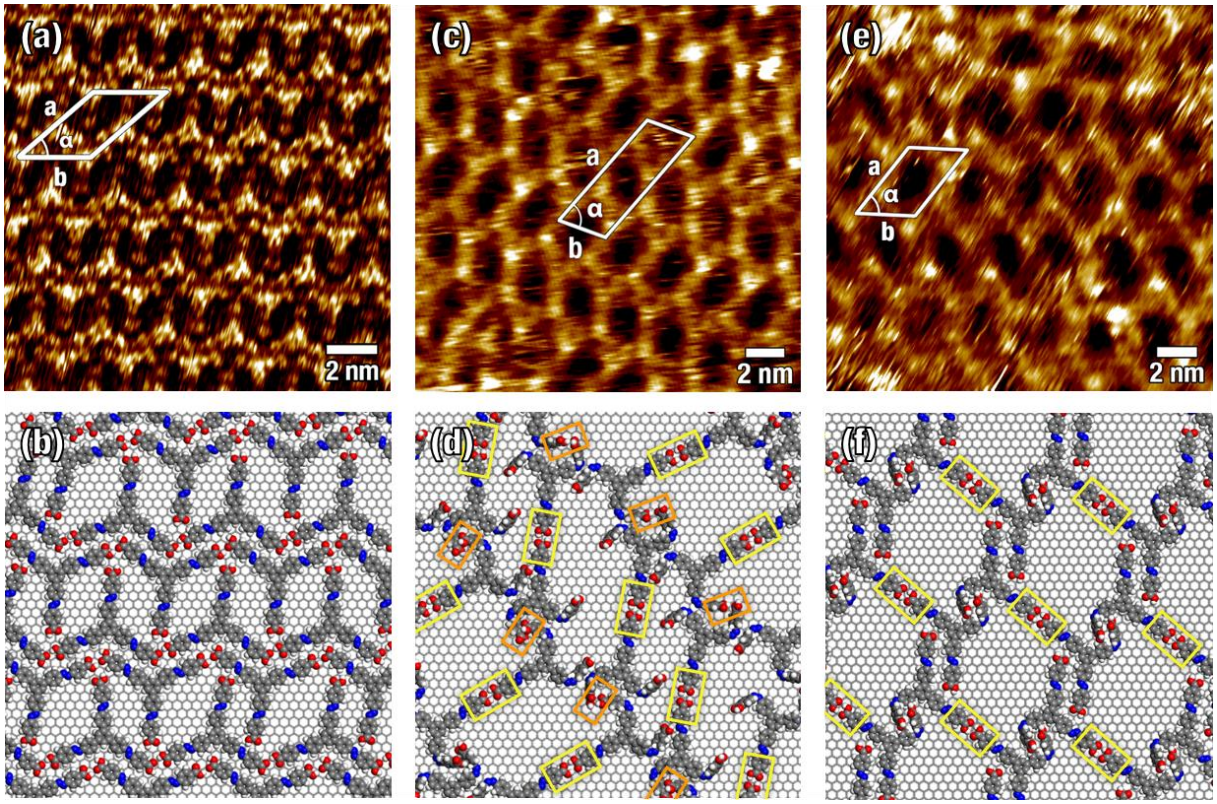

Figure 66. High resolution STM images of ordered domains of (a) (*E*,*E*,*E*)-**1**, (c) (*E*,*Z*,*Z*)-**1**, and (e) (*E*,*E*,*Z*)-**1** self-assembled at the HOPG-solution interface using 1-heptanoic acid as solvent. Supramolecular packing models obtained by MM/MD simulations for (b) (*E*,*E*,*E*)-**1**, (d) (*E*,*Z*,*Z*)-**1**, and (f) (*E*,*E*,*Z*)-**1**. The *yellow rectangles* indicate the formation of hydrogen bonded carboxylic acid dimers between (*E*)-azobenzene arms. *Orange rectangles* indicate hydrogen bonds between carboxylic moieties positioned on (*Z*)-azobenzene arms. Tunneling parameters: (a) average tunnelling current (I_T) = 40 pA, tip bias voltage (V_T) = +800 mV), (c) I_T = 30 pA, V_T = +800 mV, (e) I_T = 20 pA, V_T = +800 mV.

It is striking to observe how the ordered domains of both the photoproducts (*E*,*Z*,*Z*)-**1** and (*E*,*E*,*Z*)-**1** show a less dense crystalline packing compared to (*E*,*E*,*E*)-**1** and **5** (Figure 66, Table 5) which is in line with the larger stability in the STM imaging of the monolayers of the (*E*,*E*,*E*)-**1**. One explanation for this observation could come from the non-planar conformation of the *Z*-isomer of the azobenzene units, resulting in less favourable molecule-substrate interactions compared to the *E* form. This lower stabilisation is balanced by the formation of stronger intermolecular hydrogen bonds, such as carboxylic acid dimers, as evidenced by the larger spacing between rows of (*E*,*Z*,*Z*)-**1** and (*E*,*E*,*Z*)-**1**, compared to (*E*,*E*,*E*)-**1**. The formation of intermolecular carboxylic acid dimers between two (*E*)-azobenzene branches in the crystalline domains of (*E*,*Z*,*Z*)-**1** and (*E*,*E*,*Z*)-**1** is nicely supported by MM/MD simulations. For both (*E*,*Z*,*Z*)-**1** and (*E*,*E*,*Z*)-**1**, in order to interpret correctly the experimental data it was seen necessary to

perform the simulation over multiple different possible assemblies, following the complicated H-bonding pattern (Table 5, Figure 67). In this context, it is important to mention that the majority of the starting geometries used to model (*E,Z,Z*)-**1** and (*E,E,Z*)-**1** ended up in amorphous structures after the MM/MD run. Only a few of them presenting motion constrained by additional H-bonds showed a clear assembly pattern. In all cases, the H-bonding between two carboxylic groups takes place (yellow rectangles in Figure 66d, f, Figure 67), thus confirming its crucial role for the stabilisation of the supramolecular packing. In detail, the models adopted are composed as follows. For isomer (*E,Z,Z*)-**1**, the four molecules of the unit cell form two dimers connected by an hydrogen bond between carboxylic moieties on the (*E*) arm of the molecules (yellow rectangles, Figure 67c). The classification of the different models was done depending on the number and position of the hydrogen bonds formed between the (*Z*)-arms: (i) one hydrogen bond connects the two dimers (orange rectangles, Figure 67c I), (ii) two (*Z*)-arms form H-bonds connecting both sides of the dimers (orange rectangles, Figure 67c II), (iii) one extra hydrogen bond (green rectangles, Figure 67c III). Similarly, for (*E,E,Z*)-**1**, the two molecules in the unit cell form dimers connected by an hydrogen bond between carboxylic groups positioned on (*E*)-azobenzene arms (yellow rectangles, Figure 67b). Three possible assemblies have been studied depending on the number of additional interactions between neighbouring molecules: (i) no hydrogen bonds connect the molecules, but the out-of-plane rings of the (*Z*) arms are interacting (π-π interactions), (ii) one additional hydrogen bond connecting the (*Z*) arms (orange rectangles in Figure 67b II), (iii) instead of forming H-bonds between the (*Z*)-arms, a hydrogen bond is formed between carboxylic groups in the remaining (*E*) arms.

The need of considering also the occurrence of hydrogen bonds between carboxylic moieties positioned on (*Z*)-azobenzene arms in order to obtain a stable structure was surprising (orange rectangles in Figure 66d, Figure 67b, c). For (*E,Z,Z*)-**1**, the structure reproducing best the experimental pattern consists of model II (Table 5, Figure 66d, Figure 67c II), with the following parameters: a = 7.6 nm, b = 2.8 nm, α = 74 ° with an area A = 20 nm^2, each containing four molecules. Regarding this isomer, it is important to point out that several types of assemblies were considered and analysed, but only the assemblies presenting H-bonds between (*Z*)-azobenzene arms were able to form stable ordered assemblies, thus confirming the importance of these bonds in the stability of the assembly. For (*E,E,Z*)-**1**, the chosen model I yields an unit cell: a = 3.8 nm, b = 3.3 nm, α = 56 ° with an area A = 11 nm^2, each containing two molecules. In this case, the computed structures highlight the presence of π-π interactions between two out-of-plane phenyl rings of adjacent (*E,E,Z*)-**1** molecules dominating over the formation of additional H-bonds (Figure 66f, Figure 67b I).

Table 5. Experimental and modelled unit cell parameters for **1** and **5**, and estimated thermodynamic quantities

			a [nm]	b [nm]	α [°]	A [nm²]	N	*H-bonds*	E_{ads} [kcal/mol]	*BE* [kcal/mol]
(*E*, *E*, *E*)-**1**	experimental		(4.1 ± 0.2)	(3.0 ± 0.3)	(41 ± 5)	(8.7 ± 0.7)	2			
	theoretical		**4.3**	**2.8**	**41**	**8.0**		**2**	**-101.91**	**-6.83**
5	experimental		(4.2 ± 0.2)	(2.9 ± 0.1)	(46 ± 1)	(8.8 ± 0.4)	2			
(*E*, *Z*, *Z*)-**1**	experimental		(7.6)	(2.7)	(69)	(20)	4			
	theoretical	I	8.1	3.7	61	26		1.5	-80.50	-6.63
		II	**7.6**	**2.8**	**74**	**20**		**2**	**-78.84**	**-10.13**
		III	7.8	3.3	56	21		2.5	-78.59	-8.63
(*E*, *E*, *Z*)-**1**	experimental		(4.0)	(3.3)	(55)	(11)	2			
	theoretical	**I**	**3.8**	**3.3**	**56**	**11**		**1**	**-90.38**	**-8.87**
		II	4	3.8	55	13		2	-89.96	-6.36
		III	5.5	3.2	50	13		2	-90.59	-7.83

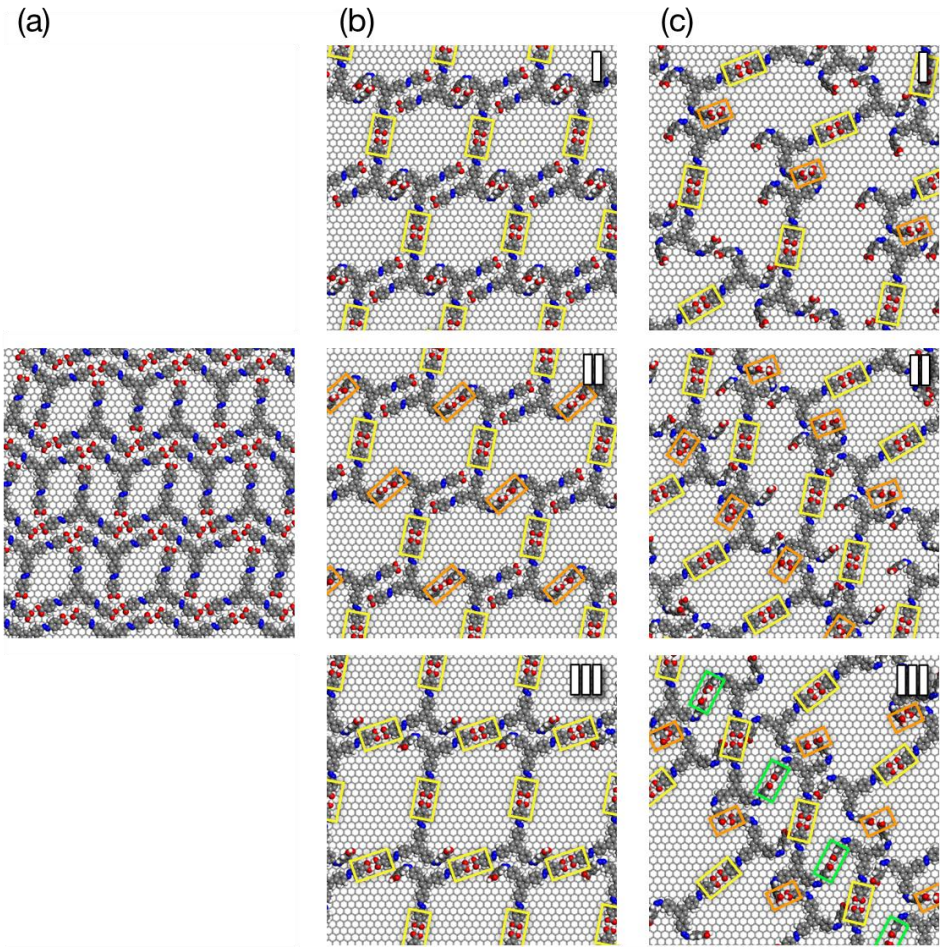

Figure 67. (a) Top view of the final structure of the MD simulations for (*E*,*E*,*E*)-**1**. (b) Top view of the final structure of the MD simulations for the model I (*top*), model II (*centre*) and model III (*bottom*) of (*E*,*E*,*Z*)-**1**. The *yellow* and *orange rectangles* show the (*E*)- and (*Z*)- H-bonds respectively. (c) Top view of the final structure of the MD simulations for the model I (*top*), model II (*centre*) and model III (*bottom*) of (*E*,*Z*,*Z*)-**1**. The *yellow rectangles* represent the (*E*)- H-bonds, the *orange rectangles* represent the (*Z*)- H-bonds which connect the vertical and horizontal rows and the *green rectangles* represent the (*Z*)- H-bonds which connect the molecules of the horizontal rows.

To obtain a more complete interpretation of our experimental findings, we casted down the different energies driving the 2D self-assemblies of (*E*,*E*,*E*)-**1**, (*E*,*Z*,*Z*)-**1** and (*E*,*E*,*Z*)-**1** on graphene. For this purpose, we have computed two parameters: adsorption energy (E_{ads}) and binding energy (*BE*), giving us a hint on the strength of the molecule-substrate and intermolecular interactions, respectively (Table 5, see methods for details). From the data, it is clear that the structural packing of both (*E*,*Z*,*Z*)-**1** and (*E*,*E*,*Z*)-**1** gives rise to a lower E_{ads} compared to (*E*,*E*,*E*)-**1**, due to the lower π-π and van der Waals interactions caused by the azobenzene units in the (*Z*)-conformation. This result rationalises the fact that no self-assembly for (*Z*,*Z*,*Z*)-**1** was observed at the experimental level. Conversely, for (*E*,*E*,*Z*)-**1** and (*E*,*Z*,*Z*)-**1** the larger BE values are related to the formation of a strong H-bonding network stabilising the supramolecular packing. The oppositive behaviour of E_{ads} and *BE* when going from (*E*,*E*,*E*)-**1** to its isomers validates our interpretation of the experimental molecular patterns visualised by STM. By and large, the computational insights confirm that the self-assembly of such large aromatic carboxylic acids is driven by a complicate interplay between intermolecular- and molecule/substrate- interactions. For the planar all-(*E*)-**1** the geometry of the 2D crystalline assembly is governed by the thermodynamics of strong molecule/substrate interactions leading to a tightly packed unit cell. The photogenerated (*Z*)-isomers show less favourable molecule/substrate interactions due to their non-planar conformation; this is, however, compensated by more stable hydrogen bonding interactions between the carboxylic groups, and/or π-π interactions between adjacent out-of-plane phenyl rings. The aforementioned intermolecular interactions allow the formation of stable supramolecular assemblies showing larger unit cells compared to all-(*E*)-**1**, which are particularly unusual in view of the known tendency of rigid carboxylic acids to form a dense crystal structure.[110]

The finding of different isomers from the all-(*E*)-**1** assembled at the solid-liquid interface could however not answer our question whether the photoswitch could undergo photoisomerisation when physisorbed on graphite. In order to cast further light onto whether the isomerization takes place or not on the basal plane of the surface, we have extended our study to the STM visualization of the isomerisation occurring in dry films, *i.e.* at the *solid-air interface*, of **1** physisorbed on the HOPG surface upon *in-situ* irradiation.

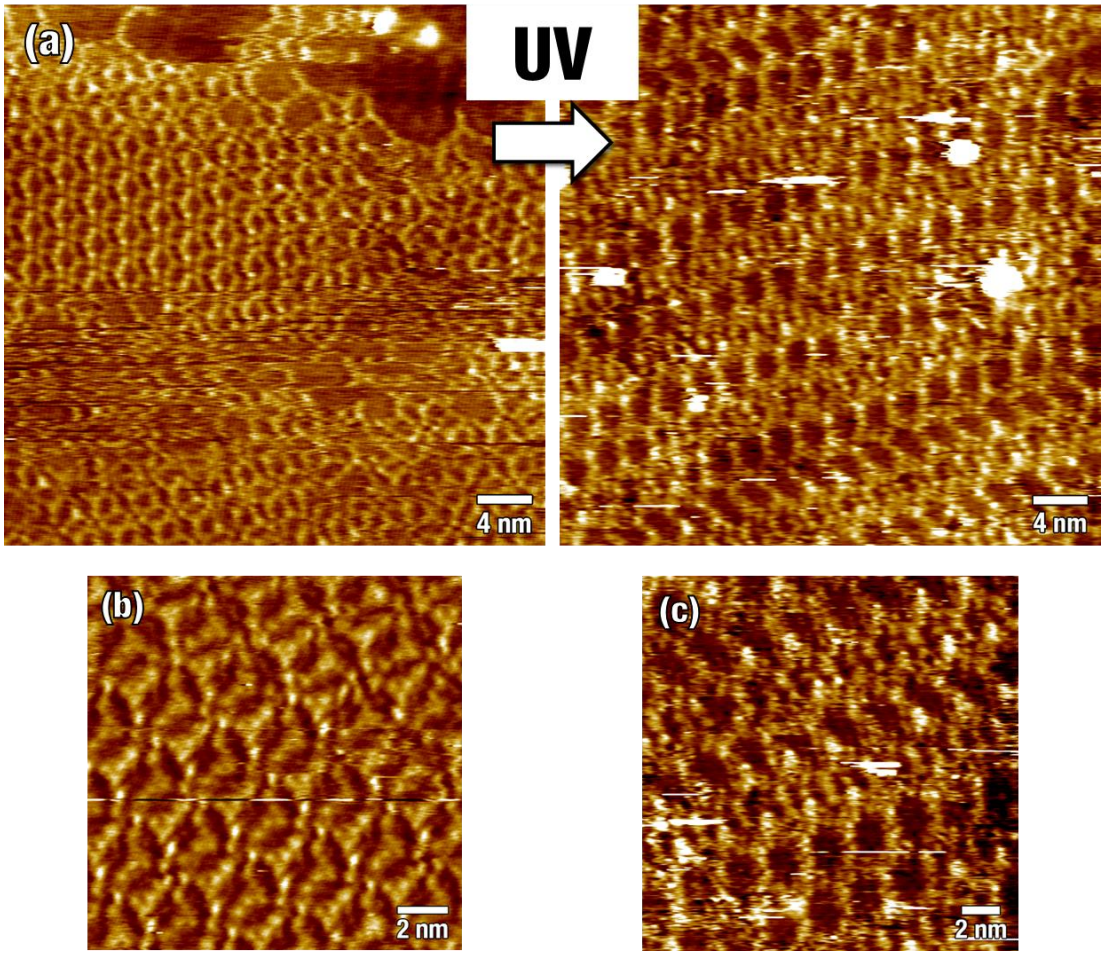

Figure 68. STM images of assemblies of **1** at the graphite-air interface, prepared by spin-coating of a c = 10 μM solution of (*E,E,E*)-**1** in THF on a freshly cleaved HOPG substrate. a) *left panel*, no irradiation (I_T = 20 pA, V_T = + 700 mV). *Right panel*, image obtained after ~ 30 min in-situ irradiation at λ_{max} = 367 nm, $P_d \approx 3$ mW cm^{-2} (I_T = 20 pA, V_T = + 700 mV). b) magnification of (*E,E,E*)-**1**, no irradiation (I_T = 20 pA, V_T = + 700 mV). c) Magnification of **1** after UV irradiation (I_T = 20 pA, V_T = + 700 mV).

In order to perform STM imaging of dry films of **1**, we set up a procedure enabling us to obtain monolayers showing ordered domains with areas of few hundreds nm^2. Such procedure consisted in depositing **1** from a non-irradiated solution (c = 10 μM in THF) on a freshly cleaved HOPG substrate and the successive removal of solution and solvent excess by spinning on a spin-coater (details in Methods). The concentration used was seen optimal for obtaining ordered monolayers of **1** arranged *face-on* on the graphite surface: higher concentrations led to the observation of linear aggregates, probably consisting of **1** arranged *edge-on*, together with additional ad-layers not allowing to obtain the desired sub-molecular resolution, and the use of lower concentrations did not lead to the observation of organised molecular monolayers. The high affinity of the large aromatic core of **1** for the basal plane of HOPG made it possible to obtain a molecular adsorbate characterised by small crystalline regions alternated by un-coated substrate regions, thus yielding a sub-monolayer coverage. From semi-quantitative point of view, the unit cell of (*E,E,E*)-**1** monitored by STM at the solid-liquid and at the solid-air interface are similar (Figure 68 and Figure 66a). Interestingly, upon performing *in-situ* irradiation of the sample with ultraviolet light, we could observe an evident variation of the original pattern visualised prior to light irradiation (Figure 68) as a result of the molecular isomerisation. In such a condition, thus in the absence of a medium capable of solvating **1**, the adsorbates cannot desorb

from the graphite substrate. The striking variation of the inter-row spacing compared to the non-irradiated situation is the most evident consequence of the external stimulus given by UV light. It is however evident how the morphology of the patterns seen upon irradiation at the solid-liquid interface is different from what obtained in the latter experiments: in such a scenario, the molecules are not capable of desorbing from the surface upon isomerisation, thus to rearrange forming 2D crystalline domains, each formed by only one *Z*-isomer, as previously mentioned, and visible in Figure 63 and Figure 66c,e. In the photoswitching experiments performed on **1** at the graphite-air interface we could on the contrary observe the neighbouring molecules within the same row being most likely present in the same configuration, nevertheless the molecular configuration of the neighbouring rows seems to vary randomly in the ordered domains. Thus, failing to form regular crystalline domains containing one, single isomer (see Figure 68). In light of these experimental evidences, we believe that we can safely state that in the STM experiments performed at the solid-liquid interface, the change in the geometry of the supramolecular 2D assemblies is due to the competitive adsorption of (*E*,*Z*,*Z*)-**1** and (*E*,*E*,*Z*)-**1** isomers, following the isomerisation of (*E*,*E*,*E*)-**1** in solution. Even though we cannot neglect that the molecules can isomerise when adsorbed on the graphite surface, we envision that in such a case the result would be largely different.

4. CONCLUSIONS

In summary, a novel family of multi-azobenzene photoswitches made by connecting the individual photochromes to a central trisubstituted 1,3,5-benzene core has been developed and fully characterised. Such star-shaped systems consisting of conformationally rigid, pseudo-planar scaffolds have been realised in order to explore the role of electronic decoupling in the isomerisation of the individual azobenzene units. The design of our tris-, bis- and mono(azobenzene) compounds limits the π-conjugation between the switches belonging to the same molecule, thus allowing their efficient isomerisation and the independent behaviour of each unit from the state of the neighbouring ones, but at the same time maintaining a high structural rigidity. An in-depth experimental insight has been gained by making use of different complementary techniques such as UV-Vis absorption spectroscopy, high performance liquid chromatography and advanced mass spectrometry methods as ion mobility. The additivity of the UV-Vis absorption spectra relative to the all-(*E*) isomer, together with the appearance of clear isosbestic points upon photoswitching of mono-, bis- and tris(azobenzene) compounds provided unambiguous evidence for an almost complete absence of electronic delocalisation between the chromophores. The latter allows a remarkably efficient photoswitching of all azobenzenes, as evidenced by their photoisomerisation quantum yields, not substantially different from the values showed by reference mono-azobenzenes. Moreover, all star-shaped compounds showed *Z*-rich UV photostationary states. Ion mobility mass spectrometry was exploited for the first time to study multi-photochromic compounds revealing the occurrence of a large molecular shape change in such rigid star-shaped azobenzene derivatives. Moreover, STM investigation on the self-assembly of the tris(azobenzene) **1** at the graphite-solution interface revealed the formation of patterns of all-(*E*)-**1**. Upon *in-situ* irradiation with ultraviolet and visible light, variation of the supramolecular packing was seen occurring, resulting from the formation of crystalline assemblies of two different partially (*Z*)-isomers. For the first time it was possible to identify by STM the existence of multiple isomeric states of a multiphotochromic compound in single-component self-assembled networks with a high level of details. In addition, by performing qualitative STM imaging on dry films of **1** at the graphite-air interface and their subsequent *in-situ* UV irradiation, it was possible to verify that the switching occurs in such conditions also to the molecules physisorbed on the solid substrate. We believe that the present results could be of great value for further research on multiphotochromic systems, and could clarify the role of non-covalent interactions in the supramolecular self-assembly of similar systems. In view of their intrinsic molecular geometry and rigidity, we envision that the azobenzene-based compounds presented here could be employed in the future as building blocks of photo-responsive materials for various applications such as light-triggered host-guest systems, or optically-responsive metal-organic frameworks.

Chapter 5.

TETRA(DITHIENYLETHENE) PORPHYRIN SCAFFOLDS:

Highly Contrasted Fluorescence Switching[5]

The work described within the present section is centred on novel multi diarylethene-containing systems. The derivatives presented here are based on a dyad architecture containing a fluorescent porphyrin core and four equivalent diarylethene, and specifically perfluorocyclopentene-bridged dithienylethene photoswitches on its periphery. Such a system was conceived to exploit the central porphyrin unit both as a symmetrical scaffold for the photochromes and for its appealing photophysical properties (*e.g.* fluorescence). The dithienylethene (DTE) units employed are connected at the *meta*-position of a tetraphenylporphyrin core: such a connectivity pattern has been chosen not only to prevent the formation of atropoisomers, but most importantly to electronically decouple the switches in order to retain their photoreactivity. Four tetra(dithienylethene)-substituted porphyrins were studied, being the free base, and the Zn(II), Ni(II) and Co(II) complexes. The effective and reversible photochemical conversion of the four derivatives was studied by UV-Vis absorption spectroscopy and ^{1}H-NMR. Interestingly, the free base and the zinc complex having all the DTE units in the open form display analogous photophysical properties to their non-photochromic analogues free base- and zinc tetraphenylporphyrin. Conversely, UV-triggered photochemical conversion of the DTE units to their corresponding closed isomer(s) results in almost complete quenching of the original emission. The luminescence showed to be reversibly on- and off-switched over several irradiation cycles both in solution and in dye-doped polystyrene thin films, allowing us to demonstrate that such compounds could be used as photo-rewritable fluorescent dyes. The high contrast obtained in the fluorescence modulation is due to the presence of a high amount (*i.e.* four) of photoswitches around the emissive core.

1. INTRODUCTION

As previously mentioned throughout this thesis, the development of stimuli-responsive molecular systems is still an extremely active area of research, aimed at *e.g.* the realisation of smart or adaptive materials, with the ultimate goal of studying and/or imitating the complex

[5] Large parts of the work displayed within this chapter have been published: Biellmann, T.; Galanti, A.; Boixel, J.; Wytko, J. A.; Guerchais, V.; Samorì, P.; Weiss, J. Fluorescence Commutation and Surface Photopatterning with Porphyrin Tetradithienylethene Switches. *Chem. Eur. J.* **2018,** *24* (7), 1631-1639.

processes occurring in natural systems. Photonic inputs represent the focus of our attention, thanks to the possibility of applying them remotely, with high spatiotemporal resolution. Among the vast class of photochromic molecules able to undergo a reversible isomerisation between at least two states with photons of different wavelength, diarylethenes represent an important category for several reasons, and most importantly they feature a thermal stability of both the forms accessible with light stimuli. Such an interesting characteristic makes such photoswitches particularly promising for their application in the field of optical memories,[2, 55, 59] since the information written with a light stimulus can be retained following the stability of the two diarylethene isomers towards thermal reactions occurring in the dark. The term "diarylethene" is a general definition for stilbene derivatives, valid for all systems comprising two (hetero)aromatic rings bridged by an ethylene moiety. In general, it is useful to replace the ethylene unit with a cyclic cyclopentene or cyclohexene moiety to avoid the $E \rightarrow Z$ isomerisation of the central double bond, which would hamper the desired photocyclisation reaction. Moreover, concerning the two aromatic rings, substitution with heteroaromatic five-membered rings with low stabilisation energy (such as furan or thiophene) generally allows the photochemical reaction to be reversible, and the two isomers to be thermally stable.[60] From now on we will therefore refer to these compounds as dithienylethene (DTE) photochromes. The most important difference between the open (o-DTE) and the closed (c-DTE) form concerns their conjugation: in case of the open-ring structure, conjugation is localised on the heteroaromatic rings, while in the closed isomer π-conjugation delocalises electrons over the whole backbone of the molecule, resulting in a lower HOMO-LUMO gap compared to its open counterpart. These changes, together with the shift in energy of the ground and excited states of the two isomers, are responsible for the resulting shift of their photophysical and redox properties. High interest that has been devoted in the last two decades towards the development of highly efficient and fatigue-resistant switches towards their applications in opto-electronic devices,[2, 17, 74] smart materials,[75] optically-driven gelators,[212] or also for gating chemical reactions.[20, 76] Above all it has been widely employed to modulate the light emission of luminophores connected to the photochromic switch.[59] The latter strategy opened the doors to the application of DTEs in in highly attractive research fields such as all-optical information storage[81] and superresolution optical microscopy.[82]

As already discussed throughout this thesis, the development of multi-photochromic systems represents an extremely appealing goal from both the fundamental research and the applicative point of view. The realisation of multiphotochromic molecular systems is however a challenging task, as usually this leads to inhibition of the photochemical reaction(s) on all, or part of the switchable moieties residing within the same molecular scaffold. We already discussed on how multi-photochromic systems are sensitive and electronic delocalisation in π-conjugated system, being the presence of the latter detrimental to the desired photoisomerisation reaction. This is particularly delicate for systems containing multiple diarylethene (DTE) units,[96] as complete closure is usually inhibited by the occurrence of intramolecular energy transfer between o-DTE and c-DTE fragments, thus preventing full conversion to all-closed state.[91] Indeed, the choice of a suitable bridging unit between the switches is key towards the realisation of systems showing suitably large conversions.[97] Photochromism is generally prevented when the switches are embedded into a large π-conjugated system, following the emergence of low-lying excited state manifolds which usually do not lead to the photoreaction pathway. Multi-DTE systems have been extensively

investigated,[91a] by examining the role of bridges of various nature, including for instance alkynyl,[98] arenyl,[97] or silyl[99] moieties and metal complexes[100] as spacers. In contrast, porphyrins have been seldom used as scaffolds for systems containing multiple DTE units, despite multi-azobenzene systems have been realised with this strategy, not always leading to promising photoresponse.[213] Thus far, two examples of multi-DTE porphyrin-related compounds were reported, being a Sn(IV) porphyrin having two phenoxide-DTE moieties coordinated in axial positions,[214] and a tetraazaporphyrin derivative incorporated across the beta-positions of the four pyrrole moieties.[119]

As previously mentioned, attaining optically-triggered modulation of the luminescence of a molecule or metal complex in a reversible fashion is extremely appealing for their application as all-optical memory elements, or as photoswitchable probes in superresolution microscopy. This is generally performed by coupling luminophores with diarylethenes: the emission quenching of the former could be obtained by either Förster resonance energy transfer (FRET), or photo-induced electron transfer. Modulation of the absorption properties or the oxidation/reduction potentials of the diarylethene unit upon its isomerisation are the cause for the emission switching.[116] For such application, high contrast between the ON- and OFF-states, reversibility and cyclability are factors of crucial importance. Achieving high contrast in the modulation of the emission of a luminophore is generally complicated by two main factors: non-quantitative conversion of the photochromic unit(s) upon achieving the photostationary state (PSS), and low (or generally below unit) quantum efficiency of the luminescence quenching process. These two drawbacks could be overcome with a conceptually simple strategy: increasing the amount of switchable (quencher) units surrounding the luminophore.

We have thus decided to follow such strategy, nevertheless relying on the combination of DTEs with porphyrins. By joining these two functional units, it has been already shown possible to modulate photoinduced intra- or intermolecular electron-,[79] energy-transfer,[215] or singlet oxygen generation,[80] for instance. Free-base porphyrin derivatives, together with some of their metal complexes (*e.g.* Zn(II)) present interesting photophysical properties,[216] and emit (mostly) by means of fluorescence in the red part of the visible light spectrum (~ 550 - 750 nm). In such region, the open isomer of DTE does not absorb light. In addition, porphyrin emission could be achieved by excitation on its Q-bands, in the red part of the visible spectrum (520 – 650 nm), but also at higher energy on the Soret band (~ 420 nm), in a region where none of the DTE isomers absorb light. Thus, it follows that the fluorescence readout could be performed at a wavelength not altering the state of the DTEs. Most importantly, the emission of free base and Zn(II) porphyrins occurs in the region of the visible spectrum where the ring-closed form of DTE absorbs light. Following such spectral overlap, it is simple to understand how the latter could work as efficient quencher for the emission of the aforementioned dye. Moreover, in light of the possibility to excite the porphyrin on the Soret band, hence at a largely different wavelength in comparison to their emission, they allow to detect the emitted light avoiding scattering from the excitation light, thus opening the door towards their application as “rewritable fluorescent photoinks.”

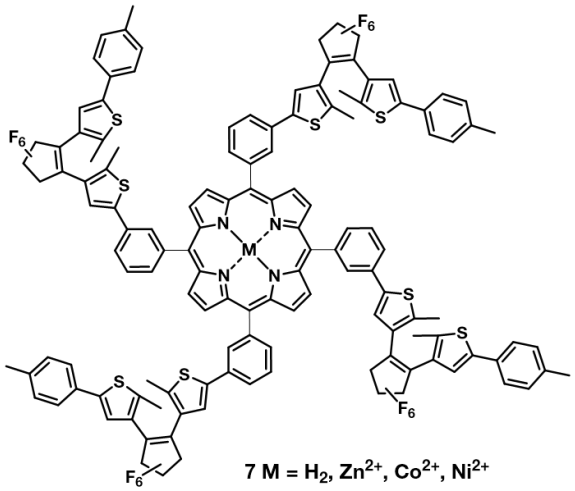

Figure 69. Structure formula of the tetra-DTE porphyrin **7** developed and synthesised by the group of Prof. J. Weiss, and used within the present study.

With these premises, we worked in collaboration with the group of Prof. J. Weiss to characterise a novel derivative of tetraphenylporphyrin containing four DTE residues **7** (Figure 69). Such molecules were developed and synthesised by the group of Prof. J. Weiss, in particular by Dr. T. Biellmann and Dr. J. Wytko with the purpose of obtaining phototunable fluorescent compounds characterised by highly contrasted emission properties. The central tetraphenylporphyrin residue was used as symmetrical framework to support four DTE units: four derivatives were synthesised, *i.e.* the free base **7H$_2$**, and the metal complexes with Zn(II), Ni(II) and Co(II), named respectively **7Zn**, **7Ni** and **7Co**, being **7H$_2$**, **7Zn** and **7Ni** characterised here. The DTE units employed in **7** are connected at the *meta*-position of a tetraphenylporphyrin core: such a connectivity pattern has been chosen not only to prevent the formation of atropoisomers, but most importantly to electronically decouple the switches in order to retain their photoreactivity. The photochromic behaviour of **7H$_2$**, **7Zn** and **7Ni** has been characterised by means of ^{1}H-NMR spectroscopy and UV-Vis absorption spectroscopy, while unfortunately it was not possible to separate and characterise further the photogenerated isomer mixture by means of HPLC.

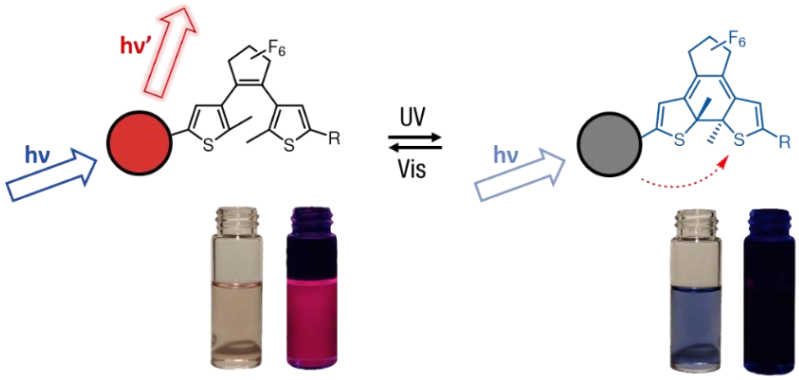

Figure 70. Simplified scheme of the emission quenching by energy transfer to the closed DTE isomer. *Left*, open-DTE: fluorescence ON. *Right*, closed-DTE: fluorescence OFF.

Notably, the free base and zinc derivatives **7H$_2$** and **7Zn** showed effective light-triggered commutation of their luminescence in solution, and also when dispersed in amorphous polymeric matrix and deposited as thin film on surfaces. Quenching of the original fluorescence emission intensity occurred by inducing the ring-closure reaction on the DTE units upon

ultraviolet (λ ≈ 312 nm) irradiation, situation which was reversed to the initial conditions by visible (490 ≤ λ ≤ 570 nm) light irradiation. Occurrence of such reversible behaviour also on the solid-supported samples allowed us to record fluorescent patterns by *in-situ* structured illumination, thus showing that the compounds studied here could be employed as photoactivable fluorescent inks.

2. METHODS

2.1. Photochemical and photophysical characterisation

All the experiments in solution have been performed using air-equilibrated spectroscopy grade CH_2Cl_2 (Merck Millipore, Uvasol). UV-Vis absorption spectra were recorded at room temperature with a Jasco V-650 spectrophotometer, in matched quartz Suprasil cuvettes (Hellma), with 1.0 cm optical path length. Photoisomerisation studies were performed with a Herolab UV 6ML 312 nm lamp, at an incident power density $P_d \approx 3.0$ mW cm^{-2} for DTE electrocyclisation reaction. Visible light irradiation was carried out using an Edmund Optics illuminator equipped with a 150 W halogen lamp and a green filter (λ_{max} = 530 nm, FWHM = 80 nm) at an incident power density $P_{d,\ 530\ nm} \approx 57$ mW cm^{-2}, for DTE cycloreversion. During light irradiation, the solutions were always vigorously stirred.

Quantification of the amount of photogenerated c-DTE isomer upon irradiation at the UV photostationary state was performed by the group of Prof. V. Guerchais (Université de Rennes I) by means of ^{1}H-NMR (300 MHz) in CD_2Cl_2. Irradiation for ^{1}H-NMR experiments was performed using a Rayonet® equipped with 300 nm lamps.

All the photophysical studies concerning the (fluorescence) emission of **7H₂** and **7Zn** were performed in air-equilibrated spectroscopy-grade CH_2Cl_2, using 1 cm or 3 mm optical path length Suprasil cuvettes (Hellma). The shorter optical path ones were specifically used to measure emission spectral features in regions where strong reabsorption occurred (*i.e.* small Stokes shift), in order to avoid distortion of the emission spectra (*e.g.* for monitoring $S_0 \leftarrow S_2$ emission of **7Zn**). Fluorescence spectra of $S_0 \leftarrow S_1$ transition for **7H₂** and **7Zn** during the photoswitching cycles were recorded upon excitation at one isosbestic point of their spectral variation (*i.e.* 429 and 430 nm for **7H₂** and **7Zn**, respectively), in order to exclude variations of light absorbed. Except for time-resolved emission measurements, concentration was kept low (c ≈ 5 x 10^{-7} M) in order to maintain the absorbance at the excitation wavelength below 0.1, thus avoiding reabsorption of the emitted light. Emission spectra were recorded on an Agilent Cary Eclipse and a Horiba Jobin Yvon Fluorolog FL3-22 fluorometers. Time-resolved measurements to determine the excited state lifetime of **7H₂** and **7Zn** were performed by time correlated single photon counting (TCSPC) with the aforementioned Horiba FL3-22 equipped with a FluoroHub

A+ TCSPC controller and a PPD picosecond single photon counting detector. Excitation was performed using NanoLED LED light sources (pulse width ≤ 1.3 ns), using λ_{exc} = 590 nm for **7H₂** and λ_{exc} = 560 nm for **7Zn**. Following the short lifetime of **7Zn** excited state, the excitation pulse was deconvoluted by measuring the instrument response function using a scattering dispersion of colloidal silica (Ludox, Sigma Aldrich) in water. Quantum yield measurements were performed for the $S_0 \leftarrow S_1$ deactivation of **7H₂** and **7Zn** by means of fluorescence, by comparison with a standard fluorophore with known quantum yield. On this purpose, free base tetraphenylporphyrin (H_2TPP, Sigma Aldrich) in toluene was used as standard (Φ_R = 0.10).[151] The measurements were performed in the dark, all-open-DTE form, and in the UV PSS, to compare emission intensity in the two states, upon excitation at the isosbestic points. Concentration was kept low enough to have $A_{\lambda exc} < 0.05$.

2.2. Deposition of 7H₂-polystyrene thin films

The experiments on the films deposited on solid were performed with **7H₂**. The compound was blended with high-molecular weight polystyrene (PS, average: 500 kDa, low polydispersity, standard for GPC, Sigma Aldrich) in 8 % w/w ratio. Solutions were made in $CHCl_3$, c = 3.0 mg/mL (PS) and spin-casted on glass microscope cover slides. The substrates were washed prior to film deposition by rinsing with acetone, isopropanol and ethanol and blown dry under a stream of nitrogen, without any further surface treatment. The deposited films showed a uniform coverage and an average thickness of ca. 20 nm, characterised by optical microscopy and surface profilometry. UV-Vis absorption spectra of the glass-supported films were measured in transmission configuration on a Jasco V-650 with a solid sample holder, while the emission spectra were recorded on an Agilent Cary Eclipse fluorometer with a movable solid sample holder accessory, in right-angle excitation geometry.

2.3. Patterning and imaging of 7H₂-PS thin films

Patterning and imaging on the fluorescent films of **7H₂** was performed by confocal laser scanning microscopy. The measurements were performed on a Zeiss LSM 710 confocal microscope system with a 10x magnification objective, with the help of Dr. Alessandro Aliprandi, whom is greatly acknowledged. Imaging was performed upon exciting the samples with a continuous wave laser at λ_{exc} = 405 nm, 1.7 s per frame, 0.3 % power. Emission of the assemblies was monitored in the λ_{em} = 414 - 721 nm range, using the lambda-mode option. The raw data recorded by means of the lambda-mode were processed using a linear unmixing tool option available in the ZEN 2011 software package (Zeiss GmbH). In order to record positive and negative fluorescent patterns, structured illumination was accomplished using different laser sources. For ultraviolet irradiation, a UV continuous wave (CW) laser was used (λ = 355 nm), by scanning on the frame for 20 s. For visible irradiation, we could not accomplish the experiments with a green laser due

to instrumental limitations, but the same laser used for excitation (λ = 405nm CW laser) showed to be effective as Vis light source for switching the DTE derivatives, thus we used higher power (30%), while scanning for a longer period on the same frame (30 s).

3. RESULTS AND DISCUSSION

3.1. Synthesis

The compounds **7H$_2$**, **7Zn** and **7Ni** described within the present chapter were synthesised by Dr. T. Biellmann in the group of Prof. J. Weiss (Université de Strasbourg). Their detailed synthesis is described elsewhere,[95b] however a brief schematic picture of the synthetic methodology used to obtain the compounds will be given here, for illustrative purposes (Scheme 7). The free-base target compound **7H$_2$** was obtained by Lewis acid-catalysed condensation of the aldehyde **7.a** with pyrrole and subsequent oxidation with *p*-chloranil, as this is a standard route for obtaining symmetrical tetra-substituted porphyrins.[217] The unsymmetrically substituted, aldehyde-terminated DTE derivative **7.a** was synthesised from the 4-bromothiophene derivative **7.c** bearing a protected aldehyde and the perfluorocyclopentene derivative **7.b**, followed by deprotection of the aldehyde under acidic conditions. The tolyl-substituent at the other end of the DTE arms was chosen in order to ease the characterisation of the photochromism of **7** by means of ^{1}H-NMR. The metalloporphyrin derivatives **7Zn** and **7Ni** were prepared by reacting **7H$_2$** with the corresponding metal salt: Zn(OAc)$_2$ and Ni(acac)$_2$, respectively.

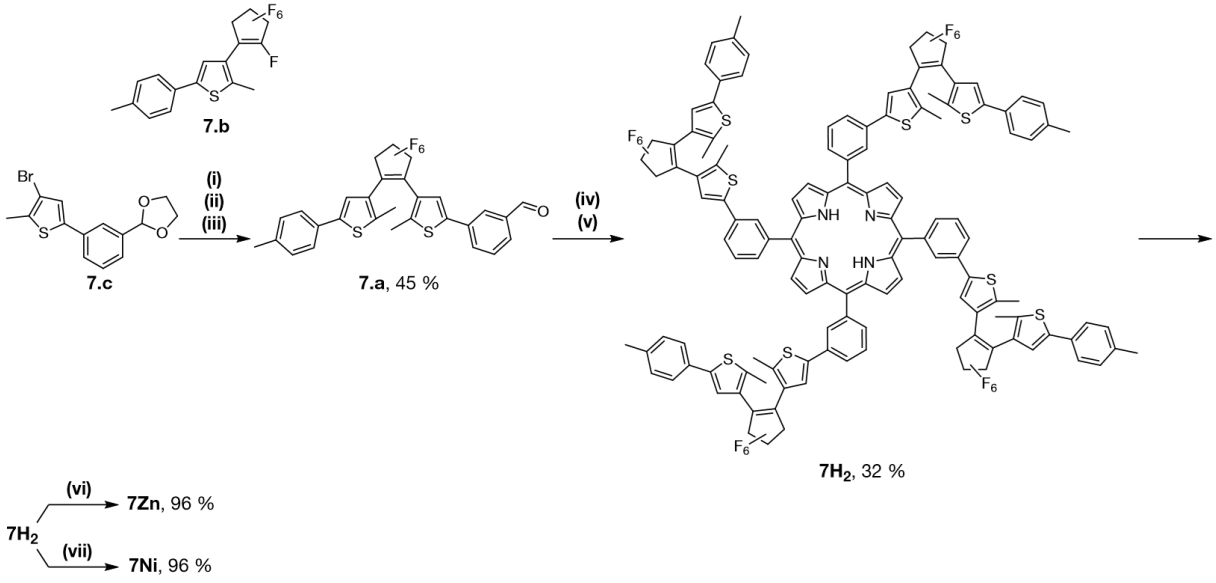

Scheme 7. Synthesis scheme of **7**. Reagents and conditions: (i) nBuLi, -78 °C, THF; (ii) **7.b**, -78 °C → R.T.; (iii) HCl; (iv) pyrrole, BF_3, R.T., CH_2Cl_2; (v) p-chloranil; (vi) $Zn(OAc)_2$, R.T., $CHCl_3$; (vii) $Ni(acac)_2$, chlorobenzene, reflux. Adapted from:[95b]

3.2. Characterisation by ^{1}H-NMR

The ^{1}H-NMR experiments have been performed in the group of Prof. V. Guerchais (Université de Rennes I) by Dr. T. Biellmann and Dr. J. Boixel, whom are greatly acknowledged. The measurements for **7H$_2$**, **7Zn** and **7Ni** without light irradiation enlightened the presence of a single peak for the beta-pyrrolic protons located at ca. 9 ppm, thus confirming the symmetry of the molecules. Typically, the (dark) ^{1}H-NMR spectrum of **7H$_2$** shows two singlets located at ca. 7.46 and 7.18 ppm, assigned to the magnetically non-equivalent protons on the thienyl units present in the four DTE fragments residing in the open form (Figure 71), whereas the protons of the methyl groups (of the DTE moieties) appear as one broad signal at ca. 1.95 ppm (Figure 72). The ^{1}H-NMR spectra of the metal complexes **7Zn** and **7Ni** display similar features (Figure 73 and Figure 74, respectively).

The photochemical conversion of the DTE moieties in **7** was monitored by ^{1}H-NMR, in order to quantify the amount of ring-closed isomer present at the PSS upon UV irradiation. Attempts of monitoring the reaction by isolating the single isomers in the mixture were also performed here by means of HPLC, nevertheless failing in resolving the mixture. Therefore, the quantity given here for the conversion to the closed isomer will most likely account for the mixture of different partially-closed-DTE isomers (*e.g.* o,o,o,c,; o,o,c,c, o,c,o,c; o,c,c,c; c,c,c,c) in which one, two, three or four DTE units are photocyclised. Upon irradiation of a CD_2Cl_2 solution of **7H$_2$** at 300 nm, the ^{1}H NMR spectrum shows the characteristic upfield-shifted signals of the two thienyl protons of the closed DTEs at δ 6.85 and 6.65 ppm (Figure 71a), whereas the magnetically non-equivalent methyl protons appear as two singlets shifted downfield, at δ 2.36 and 2.23 ppm, compared to the methyl proton of the open DTEs (Figure 72). The signals of the open-DTE units are still present at the PSS, but it is not possible to discriminate between those of the initial fully open species (*e.g.* when all four DTE units on **7** are in the open-state) and the photo-generated open-closed derivatives. Moreover, a new low field singlet at δ 8.85 ppm is attributed to the β-pyrrolic protons of the photocyclised species.

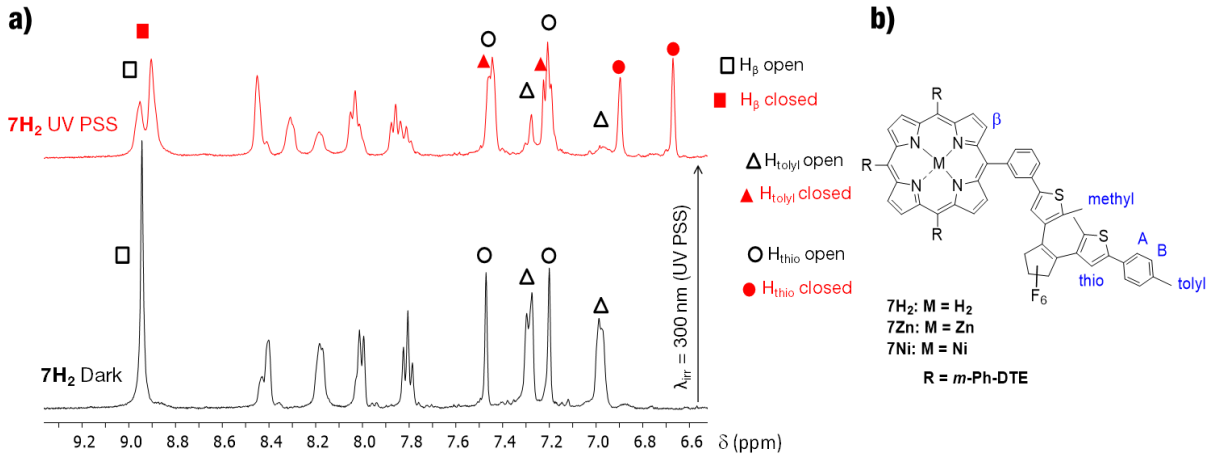

Figure 71. a) ^{1}H-NMR spectra for the aromatic region of **7H$_2$** (300 MHz, CD_2Cl_2). *Black trace* dark, no irradiation (all-open DTE isomer). *Red trace*, UV PSS, irradiation at λ = 300 nm. b) Molecular structure indicating the protons responsible for the signals used for ^{1}H-NMR characterisation. Adapted from:[95b]

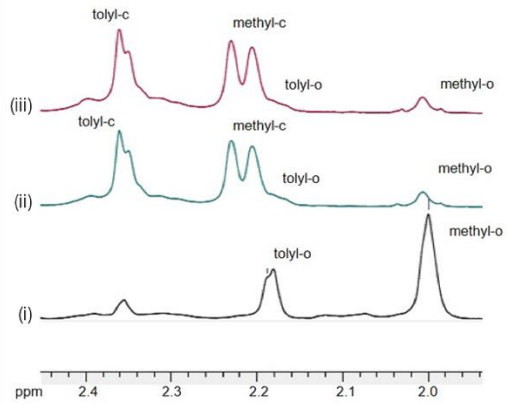

Figure 72. ^{1}H-NMR spectra for the aliphatic region of **7H$_2$** (300 MHz, CD_2Cl_2). (i) No irradiation, (ii) 5 min. irradiation, (iii) UV PSS, irradiation at λ = 300 nm. Signals are labelled as indicated in Figure 71b. Adapted from:[95b]

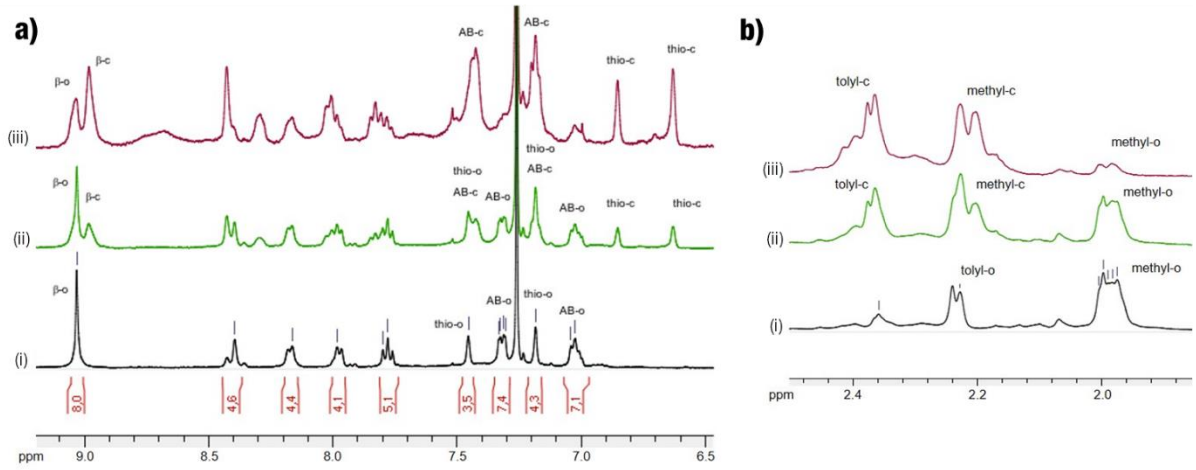

Figure 73. a) ^{1}H-NMR spectra for the aromatic region of **7Zn** (300 MHz, CD_2Cl_2). b) ^{1}H-NMR spectra for the aliphatic region of **7Zn**. (i) No irradiation, (ii) 5 min. irradiation, (iii) UV PSS, irradiation at λ = 300 nm. Signals are labelled as indicated in Figure 71b. Adapted from:[95b]

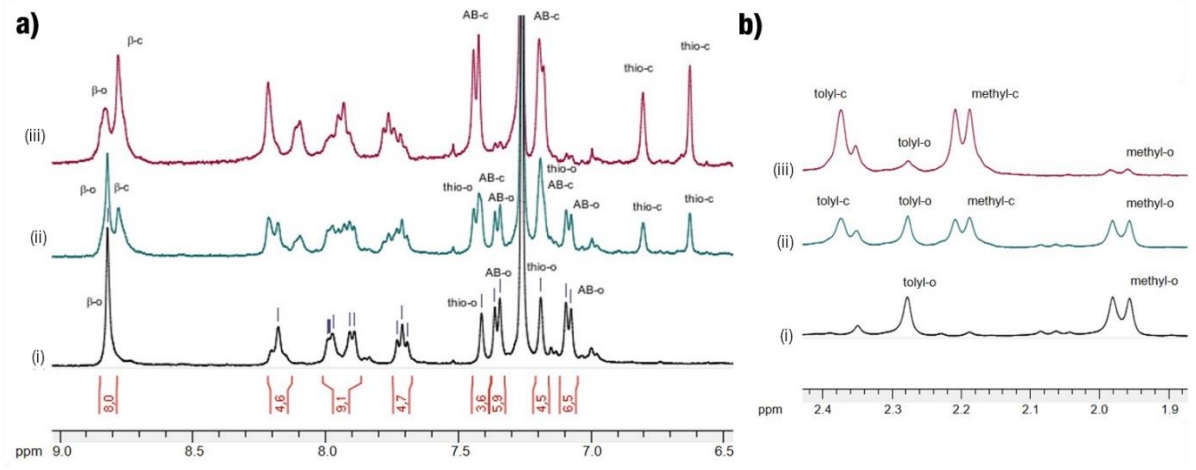

Figure 74. a) ^{1}H-NMR spectra for the aromatic region of **7Ni** (300 MHz, CD_2Cl_2). b) ^{1}H-NMR spectra for the aliphatic region of **7Ni**. (i) No irradiation, (ii) 5 min. irradiation, (iii) UV PSS, irradiation at λ = 300 nm. Signals are labelled as indicated in Figure 71b. Adapted from:[95b]

The percentage of ring-closing in the photostationary state was determined by ^{1}H NMR spectroscopy (in CD_2Cl_2), by calculating the ratio of the integration between the thienyl signals of the closed DTE units and that of the β-pyrrolic protons, both in the open and PSS states. The

photocyclisation conversion was estimated to be 62, 88, and 75% for compounds **7H$_2$**, **7Zn** and **7Ni** respectively (Table 6). The higher conversion rate found for the metalled species could be explained by a ring-closure via the triplet state of open-DTE units, due to intersystem crossing.[218] Notably, the efficiency at which the porphyrin-DTE scaffolds **7** photocyclise contrasts the reported inhibition of photoisomerisation in several compounds in which porphyrins and the switching unit are linked by a phenyl spacer substituted in *ortho*-, or *para* position.[151, 213a, 219] The *meta* substitution pattern in our edifices appears to limit efficiently the electronic delocalisation in the molecular framework, thus allowing DTE isomerisation to a higher extent.

3.3. Photophysical and photochemical properties

In first instance, the photophysical properties of **7H$_2$**, **7Zn** and **7Ni** without irradiation (all-open DTE) were determined in CH_2Cl_2, in order to assess their similarities with the non-DTE-containing tetraphenylporphyrin analogue (H_2TPP),[216a] and the zinc tetraphenylporphyrin (ZnTPP).[216b] The electronic absorption spectra of each tetra-DTE porphyrin array show the typical features of the two chromophores, with a broad band in the UV region attributed to the π-π^* transition localised on the open DTE fragments, in addition to the porphyrin's characteristic Soret and Q bands in the visible region (Figure 75 and Table 6). Four Q bands are observed for the free base **7H$_2$** at ca. 515, 550, 590 and 645 nm, while fewer (two or one) are visible for the metallated **7Zn** and **7Ni**, due to their fourfold symmetry.

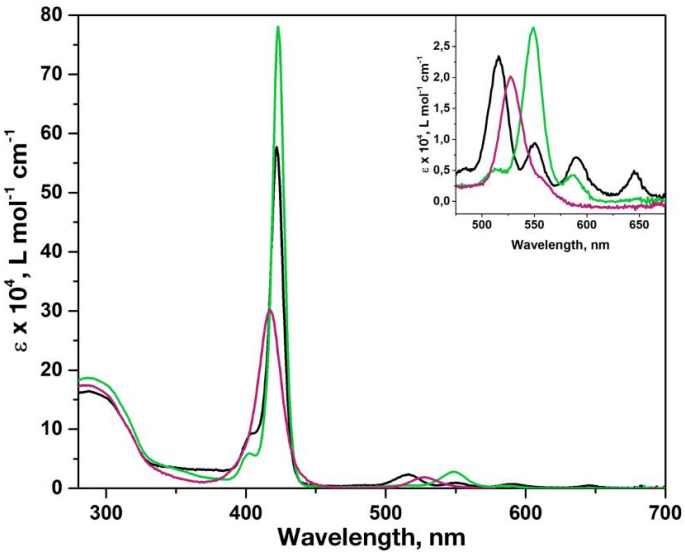

Figure 75. UV-Vis absorption spectra of **7** in CH_2Cl_2 in their all-open-DTE form, without irradiation. *Black trace*, **7H$_2$**, *green trace*, **7Zn**, *purple trace*, **7Ni**. Inset, magnification of Q-bands of **7H$_2$**, **7Zn**, **7Ni**.

The steady state emission spectra of **7** and their time-resolved decay were measured at room temperature, in air-equilibrated CH_2Cl_2. The free base **7H$_2$** and the zinc **7Zn** porphyrin derivatives showed similar features to their non-photochromic analogues H_2TPP and ZnTPP,[216] while **7Ni** is non-luminescent, as expected from closed-shell diamagnetic complexes such as NiTPP. The emission spectrum of **7H$_2$** displays two peaks, Q(0-0) and Q(0-1), respectively at 650 and 717 nm (Figure 76a, Table 6), whereas the excitation spectrum (λ_{em} = 715 nm) shows the

same features as displayed by the absorption spectrum (Figure 76b). **7H₂** displays a fluorescence quantum yield Φ_F = 7.9 ± 0.3% in CH_2Cl_2 in the open form, which is in good agreement with the homologous, non-photochromic H_2TPP, for which Φ_F = 10% in toluene.[220] The lifetime for the radiative decay of S_1 of **7H₂** in the open form displays a monoexponential decay, with τ = 8.97 ± 0.03 ns (λ_{em} = 650 nm, λ_{exc} = 590 nm, see Appendix II for TCSPC data), in agreement with literature values for H_2TPP (τ = 12 ns in benzene).[216a]

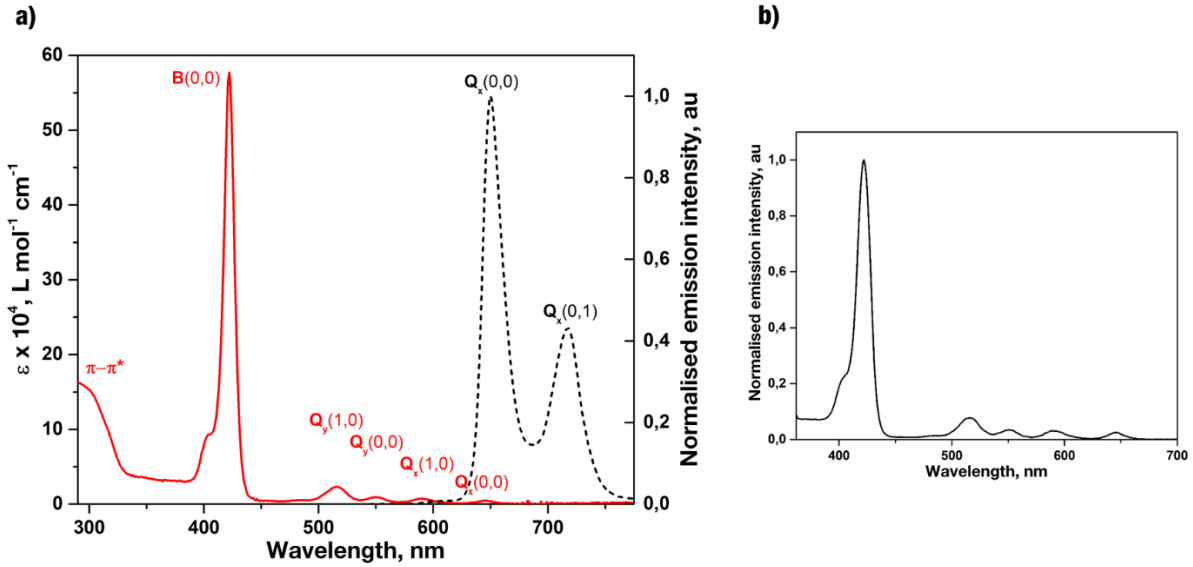

Figure 76. a) UV-Vis absorption (*full line, red*) and emission (λ_{exc} = 422 nm, *dotted line, black*) spectra of **7H₂** in air-equilibrated CH_2Cl_2, at room temperature. The transitions are indicated on the spectra (see Table 6). b) Excitation spectrum of **7H₂** (λ_{exc} = 715 nm).

Interestingly, the metallated compound **7Zn** displays also radiative deactivation from $S_0 \leftarrow S_2$, with a maximum at 426 nm, as emission by violation of Kasha's rule is a known feature for ZnTPP.[216b] In conjunction with the latter, the $S_0 \leftarrow S_1$ deactivation is the most intense feature, with two maxima at 597 and 646 nm for Q(0-0) and Q(0-1) respectively, similarly to ZnTPP (λ_{em} = 647 nm, see Figure 77a, Table 6).[216b] The same considerations made for the excitation spectrum of **7H₂** are also valid for **7Zn** (Figure 77b). In the open form, **7Zn** displays a fluorescence quantum yield Φ_F = 4.8 ± 0.2% (for the $S_0 \leftarrow S_1$ transition) in CH_2Cl_2 that is slightly higher, but still close to the homologous ZnTPP, showing Φ_F = 3.3% in toluene.[220] For **7Zn** in the open form, the lifetime of $S_0 \leftarrow S_1$ emission showed a monoexponential decay, with τ = 1.9 ± 0.1 ns (λ_{em} = 647 nm, λ_{exc} = 560 nm, see Figure A II 3), in excellent agreement with literature values for ZnTPP (τ = 2.0 ns in benzene), while the $S_0 \leftarrow S_2$ deactivation was not measured, following its short timescale (~ 1.3 ps).[221]

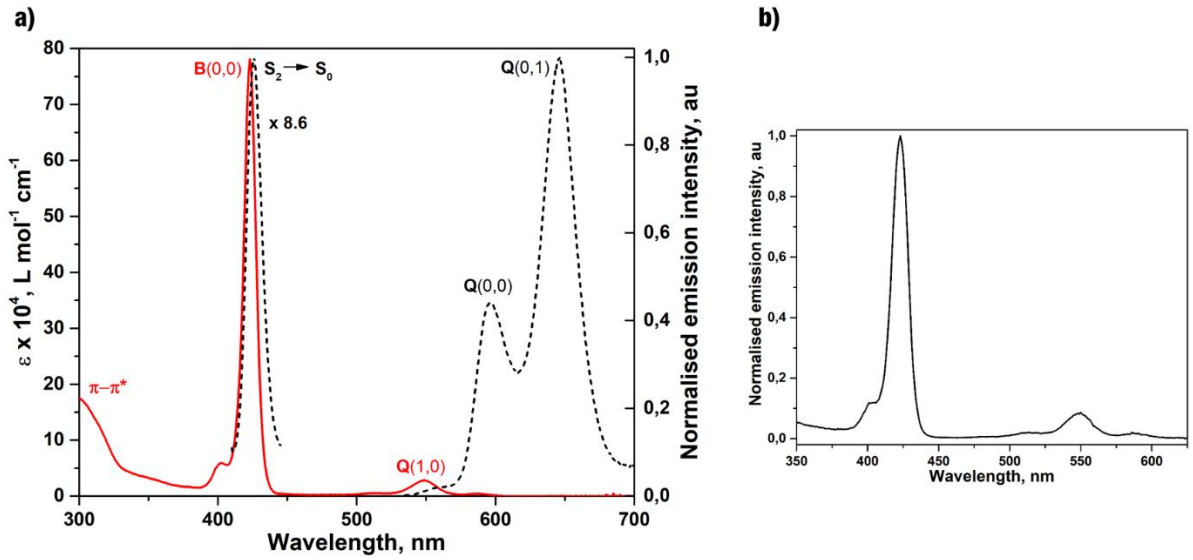

Figure 77. a) UV-Vis absorption (*full line, red*) and emission (λ_{exc} = 400 nm, *dotted line, black*) spectra of **7Zn** in air-equilibrated CH_2Cl_2, at room temperature. The transitions are indicated on the spectra (see Table 6), the $S_0 \leftarrow S_2$ deactivation is multiplied 8.6 times. b) Excitation spectrum of **7Zn** (λ_{exc} = 647 nm).

3.3.1. Photochromism and fluorescence switching in solution

Photochromism of the tetra-DTE porphyrins **7H₂**, **7Zn** and **7Ni** was followed with UV-Vis absorption spectroscopy in dichloromethane and for the emissive **7H₂**, **7Zn** the reversible fluorescence quenching was also studied by emission spectroscopy. The photophysical data of the four porphyrins in their initial open state and at the photostationary state (PSS, after irradiation at 312 nm) together with their conversions (at PSS) determined by ^{1}H NMR are summarised in Table 6. Upon irradiation of a solution of **7H₂**, a broad band appeared in the visible region (500–700 nm), which is characteristic of the formation of closed DTE units (Figure 78a, Table 6). Spectral changes were also observed in the UV part of the spectrum with a decrease of the absorption band at 290 nm and a concomitant increase of the absorption band around 360 nm. In addition, the absorption maximum of the Soret band diminished. The presence of isosbestic points through the spectral variation evidences further the (high) extent of electronic decoupling between the DTE units, as in the opposite scenario each mixed open-closed isomer (*e.g.* o,o,o,c,; o,o,c,c, o,c,o,c; o,c,c,c; c,c,c,c) would have different absorption spectra, thus not leading to the observation of such spectral features.[222] The hypochromic feature evident on the Soret band was previously observed for related mono-DTE porphyrins and tentatively attributed to an effective electronic communication through a *p*-phenyl-acetylene linker.[219b] However, in the present work, the Soret band displays a broadening which can explain an apparent hypochromism in the absence of ground state electronic interactions, we nevertheless have no further experimental evidence to explain this observation. We expect that upon performing quantum-chemical modelling on these systems it would be possible to cast further light onto

the electron delocalisation in the various isomers of the DTE units. Similarly as on **7H$_2$**, the occurrence of DTE photocyclisation is visible also on both metal complexes **7Zn** and **7Ni**, with the appearance of a broad absorption band in the visible region (Figure 80a and Figure 82a, respectively). Also in this case, the presence of clear isosbestic points and a hypochromic feature on the Soret band are evident through the reaction.

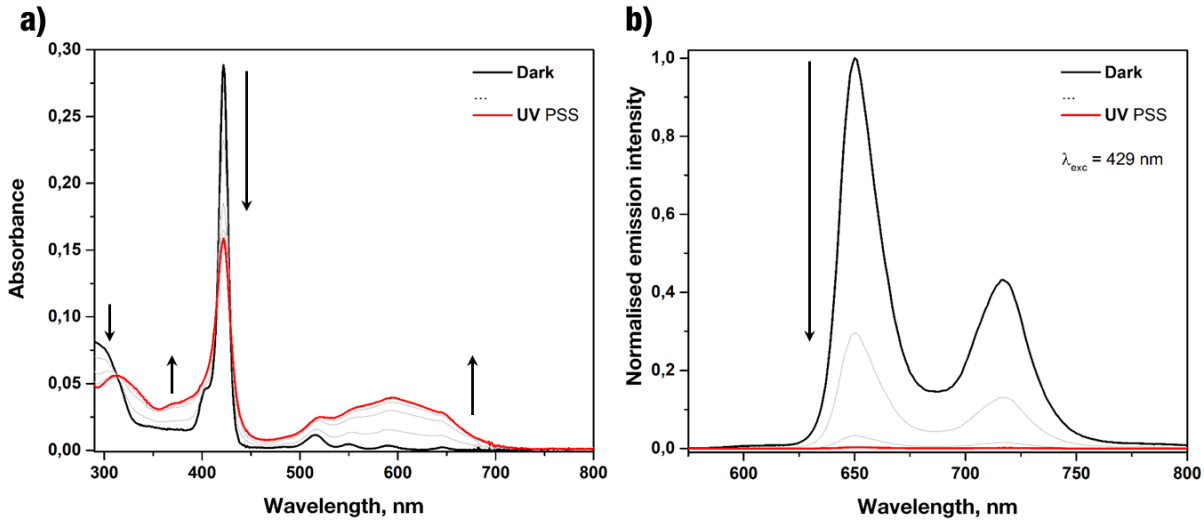

Figure 78. a) UV-Vis, and b) emission spectral variation upon irradiation of a solution of **7H$_2$** (c = 5 x 10^{-7} M, air-equilibrated CH_2Cl_2, r.t.) with UV light (λ_{irr} = 312 nm). *Black full line*, dark – no light irradiation; *red full line*, photostationary state reached upon 60 s irradiation (P_d = 3.0 mW cm^{-2}). For emission spectra, excitation was performed at the isosbestic point (λ_{exc} = 429 nm).

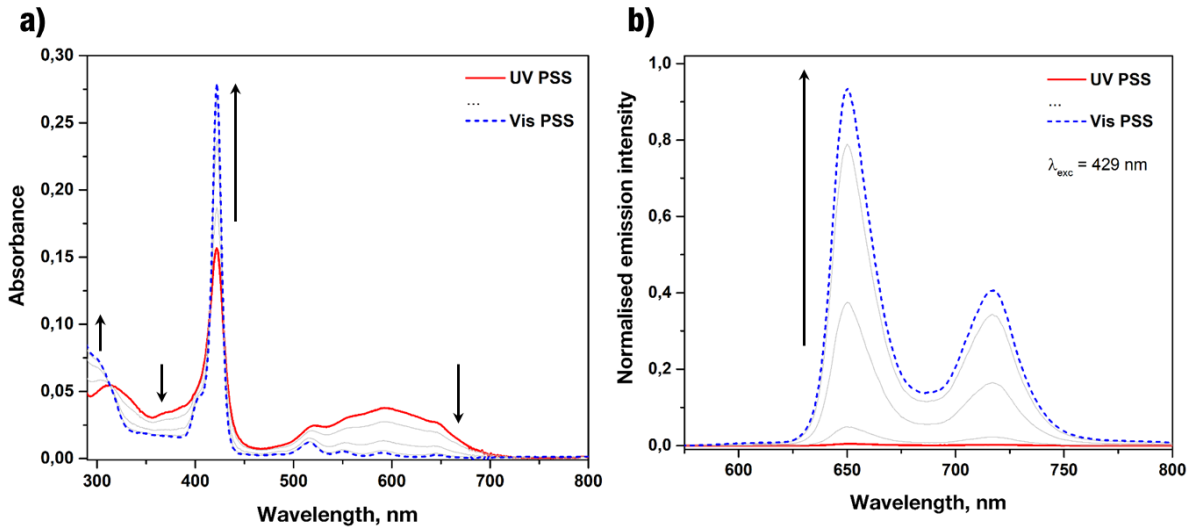

Figure 79. a) UV-Vis, and b) emission spectral variation upon irradiation of a solution of **7H$_2$** (c = 5 x 10^{-7} M, air-equilibrated CH_2Cl_2, r.t.) with Vis light (λ_{irr} = 530 nm). *Red full line*, UV photostationary state; *blue dashed line*, photostationary state reached upon 60 s irradiation (P_d = 57 mW cm^{-2}). For emission spectra, excitation was performed at the isosbestic point (λ_{exc} = 429 nm).

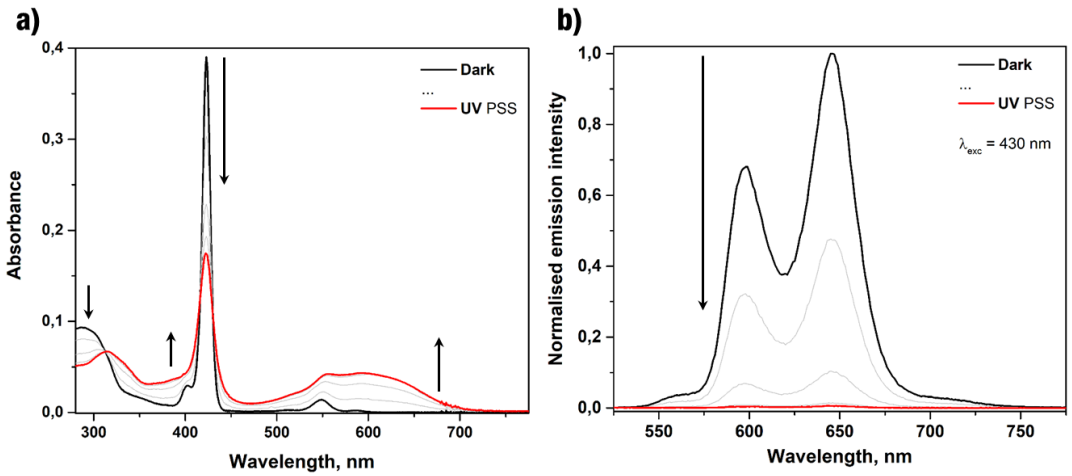

Figure 80. a) UV-Vis, and b) emission spectral variation upon irradiation of a solution of **7Zn** (c = 5 x 10^{-7} M, air-equilibrated CH_2Cl_2, r.t.) with UV light (λ_{irr} = 312 nm). *Black full line*, dark – no light irradiation; *red full line*, photostationary state reached upon 60 s irradiation (P_d = 3.0 mW cm^{-2}). For emission spectra, excitation was performed at the isosbestic point (λ_{exc} = 430 nm).

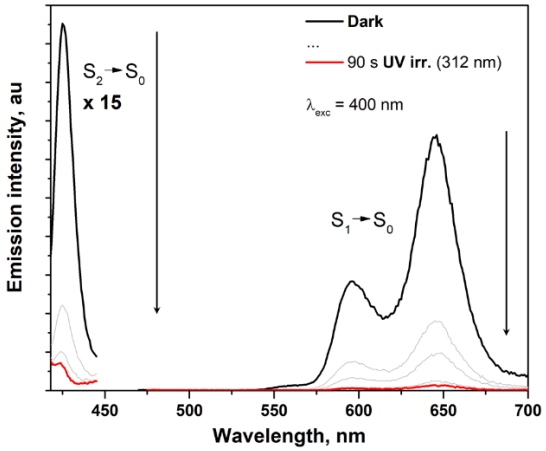

Figure 81. Emission spectral variation upon irradiation of a solution of **7Zn** (c = 1.0 x 10^{-6} M, air-equilibrated CH_2Cl_2, r.t.) with UV light (λ_{irr} = 312 nm) displaying quenching of emission from both S_2 and S_1 states upon DTE closure. *Black full line*, dark – no light irradiation; *red full line*, photostationary state reached upon 90 s irradiation. For emission spectra, λ_{exc} = 400 nm.

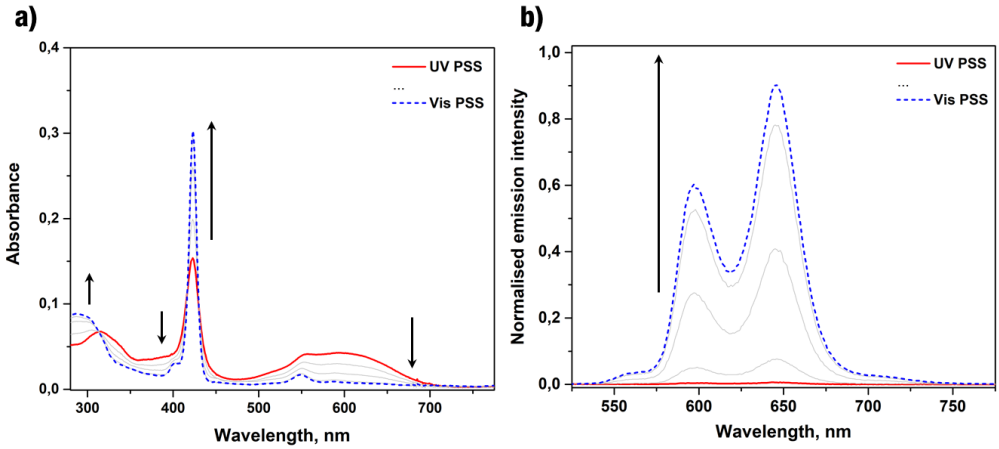

Figure 82. a) UV-Vis, and b) emission spectral variation upon irradiation of a solution of **7Zn** (c = 5 x 10^{-7} M, air-equilibrated CH_2Cl_2, r.t.) with Vis light (λ_{irr} = 530 nm). *Red full line*, UV photostationary state; *blue dashed line*, photostationary state reached upon 60 s irradiation (P_d = 57 mW cm^{-2}). For emission spectra, excitation was performed at the isosbestic point (λ_{exc} = 430 nm).

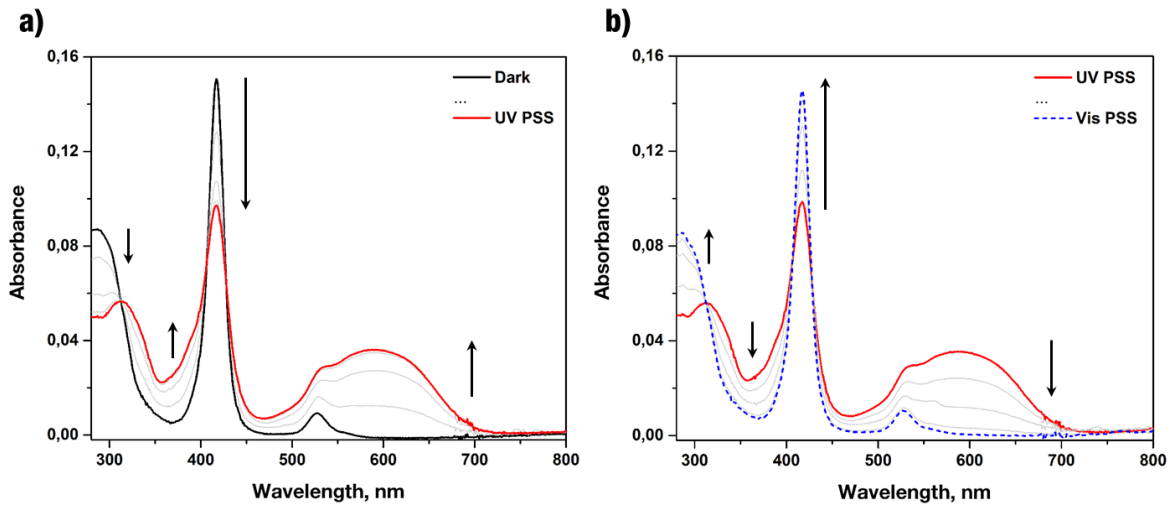

Figure 83. UV-Vis absorption spectral variation upon irradiation of a solution of **7Ni** (c = 5 x 10^{-7} M, air-equilibrated CH_2Cl_2, r.t.) with a) UV light (λ_{irr} = 312 nm) *black full line*, dark – no light irradiation; *red full line*, photostationary state reached upon 60 s irradiation (P_d = 3.0 mW cm^{-2}). b) Vis light (λ_{irr} = 530 nm). *Red full line*, UV photostationary state; *blue dashed line*, photostationary state reached upon 60 s irradiation (P_d = 57 mW cm^{-2}).

In all cases, the aforementioned photocyclisation processes are reversible. Upon irradiation with visible light (490 ≤ λ ≤ 570 nm), the original spectral features of **7H$_2$**, **7Zn** and **7Ni** are recovered, as evidenced by the disappearance of the broad band in the visible range ascribed to the c-DTE isomer(s), together with the recovery of the initial intensity of the Soret band, thus demonstrating the reversible photochromic behaviour of these compounds. However, especially for the metallated porphyrin **7Zn** only a partial recovery of the initial absorption spectrum is evident already after the first isomerisation cycle (Figure 82a). We postulate a possible degradation mechanism occurring through the triplet state, following intersystem crossing due by the heavy atom effect, nevertheless further experimental evidence is needed to confirm this observation.

As a direct consequence of the photochromism of the DTE units covalently linked to the porphyrin core, for both the fluorescent **7H$_2$** and **7Zn** a quenching of their emission was evident upon DTE closure triggered by UV light. Interestingly, the phenomenon was reversible, with the recovery of the original fluorescence upon visible (490 ≤ λ ≤ 570 nm) light irradiation, thus confirming the role of DTE units in the variation of the emission of **7H$_2$** and **7Zn**. The emission spectra (Figure 78b, 79b and Figure 80b, 82b) were recorded upon excitation of the fluorophore in non-deaerated solutions in CH_2Cl_2 at one isosbestic point of the absorption spectra (429 and 430 nm for **7H$_2$** and **7Zn**, respectively) to rule out any variation of the emission spectra due to a change in the absorption of the excitation light upon DTE isomerisation. Nevertheless, experiments performed at different excitation wavelengths showed the same phenomenon. Quenching of the fluorescence of the emissive free base porphyrin **7H$_2$** and the metallated **7Zn** was seen upon DTE ring closure: in addition, for **7Zn**, emission from S_2 (λ_{em} = 426 nm) was efficiently quenched upon DTE closure by UV irradiation (Figure 81).

In an attempt to get further insight into the nature of the emissive species, excited state lifetime measurements were also performed upon DTE switching after UV irradiation. Upon partial switching of **7H$_2$** (short UV irradiation), the measurement showed a biexponential decay, with τ_1 = 9 ± 2 ns, and τ_2 = 7.7 ± 0.8 ns and relative amplitudes of 82% and 18%, respectively (see Figure A II 2). Upon further switching (longer UV irradiation), the signal intensity was too low

to perform meaningful measurements. From these results it seems evident that upon (short) irradiation a second species with shorter emission lifetime appears. This species could be a *partially closed*-DTE isomer that still emits light, but partial emission quenching is visible following its shorter lifetime. Upon increasing UV irradiation, the emission becomes so weak that no lifetime is measurable, which reflects a low concentration of the emissive species. Unfortunately, lifetime measurements on partially switched **7Zn** were not performed because, due to instrumental limitations, the signal was too weak (non-optimal excitation wavelength and short lifetime) to be recorded.

At the PSS, attained upon UV light (312 nm) irradiation, **7H$_2$** and **7Zn** displayed fluorescence quantum yields of Φ_F = 0.05 ± 0.01% and Φ_F = 0.04 ± 0.02%, respectively. The two results are comparable within experimental error. Here it is appropriate to state that the measurements were not performed on a single, isolated photoproduct, but most likely on a mixture of different, *partially closed*-DTE isomers. We assign the evidence of residual emission at the PSS (upon UV irradiation) to the presence of low concentrations of all-open and *partially closed* - but still emissive - isomers. This hypothesis, corroborated by the lifetime measurement on **7H$_2$** upon partial switching (see above), is consistent with the low contrast in fluorescence intensity upon DTE photoswitching for similar reported compounds containing one or two DTE units.[214, 223] Overall, both compounds provided an excellent contrast between the emission spectra of the all-open and PSS states, mainly because of the presence of multiple quenchers around the fluorophore.

Table 6. Photophysical properties of open-DTE and closed-DTE derivatives (at UV PSS) of **7H$_2$**, **7Zn** and **7Ni** together with their photocyclisation conversions.

	λ_{max} **open form** [nm] (ε x 10^{-3} [M^{-1} cm^{-1}]) [a]						λ_{max} **closed form** at PSS [nm] [b]	λ_{em} **open form** [nm] [a]			Φ_F [%] [c]		% **Closed form** at PSS [d]
	DTE	Soret (0-0)	Q_y (1-0)	Q_y (0-0)	Q_x (1-0)	Q_x (0-0)		S_2-S_0	$S_1 - S_0$ Q (0-0)	$S_1 - S_0$ Q (0-1)	**Open form**	**PSS**	
7H$_2$	290 (160)	422 (580)	516 (24)	550 (9.4)	590 (7.1)	646 (4.4)	307, 593		650	717	7.9 ± 0.3	0.05 ± 0.01	62
7Ni	285 (170)	417 (300)	527 (19)	553 (1.6)			310, 589						75
7Zn	287 (190)	423 (780)	549 (28)	586 (4.2)			311, 592	426	597	646	4.8 ± 0.2	0.04 ± 0.02	88

[a]5 x 10^{-7} M in CH_2Cl_2, 298 K; [b]PSS attained under irradiation at λ = 312 nm. [c]Φ_F fluorescence quantum yield for the $S_1 - S_0$ transition of **7H$_2$** and **7Zn** in the open form and at the PSS (irr. 312 nm) determined by comparison with standard free base tetraphenylporphyrin (H_2TPP), for which $\Phi_{F,R}$ = 0.10 in toluene.[220] [d]Determined by ^{1}H NMR.

Multiple DTE switching cycles were performed and fluorescence intensity was recorded to cast a light onto the reversibility and resistance to fatigue of **7H$_2$** and **7Zn** (Figure 84). The intensity at the maximum of the fluorescence band was recorded at each irradiation step, upon excitation at the isosbestic point, as described earlier. **7H$_2$** showed a fairly satisfying reversibility, having recovered 85% of the initial emission intensity after 10 irradiation cycles in CH_2Cl_2, whereas **7Zn,** after the same number of cycles, displayed only 40% of the initial emission intensity. The latter

is a clear indication of the lower photostability upon multiple irradiation cycles displayed by **7Zn** compared to its free base analogue: such lower photostability was already evident from UV-Vis absorption, as discussed earlier. We hypothesise that the larger degradation showed by the metallated compound could occur via its triplet state, nevertheless such mechanism is still unknown and will be the subject of future investigations.

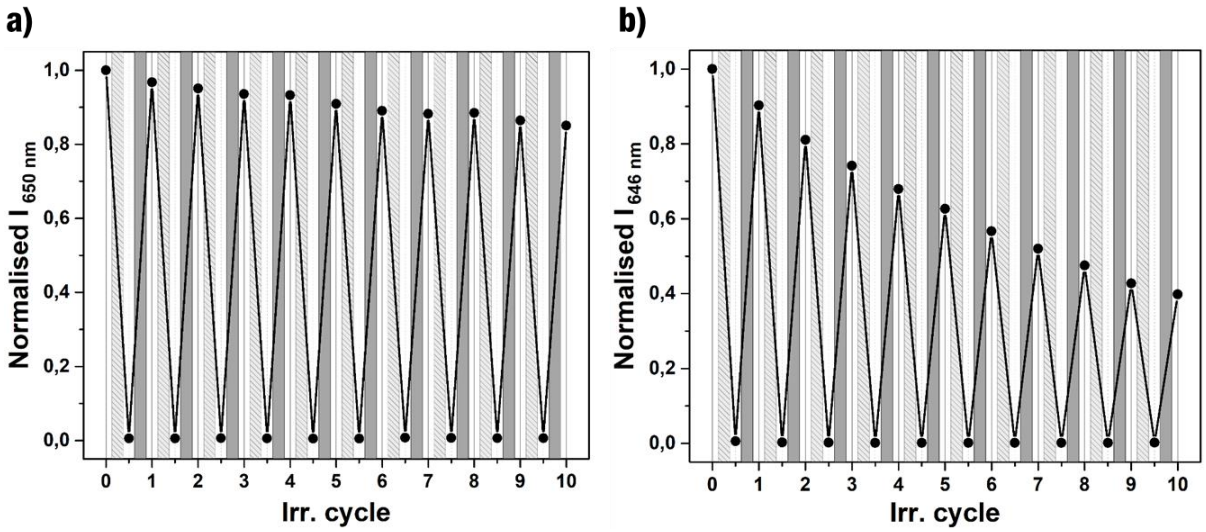

Figure 84. Variation of the emission intensity of a) $\mathbf{7H_2}$ and b) **7Zn** upon DTE repeated isomerisation by UV irradiation (*light grey area*, 312 nm; t = 40 s, P_d = 3.0 mW cm^{-2}) and subsequent ring-opening by visible irradiation (*dark grey area*, green bandpass filter λ_{max} = 530 nm, FWHM = 80 nm; t = 90 s, $P_{d\ @530\ nm}$ = 57.0 mW cm^{-2}) in CH_2Cl_2 (5.0×10^{-7} M). Emission spectra were recorded in non-degassed CH_2Cl_2 solution ($c = 5.0 \times 10^{-7}$ M) upon excitation at 429 nm for $\mathbf{7H_2}$ and 430 nm for **7Zn**; the emission intensity was taken at the maximum of the fluorescence band (650 nm for $\mathbf{7H_2}$ and 646 nm for **7Zn**).

3.3.2. Photochromism and fluorescence switching in $7H_2$ – polystyrene thin film

Following the higher reversibility showed upon repeated switching cycles on **$7H_2$**, together with its larger emission quantum yield in comparison with **7Zn**, we decided to employ the tetra-DTE free base porphyrin as a photoswitchable dye. Fluorescence switching of **$7H_2$** was also performed on thin films of a blend of **$7H_2$** (8% *w*/*w*) and polystyrene (PS, average molecular weight = 500 kDa) spin-coated on glass substrates. The film on glass displayed analogous absorption and emission features to those shown by **$7H_2$** in its fully open form in CH_2Cl_2 solution (Figure 85a). Moreover, the photochromism of DTE, together with its photoswitchable fluorescence properties were retained, as observed in the emission spectra.

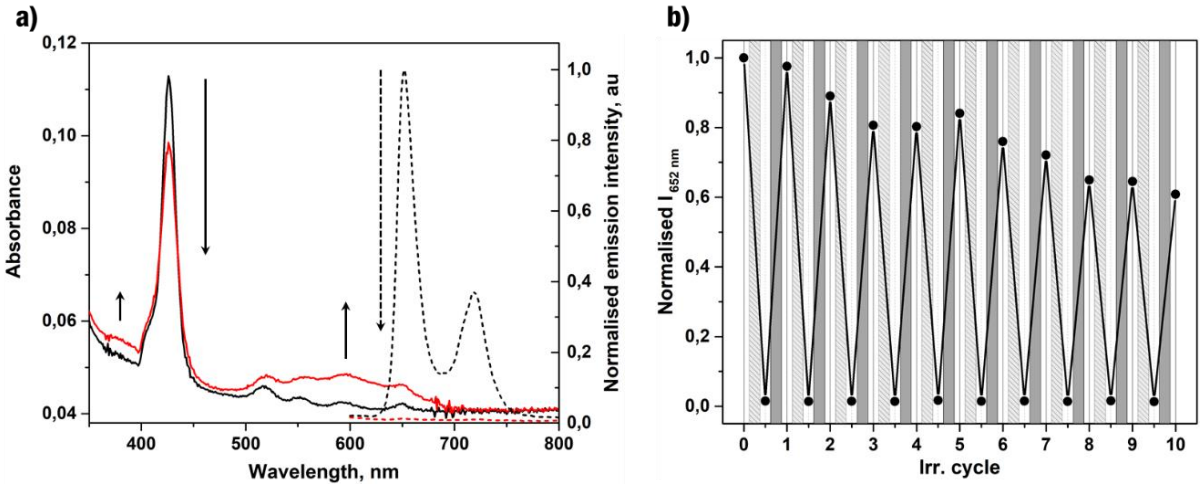

Figure 85. a) Absorption (*full line*) and emission (*dashed line*) spectral variation of **$7H_2$**-doped polystyrene film (500 kDa polystyrene, 8% *w*/*w* **$7H_2$**) spin-casted on glass upon DTE photocyclization by UV irradiation (312 nm; P_d = 3.0 mW cm^{-2}). *Black line*, pristine sample, no irradiation. *Red line*, 30 s UV irradiation. b) Variation of the emission intensity of **$7H_2$** upon alternated UV irradiation (*light grey area*, 312 nm) and visible irradiation (*dark grey area*, green bandpass filter λ_{max} = 530 nm, FWHM = 80 nm). For emission, λ_{exc} = 435 nm.

To understand the reversible nature of **$7H_2$** photochromic reaction also after its inclusion in an amorphous polymer matrix, multiple irradiation cycles were performed on a solid-supported sample. These showed the effective recovery of the initial emission intensity (Figure 85b), though a certain fatigue is evident after 10 cycles. Due to limitations of the experimental setup,[6] the data could only be used to show *qualitatively* that the photoswitching properties of **$7H_2$** were retained when the latter was dispersed into an amorphous polymer matrix and deposited as a thin film on a solid substrate. Following the success in measuring the reversible fluorescence switching in films of **$7H_2$** with PS, we investigated the use of such a blend as a photoink for rewritable fluorescence patterning of thin films on solid.

[6] In the experimental set-up used, emission on thin films was measured with a standard right-angle excitation optical scheme. Conversely, to perform quantitative measurements, the use of an integrating sphere would be necessary. For details, see Ref.[224]

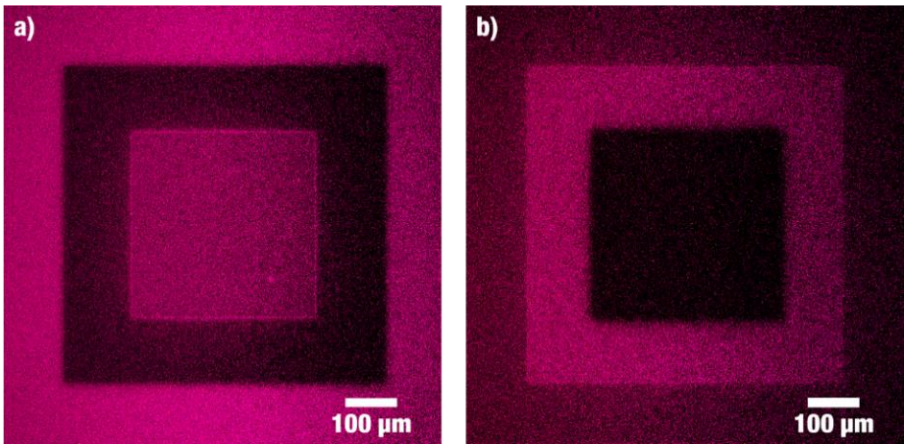

Figure 86. Confocal laser scanning microscope images taken on **7H$_2$**-doped polystyrene film (500 kDa polystyrene, 8% *w*/*w* **7H$_2$**) spin-casted on glass. The film was selectively patterned upon subsequent UV or visible laser irradiation by scanning on three square-shaped areas and progressively decreasing the scan size. a) Vis light (405 nm laser, 3% power, 30 s), UV light (355 nm laser, 20 s) and Vis light. b) UV light, visible light and UV light. Imaging was performed upon excitation of **7H$_2$** at λ_{exc} = 405 nm (0.5% power, 1.7 s per frame), collecting emission 414 ≤ λ_{em} ≤ 721 nm light.

After deposition of the blend described earlier, positive and negative fluorescent patterns were recorded by structured illumination using a confocal laser scanning microscope (Figure 86). The reversible photoactivated luminescence quenching was exploited to record multiple patterns, by scanning with a UV laser (355 nm, 20 s scan) to trigger DTE ring-closure, therefore turning off the emission (dark areas, Figure 86), or with a visible laser (405 nm, 30 s scan) to trigger DTE ring-opening and to restore the original emission of the free-base porphyrin (bright areas, Figure 86). Based on the limitations of our instrumental set-up, the light source (visible laser, λ = 405 nm) employed for writing was also used for the luminescence read-out of the recorded patterns. Nevertheless, for imaging purposes, the use of lower laser power and scanning time sufficed to preserve the written information.

4. CONCLUSIONS

The efficient and reversible photoisomerisation observed in a family of novel tetra-dithienylethene-substituted porphyrins demonstrates that a high density of functional switching units can be arranged around a porphyrin framework by covalent linkage via a *meta*-phenyl spacer. The tetra-DTE-porphyrin arrays **7H$_2$** and **7Zn** displayed reversible luminescence switching properties, due to the quenching of the singlet emissive state of the luminophore by intramolecular energy transfer to the closed form of DTE. Upon DTE photoswitching, a nearly complete quenching of the porphyrin's fluorescence was attained, providing a highly contrasted readout of the switching event. In addition to their photoregulated fluorescence, the possibility to trigger the switch and detect the output at very distinct wavelengths renders these systems of interest for applications in optical devices. Moreover, the applicability of **7H$_2$** as a photo-rewritable fluorescent ink was demonstrated, opening perspectives towards its application in all-optical memory storage and fluorescence microscopy imaging.

Chapter 6.

ANISOTROPIC GOLD NANOCRYSTALS AS SCAFFOLDS FOR PHOTOCHROMIC THIOLS:

Investigation on the Photochromism of Spiropyran-Based Thiols/Plasmonic Nanoparticle Hybrid Systems

While in the previous chapter the focus was on the grafting of multiple photochromic units to a molecular scaffold with the precision of molecular chemistry, in the present chapter the endeavour is addressed to use metallic nanostructures such as plasmonic gold nanocrystals as scaffolds on which spiropyran-based photoswitches are attached. Here we are interested in the use of anisotropic gold nanoparticles, namely gold nanorods (AuNR), principally for their appealing spectroscopic properties (*e.g.* multiple localised surface plasmon resonance bands). Spiropyran photochromes, and especially nitrospiropyran derivatives, were chosen following the notably large variation of their molecular dipole moment upon isomerisation from the spiropyran (SP) form to the merocyanine (MC) isomer. Such a combination has been made in order to study the variation of the optical properties of the anisotropic nanoparticles and to verify an eventual effect on the stability of the colloidal dispersion upon isomerisation of the photochromic unit. The spectral properties of plasmonic nanoparticles are highly sensitive towards the variation of their dielectric environment, and especially the ones having anisotropic properties such as AuNR. The latter, alongside with the surface plasmon resonance band (SPR) in the visible light range ($\lambda \approx 520$ nm) common to all gold colloids, present a second SPR mode at lower energies (named longitudinal SPR, LSPR). LSPR is commonly a sharp, intense band, and its maximum wavelength can be tuned from the visible to the near-infrared range of the electromagnetic spectrum by varying the aspect ratio of the anisotropic nanoparticles. We have employed well-established literature methods to synthesise surfactant-stabilised colloidal dispersions of AuNR with different aspect ratio, which were selected on the basis of the spectral overlap of their LSPR mode with the absorption band of the open-ring MC form of our photochromic unit. This was done in order to verify the appearance of emerging properties on the hybrid system realised by coupling the LSPR feature of AuNR with the photochrome. The photoswitches used here have been grafted on the surface of AuNR by exploiting the well-established thiol chemistry. Photochromism of the hybrid systems was studied in colloidal dispersion by UV-Vis absorption spectroscopy, where no evident light driven aggregation of the colloid was evident, though clear plasmon-dependent variation of the extinction spectra was

seen occurring upon UV irradiation. In an attempt to further characterise our hybrid system and to obtain a more detailed understanding on the behaviour of the photochromic unit grafted on the plasmonic nanoparticles, we have also performed a spectroscopic study on the solid-supported particles by dark field light scattering and Raman spectroscopy.

1. INTRODUCTION

Several examples have been reported regarding the surface functionalisation of metallic nanocrystals with thiolate self-assembled monolayers bearing photochromic moieties, mainly focussing on the possibility of driving the aggregation/disgregation of clusters of nanoparticles with the use of light, attempts performed principally with azobenzene moieties and in some examples with spiropyrans.[4b, 19a, 44b, 46, 225] Most of the works reported to date however, were done on spherical nanoparticles, meanwhile only few examples were reported with gold nanorods (AuNR).[226] In a recent example found in the literature, Cao *et al.* reported on the functionalisation of AuNR with a nitrospiropyran derivative bearing a disulfide-terminated alkyl chain, nevertheless the light response showed by the material did not lead to a straightforward interpretation.[227] In an attempt to obtain a more clear comprehension of the behaviour of such peculiar system, and also to understand if any plasmon-related effects on the photoisomerisation of the surface-attached switch are present, we focussed our attention on a similar nitrospiropyran photochromic unit (Figure 87). Our main motivation for this work was therefore to use such a photochromic unit to drive the aggregation of anisotropic colloidal particles, being the presence of two axes in the nanocrystals, and the tendency to align upon their aggregation source of our main interest. Moreover, knowing the high sensitivity of the photochromism of the dye used towards its environment (*e.g.* polarity of the medium, electric field, aggregation), we were interested in exploring its properties when confined in self-assembled monolayers on the surface of AuNR.

Gold nanorods are among the most widely studied nanoparticles presenting surface plasmon resonance properties, and the main reason lies on the fact that the wavelength and intensity of their spectral features can be tuned over a wide range of the visible and near-infrared spectrum by varying their dimensions. Moreover, one among the most interesting aspects of AuNRs resides on their morphological anisotropy, which lies on the presence of two different surfaces from the point of view of their curvature radius.[228] The latter motivated us to use a photochromic derivative which is highly sensitive towards its chemical environment, thus foreseeing to obtain two different responses due to the isomerisation of the spiropyran units immobilised in the two different surfaces of the nanorods, being the apices and the longitudinal side. In such a way, a system which can be tuned from an initial *A* state, to more than one different state(s) may be seen as *multiphotochromic*.

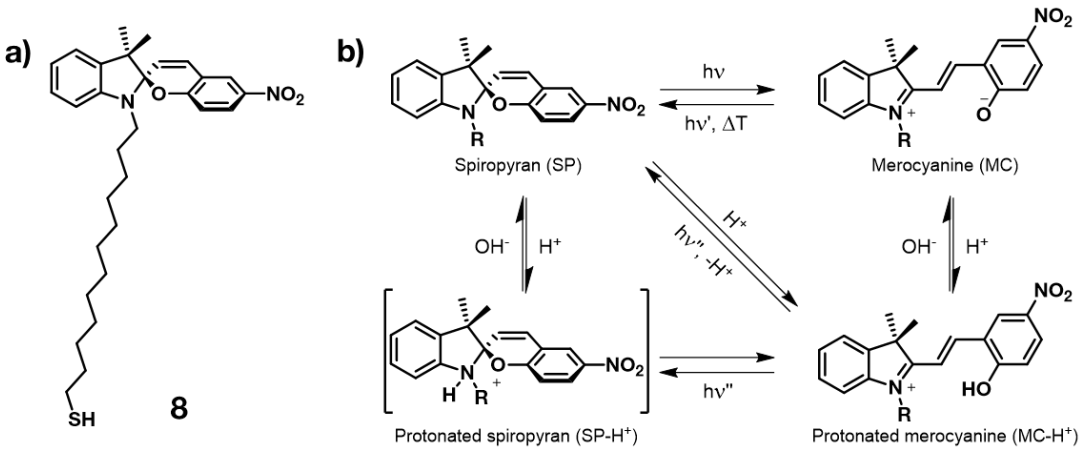

Figure 87. a) Structure formula of the nitrospiropyran derivative bearing a dodecanethiol moiety **8** used in this work (Synthesis: B. Zyska, J. Boelke, Prof. S. Hecht – Humboldt Universität zu Berlin). b) Schematic representation of the photochromism and acidochromism of nitrospiropyran derivatives, including acid-base equilibria.

Another interesting feature of metallic nanostructures is the sensitivity of their SPR to the dielectric environment. The surface plasmon resonance is originated by coherent oscillations of the surface conduction electrons coupled with an external optical field at the interface between metal and dielectric. Surface plasmon resonances are thus highly sensitive towards variations of the local refractive index in the close proximity of the metal-dielectric interfaces, and a change in the refractive index is associated to a shift of the peak position in the extinction (or scattering) spectrum of the nanostructure. Such a phenomenon renders the structures supporting SPR an important group of optical sensors, as they can be used to detect even small refractive index changes: nowadays, sensors based on SPR are widely studied and employed also in commercial applications for the detection of chemical and biological species.[139] The localised surface plasmon resonance features of silver and gold nanoparticles in the visible-NIR spectrum generally undergo a red-shift upon increasing the refractive index of the surrounding medium, and such tight dependence is the basis of localised plasmon resonance spectroscopy.[140] It has also been shown that anisotropic gold nanostructures (such as nanorods) show a higher refractive index sensitivity compared to spherical gold nanoparticles.[7, 141] In this context, spiropyran-merocyanine photochromic units are of particular interest, as the SP → MC isomerisation is associated with a large variation of the refractive index.[229] Therefore, in this study we were also interested in exploring the occurrence of shifts in the extinction spectra of the SPR features related to AuNR upon switching the coating photochrome. In addition, such spectral shifts could also be related to exciton-plasmon coupling phenomena, the latter occurring when the molecular electronic absorption is in resonance with the SPR features of the plasmonic system. In few literature examples, plasmonic systems have been combined with spiropyran-based photochromes, and the appearance of exciton-plasmon coupling effects was observed upon inducing the SP → MC isomerisation,[3b, 90] in some cases also in the ultrastrong coupling regime.[3a] Being that such effect occurs when the plasmonic mode is in resonance with MC, a study upon varying the wavelength of the SPR could enlighten its occurrence, as a splitting in the SPR band would appear only in such case.

We have chosen AuNR also for their facile and highly tuneable synthetic approach, allowing to obtain surfactant-stabilised colloidal dispersions of nanorods with a chosen aspect ratio, low monodispersity and in large amounts.[137b, 177] In such a way, no post-synthetic purification

methods (*e.g.* centrifugal fractionation)[185] are needed in order to obtain nanoparticles with the desired plasmonic properties.

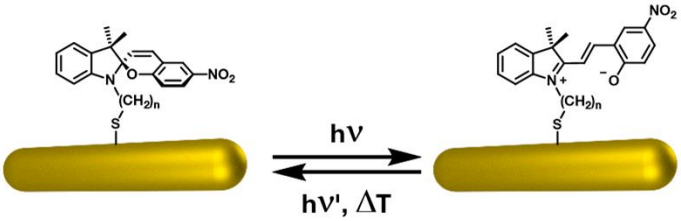

Figure 88. Schematic picture of dodecanethiol-bridged nitrospiropyran derivative **8** (n = 12) chemisorbed on AuNR, and its isomerisation.

Here we are thus interested in the functionalisation of gold nanorods (AuNR) with the spiropyran derivative **8**, via chemisorption of the latter with a thiol group, connected to the photochromic unit with an alkyl spacer consisting of a n-dodecyl chain (Synthesis: B. Zyska, J. Boelke, Prof. S. Hecht – Humboldt Universität zu Berlin). Although it is likely that the use of such alkyl spacer results in a too low chromophore-antenna distance to give rise to phenomena such as plasmon-enhanced fluorescence (on the contrary, quenching at short distances is expected),[136e] we are interested to verify if any plasmon-related effect on the photochromism of **8** is present. Raman spectroscopy was used to study the photochromic unit by following the known vibrational spectra of SP and MC,[230] thanks to the occurrence of SERS effect on the AuNR functionalised with **8**. In order to study the possible dependence of the SP-MC photochromism with the coupling with AuNR localised surface plasmon resonance bands, we performed several experiments on the functionalisation of AuNR with different aspect ratio. The latter allows to tune the longitudinal surface plasmon resonance band wavelength. In detail, we synthesised AuNR of three different aspect ratio, and subsequently functionalised them with self-assembled monolayers of **8**. We followed the photochromism of the hybrid **8**-AuNR by UV-Vis-NIR extinction spectroscopy when dispersed in an organic solvent (THF). Characterisation of the material was also performed by Raman spectroscopy on solid-supported samples.

2. METHODS

2.1. Synthesis of surfactant stabilised AuNR

Gold nanorods (AuNR) were synthesised in three different aspect ratio, using CTAB and aromatic additives, or cosurfactants to obtain the desired particle size. The AuNR with lower aspect ratio were obtained using small aromatic additives such as 5-bromosalicylic acid or sodium salicylate together with the surfactant CTAB as stabilising agents.[177] Meanwhile, the highest aspect ratio nanocrystals were obtained by using sodium oleate as co-surfactant together with CTAB as stabiliser.[137b]

The following chemicals were used for the synthesis of AuNR, in all cases commercially available, purchased from Sigma Aldrich and TCI Chemicals Europe and used as received. Hexadecyltrimethylammonium bromide (CTAB, > 98 %), silver nitrate ($AgNO_3$, > 99 %), hydrogen tetrachloroaurate trihydrate ($HAuCl_4 \cdot 3\ H_2O$, > 99.9 %), sodium borohydride ($NaBH_4$, > 99 %) and hydrochloric acid (HCl, conc. 37 % w in H_2O) were purchased from Sigma Aldrich. 5-bromosalicylic acid (> 98 %), sodium salicylate (> 98 %), sodium oleate (> 97 %) and L-ascorbic acid (> 99.5 %) were purchased from TCI Europe. Ultrapure water was used as a solvent (R = 18.2 MΩ cm). All the glassware and stirring bars used for the synthesis of AuNR and seed particles were previously washed with aqua regia, accurately rinsed and dried prior to their use.

The seed solution consisting of CTAB-stabilised spherical gold nanoparticles with a diameter lower than 5 nm was freshly prepared with the same procedure for **AuNR1**, **AuNR2** and **AuNR3** according to a reported procedure,[231] as follows: to 5 mL of a c = 0.5 mM solution of $HAuCl_4$, 5 mL of CTAB (c = 0.2 M) were added, upon stirring at room temperature. A freshly prepared c = 6 mM solution of $NaBH_4$ in water (1 mL) was flash-injected to the former mixture upon thorough stirring for 2 minutes at room temperature. After darkening to brown of the original yellow colour, the stirring was stopped. The solution is aged for 30 minutes to allow for complete decomposition of the eventual $NaBH_4$ left, and used within the day.

Colloidal dispersions of gold nanorods were synthesised as follows:

- **AuNR1**: 4.5 g of CTAB and 0.4 g of sodium salicylate were stirred in 125 mL H_2O at 50 °C until dissolution occurred in a 500 mL Erlenmeyer flask. Subsequently, the mixture was allowed to reach 30 °C and the temperature stabilised using an oil bath. The mixture was additioned with 3.0 mL of $AgNO_3$ (c = 4 mM) and left undisturbed for 15 minutes at 30 °C. A 125 mL of c = 1 mM $HAuCl_4$ was added upon slowly stirring for further 15 minutes. Afterwards, 0.5 mL of L-ascorbic acid were added (c = 0.064 M) while vigorously stirred until the mixture became colourless (30 seconds), followed by the addition of 0.4 mL seed solution, stirring for further 30 seconds and subsequently stopped. The mixture was left undisturbed at 30 °C overnight, then allowed to room temperature.
- **AuNR2**: 4.5 g of CTAB and 0.55 g of 5-bromosalicylic acid were stirred in 125 mL H_2O at 50 °C until dissolution occurred in a 500 mL Erlenmeyer flask. Subsequently, the mixture was allowed to reach 30 °C and the temperature stabilised using an oil bath. The mixture was additioned with 6.0 mL of $AgNO_3$ (c = 4 mM) and left undisturbed for 15 minutes at 30 °C. A 125 mL of c = 1 mM $HAuCl_4$ was added upon slowly stirring for further 15 minutes. Afterwards, 1.0 mL of L-ascorbic acid were added (c = 0.064 M) while vigorously stirred until the mixture became colourless (30 seconds), followed by the addition of 0.1 mL seed solution, stirring for further 30 seconds and subsequently stopped. The mixture was left undisturbed at 30 °C overnight, then allowed to room temperature.
- **AuNR3**: 4.5 g of CTAB and 0.62 g of sodium oleate were stirred in 125 mL H_2O at 50 °C until dissolution occurred in a 500 mL Erlenmeyer flask. Subsequently, the mixture was allowed to reach 30 °C and the temperature stabilised using an oil bath. The mixture was additioned with 12.0 mL of $AgNO_3$ (c = 4 mM) and left undisturbed for 15 minutes at 30 °C. A 125 mL of c = 1 mM $HAuCl_4$ was added upon slowly stirring for further 90 minutes

until the mixture became colourless. 1.05 mL of HCl conc. were added and slowly stirred for 15 minutes. Afterwards, 0.625 mL of L-ascorbic acid were added (c = 0.064 M) while vigorously stirred (30 seconds), followed by the addition of 0.05 mL seed solution, stirring for further 30 seconds and subsequently stopped. The mixture was left undisturbed at 30 °C overnight, then allowed to room temperature.

The as-prepared, surfactant AuNR colloidal dispersions in water were stored at room temperature without further purification, and showed excellent stability over long periods of time (> 6 months).

2.2. Functionalisation of AuNR with thiols

Several different strategies have been reported in the literature to substitute the surfactant coating with thiol self-assembled monolayers, following the impossibility to directly synthesise AuNR stabilised with the desired thiol coating (unlike spherical gold nanoparticles, prepared with Brust-Schiffrin method).[187c] The procedure was adopted from Gentili *et al.*[187b] and Jiang et al.[232], and adapted to obtain the functionalisation of AuNR with our alkanethiols. The method consists in the disruption of the CTAB-based micelle coating the nanocrystals in presence of the desired thiol. The addition of polar, water miscible solvents such as ethanol or THF to the colloidal dispersion affects the critical micellar concentration of CTAB, resulting in the disruption of the micelle and consequent irreversible aggregation and precipitation of the particles, if the process is performed in absence of a ligand able to stabilise them. The use of a solution of thiols instead of the neat organic solvent yields the stabilisation of the colloid by chemisorption of the thiol. The procedure was established by performing tests with commercial thiols and standardised on the AuNR showing the largest aspect ratio, **AuNR3**. For such purpose, the following commercially available thiols were used: 1-undecanethiol, and 11-mercaptoundecanoic acid. Subsequently, we applied the same procedure to functionalise **AuNR1**, **AuNR2** and **AuNR3** with the photochromic thiol **8**.

The commercially available 1-undecanethiol, and 11-mercaptoundecanoic acid thiols, together with tetrahydrofuran and ethanol were purchased from Sigma Aldrich and used as received. Nanoparticle functionalisation was performed under inert atmosphere to prevent thiol oxidation and subsequent formation of insoluble species (*e.g.* disulfides). Centrifugation is performed using Teflon high-speed centrifuge tubes suited for organic solvents (Nalgene).

Prior to functionalisation, as-prepared colloidal dispersions of AuNR were purified by two rounds of centrifugation and resuspension in water in order to remove the excess surfactant. Typically, 10 mL of the as-prepared AuNR colloidal dispersion was centrifuged once for 20 minutes at 8500 rpm (9300 x g) until complete precipitation, surnatant removal and resuspension in the same amount of ultrapure water. Another round of centrifugation and surnatant removal is performed, then the precipitate is suspended in 1 mL of H_2O and slightly (~ 5 seconds) sonicated, in order to obtain a highly concentrated rod dispersion containing a low amount of detergent. The concentrate is thus injected in a previously degassed 5 mL solution

of thiol (c = 5 mM) in THF under inert atmosphere upon vigorous stirring at room temperature. The mixture is left stirring overnight under inert atmosphere. The mixture is then sonicated and transferred in Teflon centrifuge tubes. Purification is performed by multiple (five times) centrifugal precipitation rounds (8500 rpm, 20 minutes), and resuspension in fresh THF upon gentle sonication in order to remove the surfactant left and the excess of thiol not bound to the gold nanocrystals. At the end of the final purification, the nanoparticles were dispersed in different solvents according to the organic headgroup of the thiol used to stabilise them. Alkanethiol-functionalised **AuNR3** were dispersed in different solvents depending on the polarity of the headgroup of the thiol used, being 11-mercaptoundecanoic acid-stabilised **AuNR3** dispersible in water (polar –COOH exposed on nanoparticle surface), while 1-undecanethiol-stabilised **AuNR3** dispersible in $CHCl_3$ (apolar alkyl chain). In case of the photochromic thiol **8**, AuNR were dispersible only in THF: few attempts of dispersing the nanoparticles in various solvents (H_2O, methanol, ethanol, acetone, chloroform, toluene) led to irreversible aggregation. The as-made dispersions were stored at 4 °C.

2.3. Photochromic thiol deprotection

In order to prevent thiol oxidation upon storage, and for synthetic purposes, the photochromic derivative used here is synthesised as a thioacetate ester. The thioacetate-protected photochrome **8.a** was obtained by B. Zyska and J. Boelke in the group of Prof. S. Hecht – Humboldt Universität zu Berlin), with adapted procedures from the literature.[225c] The product **8.a** was deprotected to yield **8** before nanoparticle functionalisation and used immediately, or stored under inert atmosphere. Cleavage of the thioacetate was performed by base hydrolysis of the ester, as displayed in Scheme 8. A preliminary attempt to perform ester cleavage on **8.a** by using excess NH_3 (30 % in H_2O) as a base in THF was performed, but showed to be ineffective, thus the use of a stronger base was necessary to perform the reaction. **8** was obtained in high yield (80 – 90 %) by reacting **8.a** with potassium *tert*-butoxide (KO*t*Bu) in anhydrous tetrahydrofuran at room temperature. Formation of the desired product was evidenced by ^{1}H-NMR and mass spectrometry. By comparison with the ^{1}H-NMR spectrum related to the starting material **8.a** (Figure 89), formation of **8** was displayed by the disappearance of the singlet at 2.32 ppm (Figure 90) related to the methyl protons of the acetyl protecting group, together with the upfield shift of the multiplet related to the protons of the methylene group of the alkyl chain in α-position with respect to the sulfur atom to 2.67 ppm (for **8.a** occurs at 2.86 ppm). Analogously, mass spectra showed the appearance of a singly charged cationic species which m/z corresponds with the expected mass of the protonated molecular ion [**8**-H]$^+$.

The commercial starting materials and reagents were purchased from Sigma Aldrich and used without further purification. TLC was performed on Silica gel 60 F_{254} plates, spots were detected either by fluorescence quenching under UV light at 254 nm, together with the switching of the photochromic unit and consequent fluorescence of the merocyanine upon irradiation at 365 nm. Reactions carried out in anhydrous solvent (THF) were performed in

oven-dried glassware under inert atmosphere of nitrogen. Anhydrous THF stored under molecular sieves was purchased from Sigma Aldrich, and degassed prior to its use.

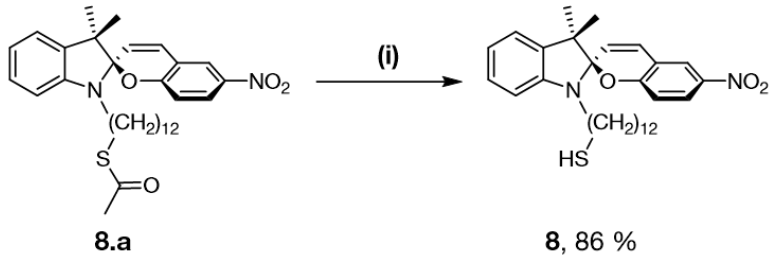

8.a **8**, 86 %

Scheme 8. Thiol deprotection reaction. Reagents and conditions: (i) KOtBu, THF.

^{1}H-NMR of the starting material an product were recorded in $CDCl_3$ on a Bruker Avance400 (400 MHz) spectrometer at 25 °C and are reported in ppm using residual $CHCl_3$ as the internal reference (7.26 ppm). Coupling constants *J* are reported in Hz, and the spectra were elaborated using the software MestReNova. Mass spectra were obtained with an ESI-Ion trap mass spectrometer (LCQ Fleet, Thermo Fisher) in positive mode, coupled with an HPLC system (Accela HPLC, reversed phase C_{18} Hypersil GOLD column, 50 × 2.1 mm, 1.9 μm, - Thermo Fisher Scientific), elution by solvent gradients of 5 – 95 % CH_3CN / 95 – 5 % H_2O with 0.1% (vol.) trifluoroacetic acid (pH ≈ 2).

To a solution of KO*t*Bu (19 mg, 0.17 mmol) in 20 mL THF, 7 mL of a solution of **8.a** (73 mg, 0.13 mmol) were added dropwise. The mixture was stirred for 3 h at room temperature till completion, checking reaction progress by TLC (cyclohexane/ethyl acetate = 7 : 3). Afterwards, solvent was evaporated *in vacuo*, the crude was dissolved in CH_2Cl_2 and washed multiple times with water and brine; HCl was added to the aqueous phase till neutral pH. The organic phase was dried on Na_2SO_4 and filtered, solvent was evaporated *in vacuo*, the desired product was obtained as a brown powder (58 mg, 86 %), and stored under inert atmosphere without further purification. Starting material **8.a** (R_f = 0.76 cyclohexane/ethyl acetate = 7 : 3); ^{1}H-NMR (400 MHz, $CDCl_3$) *δ*, ppm 8.02-7.99 (m, 2H), 7.20-7.16 (m, 1H), 7.09-7.07 (m, 1H), 6.90-6.84 (m, 2 H), 6.75 (d, 1H, *J* = 8.8 Hz), 6.57 (d, 1H, *J* = 7.6 Hz), 5.87 (d, 1 H, *J* = 10.4 Hz), 3.20-3.08 (m, 2H), 2.86 (t, 2H, *J* = 14.8 Hz), 2.32 (s, 3H), 1.55 (bs, 6H), 1.28-1.18 (m, 20H); ESI-MS (+) m/z calcd. for $C_{32}H_{43}N_2O_4S$ $[M+H]^+$ 551.29, found 551.40. Product **8** (R_f = 0.82 cyclohexane/ethyl acetate = 7 : 3); ^{1}H-NMR (400 MHz, $CDCl_3$) *δ*, ppm 8.02-7.99 (m, 2H), 7.20-7.16 (m, 1H), 7.09-7.07 (m, 1H), 6.90-6.84 (m, 2 H), 6.75 (d, 1H, *J* = 8.4 Hz), 6.57 (d, 1H, *J* = 8 Hz), 5.87 (d, 1 H, *J* = 10.4 Hz), 3.19-3.07 (m, 2H), 2.67 (t, 2H, *J* = 14.8 Hz), 1.68-1.62 (m, 4H), 1.36-1.33 (m, 4H), 1.28-1.18 (m, 16H); ESI-MS (+) m/z calcd. for $C_{30}H_{41}N_2O_3S$ $[M+H]^+$ 509.28, found 509.38.

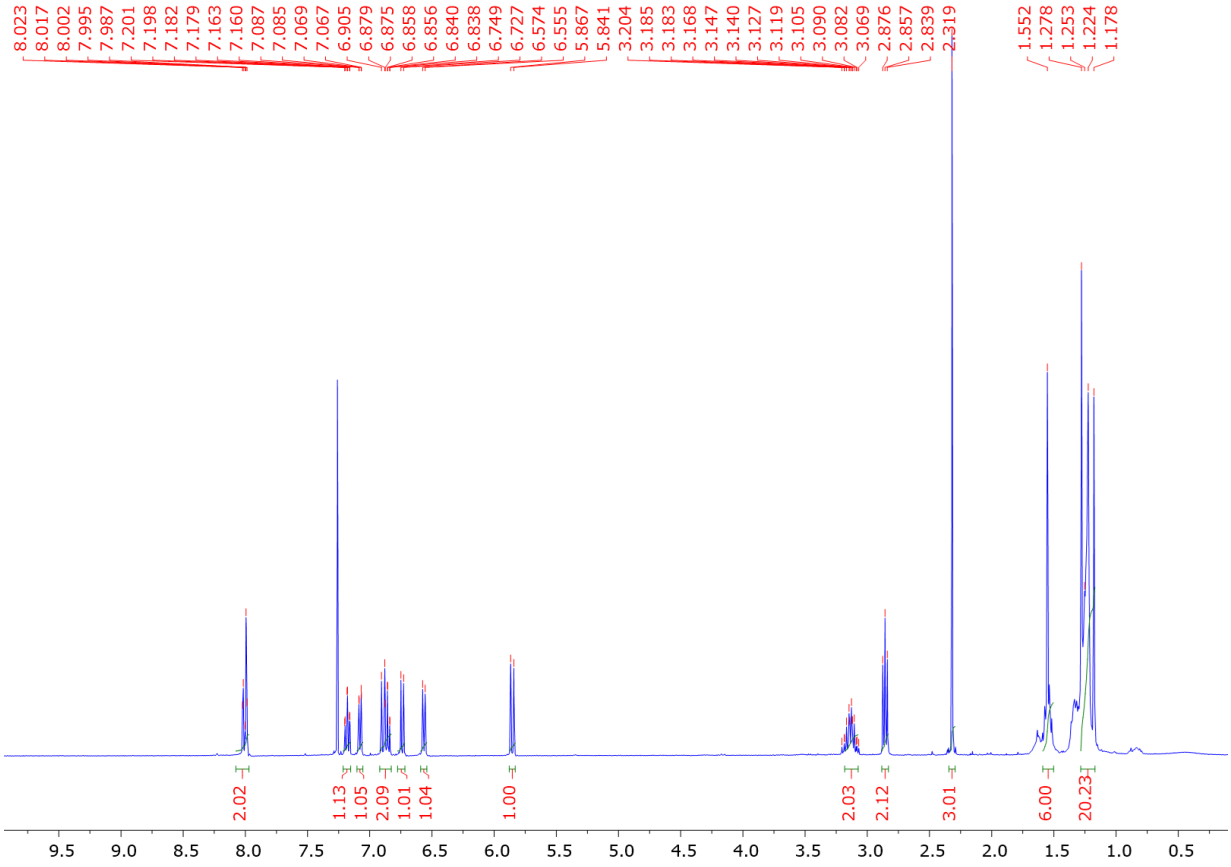

Figure 89. ^{1}H-NMR spectrum (400 MHz, CDCl3) of **8.a**.

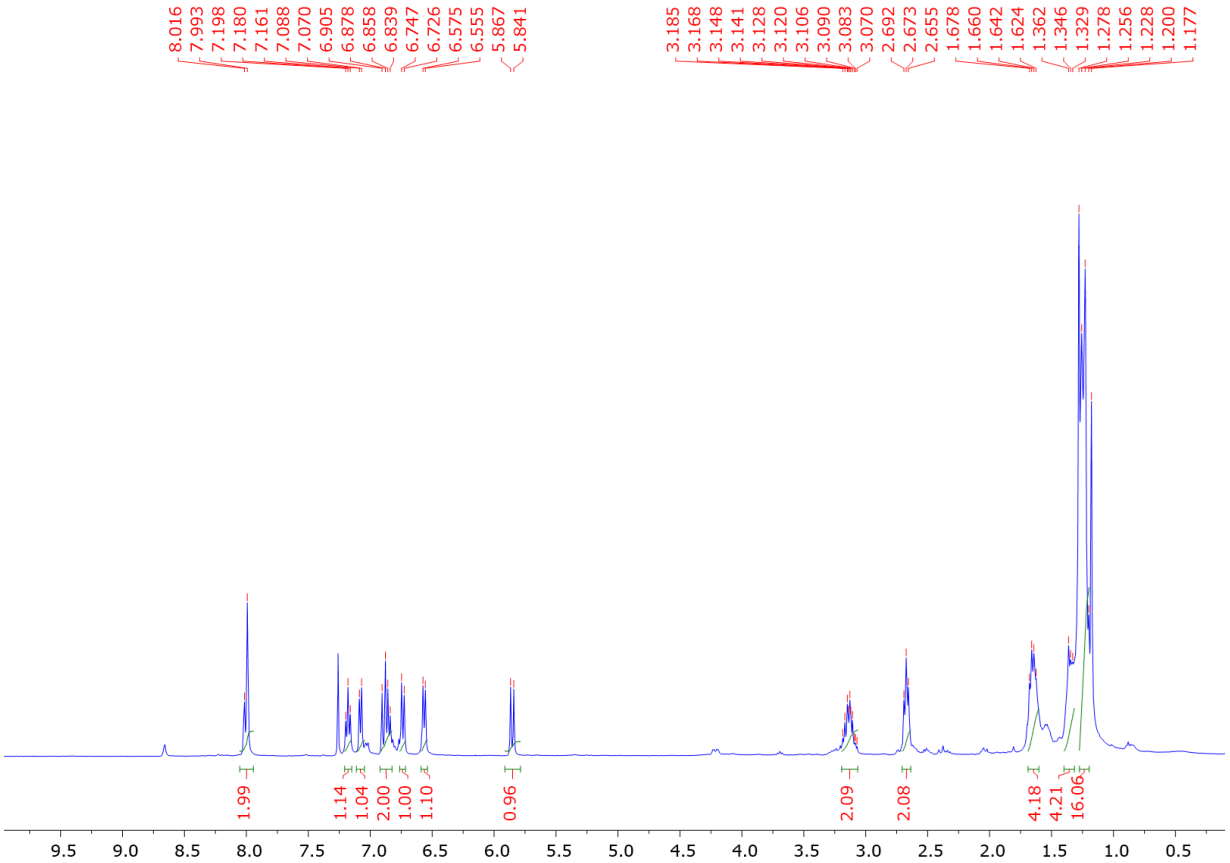

Figure 90. ^{1}H-NMR spectrum (400 MHz, $CDCl_3$) of **8**.

2.4. Nanoparticle characterisation

AuNR morphology and aspect ratio were characterised by means of UV-Vis-NIR extinction spectroscopy and scanning electron microscopy (SEM), after their synthesis and upon functionalisation with organothiols, in order to verify the absence of shape variation after the ligand exchange step. We did not experimentally establish the aggregation behaviour of AuNR in liquid with the use of dynamic light scattering (DLS). Given the non-spherical symmetry of the objects studied, interpretation of their diffusion behaviour is complicated by their anisotropic translational diffusion, together with the coupling of the latter with rotational Brownian motion, and the use of depolarised DLS, or multipolarisation DLS techniques is needed to characterise anisotropic colloids. Also, zeta potential measurements could be instrumental to study the variation in surface charge of the particles upon ligand exchange (and possibly subsequent to **8** SP → MC isomerisation), nevertheless the non-dispersibility of **8**-functionalised AuNR in H_2O made the aforementioned measurement inaccessible.

UV-Vis-NIR absorption spectra were recorded on a Jasco V-670 spectrophotometer equipped with two detectors: a photomultiplier tube (PMT, $\lambda \approx$ 190-850 nm), and a Peltier-cooled PbS detector ($\lambda \approx$ 850-~2000 nm). UV-Vis-NIR extinction spectra of as-synthesised AuNR (CTAB-coated) were recorded in water, after one centrifugation round (8500 rpm, 20 minutes), resuspension in water, and diluted ten times. The spectra were obtained using disposable polystyrene cuvettes, using ultrapure water as blank. Extinction spectra of thiol-stabilised AuNR were recorded in quartz Suprasil cuvettes (Hellma), diluting in order to work at 0.5 – 0.6 absorbance at the SPR maximum, using spectroscopy grade solvents (Uvasol – Merck Millipore). Scanning electron microscopy was performed on a Quanta FEG 250 (FEI), equipped with a cold cathode field emission gun. Images were recorded on conductive samples prepared by drop-casting AuNR dispersions on conducting silicon (Si [100] p^{++}doped) substrates, after washing the latter with acetone, isopropanol, ethanol and drying under a stream of nitrogen. The microscope was operated in high vacuum, using 2-3 nm spot size and 20-30 kV acceleration voltages. AuNR morphology and particle size statistics were determined using ImageJ software, by measuring diameter and length of over 100 AuNR per sample.

2.5. Photochemical characterisation

UV-Vis absorption and emission spectra of **8.a** in spiropyran (SP), merocyanine (MC) and protonated merocyanine (MC-H^+) forms were recorded in air-equilibrated $CHCl_3$ at 5 °C, given the fast thermal MC -> SP cyclisation occurring in the dark. The photochemical measurements done on thiol-stabilised AuNR dispersed in liquid were performed at room temperature. All the measurements were done using a Jasco V-670 spectrophotometer and an Agilent Cary Eclipse fluorimeter in quartz Suprasil cuvettes (Hellma), and spectroscopy grade solvents. Ultraviolet and visible light irradiation were performed with optical fibre-coupled LEDs (ThorLabs): for UV

light λ_{max} = 367 nm, FWHM = 9 nm, for Vis light λ_{max} = 550 nm, FWHM = 30 nm, equipped with collimating lenses to ensure a parallel orientation of the emitted light. UV light was performed at an incident power density $P_d \approx 12.0$ mW cm^{-2}, while for Vis $P_d \approx 5.0$ mW cm^{-2}. Irradiation was performed upon thorough stirring of the dispersions.

2.6. Dark field light scattering and Raman experiments

For studying the photoswitching of spiropyran derivative **8** coating gold nanorods by means of surface enhanced Raman scattering (SERS), a custom-built confocal Raman microscope set-up was used. The measurements were performed in the laboratory of Prof. H. Uji-I (Katholieke Universitat Leuven), in collaboration with Dr. S. Toyouchi. The samples were prepared by drop-casting the spiropyran-coated AuNR dispersions in THF on previously cleaned glass microscope cover slides. The Raman spectroscopy setup was based on an inverted microscope (Nikon TiU) equipped with a piezoelectric stage (P517.3CL, Physik Instrument). AuNR aggregates were located by dark field illumination: white light from a halogen lamp was focussed on the sample through a dark field condenser (Nikon TI-DF, dry, N.A. 0.95-0.80). Laser excitation and collection of scattered light from the sample were performed using an objective lens (60x, N.A. 1.25 PlanFluor, Nikon) and passed through a confocal pinhole (100 μm diameter). Spectra were recorded using a charge-coupled device (CCD) camera (DU920P, Andor) operated at -85 °C equipped with a spectrograph (iHR320, Horiba), dichroic mirrors and longpass optical filters were used in order to reject the excitation laser light. Excitation was performed either with a continuous wave (CW) 532 nm diode laser (Cobolt Samba TM 532nm), a CW 632.8 nm He-Ne laser (1145P, JDSU), or a CW 785 nm diode laser. The laser power was controlled by neutral density filters. Dark field light scattering was performed with the same instrumental setup. UV-light irradiation on the samples was performed upon irradiation of the whole sample with a λ_{max} = 367 nm LED (ThorLabs). Conversely, visible light and two-photon NIR irradiation on the samples were performed with laser sources, focussing the beam on the sample using the microscope optics, through an objective lens (60x, N.A. 1.25 PlanFluor, Nikon). For visible light, a continuous wave (CW) λ = 532 nm diode laser (Cobolt Samba TM 532nm) was used, while two-photon irradiation was accomplished with a Ti:sapphire laser tuned at λ = 780 nm and λ = 1040 nm, giving 120 fs (linearly polarised) pulses at 80 MHz repetition rate (Maitai SP, SpectraPhysics). The laser power was controlled by neutral density filters. Further analysis of the Raman spectra involved manual baseline correction and normalization.

3. RESULTS AND DISCUSSION

3.1. Photochemical and photophysical characterisation of the switch in solution

The thioacetate-protected nitrospiropyran derivative **8.a** was characterised in solution prior to its deprotection and coupling to AuNR. The absorption spectra in chloroform show the typical features of the photochromic unit (Figure 91). The ring-closed spiropyran isomer (SP), stable form in the dark at neutral or basic pH, shows a broad absorption band in the UV region ($\lambda_{max} \approx$ 360 nm), while no absorption occurs in the visible region. In acidic conditions (excess trifluoroacetic acid, 10 equiv.), the thermodynamically stable species is the protonated merocyanine (MC-H$^+$), which formation is evidenced by appearance of an absorption band located at ca. 450 nm. The spiropyran form is metastable in acidic environment, and is photogenerated by irradiation with visible light at 450 nm, while thermally converts to MC-H$^+$ in the dark. The appearance of the latter compound could be reversibly triggered to SP upon addition of a base excess (NH_3). Merocyanine (MC) instead, base form of MC-H$^+$, displays a strong absorption band centred at ca. 585 nm and it is fluorescent, with an emission band located at ca. 650 nm, the large Stokes shift is a typical feature of such fluorophore. MC is generated photochemically by UV irradiation, ($\lambda_{max} \approx$ 365 nm) of a SP solution, and shows fast cycloreversion (occurring in few minutes) to the ring-closed form SP. The MC → SP cycloreversion could be also induced by visible light irradiation ($\lambda_{max} \approx$ 530 nm). Absorption and emission spectra in THF showed analogous features and maxima wavelength for the aforementioned transitions.

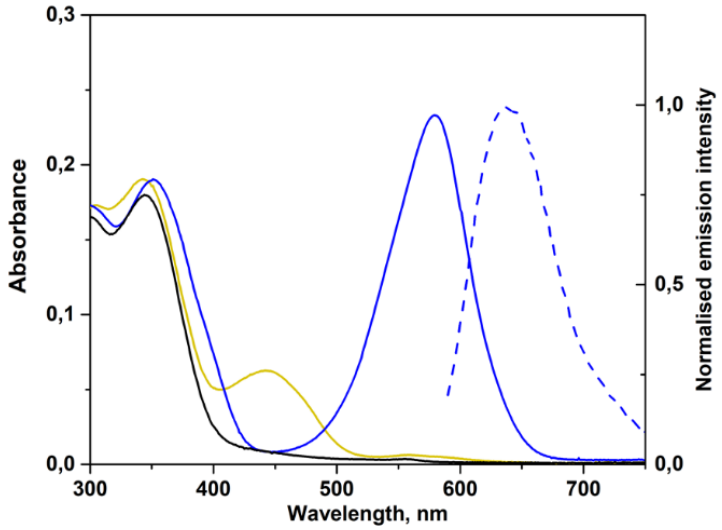

Figure 91. UV-Vis absorption and emission spectra of **8.a** in its (meta)stable isomeric forms (c = 2.0 x 10^{-5} M) in $CHCl_3$. *Black trace*, absorption spectrum of ring-closed spiropyran form in neutral/basic conditions. *Yellow trace*, absorption spectrum of protonated merocyanine form, stable at acidic pH. *Blue full line*, absorption and *blue dashed line* emission spectra of merocyanine form, metastable at neutral/basic pH, photogenerated by irradiation of spiropyran with UV light.

3.2. AuNR synthesis and functionalisation

Surfactant stabilised gold nanorods were synthesised in water by seed-mediated growth, a method first discovered by Murphy *et al*.[176, 233] A modified procedure taking advantage of the use of co-surfactants alongside with hexadecyltrimethylammonium bromide (CTAB) yielding higher size tunability and monodispersity, reported by Murray *et al.* was used.[137b, 177] For a detailed description of the synthetic mechanism, see Chapter 3, section 7. Three different aspect ratio AuNR were prepared. Rod-shaped particles with aspect ratio of: 2.0, 2.7 and 4.6 were obtained, all of them having a diameter of ca. 25 nm, with a length of ca. 50, 65 and 120 nm respectively (see Table 7, Figure 92-94). The AuNR with lower aspect ratio were obtained using small aromatic additives such as 5-bromosalicylic acid and sodium salicylate together with the surfactant cetyltrimethylammonium bromide (CTAB) as stabilising agents.[177] Meanwhile, the highest aspect ratio nanocrystals were obtained by using sodium oleate as co-surfactant together with CTAB as stabiliser.[137b] Their shape and dimension were characterised by SEM, upon drop-casting a suspension of the surfactant-stabilised particles in water upon prior lowering of the surfactant concentration by centrifugal precipitation. The absorption spectra were measured in water for the as-synthesised, surfactant-stabilised colloid, and showed the classical two localised surface plasmon resonance (SPR) peaks for gold nanorods. Being the transverse SPR mode at ca. 510-520 nm, and the intense longitudinal SPR mode, which energy is largely dependent on the aspect ratio of the rod, having maxima located respectively at ca. 605, 690 and 925 nm going form the shorter to the longer AuNRs (see Figure 95, Table 7).

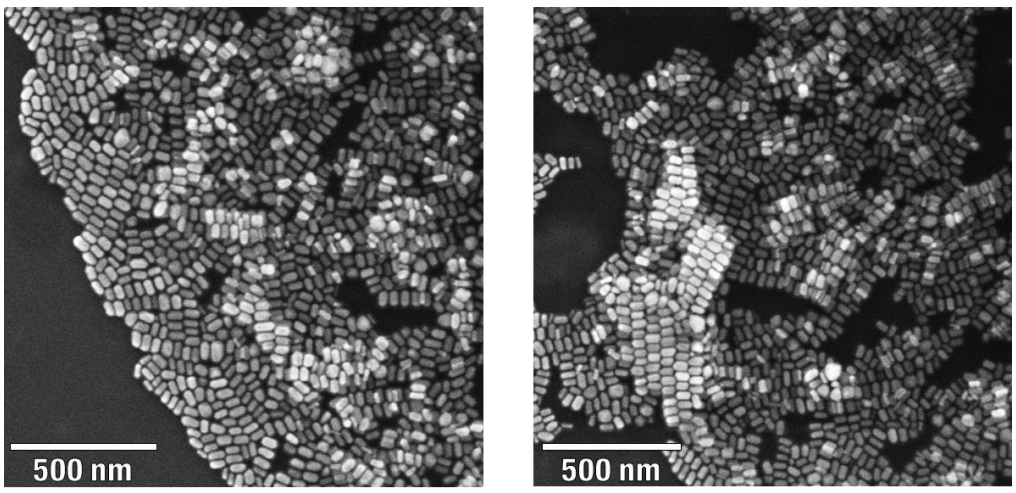

Figure 92. SEM micrographs of CTAB-stabilised **AuNR1** drop-casted on Si substrates from a water dispersion.

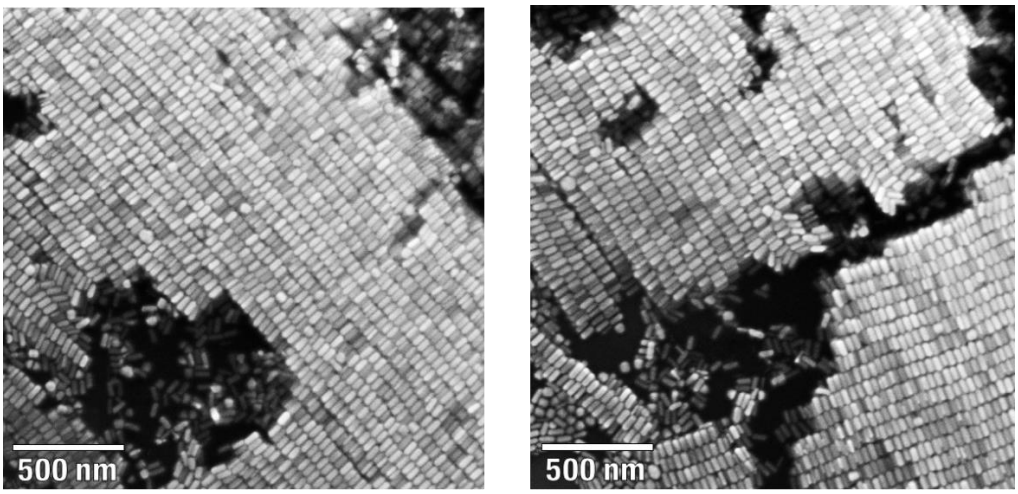

Figure 93. SEM micrographs of CTAB-stabilised **AuNR2** drop-casted on Si substrates from a water dispersion.

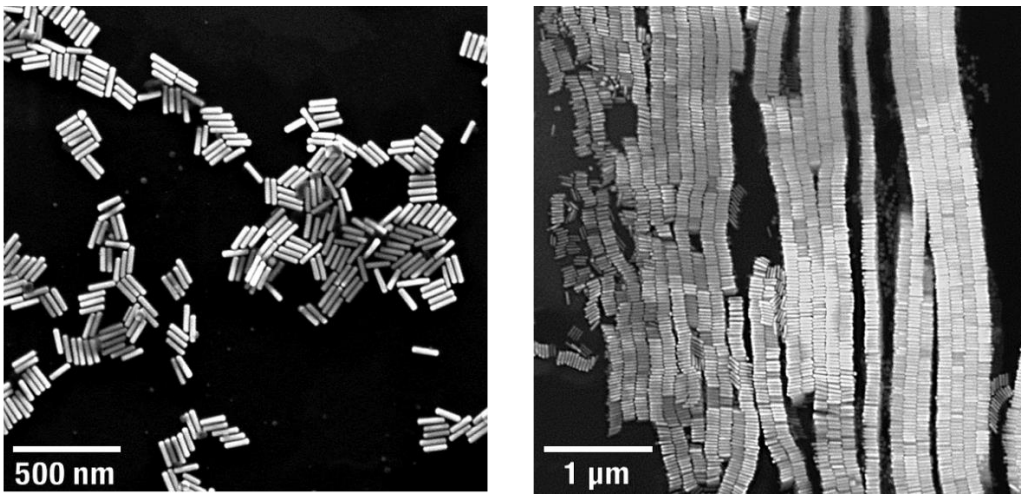

Figure 94. SEM micrographs of CTAB-stabilised **AuNR3** drop-casted on Si substrates from a water dispersion.

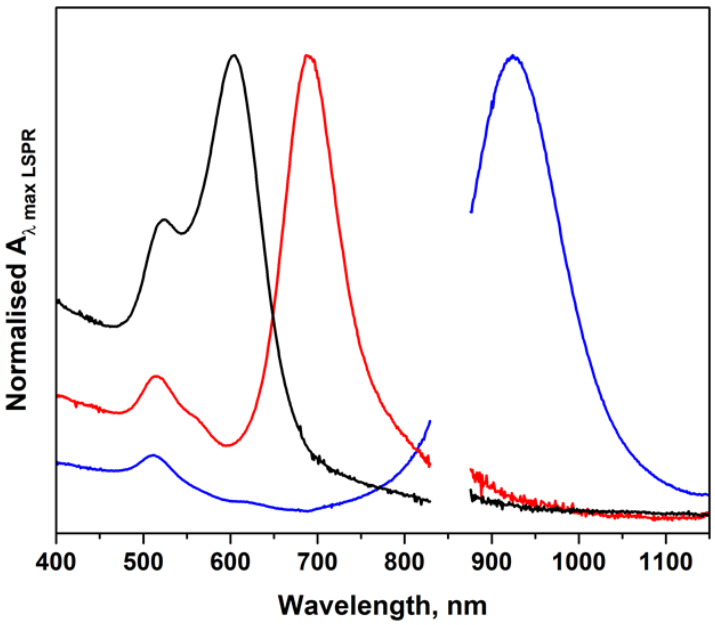

Figure 95. UV-Vis-NIR extinction spectra of as-synthesised CTAB-stabilised AuNR water dispersions. The spectra are normalised with respect to the longitudinal surface plasmon resonance band (LSPR) maximum. *Black trace*, **AuNR1**. *Red trace*, **AuNR2**. *Blue trace*, **AuNR3**.

Table 7. Structural parameters and surface plasmon resonance wavelengths for the as-synthesised, surfactant-stabilised AuNR (dispersed in H_2O) used in the present study.

	d [nm]	L [nm]	Aspect ratio	λ_{max} TSPR [nm]	λ_{max} LSPR [nm]
AuNR1	25 ± 5	50 ± 6	2.0 ± 0.5	524	605
AuNR2	24 ± 5	64 ± 6	2.7 ± 0.6	514	690
AuNR3	26 ± 3	119 ± 10	4.6 ± 0.7	510	925

Prior to perform the functionalisation of AuNR with the photochromic thiol **8**, preliminary studies on the ligand exchange with commercial thiols were made. On this purpose, we have used **AuNR3**, the nanoparticles with the highest aspect ratio, 1-undecanethiol and 11-mercaptoundecanoic acid as ligands to replace CTAB. A detailed description of the procedure used can be found in Chapter 3, section 7.1, and above (see Methods). After their purification, the nanoparticles were dispersed in different solvents according to the headgroup of the thiol used to stabilise them: **AuNR3** reacted with 1-undecanethiol were dispersed in apolar solvents (*i.e.* $CHCl_3$), while in the case of 11-mercaptoundecanoic acid the colloid was stabilised in water (polar –COOH exposed on nanoparticle surface), and showed to be stable over long periods of time. UV-Vis-NIR extinction spectra show the typical two surface plasmon resonance bands of the rod-shaped gold colloid **AuNR3**, nevertheless, compared to the original CTAB-stabilised dispersion, severe broadening of the bands, increase of the light scattering at every wavelength and reduction of the intensity ratio between the two bands evidence the occurrence of partial nanorod aggregation (Figure 98). Moreover, it is visible how 1-undecanethiol-stabilised **AuNR3** (dispersed in $CHCl_3$) seems to include larger aggregates, showing larger scattering intensity and broader SPR bands (including an additional peak at ca. 650 nm, see Figure 98). At first glance, one would suspect a partial loss of the characteristic shape and aspect ratio of the nanoparticles, compared to the as-synthesised ones. Nevertheless, investigation performed on both thiol-functionalised **AuNR3** by scanning electron microscopy confirmed the retaining of their original morphology and aspect ratio (cf. Figure 96-97, Table 8), therefore we can infer that the evidences of aggregation obtained in solution by optical spectroscopy are due to the formation of aggregates of particles retaining their original shape, thus leading to plasmon coupling of the nanorods with subsequent spectral broadening and batochromic shift of their SPR bands.

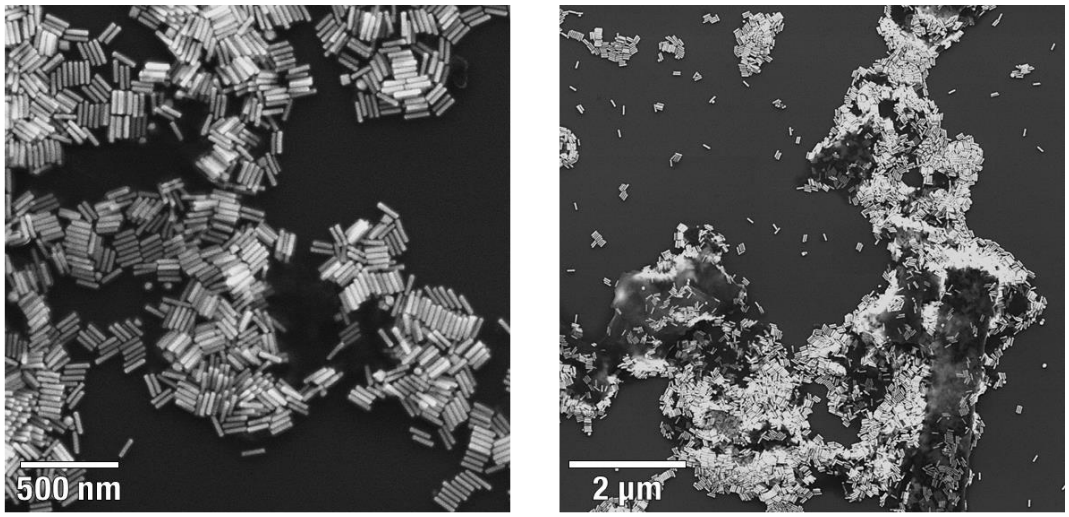

Figure 96. SEM micrographs of **AuNR3** stabilised with 1-undecanethiol. Sample prepared by drop-casting a dispersion of AuNR in $CHCl_3$ on Si substrates.

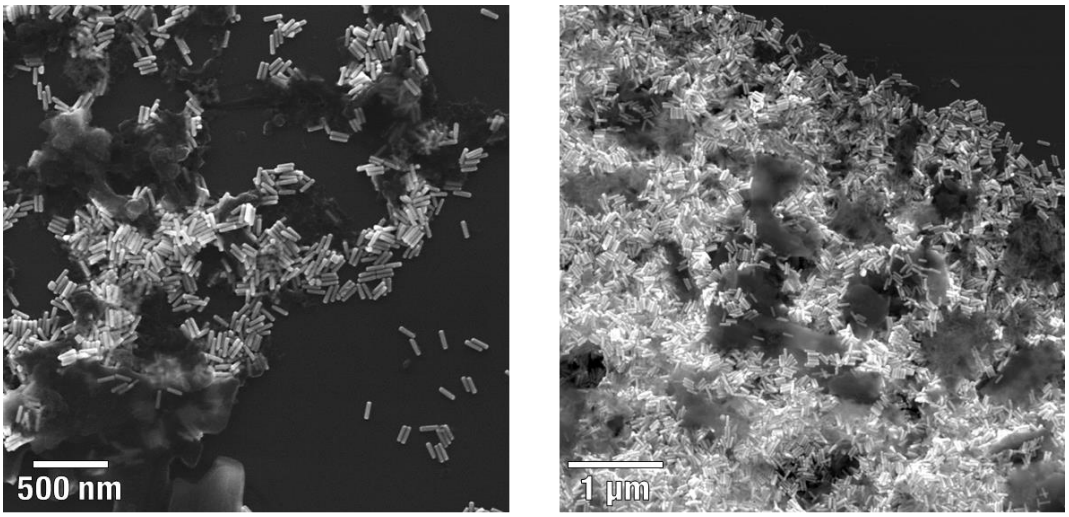

Figure 97. SEM micrographs of **AuNR3** stabilised with 11-mercaptoundecanoic acid. Sample prepared by drop-casting a dispersion of AuNR in H_2O on Si substrates.

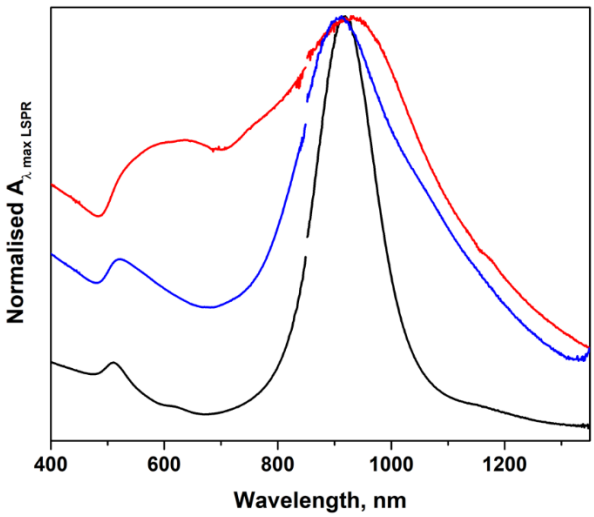

Figure 98. UV-Vis-NIR extinction spectra of dispersions of **AuNR3** functionalised with organic thiols. The spectra are normalised with respect to the longitudinal surface plasmon resonance band (LSPR) maximum. *Red trace*, **AuNR3** stabilised with 1-undecanethiol in $CHCl_3$. *Blue trace*, **AuNR3** stabilised with 11-mercaptoundecanoic acid in H_2O. *Black trace*, for comparison, also CTAB-stabilised **AuNR3** in H_2O (as reported in Figure 95) is shown.

Table 8. Structural parameters and surface plasmon resonance wavelengths for **AuNR3**, stabilised with commercial thiols 1-undecanol and 11-mercaptoundecanoic acid (dispersed in $CHCl_3$ and H_2O, respectively).

	d [nm]	L [nm]	Aspect ratio	λ_{max} TSPR [nm]	λ_{max} LSPR [nm]
1-undecanethiol	27 ± 3	120 ± 10	4.5 ± 0.6	520	930
11-mercaptoundecanoic acid	29 ± 3	122 ± 10	4.2 ± 0.5	520	910

Having verified the successful procedure for exchanging the original surfactant with alkanethiol monolayers without disrupting the original nanoparticle morphology, we applied the same ligand exchange strategy with the photochromic derivative **8**, on **AuNR1**, **AuNR2** and **AuNR3**. In all cases, **8**-stabilised AuNR showed to be readily dispersed in THF, and showed to be stable over long periods of time. Analogously to the case of non-photochromic thiols, also upon using **8** as stabiliser for AuNR we visualised a noticeable broadening, together with a bathochromic shift of the original spectral features of the gold colloid (Figure 102, Table 9). Nevertheless, nanoparticle size analysis performed by SEM showed also in this case that the original geometry and aspect ratio is retained for **AuNR1**, **AuNR2** and **AuNR3** (Figure 99-101, Table 9), as the values for diameter and length appear unchanged, within experimental error.

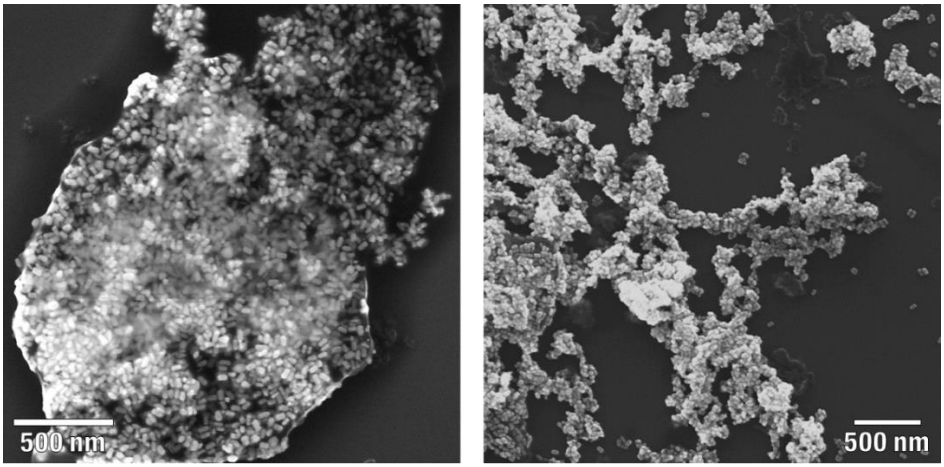

Figure 99. SEM micrographs of **AuNR1** stabilised with **8**. Sample prepared by drop-casting a dispersion of AuNR in THF on Si substrates.

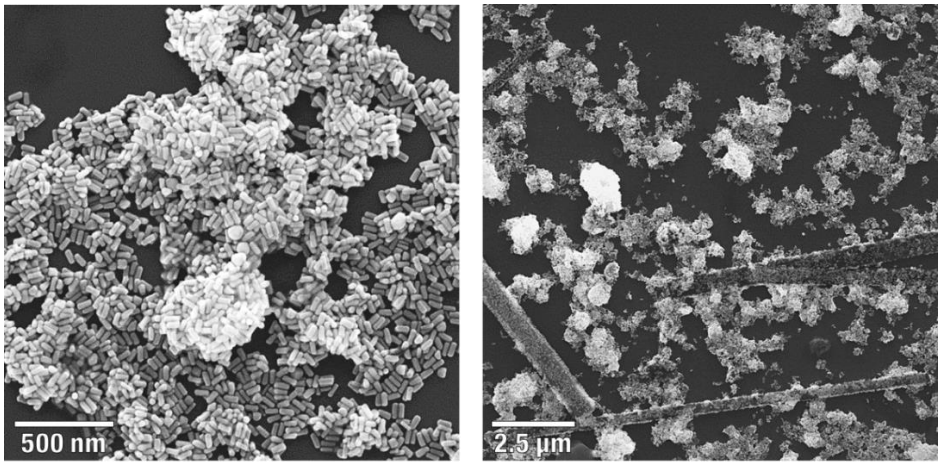

Figure 100. SEM micrographs of **AuNR2** stabilised with **8**. Sample prepared by drop-casting a dispersion of AuNR in THF on Si substrates.

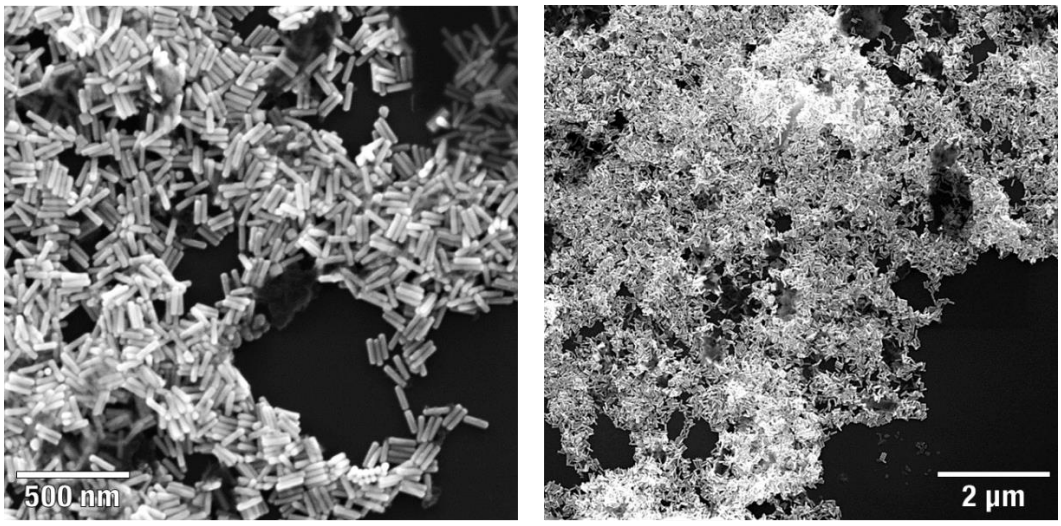

Figure 101. SEM micrographs of **AuNR3** stabilised with **8**. Sample prepared by drop-casting a dispersion of AuNR in THF on Si substrates.

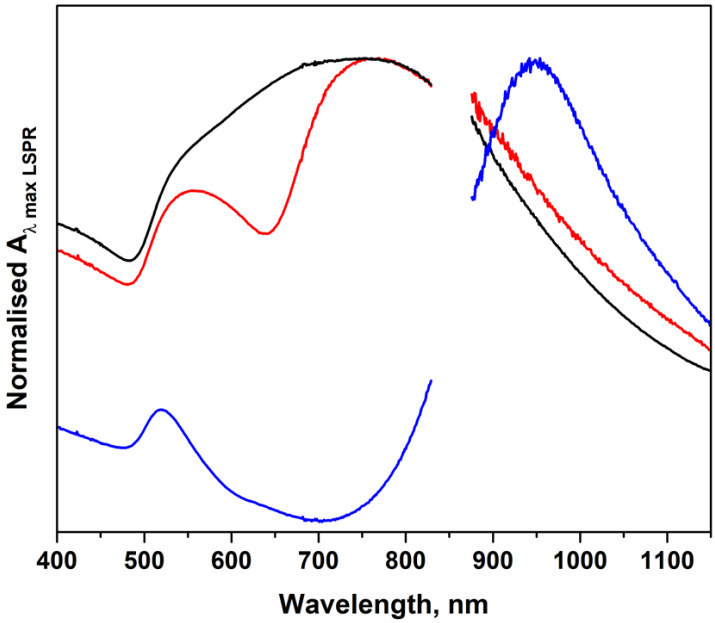

Figure 102. UV-Vis-NIR extinction spectra of dispersions of AuNR functionalised with **8** in THF. The spectra are normalised with respect to the longitudinal surface plasmon resonance band (LSPR) maximum. *Black trace*, **AuNR1**. *Red trace*, **AuNR2**. *Blue trace*, **AuNR3**.

Table 9. Structural parameters and surface plasmon resonance wavelengths for AuNR functionalised with photochromic thiol **8** (dispersed in THF) used in the present study.

	d [nm]	L [nm]	Aspect ratio	λ_{max} TSPR [nm]	λ_{max} LSPR [nm]
AuNR1	25 ± 4	50 ± 5	2.0 ± 0.4	555	747
AuNR2	27 ± 4	70 ± 5	2.6 ± 0.4	555	770
AuNR3	31 ± 4	122 ± 10	3.9 ± 0.6	520	950

As a general consideration, when comparing our AuNR functionalisation attempts with the reports found in the literature, a broadening and red-shift of the original spectral features, together with a decrease in the intensity ratio between the LSPR and TSPR bands is often

observed in their UV-Vis-NIR extinction spectra.[187b, 226a] This evidence can be rationally explained by two main effects, in both cases caused by the removal of CTAB in the surroundings of the gold nanocrystals. In first instance, the dielectric environment of the nanoparticles is strongly affected by the exchange of the CTAB (which forms a cationic double layer in water), with an alkanethiol derivative showing a largely lower polar character (AuNR are often consequently dispersed in apolar organic solvents). Such spectral shifts result from the high refractive index sensitivity of AuNR, and especially of their LSPR band. Moreover, we cannot neglect the occurrence of partial aggregation in liquid upon substituting CTAB with the alkanethiol coating. This hypothesis seems reasonable, since the original stabilising agent, a double layer of cationic surfactant[234] – which favours strong electrostatic repulsion between the particles – is replaced by a monolayer of (neutral) thiols. Furthermore, and more importantly, the presence of organic impurities surrounding the gold colloids is always observed in the samples prepared by substituting CTAB with thiol derivatives (Figure 96-97, Figure 99-101). The nanoparticles in the SEM images appear embedded in an amorphous organic matrix which exact nature could not be characterised. It is likely that the presence of such organic layer wrapping the gold colloid is another reason of partial aggregation seen in solution. Unfortunately, we did not understand the origin of such unwanted component, and further purification steps did not show its disappearance. Unfortunately, due to the embedment of our AuNR into amorphous structures, we could not observe the formation of aligned, liquid crystalline assemblies of AuNRs (*cf*. Figure 92-94), typically occurring upon slow drying of liquid dispersions of such anisotropic nanoparticles.

3.3. 8-functionalised AuNR – photochromism

In order to verify the occurrence of any interaction between the plasmonic nanoparticles and the photochromic unit, and especially with the merocyanine (MC) isomer, absorbing in the visible range of the electromagnetic spectrum (500 – 650 nm), we performed a study with nanorods characterised by a different aspect ratio, thus leading to LSPR features at different wavelength. This results in different spectral overlap between MC and AuNR (Figure 103). Photoswitching of **8**-functionalised AuNRs was followed by UV-Vis spectroscopy, upon irradiation of the THF dispersions with UV (365 nm) and Vis (530 nm) light. In addition, the eventual occurrence of MC-centred fluorescence was monitored by emission spectroscopy (λ_{exc} = 580 nm). The latter however was never observed, as expected from the too short distance of the alkyl spacer used to separate the fluorophore from the surface of the nanoparticles. Fluorescence enhancement effects are usually observed upon using dielectric spacers in the range of about 10-20 nm distance from the plasmonic surface: at lower distances the interaction between plasmonic nanoparticles and adjacent fluorophores typically results in a strong quenching of their emission.[136e] Furthermore, due to the dense character of self-assembled monolayers of thiols on gold, the distance between MC fluorophores on the AuNR surface is expected to be well below their Förster radius, thus quenching due by their vicinity is also expected.

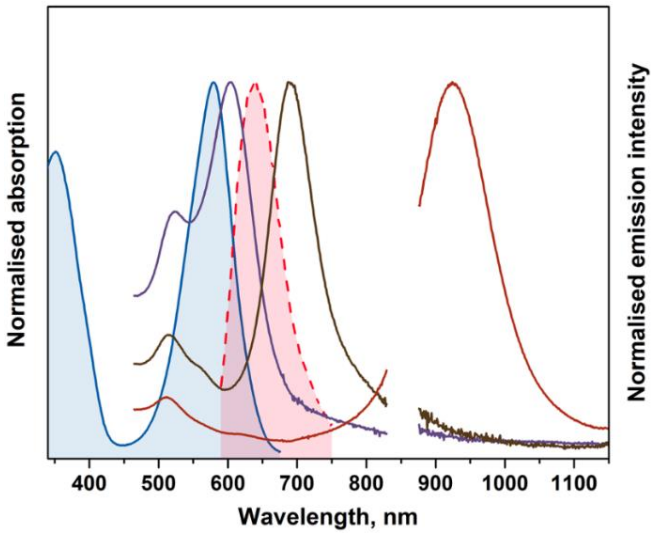

Figure 103. Overlapped absorption and emission spectra of **8.a** and extinction spectra of CTAB-stabilised AuNR used in the present work. *Blue trace, filled area* absorption, and *red dashed line, filled area* emission spectra (λ_{exc} = 580 nm) of MC in $CHCl_3$. Extinction spectra of CTAB-stabilised **AuNR1**, **AuNR2** and **AuNR3** in H_2O, *purple*, *grey* and *brown line*, respectively.

In all cases, spectral variations that could be ascribed to the occurrence of SP – MC photochromism of **8** were visible, since the spectral changes obtained upon UV irradiation were (at least partially) reversible upon subsequent exposure to Vis light (Figure 104-106). In the case of **8**-**AuNR1**, therefore the rods with lower aspect ratio and longitudinal SPR mode roughly resonant to the absorption peak of MC (Figure 103), a large variation of their optical properties was noticed, mainly with an increasing red shift in the longitudinal SPR mode upon increasing UV irradiation, until reaching a "photostationary state". Such spectral variation was accompanied by a uniform decrease in intensity in the area between 350 and 600 nm. The aforementioned shifts were partially reversible upon Vis irradiation, therefore suggesting a contribution from the photochromic unit to the phenomenon observed (Figure 104). Although, the reversibility showed to be limited, and multiple switching cycles failed, thus enlightening the fatigue of **8** photochromism upon posing the switch in such conditions. It is not clear what is the reason for the spectral changes observed: regarding the wavelength shift, one could hypothesise its occurrence with the change in the dielectric properties of the environment of AuNRs (SP form is neutral, with a low dipole moment, while MC is zwitterionic, and has a large dipole moment).[140] Nevertheless, the same phenomenon is not observed in case of the AuNRs with higher aspect ratio, therefore weakening this assumption. Together with the wavelength shift, a general broadening and intensity change could be related to a partial clustering/precipitation of the colloid, it is nevertheless difficult to prove it certainly. Moreover, we could not assess any difference in the aggregation state of AuNR by SEM upon drop-casting a pre-UV-irradiated dispersion of the aforementioned nanoparticles.

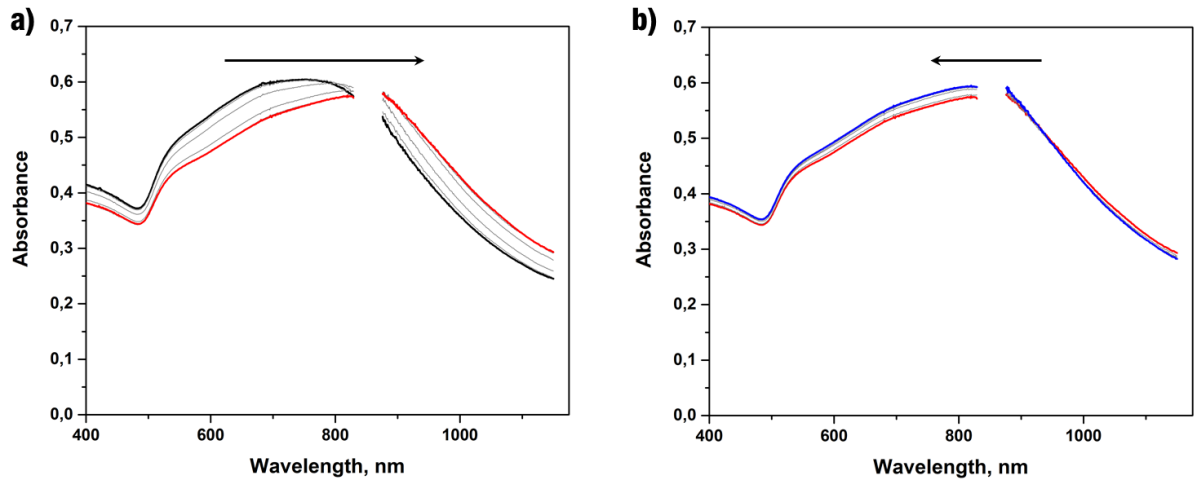

Figure 104. UV-Vis-NIR extinction spectral variation of **8**-stabilised **AuNR1** dispersion in THF upon light irradiation. a) *Black trace*, dark. *Red trace*, 180 s UV light irradiation (λ_{max} = 367 nm, P_d = 12 mW cm^{-2}). b) *Red trace*, after 180 s UV irradiation, as in a). *Blue trace*, 420 s Vis irradiation (λ_{max} = 530 nm, P_d = 5.0 mW cm^{-2}).

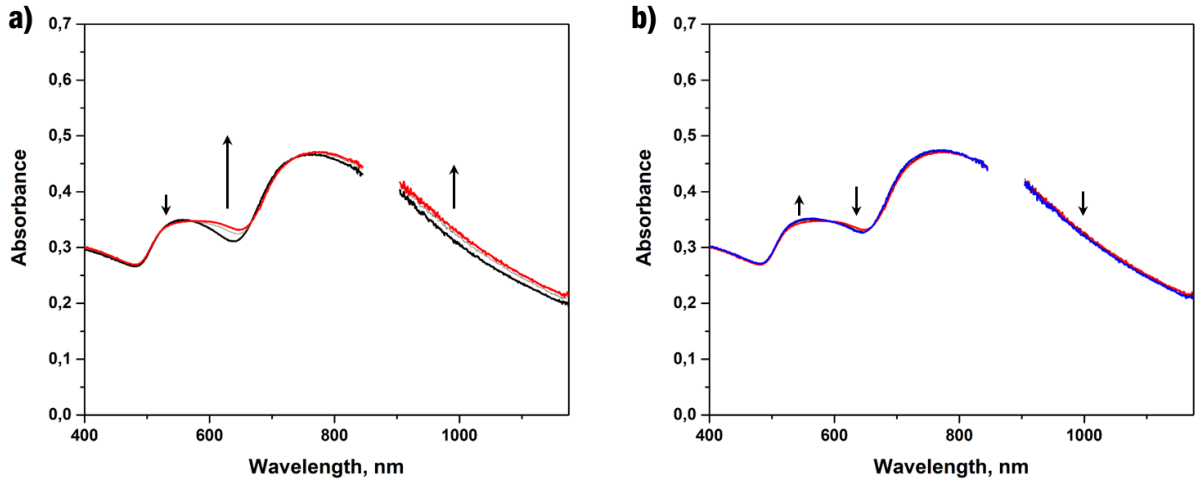

Figure 105. UV-Vis-NIR extinction spectral variation of **8**-stabilised **AuNR2** dispersion in THF upon light irradiation. a) *Black trace*, dark. *Red trace*, 60 s UV light irradiation (λ_{max} = 367 nm, P_d = 12 mW cm^{-2}). b) *Red trace*, after 60 s UV irradiation, as in a). *Blue trace*, 90 s Vis irradiation (λ_{max} = 530 nm, P_d = 5.0 mW cm^{-2}).

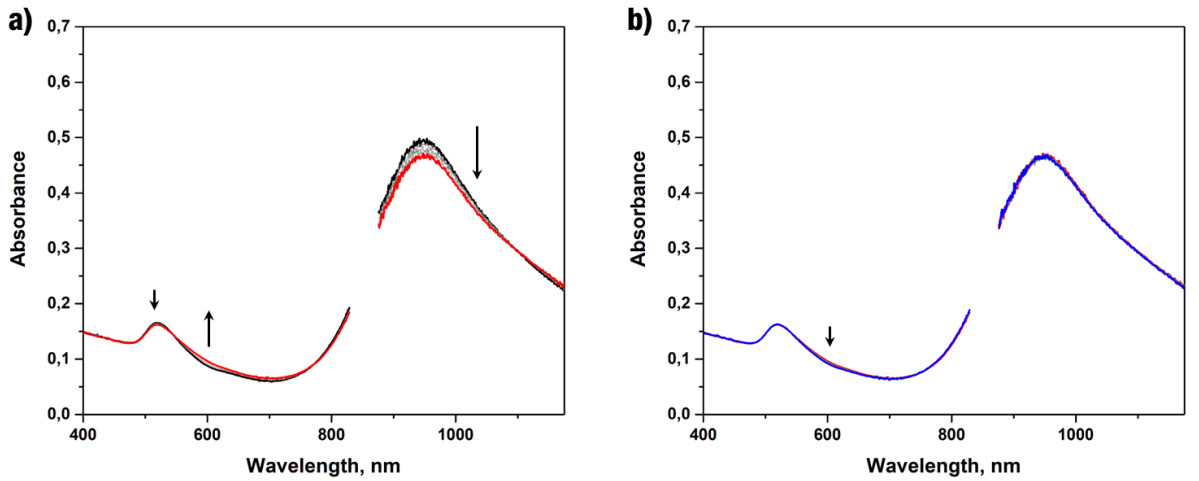

Figure 106. UV-Vis-NIR extinction spectral variation of **8**-stabilised **AuNR3** dispersion in THF upon light irradiation. a) *Black trace*, dark. *Red trace*, 60 s UV light irradiation (λ_{max} = 367 nm, P_d = 12 mW cm^{-2}). b) *Red trace*, after 60 s UV irradiation, as in a). *Blue trace*, 90 s Vis irradiation (λ_{max} = 530 nm, P_d = 5.0 mW cm^{-2}).

In case of **8**-**AuNR2**, a clearly visible spectral variation was again visible by UV irradiation, being (slightly) reversible after Vis light (Figure 105). In such case, a broadening of the transversal SPR mode and perhaps the occurrence of a band centred at ca. 600 nm is visible, together with a partial broadening of also the longitudinal SPR mode. Also in the present sample, broadening and wavelength shift of the bands could be ascribed both to a change in the dielectric constant of the nanorods surroundings and to partial aggregation, but the experimental evidence is far too little to enable the understanding of such phenomena. The occurrence of low reversibility and fatigue already on the first cycle was clearly evident also in this case. On the contrary, for **8**-**AuNR3** a lower variation in the UV-Vis-NIR extinction spectra is visible, with a small decrease of the two SPR maxima and the increase of absorbance in the area around ca. 600 nm, reversibility upon Vis irradiation in this case is barely noticeable. No variation in the emission spectra vas measured upon photoswitching. For all **8**-AuNRs, attempts of measuring an eventual acidochromism of **8** coating the particles were performed upon addition of increasing amounts of acid (trifluoroacetic acid), or base (NH_3, or 1,8-Diazabicyclo[5.4.0]undec-7-ene) were made. Nevertheless, no unambiguous variation of the extinction spectra that could be ascribed to an acid-base equilibrium on **8** was noticed.

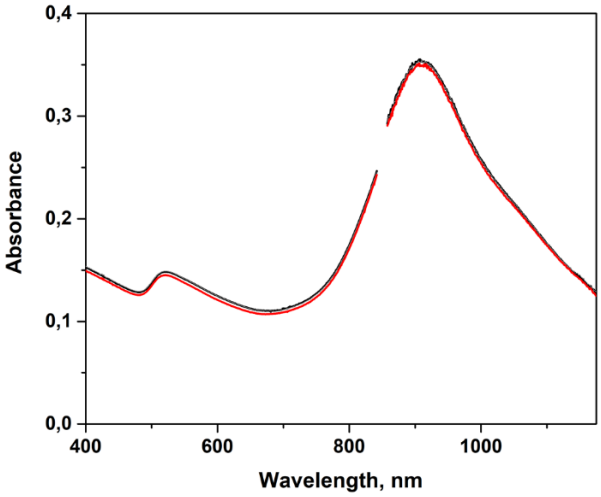

Figure 107. UV-Vis-NIR extinction spectral variation of **AuNR3** stabilised with 11-mercaptoundecanoic acid dispersion in H_2O upon UV light irradiation. *Black trace*, dark. *Red trace*, 120 s UV light irradiation (λ_{max} = 367 nm, P_d = 2.2 mW cm^{-2}).

Ultimately, in order to confirm the role of SP-MC isomerisation of the photochromic thiol **8** in the spectral variations seen here, a blank test was performed on **AuNR3** functionalised with the non-photochromic thiol 11-mercaptoundecanoic acid. The latter colloid showed to be dispersible in water, and upon UV irradiation did not show any remarkable variation in the UV-Vis-NIR extinction spectra of the suspension (Figure 107).

To resume, for AuNR functionalised with the nitrospiropyran derivative **8** we did not visualise any unambiguous evidence for the emergence of a reversible aggregation/clustering behaviour induced by the photo- or acidochromism of the responsive moiety anchored to their surface. Nevertheless, the light-induced variation of the SPR features of the colloid suggests that their photoresponse is dependent on the spectral overlap between the AuNR surface plasmon resonance bands and the absorption spectrum of the MC isomer of **8**.

3.4. 8-functionalised AuNR: dark field light scattering and SERS

In order to obtain a deeper insight on the isomerisation of the photochromic thiol **8** on the surface of the aforementioned gold nanorods, we have performed spectroscopical studies on the **8**-AuNR supported on solid substrates. The experiments were performed in collaboration with Dr. S. Toyouchi, in the group of Prof. H. Uji-i (Katholieke Universiteit Leuven), whom are greatly acknowledged.

In first instance, being puzzled by the light-induced spectral shifts shown by **8**-AuNR colloidal dispersions in THF, we have performed an attempt to measure such spectral variations by dark-field light scattering. Such a technique, taking advantage of the strong light scattering shown by gold colloids in general, and particularly by gold nanorods, allows to measure the SPR features also on single particles supported on solid substrates. Our attempt was aimed to understand whether the spectral variations seen for the colloidal dispersions of **8-AuNR1** and **8-AuNR2** are related to an aggregation process, or to a shift in the local refractive index due to the isomerisation of **8**. Being AuNR supported on solid, the eventual aggregation could be safely excluded. Nevertheless, our attempts were unsuccessful, as, due to the formation of AuNR aggregates upon deposition on solid (see Figure 99-101), it was not possible to record reproducible scattering spectra on single AuNRs. This is also related to the impossibility of locating a single nanorod in the area imaged by the microscope objective, being the spots visualised by dark field optical microscopy diffraction limited, thus not allowing to locate single particles and to distinguish them from bundles and aggregates. The latter usually present strong spectral shifts due to plasmon-plasmon coupling.[235]

Contrarily to dark field scattering spectroscopy, for doing which usually nanoparticle aggregation should be avoided, Raman spectroscopy, and especially surface-enhanced Raman spectroscopy (SERS) takes advantage of such phenomenon, as the hotspots formed by AuNR aggregates give rise to large enhancement factors due to the concentration of the electromagnetic field in such regions of space.[136b, 236] We have therefore undertaken studies by Raman spectroscopy on our **8**-stabilised AuNR in order to obtain a more detailed understanding on the SP-MC isomerisation of the thiol when anchored on the nanoparticles, and if this reaction happens at all to the molecules that are confined on the plasmonic surface. This study could be performed thanks to the distinctive vibrational fingerprint of the two isomers of the photochromic unit, allowing to unambiguously assess about the presence of a specific isomer, thus to follow the SP-MC isomerisation also when such photochrome is chemisorbed on gold surfaces as self-assembled monolayers.[230] Beforehand, we carried out Raman measurements on crystalline powders of **8.a** (without AuNR), without and with UV light irradiation (Figure 108).

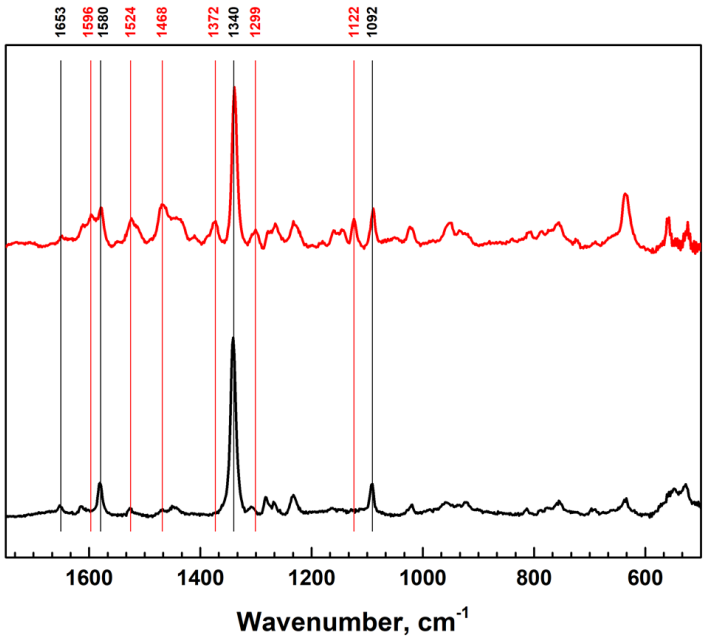

Figure 108. Raman spectra (λ = 785 nm) recorded on powders of **8.a** deposited on glass, before (*black trace*) and after (*red trace*) UV irradiation (30 s, λ_{max} = 367 nm, $P_d \approx 5$ mW cm^{-2}). The most intense vibrational modes are indicated by numbers: in *black*, related to spiropyran (SP), in *red*, related to merocyanine (MC).

The Raman spectrum taken on the powder of **8.a** deposited on glass consists of few intense bands located at 1653, 1614, 1580, 1451, 1340, 1281, 1232 and 1092 cm^{-1}, which could be related to the ring-closed spiropyran (SP) form, in excellent agreement with values reported in the literature for a similar nitrospiropyran derivative, substituted with an alkyl chain on the nitrogen atom of the indoline moiety.[230] We used especially the most intense at 1653, 1580, 1340 and 1092 (marked in black in Figure 108) to monitor the presence of such isomer. Upon irradiation with UV light triggering the isomerisation of SP to the ring-open form merocyanine (MC), we could already by naked eye visualise a strong colour change to purple, plus the appearance of a bright red-orange fluorescence, both confirming the occurrence of the desired photochemical reaction, and at least partial conversion of SP to MC isomer. The Raman spectrum recorded on a UV-irradiated sample indeed shows the appearance of additional vibrational bands, and the most intense were located at 1596, 1524, 1468, 1372, 1299 and 1122 (marked in red in Figure 108), which is also in good agreement with reported values for the MC form.[230]

Knowing the vibrational fingerprint of the two isomeric forms of the photochromic unit present on **8**, we thus investigated our AuNR. The AuNR, analogously as for the dark field light scattering measurements, were deposited by drop-casting the THF dispersions on clean glass slides, and were located by dark field microscope imaging as bright, highly scattering spots. In order to make sure about the reproducibility of the Raman spectra recorded on the **8**-functionalised AuNR, we have measured them in multiple areas of the sample: in all cases, we observed the same Raman signals. Moreover, multiple excitation laser sources were used: 532, 633 and 785 nm. The use of 633 and especially 785 nm excitation wavelength led to the highest signal/noise ratio on the Raman spectra. This evidence, together with the absence of Raman signals from the highest aspect ratio nanorods **8-AuNR3** suggests that resonant excitation with the LSPR band of AuNR is needed to obtain the large electromagnetic enhancement necessary to measure the Raman spectra of our surface-bound photochromes, though further experimental investigation would be needed to clearly demonstrate such hypothesis.

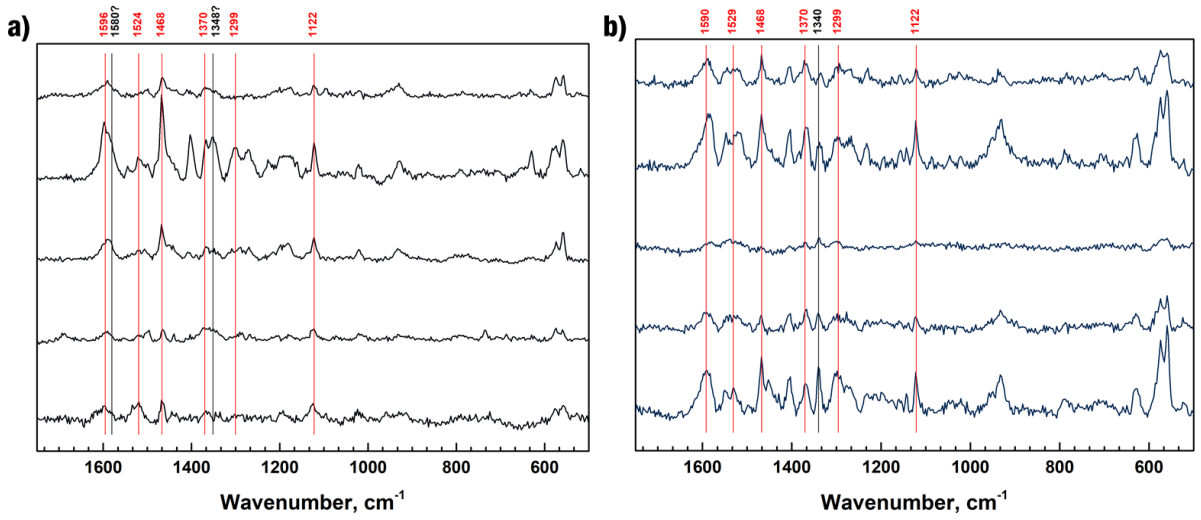

Figure 109. Raman (SERS) of **8**-functionalised AuNR (λ_{exc} = 633 nm), taken without prior light irradiation. Stacked spectra taken on five different randomly chosen spots of the sample. a) **8-AuNR1**. b) **8-AuNR2**. In *red*, signals assigned to MC. In *black*, signals assigned to SP.

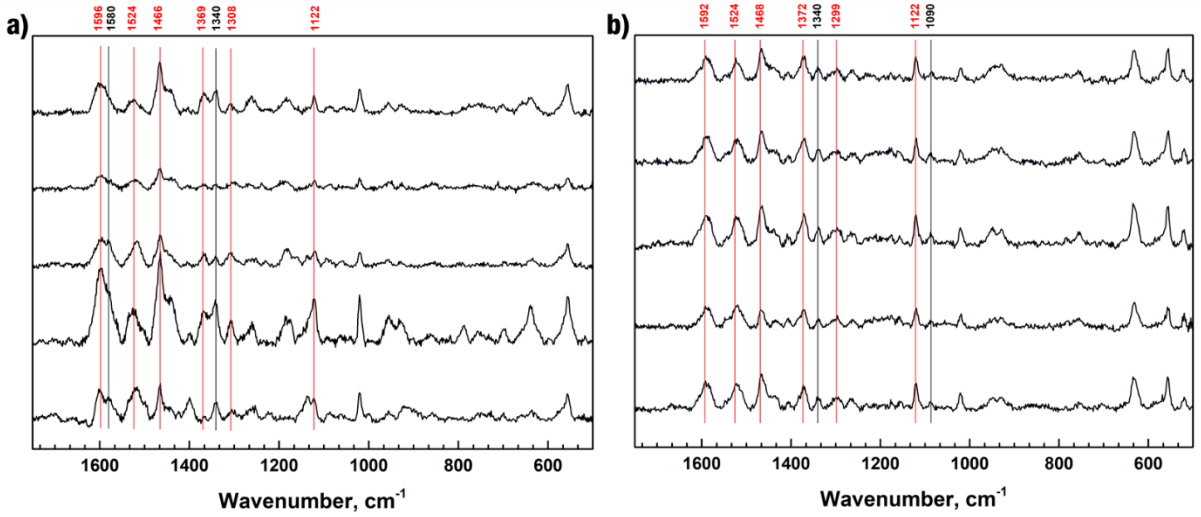

Figure 110. Raman (SERS) of **8**-functionalised AuNR (λ_{exc} = 785 nm), taken without prior light irradiation. Stacked spectra taken on five different randomly chosen spots of the sample. a) **8-AuNR1**. b) **8-AuNR2**. In *red*, signals assigned to MC. In *black*, signals assigned to SP.

The spectra measured on **8**-AuNR showed to be reproducible, and interestingly gave the same sets of signals for both **8-AuNR1** and **8-AuNR2** while, as previously mentioned, we could not measure any clearly distinguishable Raman signal on **8-AuNR3**. Interestingly, on both **8-AuNR1** and **8-AuNR2**, the SERS spectra show the most intense bands at ~ 1595, 1524, 1468, ~ 1370, ~ 1300 and 1122 cm^{-1} (marked in red in Figure 109-110). Such peaks correspond to the vibrational fingerprint of merocyanine unit, as discussed earlier (Figure 108); moreover, the spectroscopic fingerprint of SP at 1580, 1340 and 1090 cm^{-1} results barely distinguishable. These evidences suggest that in such conditions, upon grafting the nitrospiropyran photochromic unit on the AuNR surface as a self-assembled monolayer of **8**, already in absence of external light irradiation switching the SP to MC isomer, the switch is present (almost) only in the latter form, thus the MC is the stable form in the dark in such conditions. Thus, the occurrence of such phenomenon could be the reason for the limited photochromism of our system. Nonetheless, we have performed some attempts to switch **8** on **8-AuNR1** by in-situ irradiating with multiple

light sources, thus to understand whether the former retains its photo- and acidochromism when immobilised on the plasmonic nanorods. For the purpose, we have used appropriate light sources to switch the photochromic unit in the two ways: SP → MC, and MC → SP by either standard one-photon excitation, and also by two-photon light pulses. The latter was attempted as spiropyran-merocyanine derivatives are known for possessing large two-photon cross sections,[87c, 237] in such case the possibility of being interconverted between their two forms by two-photon absorption in the near-infrared region is increase further by the enhancement of two-photon processes typically occurring on the surface of AuNR.[238] We thus envisioned our systems, **8**-functionalised AuNR, as the ideal candidate for performing such experiments.

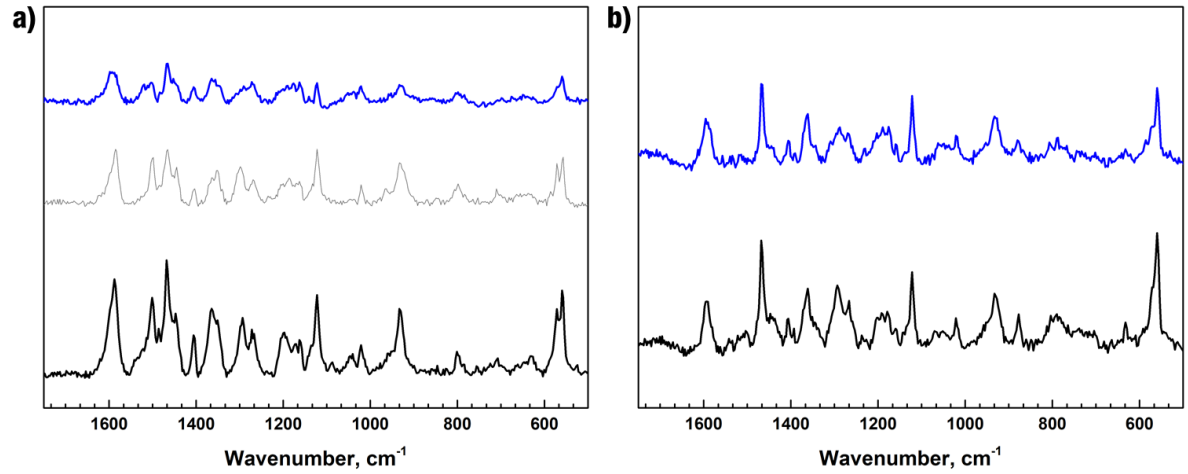

Figure 111. Raman (SERS) spectra of **8-AuNR1** deposited on glass substrates (λ_{exc} = 633 nm) upon attempts to switch MC to SP form. a) 1-photon irradiation, λ_{irr} = 532 nm. *Black trace*, no irradiation. *Grey trace*, 10 s (1.5 OD filter). *Blue trace*, 30 s (1.5 OD filter). b) 2-photon irradiation (λ_{irr} = 1040 nm). *Black trace*, no irradiation. *Blue trace*, 60 s (0.08 OD filter).

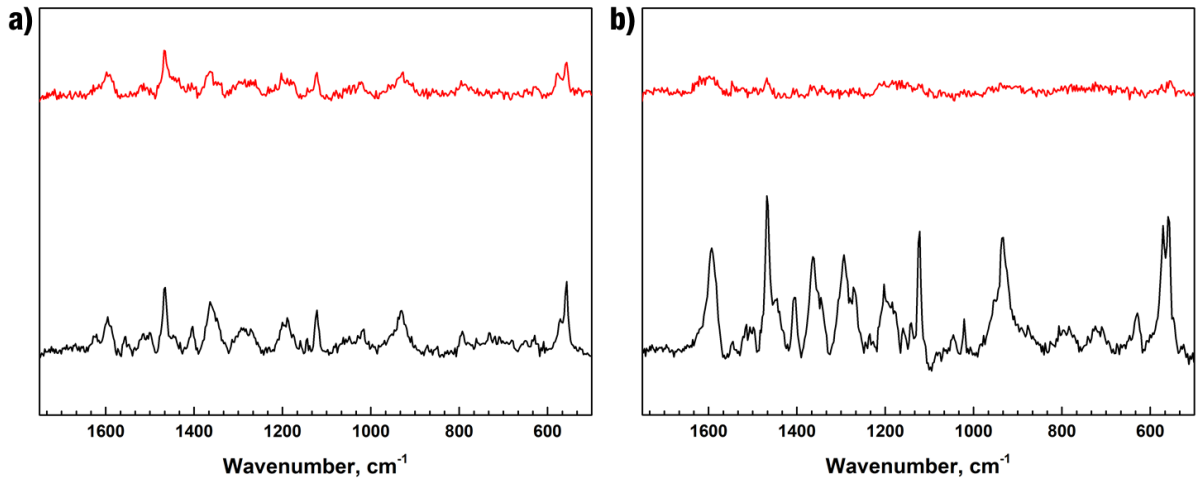

Figure 112. Raman (SERS) spectra of **8-AuNR1** deposited on glass substrates (λ_{exc} = 633 nm) upon 2-photon λ_{irr} = 780 nm irradiation. a) *Black trace*, no irradiation. *Red trace*, 12 s (low intensity, 2.5 OD filter). b) *Black trace*, no irradiation. *Red trace*, 10 s (0.9 OD filter).

For our experiments, we have attempted to induce the MC → SP isomerisation by 1-photon irradiation, using a 532 nm low-intensity continuous wave laser, while 2-photon irradiation was performed addressing the sample with a 1040 nm femtosecond laser. In order to understand whether any changes to the Raman spectra could be induced by light irradiation, also the wavelengths inducing the reverse SP → MC reaction were used, *i.e.* 1-photon irradiation was

performed with 365 nm non-coherent light, while 2-photon irradiation was provided by 780 nm femtosecond pulsed laser. Unfortunately, none of these light sources could induce noticeable changes in the Raman spectra that could be ascribed to the isomerisation of the photochrome grafted on AuNR. As visible in Figure 111, upon shining visible, or NIR 2-photon light on the **8-AuNR1** did not lead to the appearance of new Raman peaks related to the SP species: on the contrary, increasing light irradiation power only led to a loss of the vibrational features previously observed, as this could be imputed to the occurrence of the phototermal effect, leading to the degradation of the nanoparticle surface coating. Analogously, the use of 1- or 2-photon light to drive the reverse (SP → MC) reaction did not lead to any changes in the vibrational spectra, except again an evident loss of the spectral features, symptom of the degradation of **8**. Exposure of the samples to ammonia vapours was attempted, also with subsequent visible (532 nm) light irradiation, nevertheless further failure in observing variations of the aforementioned Raman features suggest the absence of acidochromism.

With the experimental evidences obtained to date, we thus can safely state that the spiropyran-merocyanine isomerisation is completely hindered by the immobilisation of **8**, tethered to the plasmonic nanoparticles surface. This loss of any photochromic and acidochromic properties could be related to multiple factors. On the one hand, the crowding due to the reciprocal vicinity of the chromophores when confined into self-assembled monolayers on the nanoparticles surface could lead to multiple chromophore-chromophore interactions, *e.g.* exciton coupling and formation of *H*- and *J*- aggregates, thus delocalising excitation energy and all together quenching the desired photochromic activity. On the other hand, also the vicinity of the photoactive unit to the surface of the nanomaterial due to the use of simple alkyl spacers could be another likely reason for the complete absence of photoswitching of **8**, in such case possibly originated by the occurrence of nonradiative energy transfer to the surface plasmon resonance of AuNR.

Conversely, the evidences gained here by means of Raman spectroscopy helped us to confirm what occurs, or more correctly *does not* occur on the surface of AuNR, yet from such experiments we could not obtain any answer regarding the extinction spectral shifts visualised upon irradiating with UV and visible light the **8**-AuNR dispersions in THF (Figure 104-106). The SERS experiments allowed us to assess the spectroscopic fingerprint of the molecules located in the immediate surroundings of the plasmonic substrate, hence on the AuNR surface, but not what is situated farther away from it. It is likely that the shifts seen in the extinction spectra are related to photochromic species not immobilised on the nanoparticles surface. This hypothesis is coherent with the observation made by means of scanning electron microscopy about the embedment of AuNR into an amorphous matrix which nature yet remains unknown upon their functionalisation various thiols. It is thus likely that in such organic matrix that we did not succeed to remove upon purification, some photochromic units are still included, hence the light-triggered isomerisation of the latter would be the origin of the aforementioned spectral shifts.

However, to date these remain only hypotheses which need further experimental evidences to be confirmed. In our opinion, one (conceptually) simple strategy to tackle part of these issues could be to vary, and specifically to increase the length of the dielectric spacer separating our plasmonic substrate to the photochrome. Increasing the distance between the two functional units could at least provide a strategy to prevent the quenching resulting from the interaction

with the plasmon resonance of the nanoparticles. Nonetheless, in order to successfully follow such strategy, modification of the chemistry used to graft the photochrome to the gold colloid would be required: alkanethiols are not suitable spacers to perform this task, as the length of the spacer needed for this purpose could range between 10-30 nm.[136e, 238]

4. CONCLUSIONS

We have reported here about the realisation of hybrid nanomaterials obtained by the coupling of noble metal gold nanoparticles, *i.e.* gold nanorods (AuNR) to a nitrospiropyran photochromic derivative **8**. The latter was employed as photoswitchable unit owing to the considerable variation of the electrical dipole moment of its two isomers: the bulky spiropyran, and the planar, conjugated merocyanine. Such a light-activated switch was combined with AuNR, exploiting the tunability of their surface plasmon resonance bands and the high sensitivity of the latter towards the variation of their dielectric medium. Different AuNR with varying aspect ratio were employed, in order to study the effect of the spectral overlap between the absorption and emission spectra of merocyanine and the surface plasmon resonance bands of the nanomaterial. The photoswitching of **8**-AuNR colloidal dispersions in liquid led to the observation of an intriguing behaviour due to the (partially) reversible shift of their UV-Vis-NIR extinction spectra, as this appeared to be dependent on the surface plasmon resonance wavelength of the nanorods used. Nevertheless, the use of SERS technique showed that isomerisation of the photoswitch could not be attained on the nanomaterial surface, thus enlightening how challenging is the realisation of hybrid systems capable of responding to light stimuli.

Chapter 7.

SUMMARY AND OUTLOOKS

In summary, the work performed within this thesis has been aimed at the characterisation of novel multichromophoric systems based on the inclusion of multiple photochromic units within single scaffolds, the latter scaling from molecular edifices to anisotropic nanoparticles, with a specific focus on the study of the emerging properties due to the combination of the various components. We have presented here three examples of systems switchable by optical stimuli, taking advantage of photochromic building blocks coming from the three most well-known main families of photoswitches available, being azobenzene, diarylethene and spiropyran, according to the property of the system that was desirable to modify by means of an optical input.

In the first experimental chapter, a novel family of multi-azobenzene photoswitches has been discussed. Such compounds, presenting a star-shaped character and a rigid aromatic backbone, were realised in order to exploit them as molecular-scale actuators, the use of which allowed to give rise to 2D surface-confined self-assemblies whose topology could be controlled between multiple states by using different light stimuli. Here we have employed a conformationally rigid molecular scaffold design in order to maximise the conformational variation of the molecules upon their photoisomerisation. Knowing the presence of through-bond and through-space interactions between the switches would have been the most likely source of quenching of their photochromic character, we have explored the role of the electronic decoupling between the units, potentially affecting their photochromic performances. The design of such systems, imposing the switches to branch out from a central trisubstituted 1,3,5-benzene core was chosen in order to limit the π-conjugation between the photochromes belonging to the same molecule, thus allowing their efficient isomerisation and the independent behaviour of each unit from the state of the neighbouring ones, but at the same time maintaining a high structural rigidity. An in-depth experimental investigation was performed by employing complementary instrumental techniques, ranging from UV-Vis absorption spectroscopy to high performance liquid chromatography and even advanced mass spectrometry methods such as ion mobility to visualise all the possible isomers of the photochromic units. The additivity of the UV-Vis absorption spectra relative to the all-(*E*) isomer, together with the appearance of clear isosbestic points upon photoswitching of mono-, bis- and tris(azobenzene) compounds provided unambiguous evidence for an almost complete absence of electronic delocalisation

between the chromophores. The latter allowing for remarkably efficient photoswitching of all azobenzenes, as evidenced by their photoisomerisation quantum yields, not substantially different from the values showed by reference mono-azobenzenes. Moreover, all star-shaped compounds showed *Z*-rich UV photostationary states. Ion mobility mass spectrometry was exploited for the first time to study multi-photochromic compounds revealing the occurrence of a large molecular shape change in such rigid star-shaped azobenzene derivatives. A detailed picture of the self-assembly of the tris(azobenzene) derivative to form surface-confined dynamic structures was also given by means of scanning tunnelling microscopy. For the first time it was possible to identify by STM the existence of multiple isomeric states of a multiphotochromic compound in single-component self-assembled networks with a high level of details. Thanks to this, our study enabled to gain an insight on the subtle interplay occurring between the non-directional and directional intermolecular interactions playing a role in defining the structural topology of the surface-confined assemblies. In addition, by performing qualitative STM imaging on dry films of our tris(azobenzene) derivative at the graphite-air interface and their subsequent *in-situ* UV irradiation, it was possible to verify that the switching occurs in such conditions also to the molecules physisorbed on the solid substrate.

We believe that the present results could be of great value for further research on multiphotochromic systems, and could clarify the role of non-covalent interactions in the supramolecular self-assembly of similar systems. Following the high potential of azobenzenes to be employed as light-powered molecular actuators, we envision that the compounds presented here could be excellent candidates for the realisation of phototriggered host-guest systems. For instance, metal-organic frameworks (MOFs) have long been regarded as the future materials for gas- and small-molecule storage following their precise structure and unrivalled internal surface area, together with the possibility to finely tune their functionalities. For the realisation of such materials, rigid, aromatic carboxylic acids represent one of the most used building blocks, and it was seen that molecules possessing C_3 symmetry such as 1,3,5-benzenetribenzoic acid and similar derivatives were particularly suitable for realising MOFs showing extremely high porosity and specific surface area.[5c] Having verified the good photochromic performance of our rigid, C_3-symmetric multi(azobenzene) scaffold, we thus foresee this as a perfect candidate for the making of novel MOFs which guest capture-release could be light-powered. In this context the use of light to induce the release of a guest trapped in the MOF cavities provides a low-energy consumption alternative for the controlled removal of the adsorbates which are usually hard to extract due to their stabilisation inside such confined space.

In the second experimental chapter, we have discussed about the investigation of a photoswitchable fluorophore whose emission intensity could be tuned in highly contrasted fashion thanks to its multiphotochromic design. A family of tetraphenylporphyrins has been used as a fluorescent scaffold for four dithienylethene units by covalently linking the latter via *meta*-phenyl spacers. The use of such design based on four photoswitches arranged around a porphyrin framework showed that the original photochromic activity of the functional units was retained upon their inclusion within the large molecular framework. Moreover, the original photophysical properties of the fluorophore were retained when the photochromes were residing in their open-ring, UV-absorbing form. Upon UV light-activated ring closure of the diarylethene units, quenching of the porphyrin fluorescence was seen occurring by resonance

energy transfer, due to the large spectral overlap occurring between the fluorophore emission spectrum and the absorption of the ring-closed form of the photochrome. Upon DTE photoswitching, a nearly complete quenching of the porphyrin's fluorescence was attained, providing a highly contrasted readout of the switching event. In addition to their photoregulated fluorescence, the possibility to trigger the switch and detect the output at very distinct wavelengths renders these systems of interest for applications in optoelectronic memory devices. At last, we have also been able to demonstrate the applicability of our switchable dyes as photo-rewritable fluorescent ink, the latter opening perspectives towards its application in all-optical memory storage and fluorescence microscopy imaging.

A vast corpus of research has been done towards the development of reversibly photoswitchable fluorophores, particularly for their tremendous potential in the field of optoelectronics and superresolution microscopy. On the one hand, despite the promising results, the path towards the realisation of convenient small-molecule synthetic probes and chemical markers for fluorescence microscopy is still long. The main challenges yet open to date are not only related to the chemical- and photostability of the fluorophores, together with the resistance to fatigue of the photoswitch, but also to the possibility of making such synthetic dyes water-soluble and to bind them to biomolecules, thus enabling their use for superresolution microscopy imaging on biological samples. Thus far, the successful examples of synthetic photochromic switches that were employed for such application are limited,[82b, 82c] hence there is still plenty of room for the synthesis and improvement of reversibly photoactivated fluorophores in order to allow their application in life sciences. On the other hand, concerning the potential use of photoswitchable dyes for optical information storage, a fundamental aspect that has been to date only partially faced concerns data retention and the possibility of performing non-destructive readout, thus to excite their fluorescence and to photoswitch its intensity with orthogonal stimuli. In fact, an intrinsic problem of the most widely used fluorophore-photoswitch dyad architectures used for this purpose consists on the fact that these systems undergo reversible emission quenching following an intramolecular energy transfer mechanism, and in most cases the excitation of the fluorophore also induces the switching reaction, thus resulting in destructive readout of the written information. So far, a few reports were provided concerning the solution of this problem, in some cases utilising an electron transfer mechanism to quench the fluorophore emission, avoiding the undesired photochromic reaction.[239] We thus believe that the synthetic challenge to obtain viable organic materials for all-optical information storage is still open towards their future improvement.

In the last experimental chapter, we have extended our concept of “multiphotochromic system” to a different length scale. With such objective, we have employed photochromic units that are particularly sensitive to their local environment and chemisorbed them to nanoparticles presenting shape anisotropy. In such a way, the purpose was to expose the photochromes chemisorbed to surfaces with different properties (*e.g.* curvature radius) to different intermolecular interactions between neighbouring molecules. This was seen promising for the realisation of objects having multiple distinct photochromic responses, due to the presence of photoswitches tethered to the different faces of the anisotropic gold colloid. Hybrid nanomaterials were realised by coupling anisotropic noble metal gold nanoparticles, *i.e.* gold nanorods to a nitrospiropyran photochromic derivative. The latter was employed as

photoswitchable unit owing to the considerable variation of the electrical dipole moment of its two isomers: the bulky spiropyran, and the planar, conjugated merocyanine. The latter property was seen highly appealing for both tuning the nanoparticle aggregation, and also to perturb the surface plasmon resonance of the gold nanorods in a remotely controlled fashion, with the use of light. Different AuNR with varying aspect ratio were employed, in order to study the effect of the spectral overlap between the absorption spectra of the open-ring merocyanine isomer and the surface plasmon resonance bands of the nanomaterial. The photoswitching of colloidal dispersions in liquid led to the observation of an intriguing behaviour due to the (partially) reversible shift of their UV-Vis-NIR extinction spectra, as this appeared to be dependent on the surface plasmon resonance wavelength of the nanorods used. Nevertheless, the use of surface-enhanced Raman scattering to monitor the state of the spiropyran-based switch showed that isomerisation of the photoswitch could not be attained on the nanomaterial surface, the latter being present only in the merocyanine form, thus enlightening how challenging is the realisation of hybrid systems capable of responding to light stimuli.

We suggest that the origin of this limited photoactivity should be imputed to two main causes: the vicinity of the switch to the metallic surface, together with the reciprocal crowding of the neighbouring photochromes within the chemisorbed self-assembled monolayer on the nanoparticles surface. Despite the failure in obtaining a clear photoresponse in such hybrid systems, we believe that the inclusion of a photochromic remote control to nanomaterials that possess anisotropic character constitutes a challenge of great scientific interest. On the one hand, the shape anisotropy allows to access aggregation behaviours that cannot be obtained from objects possessing spherical symmetry. Photoswitches have already been used to control the aggregation of nanometre-scale colloids, nevertheless such light-controlled behaviour, except few examples, showed the formation of amorphous aggregates. We envision that the use of anisotropic building blocks which aggregation could be remotely and reversibly controlled would allow to obtain the on-demand formation of "supercrystals" possessing long-range order, thus with great potential for technological application. Additionally, gold nanorods represent an extremely interesting nanomaterial due to their tuneable plasmonic properties, together with the possibility of generating strong electromagnetic fields on their immediate surroundings, giving rise to the enhancement of a variety of optical processes, such as Raman scattering or light emission. Thus, the combination of a photochromic molecule presenting at the same time large dipole moment variation, together with an emission *turn-on* behaviour upon isomerisation motivated our initial research and opened questions that still remain unanswered. Further research aimed at the improvement of such system could be performed. We believe that upon resolving the two main issues hampering the photoreactivity of the spiropyrans used *i.e.* nanoparticle-switch and switch-switch vicinity could allow us to access the functionality desired. Thus, in order to successfully attain the required switching, a possible strategy would be to increase such distance and to "dilute" the switches on the nanoparticle surface. This task cannot evidently be performed by using alkanethiols as both grafting moieties and dielectric spacers. On the contrary, we believe that a promising strategy would be to use a core-shell architecture, thus to grow dielectric silica shells on the anisotropic colloid. This would allow to precisely control the photochrome-AuNR distance in the range of several nanometres needed for the purpose and also to tune the loading of the photochrome on the surface, thus preventing dye-dye interactions in such environment.

All in all, nowadays a great deal of attention has been dedicated to the highly challenging goal of obtaining fully working multi-photochromic systems, and the basic requirements for their satisfying switching performance have been established. This wide interest stems from the possibility to use such advanced architectures to increase the complexity and functionality of synthetic, remotely controlled stimuli-responsive systems. However, most of the successful examples existing to date do not allow for their multi-addressability, as in most cases such architectures are formed by including in the same object multiple identical switches. On the contrary, the most appealing goal in the development of multi-photochromic architectures consists in the realisation of systems switchable between various, singly addressable states with wavelength-selective control. The latter is typically attained only with systems which undergo irreversible light activation, and only few reports are available regarding photoswitchable systems that can be reversibly modulated between multiple states with orthogonal stimuli.[4a, 93] We believe that there is still plenty of room for the development of multi stimuli-responsive architectures of which several technological fields could benefit, and envision this as the principal direction for the scientific research in the field within the next few years.

APPENDIX I

Z → *E* thermal isomerisation studies on 1-4 – kinetic data

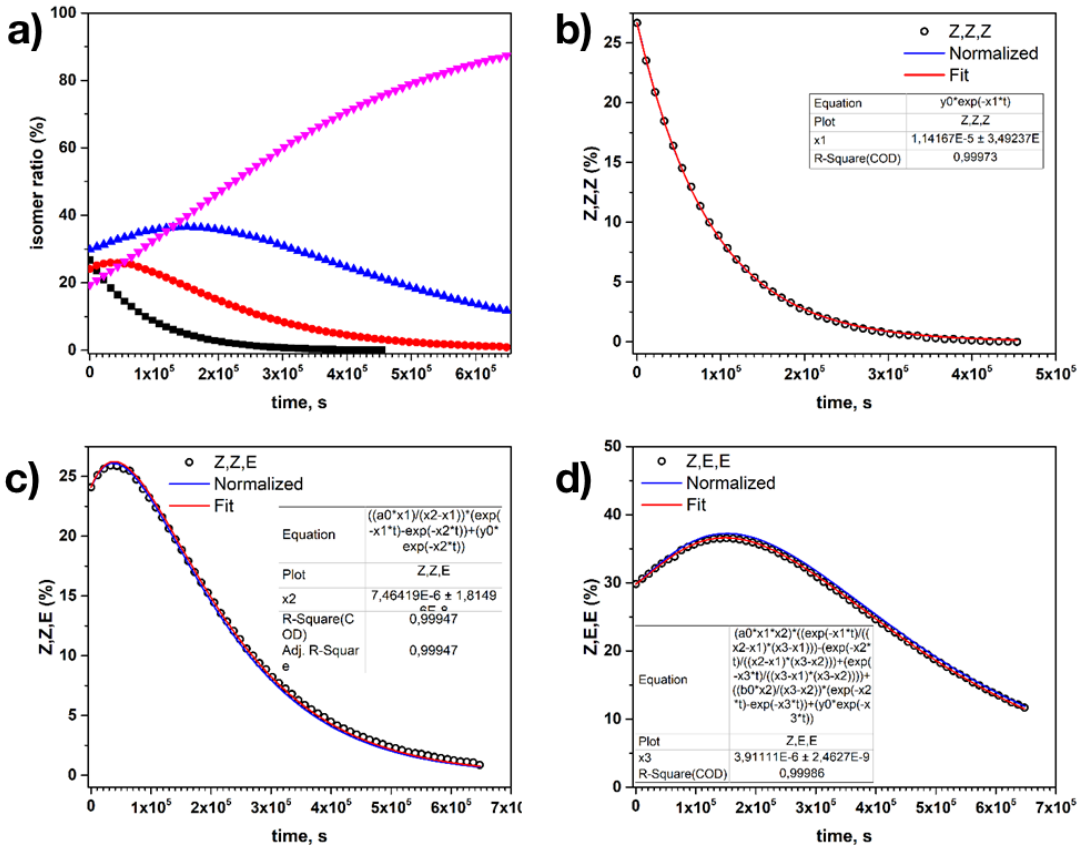

Figure A I 1. a) Thermal evolution of the isomers ratio (Z,Z,Z)-**1** (black squares), (Z,Z,E)-**1** (red dots), (Z,E,E)-**1** (blue triangle), (E,E,E)-**1** (pink triangle) followed at 25 °C by HPLC. The white dots show the amount of b) (Z,Z,Z)-**1**, c) (Z,Z,E)-**1**, and d) (Z,E,E)-**1** versus heating time. The red solid line is the fit of the temporal evolution yielding the rate constants k_1, k_2 and k_3 for each isomer according to Eq. 4.4-4.6.

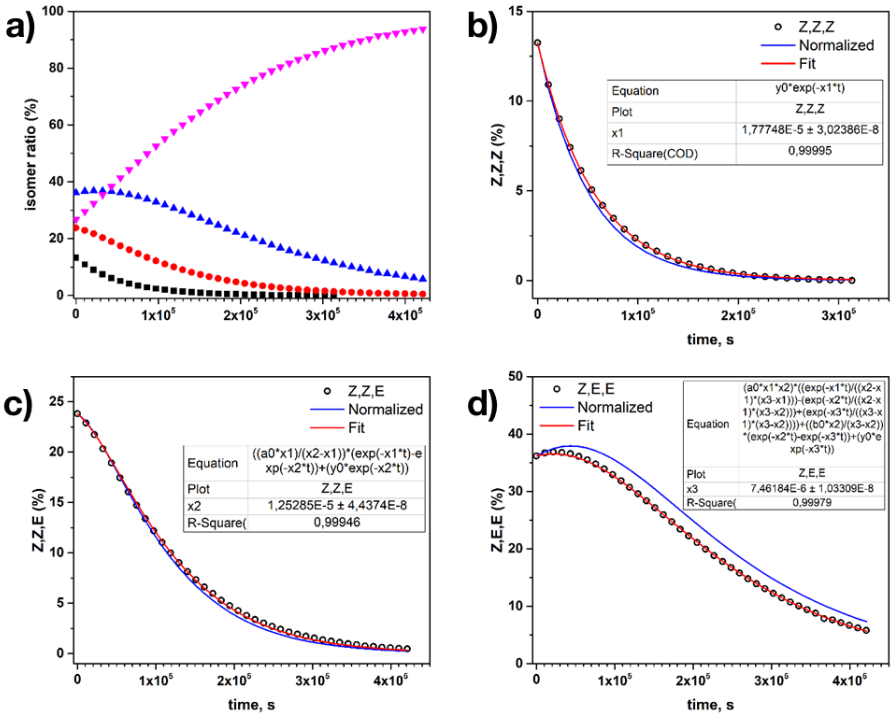

Figure A I 2. a) Thermal evolution of the isomers ratio (Z,Z,Z)-**1** (black squares), (Z,Z,E)-**1** (red dots), (Z,E,E)-**1** (blue triangle), (E,E,E)-**1** (pink triangle) followed at 30 °C by HPLC. The white dots show the amount of b) (Z,Z,Z)-**1**, c) (Z,Z,E)-**1**, and d) (Z,E,E)-**1** versus heating time. The red solid line is the fit of the temporal evolution yielding the rate constants k_1, k_2 and k_3 for each isomer according to Eq. 4.4-4.6.

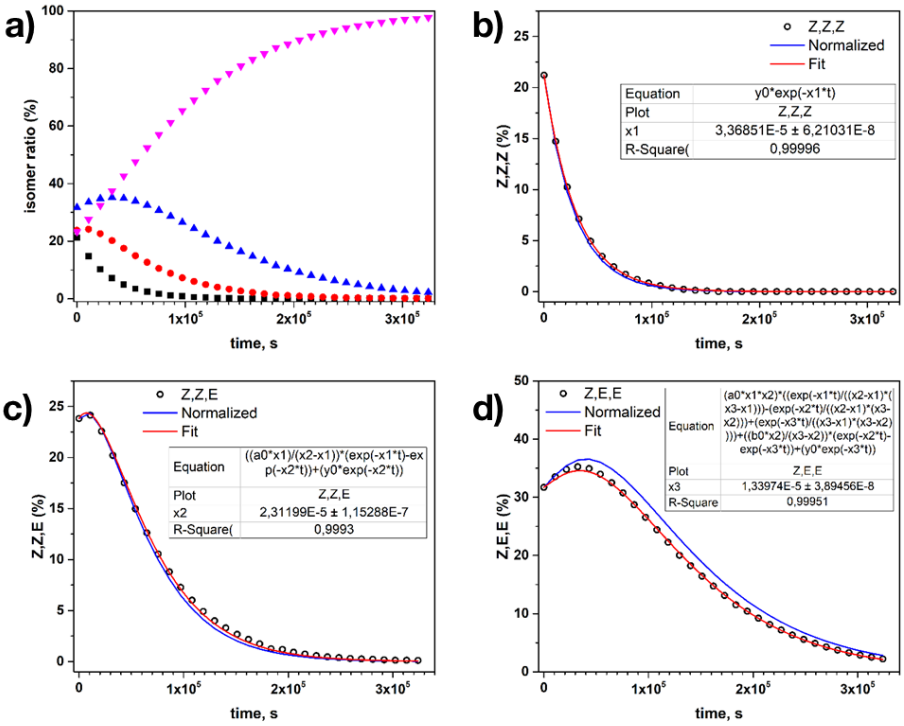

Figure A I 3. a) Thermal evolution of the isomers ratio (Z,Z,Z)-**1** (black squares), (Z,Z,E)-**1** (red dots), (Z,E,E)-**1** (blue triangle), (E,E,E)-**1** (pink triangle) followed at 35 °C by HPLC. The white dots show the amount of b) (Z,Z,Z)-**1**, c) (Z,Z,E)-**1**, and d) (Z,E,E)-**1** versus heating time. The red solid line is the fit of the temporal evolution yielding the rate constants k_1, k_2 and k_3 for each isomer according to Eq. 4.4-4.6.

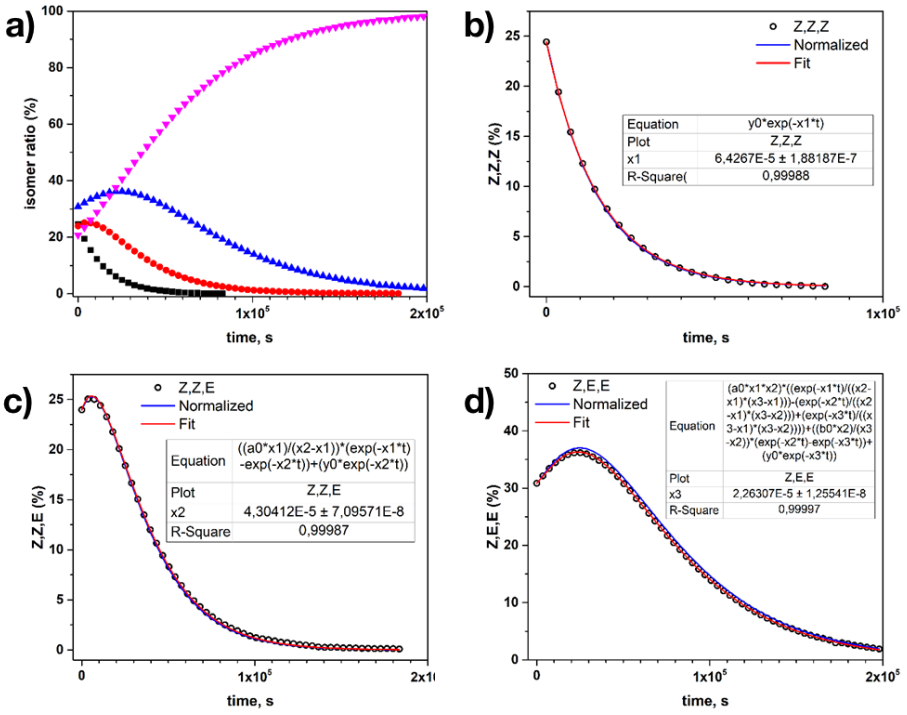

Figure A I 4. a) Thermal evolution of the isomers ratio (Z,Z,Z)-**1** (black squares), (Z,Z,E)-**1** (red dots), (Z,E,E)-**1** (blue triangle), (E,E,E)-**1** (pink triangle) followed at 40 °C by HPLC. The white dots show the amount of b) (Z,Z,Z)-**1**, c) (Z,Z,E)-**1**, and d) (Z,E,E)-**1** versus heating time. The red solid line is the fit of the temporal evolution yielding the rate constants k_1, k_2 and k_3 for each isomer according to Eq. 4.4-4.6.

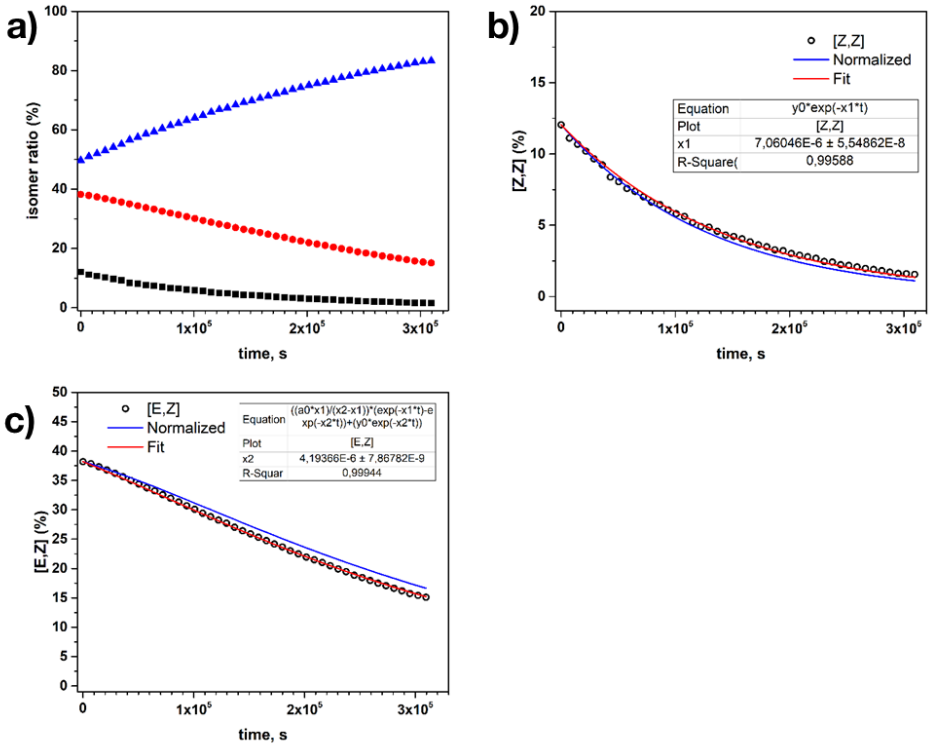

Figure A I 5. a) Thermal evolution of the isomers ratio (Z,Z)-**2** (black squares), (Z,E)-**2** (red dots), (E,E)-**2** (blue triangle) followed at 25 °C by HPLC. The white dots show the amount of b) (Z,Z)-**2**, c) (Z,E)-**2** versus heating time. The red solid line is the fit of the temporal evolution yielding the rate constants k_1 and k_2 for each isomer according to Eq. 4.4-4.6.

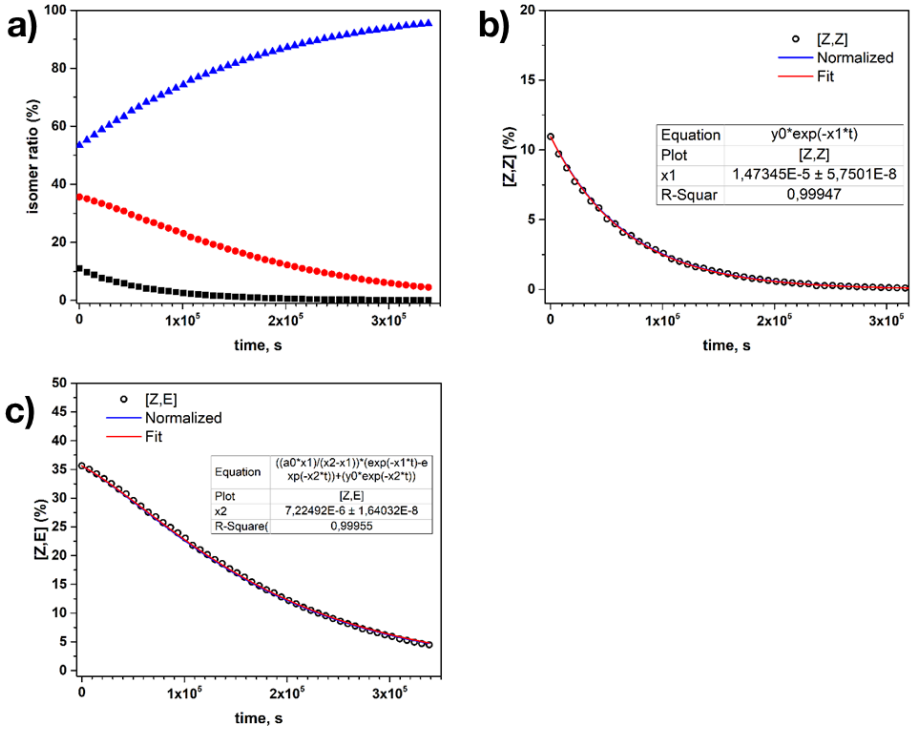

Figure A I 6. a) Thermal evolution of the isomers ratio (Z,Z)-**2** (black squares), (Z,E)-**2** (red dots), (E,E)-**2** (blue triangle) followed at 30 °C by HPLC. The white dots show the amount of b) (Z,Z)-**2**, c) (Z,E)-**2** versus heating time. The red solid line is the fit of the temporal evolution yielding the rate constants k_1 and k_2 for each isomer according to Eq. 4.4-4.6.

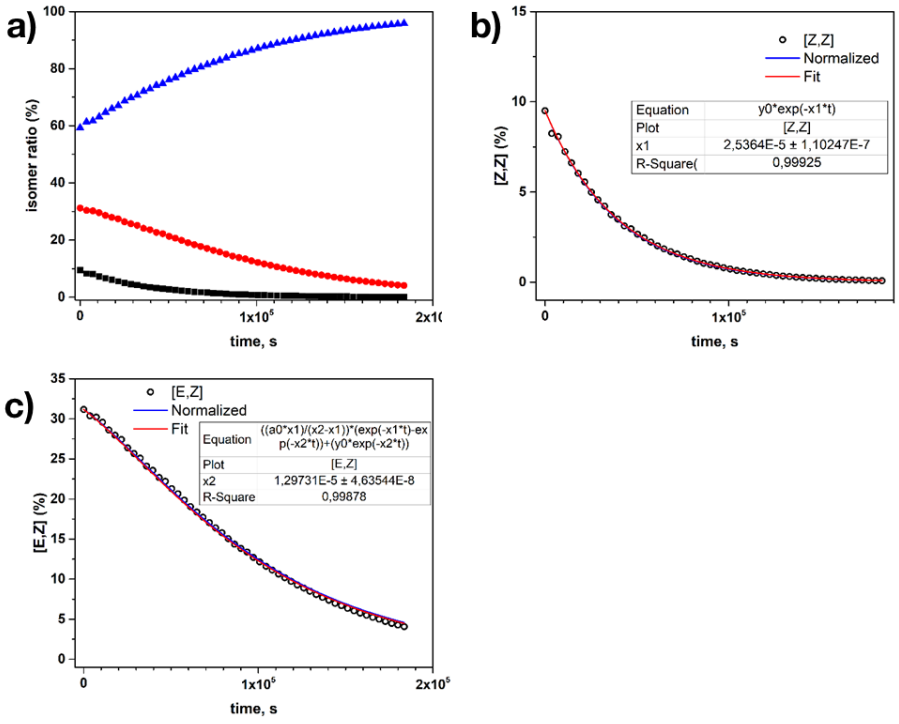

Figure A I 7. a) Thermal evolution of the isomers ratio (Z,Z)-**2** (black squares), (Z,E)-**2** (red dots), (E,E)-**2** (blue triangle) followed at 35 °C by HPLC. The white dots show the amount of b) (Z,Z)-**2**, c) (Z,E)-**2** versus heating time. The red solid line is the fit of the temporal evolution yielding the rate constants k_1 and k_2 for each isomer according to Eq. 4.4-4.6.

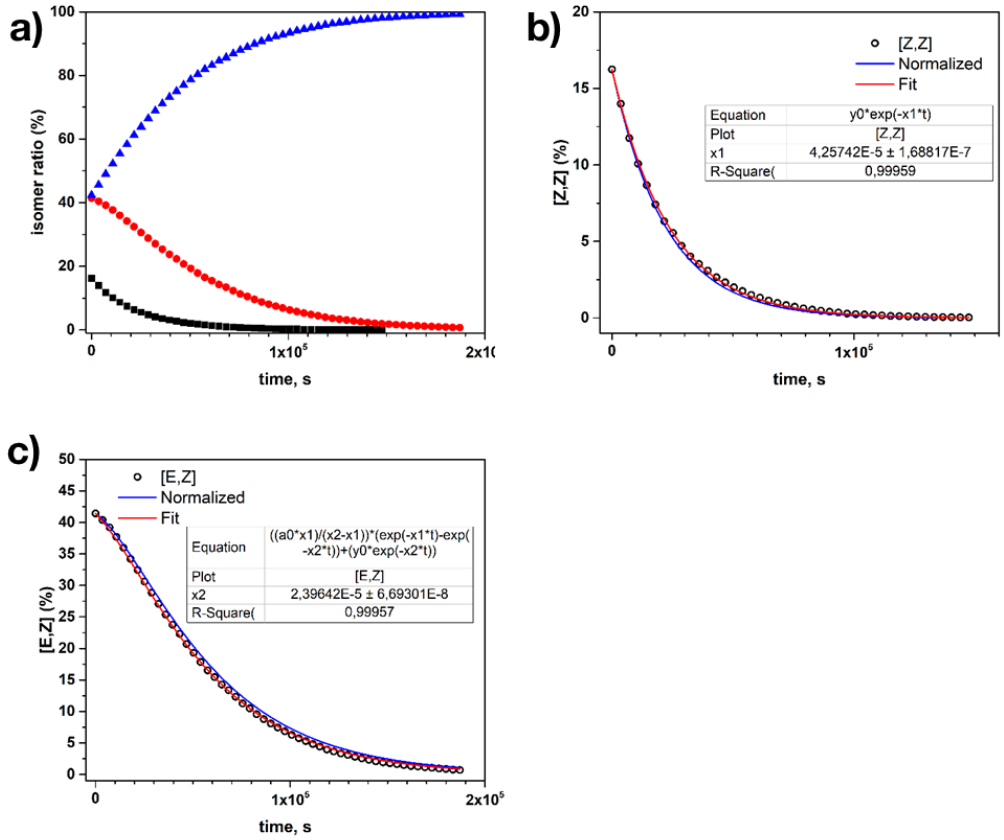

Figure A I 8. a) Thermal evolution of the isomers ratio (Z,Z)-**2** (black squares), (Z,E)-**2** (red dots), (E,E)-**2** (blue triangle) followed at 40 °C by HPLC. The white dots show the amount of b) (Z,Z)-**2**, c) (Z,E)-**2** versus heating time. The red solid line is the fit of the temporal evolution yielding the rate constants k_1 and k_2 for each isomer according to Eq. 4.4-4.6.

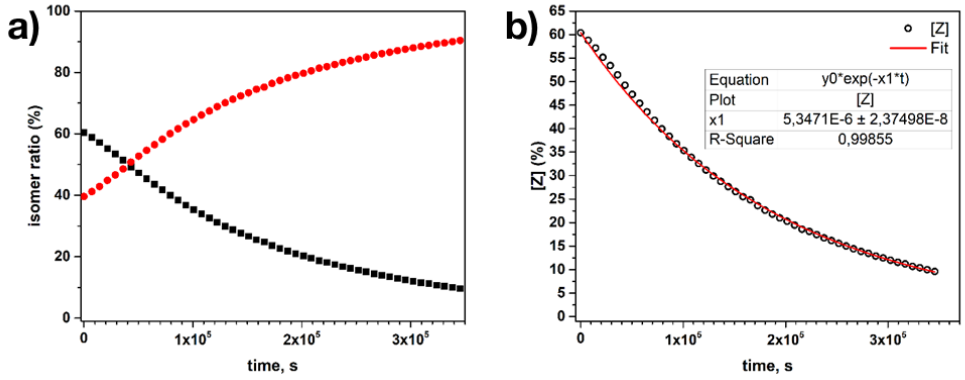

Figure A I 9. a) Thermal evolution of the isomers ratio (Z)-**3** (black squares), (E)-**3** (red dots) followed at 25 °C by HPLC. The white dots show the amount of b) (Z)-**3** versus heating time. The red solid line is the fit of the temporal evolution yielding the rate constant k_1 according to Eq. 4.4-4.6.

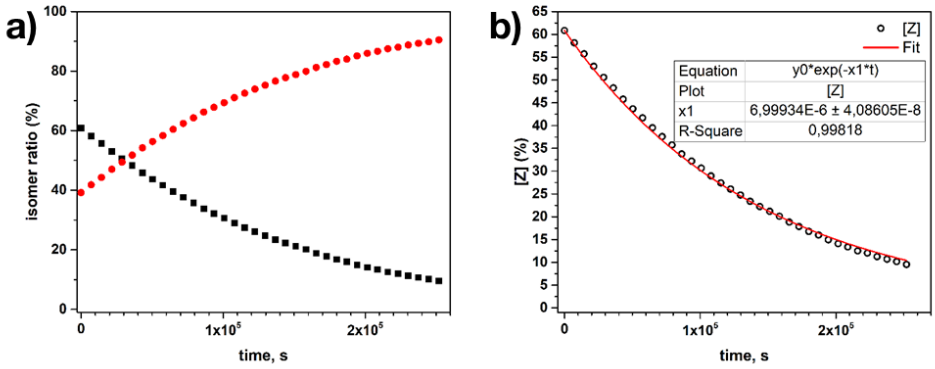

Figure A I 10. a) Thermal evolution of the isomers ratio (Z)-**3** (black squares), (E)-**3** (red dots) followed at 30 °C by HPLC. The white dots show the amount of b) (Z)-**3** versus heating time. The red solid line is the fit of the temporal evolution yielding the rate constant k_1 according to Eq. 4.4-4.6.

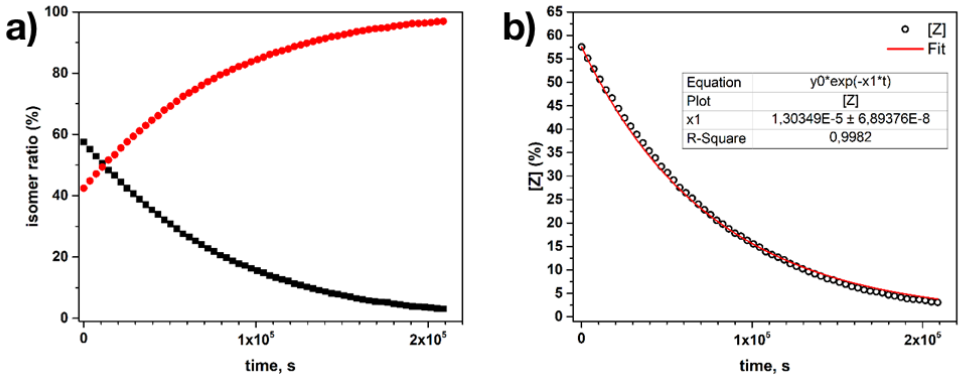

Figure A I 11. a) Thermal evolution of the isomers ratio (Z)-**3** (black squares), (E)-**3** (red dots) followed at 35 °C by HPLC. The white dots show the amount of b) (Z)-**3** versus heating time. The red solid line is the fit of the temporal evolution yielding the rate constant k_1 according to Eq. 4.4-4.6.

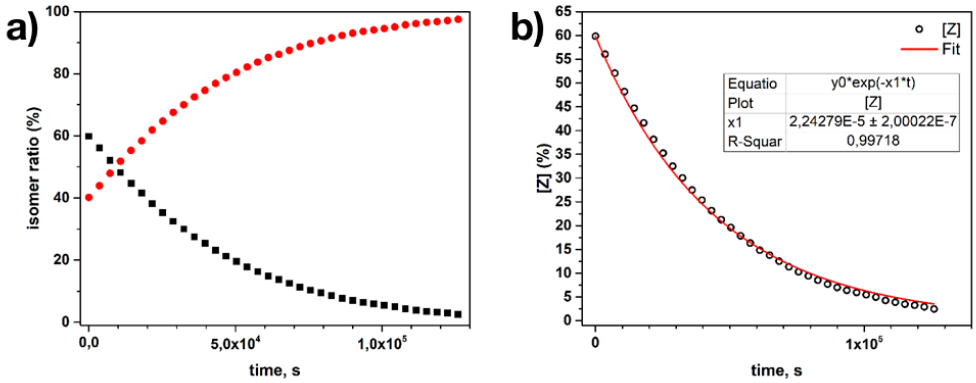

Figure A I 12. . a) Thermal evolution of the isomers ratio (Z)-**3** (black squares), (E)-**3** (red dots) followed at 40 °C by HPLC. The white dots show the amount of b) (Z)-**3** versus heating time. The red solid line is the fit of the temporal evolution yielding the rate constant k_1 according to Eq. 4.4-4.6.

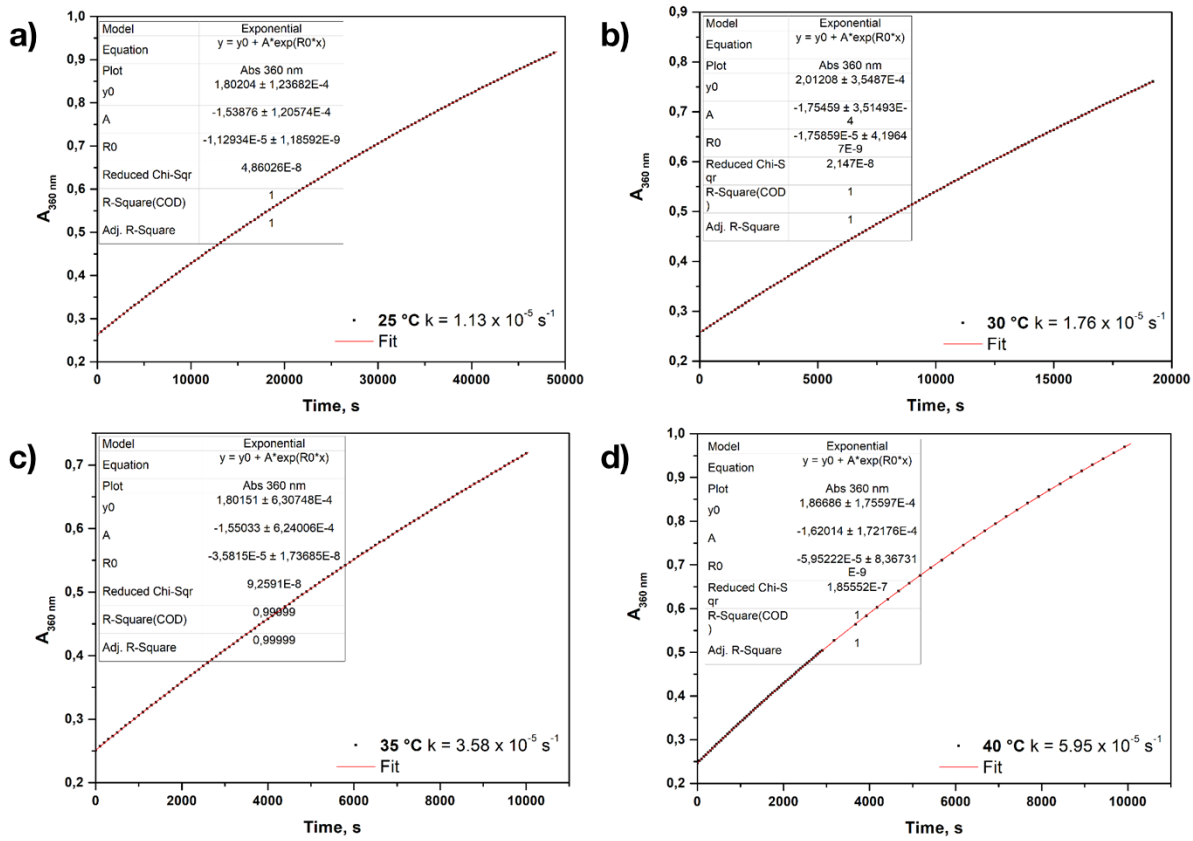

Figure A I 13. Thermal Z → E isomerisation kinetics of **4** followed by UV-Vis absorption spectroscopy. The solution (c = 6.0 x 10^{-5} M in THF) was brought to the UV PSS, then the absorbance at $\lambda_{max\ \pi\text{-}\pi^*}$ = 360 nm was monitored over time, at constant temperature. a) T = 298 K, b) T = 303 K, c) = 308 K, d) T = 313 K.

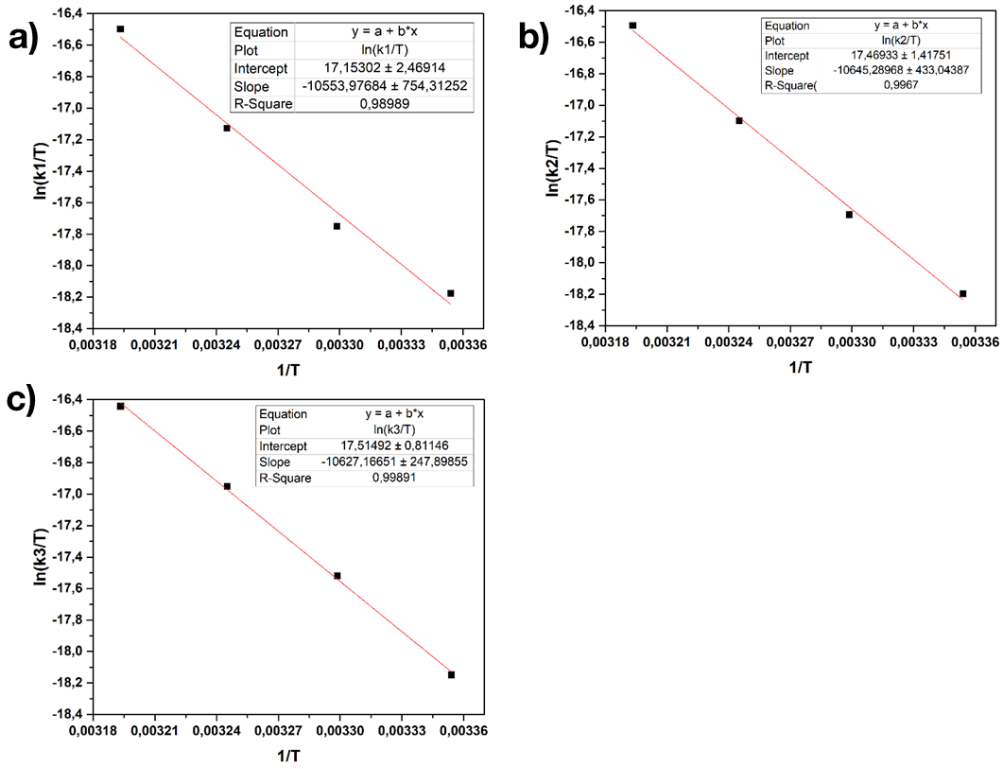

Figure A I 14. Eyring plots for thermal a) (Z,Z,Z)-**1** → (Z,Z,E)-**1**, b) (Z,Z,E)-**1** → (Z,E,E)-**1** and c) (Z,E,E)-**1** → (E,E,E)-**1** isomerisations.

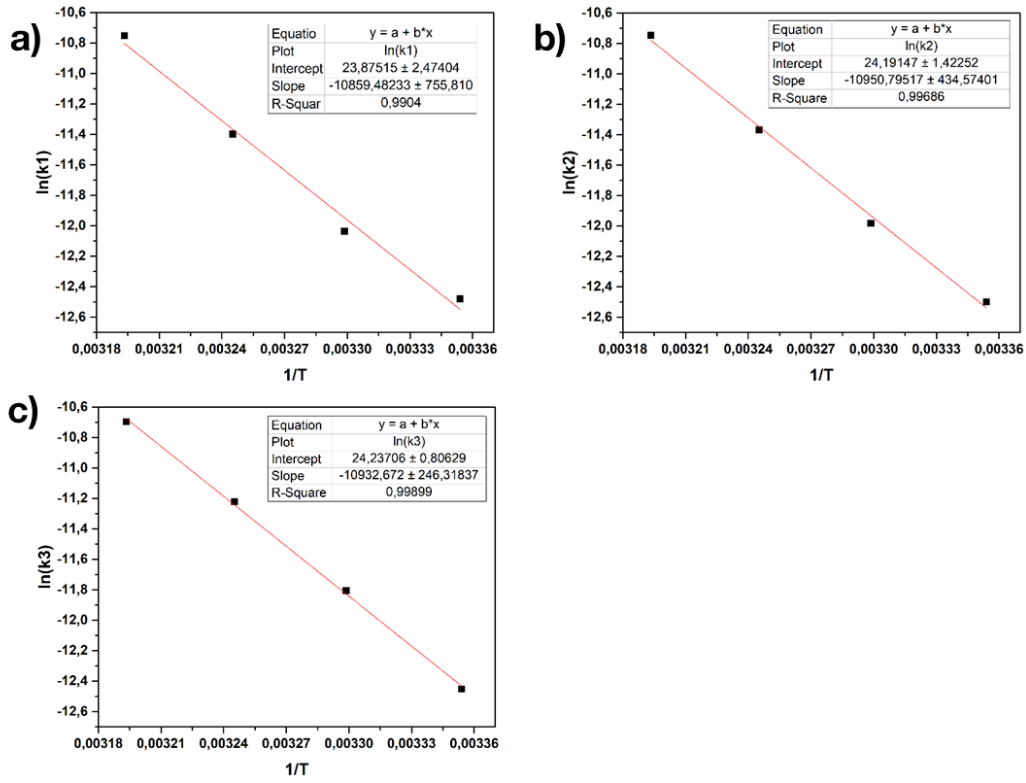

Figure A I 15. Arrhenius plots for thermal a) (Z,Z,Z)-**1** → (Z,Z,E)-**1**, b) (Z,Z,E)-**1** → (Z,E,E)-**1** and c) (Z,E,E)-**1** → (E,E,E)-**1** isomerisations.

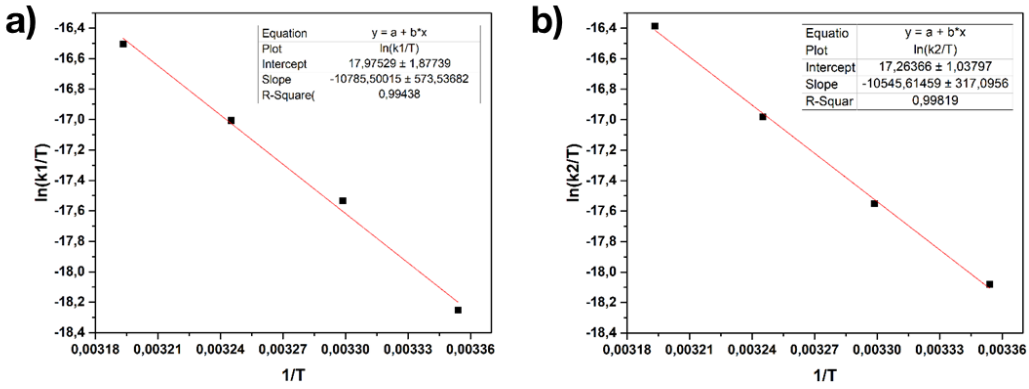

Figure A I 16. Eyring plots for thermal a) (Z,Z)-**2** → (Z, E)-**2** and b) (Z, E)-**2** → (E,E)-**2** isomerisations.

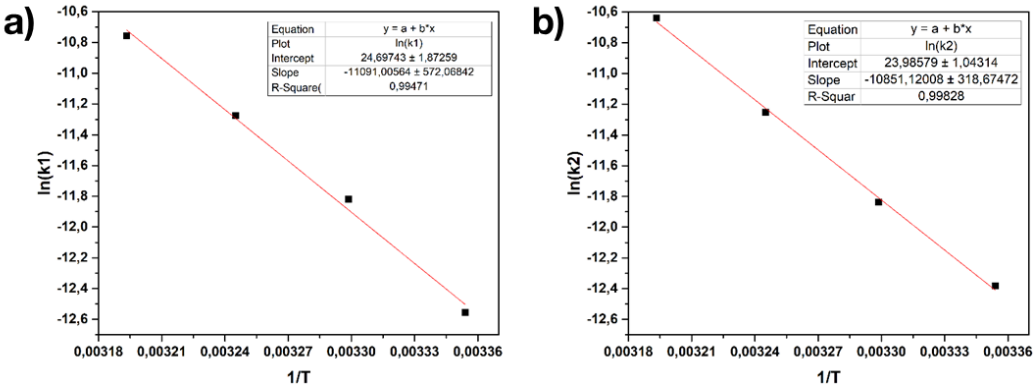

Figure A I 17. Arrhenius plots for thermal a) (Z,Z)-**2** → (Z, E)-**2** and b) (Z, E)-**2** → (E,E)-**2** isomerisations.

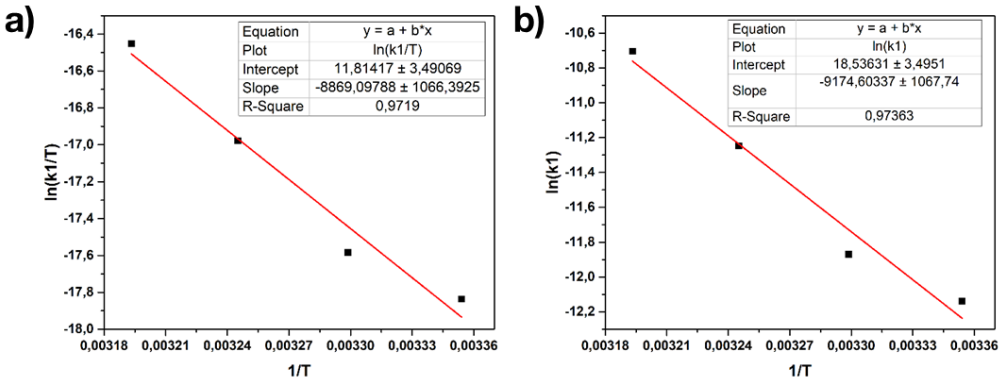

Figure A I 18. a) Eyring and b) Arrhenius plots for thermal (Z)-**3** → (E)-**3** isomerisation.

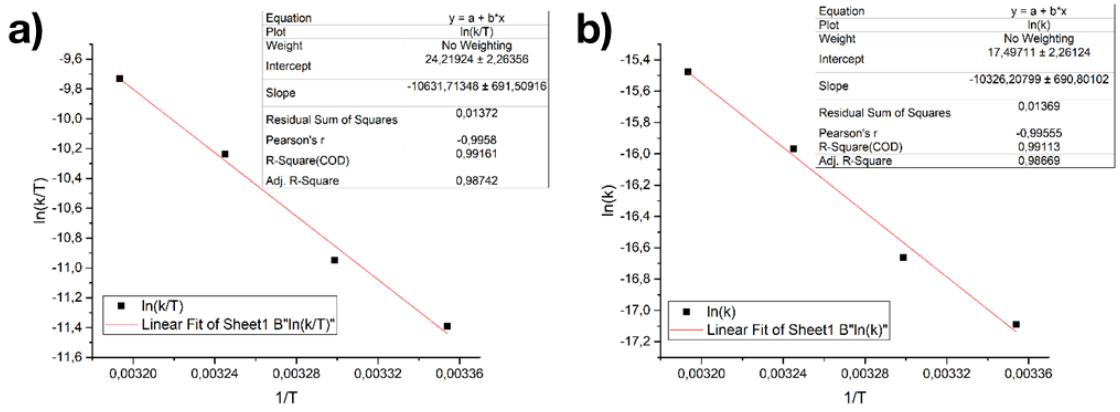

Figure A I 19. a) Eyring and b) Arrhenius plots for thermal (Z)-**4** → (E)-**4** isomerisation.

APPENDIX II

Fluorescence lifetime on 7 – TCSPC data

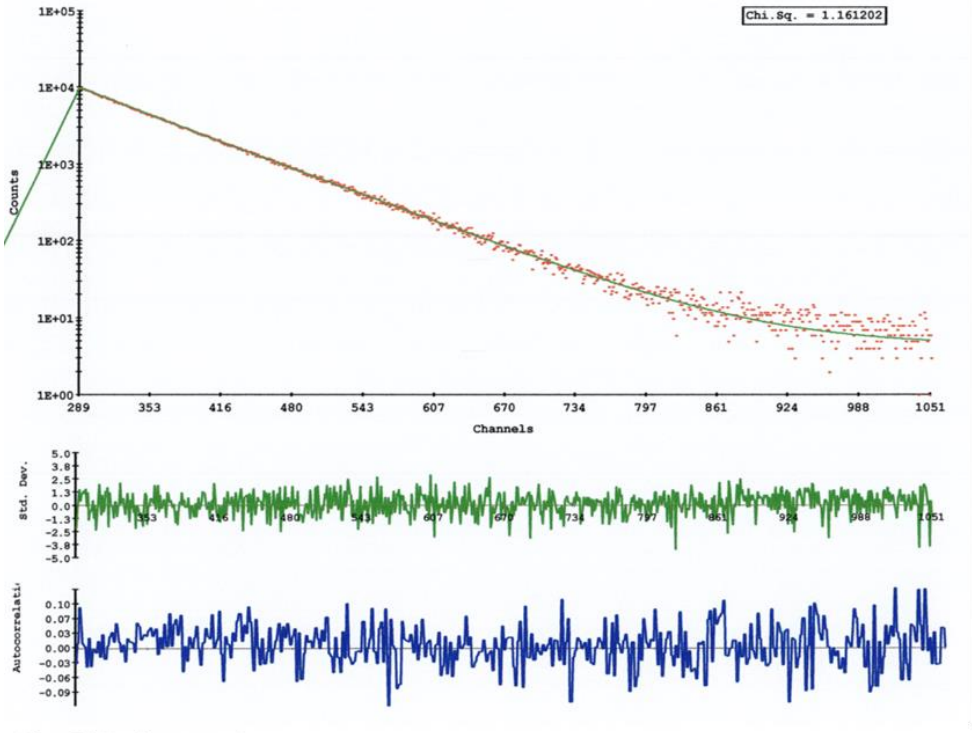

The fitted parameters are:

SHIFT = 0 ch

T1	= 41.14156	ch;	4.591372E-09 sec	S.Dev = 8.625801E-11	sec
T2	= 80.41816	ch;	8.974615E-09 sec	S.Dev = 2.741935E-11	sec
A	= 4.341198			S.Dev = 0.1693731	
B1	= 596.9815	[3.15 Rel.Ampl]	[0.06 Alpha]	S.Dev = 38.57806	
B2	= 9376.637	[96.85 Rel.Ampl]	[0.94 Alpha]	S.Dev = 22.76115	

Average Life Time = 8.712251E-09 sec

CHISQ = 1.161202 [758 degrees of freedom]

Chi-squared Probability =	0.1346275 percent
Durbin-Watson Parameter =	2.056551
Negative residuals =	42.20184 percent
Residuals < 1 s.dev =	65.79292 percent
Residuals < 2 s.dev =	95.01966 percent
Residuals < 3 s.dev =	99.21363 percent
Residuals < 4 s.dev =	99.60681 percent

Figure A II 1. TCSPC data for $S_1 - S_0$ radiative decay monitored at λ_{em} = 650 nm upon excitation at λ_{exc} = 590 nm of **7H$_2$** (dark, all-o-DTE state, no UV irradiation).

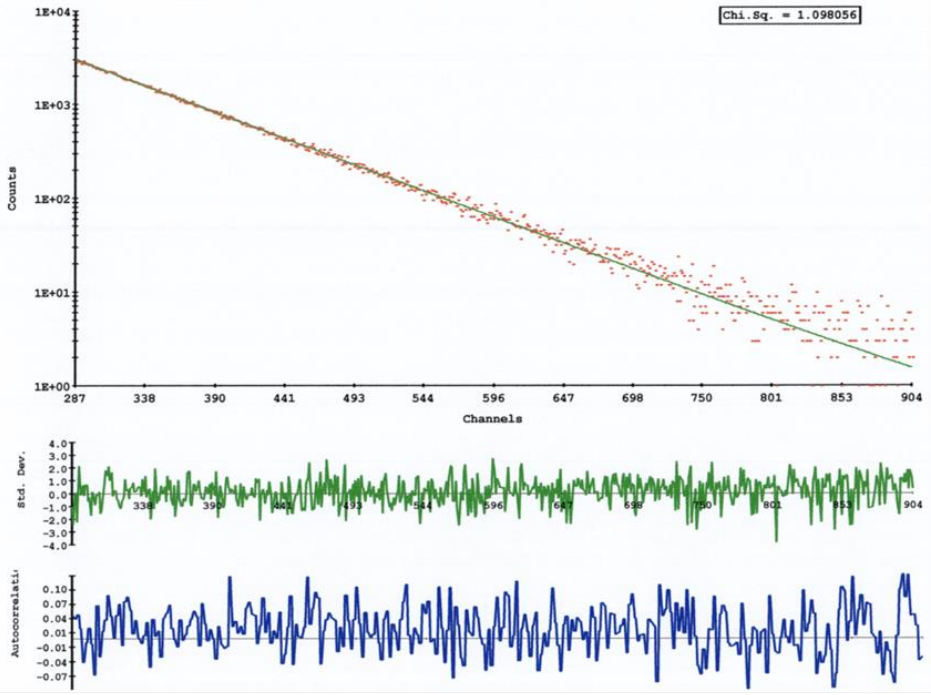

The fitted parameters are:

SHIFT = 0 ch

T1	= 81.86858	ch;	9.136481E-09 sec	S.Dev = 2.52459E-09	sec
T2	= 68.94383	ch;	7.694088E-09 sec	S.Dev = 8.344401E-10	sec
A	= 0.1802669			S.Dev = 0.1526717	
B1	= 2398.652	[81.74 Rel.Ampl]	[0.79 Alpha]	S.Dev = 41.4175	
B2	= 636.1996	[18.26 Rel.Ampl]	[0.21 Alpha]	S.Dev = 48.20383	

Average Life Time = 8.834109E-09 sec
CHISQ = 1.098056 [613 degrees of freedom]

Chi-squared Probability	=	4.636483 percent
Durbin-Watson Parameter	=	1.907109
Negative residuals	=	41.26213 percent
Residuals < 1 s.dev	=	65.53398 percent
Residuals < 2 s.dev	=	94.17476 percent
Residuals < 3 s.dev	=	99.83819 percent
Residuals < 4 s.dev	=	100 percent

Figure A II 2. TCSPC data for $S_1 - S_0$ radiative decay monitored at λ_{em} = 650 nm upon excitation at λ_{exc} = 590 nm of **7H$_2$** (upon short UV irradiation at 312 nm).

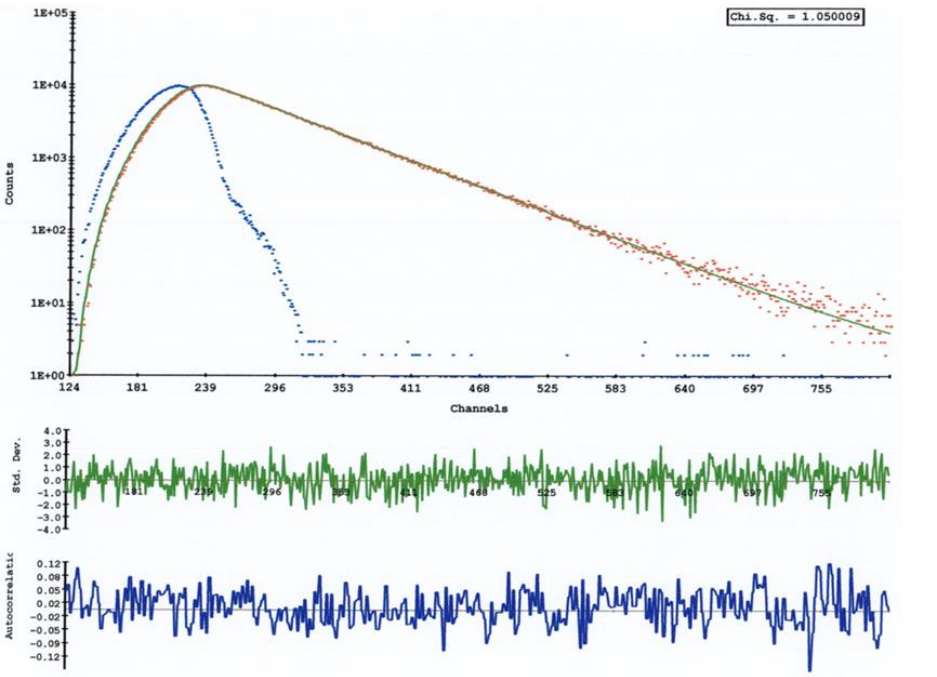

The fitted parameters are:

Hi reduced to: 812 ch

SHIFT = 1.183502	ch;	3.292078E-11	sec	S.Dev = 1.661055E-12	sec
T1 = 70.07846	ch;	1.949331E-09	sec	S.Dev = 3.251072E-10	sec
T2 = 41.54443	ch;	1.155617E-09	sec	S.Dev = 1.77229E-10	sec
A = 0.9930586				S.Dev = 0.1899676	
B1 = 2.989603E-02	[97.14 Rel.Ampl]	[0.95 Alpha]		S.Dev = 7.722357E-05	
B2 = 1.48239E-03	[2.86 Rel.Ampl]	[0.05 Alpha]		S.Dev = 1.207923E-04	

Average Life Time = 1.911834E-09 sec

CHISQ = 1.050009 [683 degrees of freedom]

Chi-squared Probability =	17.70942 percent
Durbin-Watson Parameter =	1.907401
Negative residuals =	43.83164 percent
Residuals < 1 s.dev =	68.21481 percent
Residuals < 2 s.dev =	94.04935 percent
Residuals < 3 s.dev =	99.85486 percent
Residuals < 4 s.dev =	100 percent

Figure A II 3. TCSPC data for $S_1 - S_0$ radiative decay monitored at λ_{em} = 647 nm upon excitation at λ_{exc} = 560 nm of **7Zn** (dark, all-o-DTE state, no UV irradiation).

REFERENCES

[1] (a) *Molecular Switches*. (Ed.: Feringa, B. L.), Wiley-VCH, Weinheim, **2001**; (b) Kinbara, K.; Aida, T. Toward Intelligent Molecular Machines: Directed Motions of Biological and Artificial Molecules and Assemblies. *Chem. Rev.* **2005,** *105* (4), 1377-400.

[2] Leydecker, T.; Herder, M.; Pavlica, E.; Bratina, G.; Hecht, S.; Orgiu, E.; Samorì, P. Flexible Non-Volatile Optical Memory Thin-Film Transistor Device with over 256 Distinct Levels Based on an Organic Bicomponent Blend. *Nat. Nanotechnol.* **2016,** *11* (9), 769-75.

[3] (a) Schwartz, T.; Hutchison, J. A.; Genet, C.; Ebbesen, T. W. Reversible Switching of Ultrastrong Light-Molecule Coupling. *Phys. Rev. Lett.* **2011,** *106* (19), 196405; (b) Baudrion, A. L.; Perron, A.; Veltri, A.; Bouhelier, A.; Adam, P. M.; Bachelot, R. Reversible Strong Coupling in Silver Nanoparticle Arrays Using Photochromic Molecules. *Nano Lett.* **2013,** *13* (1), 282-6.

[4] (a) Lerch, M. M.; Hansen, M. J.; Velema, W. A.; Szymanski, W.; Feringa, B. L. Orthogonal Photoswitching in a Multifunctional Molecular System. *Nat. Commun.* **2016,** *7*, 12054; (b) Manna, D.; Udayabhaskararao, T.; Zhao, H.; Klajn, R. Orthogonal Light-Induced Self-Assembly of Nanoparticles Using Differently Substituted Azobenzenes. *Angew. Chem., Int. Ed.* **2015,** *54* (42), 12394-7.

[5] (a) Ghosh, K.; Hu, J.; White, H. S.; Stang, P. J. Construction of Multifunctional Cuboctahedra Via Coordination-Driven Self-Assembly. *J. Am. Chem. Soc.* **2009,** *131* (19), 6695-7; (b) Lackinger, M.; Heckl, W. M. Carboxylic Acids: Versatile Building Blocks and Mediators for Two-Dimensional Supramolecular Self-Assembly. *Langmuir* **2009,** *25* (19), 11307-21; (c) Furukawa, H.; Ko, N.; Go, Y. B.; Aratani, N.; Choi, S. B.; Choi, E.; Yazaydin, A. O.; Snurr, R. Q.; O'Keeffe, M.; Kim, J.; Yaghi, O. M. Ultrahigh Porosity in Metal-Organic Frameworks. *Science* **2010,** *329* (5990), 424-8.

[6] Guglielmetti, R., 4n+2 Systems: Spiropyrans. In *Photochromism: Molecules and Systems, Rev. Ed.* (Ed.: Dürr, H.; Bouas-Laurent, H.), Elsevier, Amsterdam, **2003**; chapter

[7] Chen, H.; Kou, X.; Yang, Z.; Ni, W.; Wang, J. Shape- and Size-Dependent Refractive Index Sensitivity of Gold Nanoparticles. *Langmuir* **2008,** *24* (10), 5233-7.

[8] (a) Balzani, V.; Credi, A.; Raymo, F. M.; Stoddart, J. F. Artificial Molecular Machines. *Angew. Chem., Int. Ed.* **2000,** *39* (19), 3348-3391; ; (b) Erbas-Cakmak, S.; Leigh, D. A.; McTernan, C. T.; Nussbaumer, A. L. Artificial Molecular Machines. *Chem. Rev.* **2015,** *115* (18), 10081-206; (c) Kassem, S.; van Leeuwen, T.; Lubbe, A. S.; Wilson, M. R.; Feringa, B. L.; Leigh, D. A. Artificial Molecular Motors. *Chem. Soc. Rev.* **2017,** *46* (9), 2592-2621; (d) Leigh, D. A. Genesis of the Nanomachines: The 2016 Nobel Prize in Chemistry. *Angew. Chem., Int. Ed.* **2016,** *55* (47), 14506-14508.

[9] (a) Stoddart, J. F. Mechanically Interlocked Molecules (Mims)-Molecular Shuttles, Switches, and Machines (Nobel Lecture). *Angew. Chem., Int. Ed.* **2017,** *56* (37), 11094-11125; (b) Feringa, B. L. The Art of Building Small: From Molecular Switches to Motors (Nobel Lecture). *Angew. Chem., Int. Ed.* **2017,** *56* (37), 11060-11078; (c) Sauvage, J. P. From Chemical Topology to Molecular Machines (Nobel Lecture). *Angew. Chem., Int. Ed.* **2017,** *56* (37), 11080-11093.

[10] Balzani, V.; Credi, A.; Venturi, M. Light Powered Molecular Machines. *Chem. Soc. Rev.* **2009,** *38* (6), 1542-50.

[11] Chatterjee, M. N.; Kay, E. R.; Leigh, D. A. Beyond Switches: Ratcheting a Particle Energetically Uphill with a Compartmentalized Molecular Machine. *J. Am. Chem. Soc.* **2006,** *128* (12), 4058-73.

[12] Serreli, V.; Lee, C. F.; Kay, E. R.; Leigh, D. A. A Molecular Information Ratchet. *Nature* **2007,** *445* (7127), 523-7.

[13] Lehn, J. M. From Supramolecular Chemistry Towards Constitutional Dynamic Chemistry and Adaptive Chemistry. *Chem. Soc. Rev.* **2007,** *36* (2), 151-60.

[14] (a) Mattia, E.; Otto, S. Supramolecular Systems Chemistry. *Nat. Nanotechnol.* **2015,** *10* (2), 111-9; (b) Sorrenti, A.; Leira-Iglesias, J.; Markvoort, A. J.; de Greef, T. F. A.; Hermans, T. M. Non-Equilibrium Supramolecular Polymerization. *Chem. Soc. Rev.* **2017,** *46* (18), 5476-5490.

[15] (a) Kathan, M.; Hecht, S. Photoswitchable Molecules as Key Ingredients to Drive Systems Away from the Global Thermodynamic Minimum. *Chem. Soc. Rev.* **2017,** *46* (18), 5536-5550; (b) Herder, M.; Lehn, J. M. The Photodynamic Covalent Bond: Sensitized Alkoxyamines as a Tool to Shift Reaction Networks out-of-Equilibrium Using Light Energy. *J. Am. Chem. Soc.* **2018,** *140* (24), 7647-7657.

[16] (a) Kobatake, S.; Takami, S.; Muto, H.; Ishikawa, T.; Irie, M. Rapid and Reversible Shape Changes of Molecular Crystals on Photoirradiation. *Nature* **2007,** *446* (7137), 778-81; (b) Gelebart, A. H.; Jan Mulder, D.; Varga, M.; Konya, A.; Vantomme, G.; Meijer, E. W.; Selinger, R. L. B.; Broer, D. J. Making Waves in a Photoactive Polymer Film. *Nature* **2017,** *546* (7660), 632-636; (c) Iamsaard, S.; Aßhoff, S. J.; Matt, B.; Kudernac, T.; Cornelissen, J. J.; Fletcher, S. P.; Katsonis, N. Conversion of Light into Macroscopic Helical Motion. *Nat. Chem.* **2014,** *6* (3), 229-35.

[17] (a) Orgiu, E.; Crivillers, N.; Herder, M.; Grubert, L.; Patzel, M.; Frisch, J.; Pavlica, E.; Duong, D. T.; Bratina, G.; Salleo, A.; Koch, N.; Hecht, S.; Samori, P. Optically Switchable Transistor Via Energy-Level Phototuning in a Bicomponent Organic Semiconductor. *Nat. Chem.* **2012,** *4* (8), 675-9; (b) Orgiu, E.; Samori, P. 25th Anniversary Article: Organic Electronics Marries Photochromism: Generation of Multifunctional Interfaces, Materials, and Devices. *Advanced Materials* **2014,** *26* (12), 1827-45.

[18] Bates, M.; Huang, B.; Dempsey, G. T.; Zhuang, X. Multicolor Super-Resolution Imaging with Photo-Switchable Fluorescent Probes. *Science* **2007,** *317* (5845), 1749-53.

[19] (a) Ferris, D. P.; Zhao, Y. L.; Khashab, N. M.; Khatib, H. A.; Stoddart, J. F.; Zink, J. I. Light-Operated Mechanized Nanoparticles. *J. Am. Chem. Soc.* **2009,** *131* (5), 1686-8; (b) Lau, Y. A.; Henderson, B. L.; Lu, J.; Ferris, D. P.; Tamanoi, F.; Zink, J. I. Continuous Spectroscopic Measurements of Photo-Stimulated Release of Molecules by Nanomachines in a Single Living Cell. *Nanoscale* **2012,** *4* (11), 3482-9.

[20] Gostl, R.; Senf, A.; Hecht, S. Remote-Controlling Chemical Reactions by Light: Towards Chemistry with High Spatio-Temporal Resolution. *Chem. Soc. Rev.* **2014,** *43* (6), 1982-96.

[21] (a) Ceroni, P.; Credi, A.; Venturi, M.; Balzani, V. Light-Powered Molecular Devices and Machines. *Photochem. Photobiol. Sci.* **2010,** *9* (12), 1561-73; (b) Brieke, C.; Rohrbach, F.; Gottschalk, A.; Mayer, G.; Heckel, A. Light-Controlled Tools. *Angew. Chem., Int. Ed.* **2012,** *51* (34), 8446-76.

[22] Marckwald, W. *Z. Phys. Chem.* **1899,** *30*, 140.

[23] Hirshberg, Y. Photochromie Dans La Série De La Bianthrone. *Compt. Rend. Acad. Sci.* **1950,** *231*, 903.

[24] Fischer, E.; Hirshberg, Y. Formation of Coloured Forms of Spirans by Low-Temperature Irradiation. *J. Chem. Soc.* **1952**, 4522-4524.

[25] Hirshberg, Y. Reversible Formation and Eradication of Colors by Irradiation at Low Temperatures. A Photochemical Memory Model. *J. Am. Chem. Soc.* **1956,** *78* (10), 2304-2312.

[26] Goulet-Hanssens, A.; Utecht, M.; Mutruc, D.; Titov, E.; Schwarz, J.; Grubert, L.; Bleger, D.; Saalfrank, P.; Hecht, S. Electrocatalytic Z --> E Isomerization of Azobenzenes. *J Am Chem Soc* **2016,** *139* (1), 335-341.

[27] Bléger, D. Orchestrating Molecular Motion with Light - from Single (Macro)Molecules to Materials. *Macromol. Chem. Phys.* **2016,** *217* (2), 189-198.

[28] Bandara, H. M.; Burdette, S. C. Photoisomerization in Different Classes of Azobenzene. *Chem Soc Rev* **2012,** *41* (5), 1809-25.

[29] Bortolus, P.; Monti, S. Cis-Trans Photoisomerization of Azobenzene - Solvent and Triplet Donor Effects. *J. Phys. Chem.* **1979,** *83* (6), 648-652.

[30] Blevins, A. A.; Blanchard, G. J. Effect of Positional Substitution on the Optical Response of Symmetrically Disubstituted Azobenzene Derivatives. *J. Phys. Chem. B* **2004,** *108* (16), 4962-4968.

[31] (a) Brode, W. R.; Gould, J. H.; Wyman, G. M. The Relation between the Absorption Spectra and the Chemical Constitution of Dyes. Xxv. Phototropism and Cis-Trans Isomerism in Aromatic Azo Compounds. *J. Am. Chem. Soc.* **1952,** *74* (18), 4641-4646; (b) Emond, M.; Le Saux, T.; Maurin, S.; Baudin, J. B.; Plasson, R.; Jullien, L. 2-Hydroxyazobenzenes to Tailor Ph Pulses and Oscillations with Light. *Chem. Eur. J.* **2010,** *16* (29), 8822-31.

[32] Bleger, D.; Schwarz, J.; Brouwer, A. M.; Hecht, S. O-Fluoroazobenzenes as Readily Synthesized Photoswitches Offering Nearly Quantitative Two-Way Isomerization with Visible Light. *J. Am. Chem. Soc.* **2012,** *134* (51), 20597-600.

[33] Siewertsen, R.; Neumann, H.; Buchheim-Stehn, B.; Herges, R.; Nather, C.; Renth, F.; Temps, F. Highly Efficient Reversible Z-E Photoisomerization of a Bridged Azobenzene with Visible Light through Resolved S(1)(N Pi*) Absorption Bands. *J. Am. Chem. Soc.* **2009,** *131* (43), 15594-5.

[34] Beharry, A. A.; Sadovski, O.; Woolley, G. A. Azobenzene Photoswitching without Ultraviolet Light. *J. Am. Chem. Soc.* **2011,** *133* (49), 19684-7.

[35] (a) Nakatani, K.; Piard, J.; Yu, P.; Métivier, R., Introduction: Organic Photochromic Molecules. In *Photochromic Materials: Preparation, Properties and Applications* (Ed.: Tian, H.; Zhang, J.), Wiley-VCH, **2016**; chapter 1; (b) Beharry, A. A.; Woolley, G. A. Azobenzene Photoswitches for Biomolecules. *Chem. Soc. Rev.* **2011,** *40* (8), 4422-37; (c) *Smart Light-Responsive Materials*. (Ed.: Zhao, Y.; Ikeda, T.), John Wiley & Sons: Hoboken, NJ, **2009**.

[36] (a) Griffiths, J. Ii. Photochemistry of Azobenzene and Its Derivatives. *Chem. Soc. Rev.* **1972,** *1* (4), 481; (b) Bullock, D. J. W.; Cumper, C. W. N.; Vogel, A. I. 989. Physical Properties and Chemical Constitution. Part Xliii. The Electric Dipole Moments of Azobenzene, Azopyridines, and Azoquinolines. *J. Chem. Soc.* **1965,** *0*, 5316-5323.

[37] (a) Fliegl, H.; Köhn, A.; Hättig, C.; Ahlrichs, R. Ab Initio Calculation of the Vibrational and Electronic Spectra of Trans- and Cis-Azobenzene. *J. Am. Chem. Soc.* **2003,** *125* (32), 9821-9827; (b) Hartley, G. S. The Cis-Form of Azobenzene. *Nature* **1937,** *140* (3537), 281-281.

[38] Bléger, D.; Yu, Z.; Hecht, S. Toward Optomechanics: Maximizing the Photodeformation of Individual Molecules. *Chem. Commun.* **2011,** *47* (45), 12260-6.

[39] (a) Cisnetti, F.; Ballardini, R.; Credi, A.; Gandolfi, M. T.; Masiero, S.; Negri, F.; Pieraccini, S.; Spada, G. P. Photochemical and Electronic Properties of Conjugated Bis(Azo) Compounds: An Experimental and Computational Study. *Chem. Eur. J.* **2004,** *10* (8), 2011-21; (b) Bléger, D.; Dokic, J.; Peters, M. V.; Grubert, L.;

Saalfrank, P.; Hecht, S. Electronic Decoupling Approach to Quantitative Photoswitching in Linear Multiazobenzene Architectures. *J. Phys. Chem. B* **2011,** *115* (33), 9930-40.

[40] (a) Shinkai, S.; Nakaji, T.; Nishida, Y.; Ogawa, T.; Manabe, O. Photoresponsive Crown Ethers. 1. Cis-Trans Isomerism of Azobenzene as a Tool to Enforce Conformational Changes of Crown Ethers and Polymers. *J. Am. Chem. Soc.* **1980,** *102* (18), 5860-5865; (b) Shinkai, S.; Nakaji, T.; Ogawa, T.; Shigematsu, K.; Manabe, O. Photoresponsive Crown Ethers. 2. Photocontrol of Ion Extraction and Ion Transport by a Bis(Crown Ether) with a Butterfly-Like Motion. *J. Am. Chem. Soc.* **1981,** *103* (1), 111-115; (c) Shinkai, S.; Ogawa, T.; Nakaji, T.; Kusano, Y.; Nanabe, O. Photocontrolled Extraction Ability of Azobenzene-Bridged Azacrown Ether. *Tetrahedron Lett.* **1979,** *20* (47), 4569-4572.

[41] Muraoka, T.; Kinbara, K.; Kobayashi, Y.; Aida, T. Light-Driven Open-Close Motion of Chiral Molecular Scissors. *J. Am. Chem. Soc.* **2003,** *125* (19), 5612-3.

[42] Ragazzon, G.; Baroncini, M.; Silvi, S.; Venturi, M.; Credi, A. Light-Powered Autonomous and Directional Molecular Motion of a Dissipative Self-Assembling System. *Nat. Nanotechnol.* **2015,** *10*, 70-75.

[43] Banghart, M.; Borges, K.; Isacoff, E.; Trauner, D.; Kramer, R. H. Light-Activated Ion Channels for Remote Control of Neuronal Firing. *Nat Neurosci* **2004,** *7* (12), 1381-6.

[44] (a) Manna, A.; Chen, P.-L.; Akiyama, H.; Wei, T.-X.; Tamada, K.; Knoll, W. Optimized Photoisomerization on Gold Nanoparticles Capped by Unsymmetrical Azobenzene Disulfides. *Chem. Mater.* **2003,** *15* (1), 20-28; (b) Raimondo, C.; Reinders, F.; Soydaner, U.; Mayor, M.; Samorì, P. Light-Responsive Reversible Solvation and Precipitation of Gold Nanoparticles. *Chem. Commun.* **2010,** *46* (7), 1147-9.

[45] Klajn, R.; Bishop, K. J.; Grzybowski, B. A. Light-Controlled Self-Assembly of Reversible and Irreversible Nanoparticle Suprastructures. *Proc. Natl. Acad. Sci. USA* **2007,** *104* (25), 10305-9.

[46] Klajn, R.; Wesson, P. J.; Bishop, K. J.; Grzybowski, B. A. Writing Self-Erasing Images Using Metastable Nanoparticle "Inks". *Angew. Chem., Int. Ed.* **2009,** *48* (38), 7035-9.

[47] Murase, T.; Sato, S.; Fujita, M. Switching the Interior Hydrophobicity of a Self-Assembled Spherical Complex through the Photoisomerization of Confined Azobenzene Chromophores. *Angew. Chem., Int. Ed.* **2007,** *46* (27), 5133-6.

[48] (a) Coudert, F.-X. Responsive Metal–Organic Frameworks and Framework Materials: Under Pressure, Taking the Heat, in the Spotlight, with Friends. *Chemistry of Materials* **2015,** *27* (6), 1905-1916; (b) Jones, C. L.; Tansell, A. J.; Easun, T. L. The Lighter Side of Mofs: Structurally Photoresponsive Metal–Organic Frameworks. *J. Mater. Chem. A* **2016,** *4* (18), 6714-6723.

[49] Yanai, N.; Uemura, T.; Inoue, M.; Matsuda, R.; Fukushima, T.; Tsujimoto, M.; Isoda, S.; Kitagawa, S. Guest-to-Host Transmission of Structural Changes for Stimuli-Responsive Adsorption Property. *J. Am. Chem. Soc.* **2012,** *134* (10), 4501-4.

[50] Park, J.; Yuan, D.; Pham, K. T.; Li, J. R.; Yakovenko, A.; Zhou, H. C. Reversible Alteration of Co2 Adsorption Upon Photochemical or Thermal Treatment in a Metal-Organic Framework. *J. Am. Chem. Soc.* **2012,** *134* (1), 99-102.

[51] Brown, J. W.; Henderson, B. L.; Kiesz, M. D.; Whalley, A. C.; Morris, W.; Grunder, S.; Deng, H.; Furukawa, H.; Zink, J. I.; Stoddart, J. F.; Yaghi, O. M. Photophysical Pore Control in an Azobenzene-Containing Metal–Organic Framework. *Chem. Sci.* **2013,** *4* (7), 2858.

[52] Lyndon, R.; Konstas, K.; Ladewig, B. P.; Southon, P. D.; Kepert, P. C.; Hill, M. R. Dynamic Photo-Switching in Metal-Organic Frameworks as a Route to Low-Energy Carbon Dioxide Capture and Release. *Angew. Chem., Int. Ed.* **2013,** *52* (13), 3695-8.

[53] Wang, L.; Li, Q. Photochromism into Nanosystems: Towards Lighting up the Future Nanoworld. *Chem. Soc. Rev.* **2017**.

[54] Yu, Y.; Nakano, M.; Ikeda, T. Directed Bending of a Polymer Film by Light. *Nature* **2003,** *425* (6954), 145.

[55] Irie, M. Diarylethenes for Memories and Switches. *Chem. Rev.* **2000,** *100* (5), 1685-1716.

[56] Li, W.; Jiao, C.; Li, X.; Xie, Y.; Nakatani, K.; Tian, H.; Zhu, W. Separation of Photoactive Conformers Based on Hindered Diarylethenes: Efficient Modulation in Photocyclization Quantum Yields. *Angew. Chem., Int. Ed.* **2014,** *53* (18), 4603-7.

[57] Irie, M.; Lifka, T.; Kobatake, S.; Kato, N. Photochromism of 1,2-Bis(2-Methyl-5-Phenyl-3-Thienyl)Perfluorocyclopentene in a Single-Crystalline Phase. *J. Am. Chem. Soc.* **2000,** *122* (20), 4871-4876.

[58] Irie, M.; Mohri, M. Thermally Irreversible Photochromic Systems. Reversible Photocyclization of Diarylethene Derivatives. *J. Org. Chem.* **1988,** *53* (4), 803-808.

[59] Irie, M.; Fukaminato, T.; Matsuda, K.; Kobatake, S. Photochromism of Diarylethene Molecules and Crystals: Memories, Switches, and Actuators. *Chem. Rev.* **2014,** *114* (24), 12174-277.

[60] Irie, M.; Uchida, K. Synthesis and Properties of Photochromic Diarylethenes with Heterocyclic Aryl Groups. *Bull. Chem. Soc. Jpn.* **1998,** *71* (5), 985-996.

[61] Kobatake, S.; Uchida, K.; Tsuchida, E.; Irie, M. Photochromism of Diarylethenes Having Isopropyl Groups at the Reactive Carbons. Thermal Cycloreversion of the Closed-Ring Isomers. *Chem. Lett.* **2000,** *29* (11), 1340-1341.

[62] Morimitsu, K.; Shibata, K.; Kobatake, S.; Irie, M. Dithienylethenes with a Novel Photochromic Performance. *J. Org. Chem.* **2002,** *67* (13), 4574-4578.

[63] Morimitsu, K.; Kobatake, S.; Nakamura, S.; Irie, M. Efficient Photocycloreversion Reaction of Diarylethenes by Introduction of Cyano Subsutituents to the Reactive Carbons. *Chem. Lett.* **2003,** *32* (9), 858-859.

[64] Kobatake, S.; Terakawa, Y. Acid-Induced Photochromic System Switching of Diarylethene Derivatives between P- and T-Types. *Chem. Commun.* **2007,** (17), 1698-700.

[65] Seefeldt, B.; Altenhoner, K.; Tosic, O.; Geisler, T.; Sauer, M.; Mattay, J. Kinetic Studies on Visible-Light-Switchable Photochromic Fluorophores Based on Diarylethenes. *Photochem. Photobiol. Sci.* **2011,** *10* (9), 1488-95.

[66] (a) Ko, C. C.; Kwok, W. M.; Yam, V. W.; Phillips, D. L. Triplet Mlct Photosensitization of the Ring-Closing Reaction of Diarylethenes by Design and Synthesis of a Photochromic Rhenium(I) Complex of a Diarylethene-Containing 1,10-Phenanthroline Ligand. *Chem. Eur. J.* **2006,** *12* (22), 5840-8; (b) Monaco, S.; Semeraro, M.; Tan, W.; Tian, H.; Ceroni, P.; Credi, A. Multifunctional Switching of a Photo- and Electro-Chemiluminescent Iridium-Dithienylethene Complex. *Chem. Commun.* **2012,** *48* (69), 8652-4; (c) Jukes, R. T.; Adamo, V.; Hartl, F.; Belser, P.; De Cola, L. Photochromic Dithienylethene Derivatives Containing Ru(Ii) or Os(Ii) Metal Units. Sensitized Photocyclization from a Triplet State. *Inorg. Chem.* **2004,** *43* (9), 2779-92; (d) Indelli, M. T.; Carli, S.; Ghirotti, M.; Chiorboli, C.; Ravaglia, M.; Garavelli, M.; Scandola, F. Triplet Pathways in Diarylethene Photochromism: Photophysical and Computational Study of Dyads Containing Ruthenium(Ii) Polypyridine and 1,2-Bis(2-Methylbenzothiophene-3-Yl)Maleimide Units. *J. Am. Chem. Soc.* **2008,** *130* (23), 7286-99.

[67] Murata, R.; Yago, T.; Wakasa, M. Cyclization Reaction of Diarylethene through the Triplet Excited State. *Bull. Chem. Soc. Jpn.* **2011,** *84* (12), 1336-1338.

[68] (a) Fredrich, S.; Gostl, R.; Herder, M.; Grubert, L.; Hecht, S. Switching Diarylethenes Reliably in Both Directions with Visible Light. *Angew. Chem., Int. Ed.* **2016,** *55* (3), 1208-12; (b) Fukaminato, T.; Doi, T.; Tanaka, M.; Irie, M. Photocyclization Reaction of Diarylethene–Perylenebisimide Dyads Upon Irradiation with Visible (>500 Nm) Light. *J. Phys. Chem. C* **2009,** *113* (27), 11623-11627.

[69] (a) Morimoto, M.; Irie, M. A Diarylethene Cocrystal That Converts Light into Mechanical Work. *J. Am. Chem. Soc.* **2010,** *132* (40), 14172-8; (b) Terao, F.; Morimoto, M.; Irie, M. Light-Driven Molecular-Crystal Actuators: Rapid and Reversible Bending of Rodlike Mixed Crystals of Diarylethene Derivatives. *Angew. Chem., Int. Ed.* **2012,** *51* (4), 901-4.

[70] (a) de Jong, J. J.; Lucas, L. N.; Kellogg, R. M.; van Esch, J. H.; Feringa, B. L. Reversible Optical Transcription of Supramolecular Chirality into Molecular Chirality. *Science* **2004,** *304* (5668), 278-81; (b) Lucas, L. N.; van Esch, J.; Feringa, B. L.; Kellogg, R. M. Photocontrolled Self-Assembly of Molecular Switches. *Chem. Commun.* **2001,** (8), 759-760.

[71] (a) Bonacchi, S.; El Garah, M.; Ciesielski, A.; Herder, M.; Conti, S.; Cecchini, M.; Hecht, S.; Samorì, P. Surface-Induced Selection During in Situ Photoswitching at the Solid/Liquid Interface. *Angew. Chem., Int. Ed.* **2015,** *54* (16), 4865-4869; (b) Yokoyama, S.; Hirose, T.; Matsuda, K. Phototriggered Formation and Disappearance of Surface-Confined Self-Assembly Composed of Photochromic 2-Thienyl-Type Diarylethene: A Cooperative Model at the Liquid/Solid Interface. *Chem. Commun.* **2014,** *50* (45), 5964-6; (c) Yokoyama, S.; Hirose, T.; Matsuda, K. Photoinduced Four-State Three-Step Ordering Transformation of Photochromic Terthiophene at a Liquid/Solid Interface Based on Two Principles: Photochromism and Polymorphism. *Langmuir* **2015,** *31* (23), 6404-14; (d) Yokoyama, S.; Hirose, T.; Matsuda, K. Effects of Alkyl Chain Length and Hydrogen Bonds on the Cooperative Self-Assembly of 2-Thienyl-Type Diarylethenes at a Liquid/Highly Oriented Pyrolytic Graphite (Hopg) Interface. *Chem. Eur. J.* **2015,** *21* (39), 13569-76; (e) Frath, D.; Sakano, T.; Imaizumi, Y.; Yokoyama, S.; Hirose, T.; Matsuda, K. Diarylethene Self-Assembled Monolayers: Cocrystallization and Mixing-Induced Cooperativity Highlighted by Scanning Tunneling Microscopy at the Liquid/Solid Interface. *Chem. Eur. J.* **2015,** *21* (32), 11350-8; (f) Frath, D.; Yokoyama, S.; Hirose, T.; Matsuda, K. Photoresponsive Supramolecular Self-Assemblies at the Liquid/Solid Interface. *Journal of Photochemistry and Photobiology C: Photochemistry Reviews* **2017**; (g) Maeda, N.; Hirose, T.; Matsuda, K. Discrimination between Conglomerates and Pseudoracemates Using Surface Coverage Plots in 2d Self-Assemblies at the Liquid-Graphite Interface. *Angew. Chem., Int. Ed.* **2017,** *56* (9), 2371-2375.

[72] Katsonis, N.; Minoia, A.; Kudernac, T.; Mutai, T.; Xu, H.; Uji, I. H.; Lazzaroni, R.; Feyter, S. D.; Feringa, B. L. Locking of Helicity and Shape Complementarity in Diarylethene Dimers on Graphite. *J. Am. Chem. Soc.* **2008,** *130* (2), 386-7.

[73] Tahara, K.; Inukai, K.; Adisoejoso, J.; Yamaga, H.; Balandina, T.; Blunt, M. O.; De Feyter, S.; Tobe, Y. Tailoring Surface-Confined Nanopores with Photoresponsive Groups. *Angew. Chem., Int. Ed.* **2013,** *52* (32), 8373-6.

[74] (a) Jia, C.; Migliore, A.; Xin, N.; Huang, S.; Wang, J.; Yang, Q.; Wang, S.; Chen, H.; Wang, D.; Feng, B.; Liu, Z.; Zhang, G.; Qu, D. H.; Tian, H.; Ratner, M. A.; Xu, H. Q.; Nitzan, A.; Guo, X. Covalently Bonded Single-Molecule Junctions with Stable and Reversible Photoswitched Conductivity. *Science* **2016,** *352* (6292), 1443-5; (b) Gemayel, M. E.; Borjesson, K.; Herder, M.; Duong, D. T.; Hutchison, J. A.; Ruzie, C.; Schweicher, G.; Salleo, A.; Geerts, Y.; Hecht, S.; Orgiu, E.; Samori, P. Optically Switchable Transistors by Simple Incorporation of Photochromic Systems into Small-Molecule Semiconducting Matrices. *Nat. Commun.* **2015,** *6*, 6330.

[75] Williams, D. E.; Martin, C. R.; Dolgopolova, E. A.; Swifton, A.; Godfrey, D. C.; Ejegbavwo, O. A.; Pellechia, P. J.; Smith, M. D.; Shustova, N. B. Flipping the Switch: Fast Photoisomerization in a Confined Environment. *J. Am. Chem. Soc.* **2018,** *140* (24), 7611-7622.

[76] (a) Lemieux, V.; Gauthier, S.; Branda, N. R. Selective and Sequential Photorelease Using Molecular Switches. *Angew. Chem., Int. Ed.* **2006,** *45* (41), 6820-4; (b) Kathan, M.; Eisenreich, F.; Jurissek, C.; Dallmann, A.; Gurke, J.; Hecht, S. Light-Driven Molecular Trap Enables Bidirectional Manipulation of Dynamic Covalent Systems. *Nat. Chem.* **2018**.

[77] (a) Kathan, M.; Kovaricek, P.; Jurissek, C.; Senf, A.; Dallmann, A.; Thunemann, A. F.; Hecht, S. Control of Imine Exchange Kinetics with Photoswitches to Modulate Self-Healing in Polysiloxane Networks by Light Illumination. *Angew Chem Int Ed Engl* **2016**; (b) Valderrey, V.; Bonasera, A.; Fredrich, S.; Hecht, S. Light-Activated Sensitive Probes for Amine Detection. *Angew Chem Int Ed Engl* **2017,** *56* (7), 1914-1918.

[78] van der Molen, S. J.; Liao, J.; Kudernac, T.; Agustsson, J. S.; Bernard, L.; Calame, M.; van Wees, B. J.; Feringa, B. L.; Schonenberger, C. Light-Controlled Conductance Switching of Ordered Metal-Molecule-Metal Devices. *Nano Lett.* **2009,** *9* (1), 76-80.

[79] (a) Liddell, P. A.; Kodis, G.; Moore, A. L.; Moore, T. A.; Gust, D. Photonic Switching of Photoinduced Electron Transfer in a Dithienylethene–Porphyrin–Fullerene Triad Molecule. *J. Am. Chem. Soc.* **2002,** *124* (26), 7668-7669; (b) Frey, J.; Kodis, G.; Straight, S. D.; Moore, T. A.; Moore, A. L.; Gust, D. Photonic Modulation of Electron Transfer with Switchable Phase Inversion. *J. Phys. Chem. A* **2013,** *117* (3), 607-15.

[80] Hou, L.; Zhang, X.; Pijper, T. C.; Browne, W. R.; Feringa, B. L. Reversible Photochemical Control of Singlet Oxygen Generation Using Diarylethene Photochromic Switches. *J. Am. Chem. Soc.* **2014,** *136* (3), 910-3.

[81] (a) Straight, S. D.; Liddell, P. A.; Terazono, Y.; Moore, T. A.; Moore, A. L.; Gust, D. All-Photonic Molecular Xor and nor Logic Gates Based on Photochemical Control of Fluorescence in a Fulgimide–Porphyrin–Dithienylethene Triad. *Adv. Funct. Mater.* **2007,** *17* (5), 777-785; (b) Karnbratt, J.; Hammarson, M.; Li, S.; Anderson, H. L.; Albinsson, B.; Andreasson, J. Photochromic Supramolecular Memory with Nondestructive Readout. *Angew. Chem., Int. Ed.* **2010,** *49* (10), 1854-7; (c) Andreasson, J.; Pischel, U.; Straight, S. D.; Moore, T. A.; Moore, A. L.; Gust, D. All-Photonic Multifunctional Molecular Logic Device. *J. Am. Chem. Soc.* **2011,** *133* (30), 11641-8; (d) Pärs, M.; Gräf, K.; Bauer, P.; Thelakkat, M.; Köhler, J. Optical Gating of Perylene Bisimide Fluorescence Using Dithienylcyclopentene Photochromic Switches. *Appl. Phys. Lett.* **2013,** *103* (22), 221115; (e) Balter, M.; Li, S.; Nilsson, J. R.; Andreasson, J.; Pischel, U. An All-Photonic Molecule-Based Parity Generator/Checker for Error Detection in Data Transmission. *J. Am. Chem. Soc.* **2013,** *135* (28), 10230-3.

[82] (a) Nevskyi, O.; Sysoiev, D.; Oppermann, A.; Huhn, T.; Woll, D. Nanoscopic Visualization of Soft Matter Using Fluorescent Diarylethene Photoswitches. *Angew. Chem., Int. Ed.* **2016**; (b) Roubinet, B.; Bossi, M. L.; Alt, P.; Leutenegger, M.; Shojaei, H.; Schnorrenberg, S.; Nizamov, S.; Irie, M.; Belov, V. N.; Hell, S. W. Carboxylated Photoswitchable Diarylethenes for Biolabeling and Super-Resolution Resolft Microscopy. *Angew. Chem., Int. Ed.* **2016,** *55* (49), 15429-15433; (c) Roubinet, B.; Weber, M.; Shojaei, H.; Bates, M.; Bossi, M. L.; Belov, V. N.; Irie, M.; Hell, S. W. Fluorescent Photoswitchable Diarylethenes for Biolabeling and Single-Molecule Localization Microscopies with Optical Superresolution. *J. Am. Chem. Soc.* **2017,** *139* (19), 6611-6620.

[83] Minkin, V. I. Photo-, Thermo-, Solvato-, and Electrochromic Spiroheterocyclic Compounds. *Chem. Rev.* **2004,** *104* (5), 2751-76.

[84] Kortekaas, L.; Chen, J.; Jacquemin, D.; Browne, W. R. Proton-Stabilized Photochemically Reversible E/ Z Isomerization of Spiropyrans. *J. Phys. Chem. B* **2018,** *122* (24), 6423-6430.

[85] Klajn, R. Spiropyran-Based Dynamic Materials. *Chem. Soc. Rev.* **2014,** *43* (1), 148-84.

[86] (a) Levitus, M.; Glasser, G.; Neher, D.; Aramendía, P. F. Direct Measurement of the Dipole Moment of a Metastable Merocyanine by Electromechanical Interferometry. *Chem. Phys. Lett.* **1997,** *277* (1-3), 118-124; (b) Bletz, M.; Pfeifer-Fukumura, U.; Kolb, U.; Baumann, W. Ground- and First-Excited-Singlet-State Electric Dipole Moments of Some Photochromic Spirobenzopyrans in Their Spiropyran and Merocyanine Form. *J. Phys. Chem. A* **2002,** *106* (10), 2232-2236; (c) Shen, Q.; Cao, Y.; Liu, S.; Steigerwald, M. L.; Guo, X. Conformation-Induced Electrostatic Gating of the Conduction of Spiropyran-Coated Organic Thin-Film Transistors. *J. Phys. Chem. C* **2009,** *113* (24), 10807-10812.

[87] (a) Ueda, M.; Kim, H. B.; Ichimura, K. Photocontrolled Aggregation of Colloidal Silica. *J. Mater. Chem.* **1994,** *4* (6), 883-889; (b) Ueda, M.; Kudo, K.; Ichimura, K. Photochromic Behaviour of a Spirobenzopyran Chemisorbed on a Colloidal Silica Surface. *J. Mater. Chem.* **1995,** *5* (7), 1007; (c) Piech, M.; George, M. C.; Bell, N. S.; Braun, P. V. Patterned Colloid Assembly by Grafted Photochromic Polymer Layers. *Langmuir* **2006,** *22* (4), 1379-82; (d) Piech, M.; Bell, N. S. Controlled Synthesis of Photochromic Polymer Brushes by Atom Transfer Radical Polymerization. *Macromolecules* **2006,** *39* (3), 915-922; (e) Bell, N. S.; Piech, M. Photophysical Effects between Spirobenzopyran-Methyl Methacrylate-Functionalized Colloidal Particles. *Langmuir* **2006,** *22* (4), 1420-7; (f) Wu, Y.; Zhang, C.; Qu, X.; Liu, Z.; Yang, Z. Light-Triggered Reversible Phase Transfer of Composite Colloids. *Langmuir* **2010,** *26* (12), 9442-8.

[88] (a) Parthenopoulos, D. A.; Rentzepis, P. M. Three-Dimensional Optical Storage Memory. *Science* **1989,** *245* (4920), 843-5; (b) Matczyszyn, K.; Olesiak-Banska, J.; Nakatani, K.; Yu, P.; Murugan, N. A.; Zalesny, R.; Roztoczynska, A.; Bednarska, J.; Bartkowiak, W.; Kongsted, J.; Agren, H.; Samoc, M. One- and Two-Photon

Absorption of a Spiropyran-Merocyanine System: Experimental and Theoretical Studies. *J. Phys. Chem. B* **2015,** *119* (4), 1515-22.

[89] Kundu, P. K.; Samanta, D.; Leizrowice, R.; Margulis, B.; Zhao, H.; Borner, M.; Udayabhaskararao, T.; Manna, D.; Klajn, R. Light-Controlled Self-Assembly of Non-Photoresponsive Nanoparticles. *Nat. Chem.* **2015,** *7* (8), 646-52.

[90] Zheng, Y. B.; Kiraly, B.; Cheunkar, S.; Huang, T. J.; Weiss, P. S. Incident-Angle-Modulated Molecular Plasmonic Switches: A Case of Weak Exciton-Plasmon Coupling. *Nano Lett.* **2011,** *11* (5), 2061-5.

[91] (a) Fihey, A.; Perrier, A.; Browne, W. R.; Jacquemin, D. Multiphotochromic Molecular Systems. *Chem. Soc. Rev.* **2015,** *44* (11), 3719-59; (b) Perrier, A.; Maurel, F.; Jacquemin, D. Single Molecule Multiphotochromism with Diarylethenes. *Acc. Chem. Res.* **2012,** *45* (8), 1173-82.

[92] (a) Kobayashi, Y.; Mutoh, K.; Abe, J. Fast Photochromic Molecules toward Realization of Photosynergetic Effects. *J. Phys. Chem. Lett.* **2016,** *7* (18), 3666-75; (b) Mutoh, K.; Kobayashi, Y.; Yamane, T.; Ikezawa, T.; Abe, J. Rate-Tunable Stepwise Two-Photon-Gated Photoresponsive Systems Employing a Synergetic Interaction between Transient Biradical Units. *J. Am. Chem. Soc.* **2017,** *139* (12), 4452-4461; (c) Yonekawa, I.; Mutoh, K.; Kobayashi, Y.; Abe, J. Intensity-Dependent Photoresponse of Biphotochromic Molecule Composed of a Negative and a Positive Photochromic Unit. *J. Am. Chem. Soc.* **2018,** *140* (3), 1091-1097; (d) Zhao, W. L.; Carreira, E. M. A Smart Photochromophore through Synergistic Coupling of Photochromic Subunits. *J. Am. Chem. Soc.* **2002,** *124* (8), 1582-1583.

[93] Zhao, F.; Grubert, L.; Hecht, S.; Bleger, D. Orthogonal Switching in Four-State Azobenzene Mixed-Dimers. *Chem. Commun.* **2017,** *53* (23), 3323-3326.

[94] Fihey, A.; Russo, R.; Cupellini, L.; Jacquemin, D.; Mennucci, B. Is Energy Transfer Limiting Multiphotochromism? Answers from Ab Initio Quantifications. *Phys. Chem. Chem. Phys.* **2017,** *19* (3), 2044-2052.

[95] (a) Li, C.; Yan, H.; Zhao, L. X.; Zhang, G. F.; Hu, Z.; Huang, Z. L.; Zhu, M. Q. A Trident Dithienylethene-Perylenemonoimide Dyad with Super Fluorescence Switching Speed and Ratio. *Nat. Commun.* **2014,** *5*, 5709; (b) Biellmann, T.; Galanti, A.; Boixel, J.; Wytko, J. A.; Guerchais, V.; Samorì, P.; Weiss, J. Fluorescence Commutation and Surface Photopatterning with Porphyrin Tetradithienylethene Switches. *Chem. Eur. J.* **2018,** *24* (7), 1631-1639.

[96] Peters, A.; Branda, N. R. Limited Photochromism in Covalently Linked Double 1,2-Dithienylethenes. *Adv. Mater. Opt. Electron.* **2000,** *10* (6), 245-249.

[97] Choi, H.; Jung, I.; Song, K. H.; Song, K.; Shin, D.-S.; Kang, S. O.; Ko, J. Synthesis and Photochromic Reactivity of Diarylethene Trimers Bridged by Ethenyl and Ethynyl Unit. *Tetrahedron* **2006,** *62* (38), 9059-9065.

[98] Kaieda, T.; Kobatake, S.; Miyasaka, H.; Murakami, M.; Iwai, N.; Nagata, Y.; Itaya, A.; Irie, M. Efficient Photocyclization of Dithienylethene Dimer, Trimer, and Tetramer: Quantum Yield and Reaction Dynamics. *J. Am. Chem. Soc.* **2002,** *124* (9), 2015-2024.

[99] Areephong, J.; Browne, W. R.; Feringa, B. L. Three-State Photochromic Switching in a Silyl Bridged Diarylethene Dimer. *Org Biomol Chem* **2007,** *5* (8), 1170-4.

[100] (a) Ordronneau, L.; Aubert, V.; Guerchais, V.; Boucekkine, A.; Le Bozec, H.; Singh, A.; Ledoux, I.; Jacquemin, D. The First Hexadithienylethene-Substituted Tris(Bipyridine)Metal Complexes as Quadratic Nlo Photoswitches: Combined Experimental and Dft Studies. *Chem. Eur. J.* **2013,** *19* (19), 5845-9; (b) Harvey, E. C.; Feringa, B. L.; Vos, J. G.; Browne, W. R.; Pryce, M. T. Transition Metal Functionalized Photo- and Redox-Switchable Diarylethene Based Molecular Switches. *Coord. Chem. Rev.* **2015,** *282-283*, 77-86.

[101] (a) Barth, J. V.; Costantini, G.; Kern, K. Engineering Atomic and Molecular Nanostructures at Surfaces. *Nature* **2005,** *437* (7059), 671-9; (b) De Feyter, S.; De Schryver, F. C. Two-Dimensional Supramolecular Self-Assembly Probed by Scanning Tunneling Microscopy. *Chem. Soc. Rev.* **2003,** *32* (3), 139-150; (c) Bartels, L. Tailoring Molecular Layers at Metal Surfaces. *Nat. Chem.* **2010,** *2* (2), 87-95; (d) Clair, S.; Pons, S.; Seitsonen, A. P.; Brune, H.; Kern, K.; Barth, J. V. Stm Study of Terephthalic Acid Self-Assembly on Au(111): Hydrogen-Bonded Sheets on an Inhomogeneous Substrate. *J. Phys. Chem. B* **2004,** *108* (38), 14585-14590; (e) Cai, L.; Sun, Q.; Bao, M.; Ma, H.; Yuan, C.; Xu, W. Competition between Hydrogen Bonds and Coordination Bonds Steered by the Surface Molecular Coverage. *ACS Nano* **2017,** *11* (4), 3727-3732.

[102] (a) Elemans, J. A.; Lei, S.; De Feyter, S. Molecular and Supramolecular Networks on Surfaces: From Two-Dimensional Crystal Engineering to Reactivity. *Angew. Chem., Int. Ed.* **2009,** *48* (40), 7298-332; (b) Ciesielski, A.; Palma, C. A.; Bonini, M.; Samorì, P. Towards Supramolecular Engineering of Functional Nanomaterials: Pre-Programming Multi-Component 2d Self-Assembly at Solid-Liquid Interfaces. *Adv. Mater.* **2010,** *22* (32), 3506-20; (c) Kudernac, T.; Lei, S.; Elemans, J. A.; De Feyter, S. Two-Dimensional Supramolecular Self-Assembly: Nanoporous Networks on Surfaces. *Chem. Soc. Rev.* **2009,** *38* (2), 402-21.

[103] (a) Zwaneveld, N. A. A.; Pawlak, R.; Abel, M.; Catalin, D.; Gigmes, D.; Bertin, D.; Porte, L. Organized Formation of 2d Extended Covalent Organic Frameworks at Surfaces. *J. Am. Chem. Soc.* **2008,** *130* (21), 6678-+; (b) Grill, L.; Dyer, M.; Lafferentz, L.; Persson, M.; Peters, M. V.; Hecht, S. Nano-Architectures by Covalent Assembly of Molecular Building Blocks. *Nat. Nanotechnol.* **2007,** *2* (11), 687-91; (c) Cardenas, L.; Gutzler, R.; Lipton-Duffin, J.; Fu, C.; Brusso, J. L.; Dinca, L. E.; Vondráček, M.; Fagot-Revurat, Y.; Malterre, D.; Rosei, F.; Perepichka, D. F. Synthesis and Electronic Structure of a Two Dimensional Π-Conjugated Polythiophene. *Chem. Sci.* **2013,** *4* (8), 3263.

[104] (a) Maeda, N.; Hirose, T.; Yokoyama, S.; Matsuda, K. Rational Design of Highly Photoresponsive Surface-Confined Self-Assembly of Diarylethenes: Reversible Three-State Photoswitching at the Liquid/Solid Interface. *J. Phys. Chem. C* **2016,** *120* (17), 9317-9325; (b) Iritani, K.; Tahara, K.; De Feyter, S.; Tobe, Y. Host-Guest Chemistry in Integrated Porous Space Formed by Molecular Self-Assembly at Liquid-Solid Interfaces. *Langmuir* **2017,** *33* (19), 4601-4618; (c) El Malah, T.; Ciesielski, A.; Piot, L.; Troyanov, S. I.; Mueller, U.; Weidner, S.; Samorì, P.; Hecht, S. Conformationally Pre-Organized and Ph-Responsive Flat Dendrons: Synthesis and Self-Assembly at the Liquid-Solid Interface. *Nanoscale* **2012,** *4* (2), 467-72; (d) Teyssandier, J.; De Feyter, S.; Mali, K. S. Host-Guest Chemistry in Two-Dimensional Supramolecular Networks. *Chem. Commun.* **2016,** *52* (77), 11465-11487.

[105] Amabilino, D. B.; De Feyter, S.; Lazzaroni, R.; Gomar-Nadal, E.; Veciana, J.; Rovira, C.; Abdel-Mottaleb, M. M.; Mamdouh, W.; Iavicoli, P.; Psychogyiopoulou, K.; Linares, M.; Minoia, A.; Xu, H.; Puigmartí-Luis, J. Monolayer Self-Assembly at Liquid–Solid Interfaces: Chirality and Electronic Properties of Molecules at Surfaces. *J. Phys.: Cond. Matter* **2008,** *20* (18), 184003.

[106] Uemura, S.; Tanoue, R.; Yilmaz, N.; Ohira, A.; Kunitake, M. Molecular Dynamics in Two-Dimensional Supramolecular Systems Observed by Stm. *Materials (Basel)* **2010,** *3* (8), 4252-4276.

[107] (a) Lackinger, M.; Griessl, S.; Markert, T.; Jamitzky, F.; Heckl, W. M. Self-Assembly of Benzene-Dicarboxylic Acid Isomers at the Liquid Solid Interface: Steric Aspects of Hydrogen Bonding. *J. Phys. Chem. B* **2004,** *108* (36), 13652-13655; (b) Zhou, H.; Dang, H.; Yi, J. H.; Nanci, A.; Rochefort, A.; Wuest, J. D. Frustrated 2d Molecular Crystallization. *J. Am. Chem. Soc.* **2007,** *129* (45), 13774-5; (c) Blunt, M.; Lin, X.; Gimenez-Lopez, M. d. C.; Schröder, M.; Champness, N. R.; Beton, P. H. Directing Two-Dimensional Molecular Crystallization Using Guest Templates. *Chem. Commun.* **2008,** (20), 2304-6.

[108] (a) Griessl, S.; Lackinger, M.; Edelwirth, M.; Hietschold, M.; Heckl, W. M. Self-Assembled Two-Dimensional Molecular Host-Guest Architectures from Trimesic Acid. *Single Mol.* **2002,** *3* (1), 25-31; (b) Ruben, M.; Payer, D.; Landa, A.; Comisso, A.; Gattinoni, C.; Lin, N.; Collin, J. P.; Sauvage, J. P.; De Vita, A.; Kern, K. 2d Supramolecular Assemblies of Benzene-1,3,5-Triyl-Tribenzoic Acid: Temperature-Induced Phase Transformations and Hierarchical Organization with Macrocyclic Molecules. *J. Am. Chem. Soc.* **2006,** *128* (49), 15644-51; (c) Lackinger, M.; Griessl, S.; Heckl, W. A.; Hietschold, M.; Flynn, G. W. Self-Assembly of Trimesic Acid at the Liquid-Solid Interfaces - a Study of Solvent-Induced Polymorphism. *Langmuir* **2005,** *21* (11), 4984-4988; (d) Ye, Y. C.; Sun, W.; Wang, Y. F.; Shao, X.; Xu, X. G.; Cheng, F.; Li, J. L.; Wu, K. A Unified Model: Self-Assembly of Trimesic Acid on Gold. *J. Phys. Chem. C* **2007,** *111* (28), 10138-10141; (e) Ha, N. T. N.; Gopakumar, T. G.; Gutzler, R.; Lackinger, M.; Tang, H.; Hietschold, M. Influence of Solvophobic Effects on Self-Assembly of Trimesic Acid at the Liquid-Solid Interface. *J. Phys. Chem. C* **2010,** *114* (8), 3531-3536; (f) Eder, G.; Kloft, S.; Martsinovich, N.; Mahata, K.; Schmittel, M.; Heckl, W. M.; Lackinger, M. Incorporation Dynamics of Molecular Guests into Two-Dimensional Supramolecular Host Networks at the Liquid-Solid Interface. *Langmuir* **2011,** *27* (22), 13563-71.

[109] (a) Weber, U. K.; Burlakov, V. M.; Perdigao, L. M.; Fawcett, R. H.; Beton, P. H.; Champness, N. R.; Jefferson, J. H.; Briggs, G. A.; Pettifor, D. G. Role of Interaction Anisotropy in the Formation and Stability of Molecular Templates. *Phys. Rev. Lett.* **2008,** *100* (15), 156101; (b) Eichhorst-Gerner, K.; Stabel, A.; Moessner, G.; Declerq, D.; Valiyaveettil, S.; Enkelmann, V.; Mullen, K.; Rabe, J. P. Self-Assembly of a Two-Component Hydrogen-Bonded Network: Comparison of the Two-Dimensional Structure Observed by Scanning Tunneling Microscopy and the Three-Dimensional Crystal Lattice. *Angew. Chem., Int. Ed.* **1996,** *35* (13-14), 1492-1495; (c) Stabel, A.; Heinz, R.; De Schryver, F. C.; Rabe, J. P. Ostwald Ripening of Two-Dimensional Crystals at the Solid-Liquid Interface. *J. Phys. Chem.* **1995,** *99* (2), 505-507.

[110] Dienstmaier, J. F.; Mahata, K.; Walch, H.; Heckl, W. M.; Schmittel, M.; Lackinger, M. On the Scalability of Supramolecular Networks - High Packing Density Vs Optimized Hydrogen Bonds in Tricarboxylic Acid Monolayers. *Langmuir* **2010,** *26* (13), 10708-16.

[111] (a) Alemani, M.; Peters, M. V.; Hecht, S.; Rieder, K. H.; Moresco, F.; Grill, L. Electric Field-Induced Isomerization of Azobenzene by Stm. *J. Am. Chem. Soc.* **2006,** *128* (45), 14446-7; (b) Pace, G.; Ferri, V.; Grave, C.; Elbing, M.; von Hänisch, C.; Zharnikov, M.; Mayor, M.; Rampi, M. A.; Samorì, P. Cooperative Light-Induced Molecular Movements of Highly Ordered Azobenzene Self-Assembled Monolayers. *Proc. Natl. Acad. Sci. U. S. A.* **2007,** *104* (24), 9937-42.

[112] (a) Feng, C. L.; Zhang, Y.; Jin, J.; Song, Y.; Xie, L.; Qu, G.; Jiang, L.; Zhu, D. Completely Interfacial Photoisomerization of 4-Hydroxy-30-Trifluoromethyl-Azobenzene Studied by Stm on Hopg. *Surf. Sci.* **2002,** *513*, 111-118; (b) Bléger, D.; Ciesielski, A.; Samorì, P.; Hecht, S. Photoswitching Vertically Oriented Azobenzene Self-Assembled Monolayers at the Solid-Liquid Interface. *Chem. Eur. J.* **2010,** *16* (48), 14256-60.

[113] Vanoppen, P.; Grim, P. C. M.; Rücker, M.; De Feyter, S.; Moessner, G.; Valiyaveettil, S.; Müllen, K.; De Schryver, F. C. Solvent Codeposition and Cis-Trans Isomerization of Isophthalic Acid Derivatives Studied by Stm. *J. Phys. Chem.* **1996,** *100* (50), 19636-19641.

[114] (a) Shen, Y. T.; Guan, L.; Zhu, X. Y.; Zeng, Q. D.; Wang, C. Submolecular Observation of Photosensitive Macrocycles and Their Isomerization Effects on Host-Guest Network. *J. Am. Chem. Soc.* **2009,** *131* (17), 6174-6180; (b) Shen, Y. T.; Deng, K.; Zhang, X. M.; Feng, W.; Zeng, Q. D.; Wang, C.; Gong, J. R. Switchable Ternary Nanoporous Supramolecular Network on Photo-Regulation. *Nano Lett.* **2011,** *11* (8), 3245-50; (c) Shen, Y.-t.;

Deng, K.; Zhang, X.-m.; Lei, D.; Xia, Y.; Zeng, Q.-d.; Wang, C. Selective and Competitive Adsorptions of Guest Molecules in Phase-Separated Networks. *J. Phys. Chem. C* **2011,** *115* (40), 19696-19701.

[115] Folling, J.; Belov, V.; Kunetsky, R.; Medda, R.; Schonle, A.; Egner, A.; Eggeling, C.; Bossi, M.; Hell, S. W. Photochromic Rhodamines Provide Nanoscopy with Optical Sectioning. *Angew. Chem., Int. Ed.* **2007,** *46* (33), 6266-70.

[116] Fukaminato, T. Single-Molecule Fluorescence Photoswitching: Design and Synthesis of Photoswitchable Fluorescent Molecules. *J. Photochem. Photobiol. C* **2011,** *12* (3), 177-208.

[117] Yildiz, I.; Deniz, E.; Raymo, F. M. Fluorescence Modulation with Photochromic Switches in Nanostructured Constructs. *Chem Soc Rev* **2009,** *38* (7), 1859-67.

[118] Kawai, T.; Sasaki, T.; Irie, M. A Photoresponsive Laser Dye Containing Photochromic Dithienylethene Units. *Chem. Commun.* **2001,** (8), 711-712.

[119] Tian, H.; Chen, B. Z.; Tu, H. Y.; Mullen, K. Novel Bisthienylethene-Based Photochromic Tetraazaporphyrin with Photoregulating Luminescence. *Adv. Mater.* **2002,** *14* (12), 918-923.

[120] (a) Burda, C.; Chen, X.; Narayanan, R.; El-Sayed, M. A. Chemistry and Properties of Nanocrystals of Different Shapes. *Chem. Rev.* **2005,** *105* (4), 1025-102; (b) Xia, Y.; Xiong, Y.; Lim, B.; Skrabalak, S. E. Shape-Controlled Synthesis of Metal Nanocrystals: Simple Chemistry Meets Complex Physics? *Angew. Chem., Int. Ed.* **2009,** *48* (1), 60-103.

[121] Daniel, M. C.; Astruc, D. Gold Nanoparticles: Assembly, Supramolecular Chemistry, Quantum-Size-Related Properties, and Applications toward Biology, Catalysis, and Nanotechnology. *Chem. Rev.* **2004,** *104* (1), 293-346.

[122] Faraday, M. The Bakerian Lecture: Experimental Relations of Gold (and Other Metals) to Light. *Phil. Trans. R. Soc. Lond.* **1857,** *147* (0), 145-181.

[123] (a) Mie, G. Beiträge Zur Optik Trüber Medien, Speziell Kolloidaler Metallösungen. *Ann. Phys. (Berlin)* **1908,** *330* (3), 377-445; (b) Zsigmondy, R. A. Properties of Colloids. Nobel Lecture. *NobelPrize.org* **1926**.

[124] de Aberasturi, D. J.; Serrano-Montes, A. B.; Liz-Marzán, L. M. Modern Applications of Plasmonic Nanoparticles: From Energy to Health. *Adv. Optical Mater.* **2015,** *3* (5), 602-617.

[125] Xin, H.; Namgung, B.; Lee, L. P. Nanoplasmonic Optical Antennas For life Sciences and Medicine. *Nat. Rev. Mats.* **2018,** *3* (8), 228-243.

[126] Atwater, H. A.; Polman, A. Plasmonics for Improved Photovoltaic Devices. *Nat. Mater.* **2010,** *9* (3), 205-13.

[127] Meinzer, N.; Barnes, W. L.; Hooper, I. R. Plasmonic Meta-Atoms and Metasurfaces. *Nat. Photonics* **2014,** *8* (12), 889-898.

[128] Huang, X.; Neretina, S.; El-Sayed, M. A. Gold Nanorods: From Synthesis and Properties to Biological and Biomedical Applications. *Adv. Mater.* **2009,** *21* (48), 4880-910.

[129] Nehl, C. L.; Hafner, J. H. Shape-Dependent Plasmon Resonances of Gold Nanoparticles. *J. Mater. Chem.* **2008,** *18* (21), 2415.

[130] (a) Turkevich, J.; Stevenson, P. C.; Hillier, J. A Study of the Nucleation and Growth Processes in the Synthesis of Colloidal Gold. *Discuss. Faraday Soc.* **1951,** *11*, 55; (b) Frens, G. Controlled Nucleation for the Regulation of the Particle Size in Monodisperse Gold Suspensions. *Nature: Phys. Sci.* **1973,** *241* (105), 20-22.

[131] Sardar, R.; Funston, A. M.; Mulvaney, P.; Murray, R. W. Gold Nanoparticles: Past, Present, and Future. *Langmuir* **2009,** *25* (24), 13840-51.

[132] (a) Brust, M.; Walker, M.; Bethell, D.; Schiffrin, D. J.; Whyman, R. Synthesis of Thiol-Derivatised Gold Nanoparticles in a Two-Phase Liquid-Liquid System. *J. Chem. Soc., Chem. Commun.* **1994**, 801-802; (b) Brust, M.; Fink, J.; Bethell, D.; Schiffrin, D. J.; Kiely, C. Synthesis and Reactions of Functionalised Gold Nanoparticles. *J. Chem. Soc., Chem. Commun.* **1995**, 1655-1656.

[133] Love, J. C.; Estroff, L. A.; Kriebel, J. K.; Nuzzo, R. G.; Whitesides, G. M. Self-Assembled Monolayers of Thiolates on Metals as a Form of Nanotechnology. *Chem. Rev.* **2005,** *105* (4), 1103-1169.

[134] (a) Zhang, H.; Jin, M. S.; Xiong, Y. J.; Lim, B.; Xia, Y. N. Shape-Controlled Synthesis of Pd Nanocrystals and Their Catalytic Applications. *Acc. Chem. Res.* **2013,** *46* (8), 1783-1794; (b) Gawande, M. B.; Goswami, A.; Felpin, F. X.; Asefa, T.; Huang, X.; Silva, R.; Zou, X.; Zboril, R.; Varma, R. S. Cu and Cu-Based Nanoparticles: Synthesis and Applications in Catalysis. *Chem. Rev.* **2016,** *116* (6), 3722-811.

[135] (a) Nikoobakht, B.; Wang, Z. L.; El-Sayed, M. A. Self-Assembly of Gold Nanorods. *J. Phys. Chem. B* **2000,** *104* (36), 8635-8640; (b) Diroll, B. T.; Greybush, N. J.; Kagan, C. R.; Murray, C. B. Smectic Nanorod Superlattices Assembled on Liquid Subphases: Structure, Orientation, Defects, and Optical Polarization. *Chem. Mater.* **2015,** *27* (8), 2998-3008; (c) Jana, N. R. Shape Effect in Nanoparticle Self-Assembly. *Angew. Chem., Int. Ed.* **2004,** *43* (12), 1536-40; (d) Guerrero-Martinez, A.; Perez-Juste, J.; Carbo-Argibay, E.; Tardajos, G.; Liz-Marzan, L. M. Gemini-Surfactant-Directed Self-Assembly of Monodisperse Gold Nanorods into Standing Superlattices. *Angew. Chem., Intl. Ed.* **2009,** *48* (50), 9484-8; (e) Peng, B.; Li, G.; Li, D.; Dodson, S.; Zhang, Q.; Zhang, J.; Lee, Y. H.; Demir, H. V.; Ling, X. Y.; Xiong, Q. Vertically Aligned Gold Nanorod Monolayer on Arbitrary Substrates: Self-Assembly and Femtomolar Detection of Food Contaminants. *ACS Nano* **2013,** *7* (7), 5993-6000; (f) Sreeprasad, T. S.; Samal, A. K.; Pradeep, T. One-, Two-, and Three-Dimensional Superstructures of Gold Nanorods Induced by Dimercaptosuccinic Acid. *Langmuir* **2008,** *24* (9), 4589-99; (g) Sun, Z.; Ni, W.; Yang, Z.; Kou, X.; Li, L.; Wang, J. Ph-Controlled Reversible Assembly and Disassembly of Gold Nanorods. *Small* **2008,** *4* (9), 1287-92; (h) Thai, T.; Zheng, Y.; Ng, S. H.; Mudie, S.; Altissimo, M.; Bach,

U. Self-Assembly of Vertically Aligned Gold Nanorod Arrays on Patterned Substrates. *Angew. Chem., Intl. Ed.* **2012,** *51* (35), 8732-5; (i) Xie, Y.; Guo, S.; Ji, Y.; Guo, C.; Liu, X.; Chen, Z.; Wu, X.; Liu, Q. Self-Assembly of Gold Nanorods into Symmetric Superlattices Directed by Oh-Terminated Hexa(Ethylene Glycol) Alkanethiol. *Langmuir* **2011,** *27* (18), 11394-400.

[136] (a) Alvarez-Puebla, R. A.; Agarwal, A.; Manna, P.; Khanal, B. P.; Aldeanueva-Potel, P.; Carbo-Argibay, E.; Pazos-Perez, N.; Vigderman, L.; Zubarev, E. R.; Kotov, N. A.; Liz-Marzan, L. M. Gold Nanorods 3d-Supercrystals as Surface Enhanced Raman Scattering Spectroscopy Substrates for the Rapid Detection of Scrambled Prions. *Proc. Natl. Acad. Sci. USA* **2011,** *108* (20), 8157-61; (b) Jackson, J. B.; Halas, N. J. Surface-Enhanced Raman Scattering on Tunable Plasmonic Nanoparticle Substrates. *Proc. Natl. Acad. Sci. USA* **2004,** *101* (52), 17930-5; (c) Talley, C. E.; Jackson, J. B.; Oubre, C.; Grady, N. K.; Hollars, C. W.; Lane, S. M.; Huser, T. R.; Nordlander, P.; Halas, N. J. Surface-Enhanced Raman Scattering from Individual Au Nanoparticles and Nanoparticle Dimer Substrates. *Nano Lett.* **2005,** *5* (8), 1569-74; (d) Su, L.; Yuan, H.; Lu, G.; Rocha, S.; Orrit, M.; Hofkens, J.; Uji-i, H. Super-Resolution Localization and Defocused Fluorescence Microscopy on Resonantly Coupled Single-Molecule, Single-Nanorod Hybrids. *ACS Nano* **2016,** *10* (2), 2455-66; (e) Abadeer, N. S.; Brennan, M. R.; Wilson, W. L.; Murphy, C. J. Distance and Plasmon Wavelength Dependent Fluorescence of Molecules Bound to Silica-Coated Gold Nanorods. *ACS Nano* **2014,** *8* (8), 8392-406; (f) Khatua, S.; Paulo, P. M.; Yuan, H.; Gupta, A.; Zijlstra, P.; Orrit, M. Resonant Plasmonic Enhancement of Single-Molecule Fluorescence by Individual Gold Nanorods. *ACS Nano* **2014,** *8* (5), 4440-9; (g) Fu, Y.; Zhang, J.; Lakowicz, J. R. Plasmon-Enhanced Fluorescence from Single Fluorophores End-Linked to Gold Nanorods. *J. Am. Chem. Soc.* **2010,** *132* (16), 5540-1; (h) Wientjes, E.; Renger, J.; Curto, A. G.; Cogdell, R.; van Hulst, N. F. Strong Antenna-Enhanced Fluorescence of a Single Light-Harvesting Complex Shows Photon Antibunching. *Nat. Commun.* **2014,** *5*, 4236.

[137] (a) Dreaden, E. C.; Alkilany, A. M.; Huang, X.; Murphy, C. J.; El-Sayed, M. A. The Golden Age: Gold Nanoparticles for Biomedicine. *Chem Soc Rev* **2012,** *41* (7), 2740-79; (b) Ye, X.; Zheng, C.; Chen, J.; Gao, Y.; Murray, C. B. Using Binary Surfactant Mixtures to Simultaneously Improve the Dimensional Tunability and Monodispersity in the Seeded Growth of Gold Nanorods. *Nano Lett.* **2013,** *13* (2), 765-71.

[138] Payne, E. K.; Shuford, K. L.; Park, S.; Schatz, G. C.; Mirkin, C. A. Multipole Plasmon Resonances in Gold Nanorods. *J. Phys. Chem. B* **2006,** *110* (5), 2150-4.

[139] Homola, J. Surface Plasmon Resonance Sensors for Detection of Chemical and Biological Species. *Chem. Rev.* **2008,** *108* (2), 462-93.

[140] Willets, K. A.; Van Duyne, R. P. Localized Surface Plasmon Resonance Spectroscopy and Sensing. *Annu. Rev. Phys. Chem.* **2007,** *58*, 267-97.

[141] Otte, M. A.; Sepulveda, B.; Ni, W.; Juste, J. P.; Liz-Marzan, L. M.; Lechuga, L. M. Identification of the Optimal Spectral Region for Plasmonic and Nanoplasmonic Sensing. *ACS Nano* **2010,** *4* (1), 349-57.

[142] *Organic Photochromes*. (Ed.: Eltsov, A. V.), Consultants Bureau, New York, **1990**.

[143] Valeur, B., *Molecular Fluorescence: Principles and Applications*. (Ed.: Wiley-VCH), **2001**.

[144] Klàn, P.; Wirz, J., *Photochemistry of Organic Compounds: From Concepts to Practice*. (Ed.: Wiley), **2009**.

[145] *The Exploration of Supramolecular Systems and Nanostructures by Photochemical Techniques*. (Ed.: Ceroni, P., Lecture Notes in Chemistry, 78), Springer, **2012**.

[146] Demas, J. N.; Crosby, G. A. The Measurement of Photoluminescence Quantum Yields. A Review. *J. Phys. Chem.* **1971,** *75* (8), 991-1023.

[147] Vavilov, S. I. Die Fluoreszenzausbeute Von Farbstofflösungen. *Z. Phys.* **1924,** *22*, 266.

[148] (a) Weber, G.; Teale, F. W. J. Determination of the Absolute Quantum Yield of Fluorescent Solutions. *Trans. Faraday Soc.* **1957,** *53*, 646; (b) Hercules, D. M.; Frankel, H. Colloidal Silica as a Standard for Measuring Absolute Fluorescence Yield. *Science* **1960,** *131* (3413), 1611-2.

[149] Braslavsky, S. E.; Heibel, G. E. Time-Resolved Photothermal and Photoacoustic Methods Applied to Photoinduced Processes in Solution. *Chem. Rev.* **1992,** *92* (6), 1381-1410.

[150] Suzuki, K.; Kobayashi, A.; Kaneko, S.; Takehira, K.; Yoshihara, T.; Ishida, H.; Shiina, Y.; Oishi, S.; Tobita, S. Reevaluation of Absolute Luminescence Quantum Yields of Standard Solutions Using a Spectrometer with an Integrating Sphere and a Back-Thinned Ccd Detector. *Phys. Chem. Chem. Phys.* **2009,** *11* (42), 9850-60.

[151] Myles, A. J.; Branda, N. R. Porphyrinic Phenoxynaphthacenequinones. *Tetrahedron Lett.* **2000,** *41* (20), 3785-3788.

[152] Lakowicz, J. R., *Principles of Fluorescence Spectroscopy*. (Ed.: Springer), 3 ed.); **2006**.

[153] Kuhn, H. J.; Braslavsky, S. E.; Schmidt, R. Chemical Actinometry. *Pure Appl. Chem.* **2004,** *76* (12), 2105-2146.

[154] Ladanyi, V.; Dvorak, P.; Al Anshori, J.; Vetrakova, L.; Wirz, J.; Heger, D. Azobenzene Photoisomerization Quantum Yields in Methanol Redetermined. *Photochem. Photobiol. Sci.* **2017,** *16* (12), 1757-1761.

[155] Hatchard, C. G.; Parker, C. A. A New Sensitive Chemical Actinometer. Ii. Potassium Ferrioxalate as a Standard Chemical Actinometer. *Proc. R. Soc. Lond. A.* **1956,** *235* (1203), 518-536.

[156] Glaze, A. P.; Heller, H. G.; Whittall, J. Photochromic Heterocyclic Fulgides. Part 7. (E)-Adamantylidene-[1-(2,5-Dimethyl-3-Furyl)Ethylidene]Succinic Anhydride and Derivatives: Model Photochromic Compounds for Optical Recording Media. *J. Chem. Soc., Perkin Trans. 2* **1992,** (4), 591.

[157] Montalti, M.; Credi, A.; Prodi, L.; Gandolfi, M. T., *Handbook of Photochemistry, Third Edition*. (Ed.: CRC Press, Boca Raton, **2006**.

[158] Zrimsek, A. B.; Chiang, N.; Mattei, M.; Zaleski, S.; McAnally, M. O.; Chapman, C. T.; Henry, A.-I.; Schatz, G. C.; Van Duyne, R. P. Single-Molecule Chemistry with Surface- and Tip-Enhanced Raman Spectroscopy. *Chem. Rev.* **2016**.

[159] Dieringer, J. A.; McFarland, A. D.; Shah, N. C.; Stuart, D. A.; Whitney, A. V.; Yonzon, C. R.; Young, M. A.; Zhang, X.; Van Duyne, R. P. Introductory Lecture : Surface Enhanced Raman Spectroscopy: New Materials, Concepts, Characterization Tools, and Applications. *Faraday Discuss.* **2006,** *132*, 9-26.

[160] (a) Fleischmann, M.; Hendra, P. J.; McQuillan, A. J. Raman Spectra of Pyridine Adsorbed at a Silver Electrode. *Chem. Phys. Lett.* **1974,** *26* (2), 163-166; (b) Albrecht, M. G.; Creighton, J. A. Anomalously Intense Raman Spectra of Pyridine at a Silver Electrode. *J. Am. Chem. Soc.* **1977,** *99* (15), 5215-5217; (c) Jeanmaire, D. L.; Van Duyne, R. P. Surface Raman Spectroelectrochemistry: Part I. Heterocyclic, Aromatic, and Aliphatic Amines Adsorbed on the Anodized Silver Electrode. *J. Electroanal. Chem. Interfacial Electrochem.* **1977,** *84* (1), 1-20.

[161] (a) Révész, Á.; Schröder, D.; Rokob, T. A.; Havlík, M.; Dolenský, B. In-Flight Epimerization of a Bis-Tröger Base. *Angew. Chem., Int. Ed.* **2011,** *50* (10), 2401-4; (b) Thiel, J.; Yang, D.; Rosnes, M. H.; Liu, X.; Yvon, C.; Kelly, S. E.; Song, Y. F.; Long, D. L.; Cronin, L. Observing the Hierarchical Self-Assembly and Architectural Bistability of Hybrid Molecular Metal Oxides Using Ion-Mobility Mass Spectrometry. *Angew. Chem., Int. Ed.* **2011,** *50* (38), 8871-5; (c) Urner, L. H.; Thota, B. N.; Nachtigall, O.; Warnke, S.; von Helden, G.; Haag, R.; Pagel, K. Online Monitoring the Isomerization of an Azobenzene-Based Dendritic Bolaamphiphile Using Ion Mobility-Mass Spectrometry. *Chem. Commun.* **2015,** *51* (42), 8801-4; (d) Bull, J. N.; Scholz, M. S.; Coughlan, N. J.; Kawai, A.; Bieske, E. J. Monitoring Isomerization of Molecules in Solution Using Ion Mobility Mass Spectrometry. *Anal. Chem.* **2016,** *88* (24), 11978-11981.

[162] McDaniel, E. W.; Martin, D. W.; Barnes, W. S. Drift Tube-Mass Spectrometer for Studies of Low-Energy Ion-Molecule Reactions. *Rev. Sci. Instrum.* **1962,** *33* (1), 2-7.

[163] Kanu, A. B.; Dwivedi, P.; Tam, M.; Matz, L.; Hill, H. H., Jr. Ion Mobility-Mass Spectrometry. *J. Mass. Spectrom.* **2008,** *43* (1), 1-22.

[164] D'Atri, V.; Porrini, M.; Rosu, F.; Gabelica, V. Linking Molecular Models with Ion Mobility Experiments. Illustration with a Rigid Nucleic Acid Structure. *J. Mass. Spectrom.* **2015,** *50* (5), 711-26.

[165] Duez, Q.; Chirot, F.; Lienard, R.; Josse, T.; Choi, C.; Coulembier, O.; Dugourd, P.; Cornil, J.; Gerbaux, P.; De Winter, J. Polymers for Traveling Wave Ion Mobility Spectrometry Calibration. *J. Am. Soc. Mass. Spectrom.* **2017,** *28* (11), 2483-2491.

[166] Forsythe, J. G.; Petrov, A. S.; Walker, C. A.; Allen, S. J.; Pellissier, J. S.; Bush, M. F.; Hud, N. V.; Fernandez, F. M. Collision Cross Section Calibrants for Negative Ion Mode Traveling Wave Ion Mobility-Mass Spectrometry. *Analyst* **2015,** *140* (20), 6853-61.

[167] *Scanning Microscopy for Nanotechnology: Techniques and Applications*. (Ed.: Zhou, W.; Lin Wang, Z.), Springer-Verlag, New York, **2007**.

[168] Wang, Z. L.; Lee, J. L., Electron Microscopy Techniques for Imaging and Analysis of Nanoparticles. In *Developments in Surface Contamination and Cleaning* (Ed.: Kohli, R.; Mittal, K. L.), Elsevier, **2008**; Vol. 1, pp 395-443 chapter 9.

[169] Binnig, G.; Rohrer, H.; Gerber, C.; Weibel, E. Surface Studies by Scanning Tunneling Microscopy. *Phys. Rev. Lett.* **1982,** *49* (1), 57-61.

[170] (a) Gimzewski, J. K.; Joachim, C. Nanoscale Science of Single Molecules Using Local Probes. *Science* **1999,** *283* (5408), 1683-1688; (b) Shirai, Y.; Osgood, A. J.; Zhao, Y.; Yao, Y.; Saudan, L.; Yang, H.; Yu-Hung, C.; Alemany, L. B.; Sasaki, T.; Morin, J. F.; Guerrero, J. M.; Kelly, K. F.; Tour, J. M. Surface-Rolling Molecules. *J. Am. Chem. Soc.* **2006,** *128* (14), 4854-64.

[171] (a) *Templates in Chemistry Iii*. (Ed.: Broekmann, P.; Dötz, K.-H.; Schalley, C. A.), *Top. Curr. Chem.*), *287*), Springer, **2009**; (b) *Scanning Probe Microscopies Beyond Imaging: Manipulation of Molecules and Nanostructures*. (Ed.: Samorì, P.), Wiley-VCH, **2006**.

[172] Krull, C., *Electronic Structure of Metal Phthalocyanines on Ag(100)*. (Ed.: *Springer Theses*), Springer, **2014**.

[173] (a) Tersoff, J.; Hamann, D. R. Theory and Application for the Scanning Tunneling Microscope. *Phys. Rev. Lett.* **1983,** *50* (25), 1998-2001; (b) Tersoff, J.; Hamann, D. R. Theory of the Scanning Tunneling Microscope. *Phys. Rev. B* **1985,** *31* (2), 805-813.

[174] Bardeen, J. Tunnelling from a Many-Particle Point of View. *Phys. Rev. Lett.* **1961,** *6* (2), 57-59.

[175] Giancarlo, L. C.; Flynn, G. W. Scanning Tunneling and Atomic Force Microscopy Probes of Self-Assembled, Physisorbed Monolayers: Peeking at the Peaks. *Annu. Rev. Phys. Chem.* **1998,** *49*, 297-336.

[176] Jana, N. R.; Gearheart, L.; Murphy, C. J. Seed-Mediated Growth Approach for Shape-Controlled Synthesis of Spheroidal and Rod-Like Gold Nanoparticles Using a Surfactant Template. *Adv. Mater.* **2001,** *13* (18), 1389-1393.

[177] Ye, X.; Jin, L.; Caglayan, H.; Chen, J.; Xing, G.; Zheng, C.; Doan-Nguyen, V.; Kang, Y.; Engheta, N.; Kagan, C. R.; Murray, C. B. Improved Size-Tunable Synthesis of Monodisperse Gold Nanorods through the Use of Aromatic Additives. *ACS Nano* **2012,** *6* (3), 2804-2817.

[178] Wiesner, J.; Wokaun, A. Anisometric Gold Colloids. Preparation, Characterization, and Optical Properties. *Chem. Phys. Lett.* **1989,** *157* (6), 569-575.

[179] van der Zande, B. M. I.; Böhmer, M. R.; Fokkink, L. G. J.; Schönenberger, C. Aqueous Gold Sols of Rod-Shaped Particles. *J. Phys. Chem. B* **1997,** *101* (6), 852-854.

[180] Yu; Chang, S.-S.; Lee, C.-L.; Wang, C. R. C. Gold Nanorods: Electrochemical Synthesis and Optical Properties. *J. Phys. Chem. B* **1997,** *101* (34), 6661-6664.
[181] Lohse, S. E.; Murphy, C. J. The Quest for Shape Control: A History of Gold Nanorod Synthesis. *Chem. Mater.* **2013,** *25* (8), 1250-1261.
[182] Lin, Z.; Cai, J. J.; Scriven, L. E.; Davis, H. T. Spherical-to-Wormlike Micelle Transition in Ctab Solutions. *J. Phys. Chem.* **1994,** *98* (23), 5984-5993.
[183] Scarabelli, L.; Sanchez-Iglesias, A.; Perez-Juste, J.; Liz-Marzan, L. M. A "Tips and Tricks" Practical Guide to the Synthesis of Gold Nanorods. *J. Phys. Chem. Lett.* **2015,** *6* (21), 4270-9.
[184] Rodriguez-Fernandez, J.; Perez-Juste, J.; Mulvaney, P.; Liz-Marzan, L. M. Spatially-Directed Oxidation of Gold Nanoparticles by Au(Iii)-Ctab Complexes. *J. Phys. Chem. B* **2005,** *109* (30), 14257-61.
[185] Sharma, V.; Park, K.; Srinivasarao, M. Shape Separation of Gold Nanorods Using Centrifugation. *Proc. Natl. Acad. Sci. USA* **2009,** *106* (13), 4981-5.
[186] Park, K.; Koerner, H.; Vaia, R. A. Depletion-Induced Shape and Size Selection of Gold Nanoparticles. *Nano Lett.* **2010,** *10* (4), 1433-9.
[187] (a) Liao, H.; Hafner, J. H. Gold Nanorod Bioconjugates. *Chem. Mater.* **2005,** *17* (18), 4636-4641; (b) Gentili, D.; Ori, G.; Comes Franchini, M. Double Phase Transfer of Gold Nanorods for Surface Functionalization and Entrapment into Peg-Based Nanocarriers. *Chem. Commun.* **2009,** (39), 5874-6; (c) Vigderman, L.; Manna, P.; Zubarev, E. R. Quantitative Replacement of Cetyl Trimethylammonium Bromide by Cationic Thiol Ligands on the Surface of Gold Nanorods and Their Extremely Large Uptake by Cancer Cells. *Angew. Chem., Int. Ed.* **2012,** *51* (3), 636-41; (d) Sugikawa, K.; Nagata, S.; Furukawa, Y.; Kokado, K.; Sada, K. Stable and Functional Gold Nanorod Composites with a Metal–Organic Framework Crystalline Shell. *Chem. Mater.* **2013,** *25* (13), 2565-2570; (e) Locatelli, E.; Monaco, I.; Comes Franchini, M. Surface Modifications of Gold Nanorods for Applications in Nanomedicine. *RSC Adv.* **2015,** *5* (28), 21681-21699.
[188] (a) Gittins, D. I.; Caruso, F. Tailoring the Polyelectrolyte Coating of Metal Nanoparticles. *J. Phys. Chem. B* **2001,** *105* (29), 6846-6852; (b) Gole, A.; Murphy, C. J. Polyelectrolyte-Coated Gold Nanorods: Synthesis, Characterization and Immobilization. *Chem. Mater.* **2005,** *17* (6), 1325-1330.
[189] (a) Wijaya, A.; Hamad-Schifferli, K. Ligand Customization and DNA Functionalization of Gold Nanorods Via Round-Trip Phase Transfer Ligand Exchange. *Langmuir* **2008,** *24* (18), 9966-9; (b) Pan, S.; He, L.; Peng, J.; Qiu, F.; Lin, Z. Chemical-Bonding-Directed Hierarchical Assembly of Nanoribbon-Shaped Nanocomposites of Gold Nanorods and Poly(3-Hexylthiophene). *Angew. Chem., Int. Ed.* **2016**.
[190] Côté, A. P.; El-Kaderi, H. M.; Furukawa, H.; Hunt, J. R.; Yaghi, O. M. Reticular Synthesis of Microporous and Mesoporous 2d Covalent Organic Frameworks. *J. Am. Chem. Soc.* **2007,** *129* (43), 12914-5.
[191] (a) Bahrenburg, J.; Sievers, C. M.; Schonborn, J. B.; Hartke, B.; Renth, F.; Temps, F.; Nather, C.; Sonnichsen, F. D. Photochemical Properties of Multi-Azobenzene Compounds. *Photochem. Photobiol. Sci.* **2013,** *12* (3), 511-8; (b) Lee, S.; Oh, S.; Lee, J.; Malpani, Y.; Jung, Y. S.; Kang, B.; Lee, J. Y.; Ozasa, K.; Isoshima, T.; Lee, S. Y.; Hara, M.; Hashizume, D.; Kim, J. M. Stimulus-Responsive Azobenzene Supramolecules: Fibers, Gels, and Hollow Spheres. *Langmuir* **2013,** *29* (19), 5869-77; (c) Kind, J.; Kaltschnee, L.; Leyendecker, M.; Thiele, C. M. Distinction of Trans-Cis Photoisomers with Comparable Optical Properties in Multiple-State Photochromic Systems - Examining a Molecule with Three Azobenzenes Via in Situ Irradiation Nmr Spectroscopy. *Chem. Commun.* **2016,** *52* (84), 12506-12509; (d) Koch, M.; Saphiannikova, M.; Santer, S.; Guskova, O. Photoisomers of Azobenzene Star with a Flat Core: Theoretical Insights into Multiple States from Dft and Md Perspective. *J. Phys. Chem. B* **2017,** *121* (37), 8854-8867.
[192] (a) Bléger, D.; Liebig, T.; Thiermann, R.; Maskos, M.; Rabe, J. P.; Hecht, S. Light-Orchestrated Macromolecular "Accordions": Reversible Photoinduced Shrinking of Rigid-Rod Polymers. *Angew. Chem., Int. Ed.* **2011,** *50* (52), 12559-63; (b) Yu, Z.; Hecht, S. Reversible and Quantitative Denaturation of Amphiphilic Oligo(Azobenzene) Foldamers. *Angew. Chem., Int. Ed.* **2011,** *50* (7), 1640-3.
[193] Segarra-Maset, M. D.; van Leeuwen, P. W. N. M.; Freixa, Z. Light Switches the Ligand! Photochromic Azobenzene-Phosphanes. *Eur. J. Inorg. Chem.* **2010,** *2010* (14), 2075-2078.
[194] Vijayaraghavan, S.; Ecija, D.; Auwarter, W.; Joshi, S.; Seufert, K.; Drach, M.; Nieckarz, D.; Szabelski, P.; Aurisicchio, C.; Bonifazi, D.; Barth, J. V. Supramolecular Assembly of Interfacial Nanoporous Networks with Simultaneous Expression of Metal-Organic and Organic-Bonding Motifs. *Chem. Eur. J.* **2013,** *19* (42), 14143-50.
[195] Surin, M.; Samori, P. Multicomponent Monolayer Architectures at the Solid-Liquid Interface: Towards Controlled Space-Confined Properties and Reactivity of Functional Building Blocks. *Small* **2007,** *3* (2), 190-4.
[196] (a) Gutzler, R.; Lappe, S.; Mahata, K.; Schmittel, M.; Heckl, W. M.; Lackinger, M. Aromatic Interaction Vs. Hydrogen Bonding in Self-Assembly at the Liquid-Solid Interface. *Chemical Communications* **2009,** (6), 680-2; (b) Song, W.; Martsinovich, N.; Heckl, W. M.; Lackinger, M. Born-Haber Cycle for Monolayer Self-Assembly at the Liquid-Solid Interface: Assessing the Enthalpic Driving Force. *J Am Chem Soc* **2013,** *135* (39), 14854-62; (c) Gutzler, R.; Cardenas, L.; Rosei, F. Kinetics and Thermodynamics in Surface-Confined Molecular Self-Assembly. *Chemical Science* **2011,** *2* (12), 2290.
[197] (a) Dri, C.; Peters, M. V.; Schwarz, J.; Hecht, S.; Grill, L. Spatial Periodicity in Molecular Switching. *Nat. Nanotechnol.* **2008,** *3* (11), 649-53; (b) Scheil, K.; Gopakumar, T. G.; Bahrenburg, J.; Temps, F.; Maurer, R. J.;

Reuter, K.; Berndt, R. Switching of an Azobenzene-Tripod Molecule on Ag(111). *J. Phys. Chem. Lett.* **2016,** *7* (11), 2080-4.
[198] Santos, J. J.; Toma, S. H.; Lalli, P. M.; Riccio, M. F.; Eberlin, M. N.; Toma, H. E.; Araki, K. Exploring the Coordination Chemistry of Isomerizable Terpyridine Derivatives for Successful Analyses of Cis and Trans Isomers by Travelling Wave Ion Mobility Mass Spectrometry. *Analyst* **2012,** *137* (17), 4045-51.
[199] *MS Modeling, v7.0.0.0* **2015,** *Accelrys Software Inc.: San Diego, CA*.
[200] Chai, J.-D.; Head-Gordon, M. Long-Range Corrected Hybrid Density Functionals with Damped Atom–Atom Dispersion Corrections. *Phys. Chem. Chem. Phys.* **2008,** *10* (44), 6615.
[201] Osella, S.; Narita, A.; Schwab, M. G.; Hernandez, Y.; Feng, X.; Müllen, K.; Beljonne, D. Graphene Nanoribbons as Low Band Gap Donor Materials for Organic Photovoltaics: Quantum Chemical Aided Design. *ACS Nano* **2012,** *6* (6), 5539-5548.
[202] Mayo, S. L.; Olafson, B. D.; Goddard, W. A. Dreiding: A Generic Force Field for Molecular Simulations. *J. Phys. Chem.* **1990,** *94* (26), 8897-8909.
[203] Gasteiger, J.; Marsili, M. A New Model for Calculating Atomic Charges in Molecules. *Tetrahedron Lett.* **1978,** *34*, 3181-3184.
[204] Bao, C.; Lu, R.; Jin, M.; Xue, P.; Tan, C.; Xu, T.; Liu, G.; Zhao, Y. Helical Stacking Tuned by Alkoxy Side Chains in Pi-Conjugated Triphenylbenzene Discotic Derivatives. *Chem. Eur. J.* **2006,** *12* (12), 3287-94.
[205] Wang, T. C.; Bury, W.; Gómez-Gualdrón, D. A.; Vermeuler, N. A.; Mondloch, J. E.; Deria, P.; Zhang, K.; Moghadam, P. Z.; Sarjeant, A. A.; Snurr, R. Q.; Stoddart, J. F.; Hupp, J. T.; Farha, O. K. Ultrahigh Surface Area Zirconium Mofs and Insights into the Applicability of the Bet Theory. *J. Am. Chem. Soc.* **2015,** *137* (10), 3585-3591.
[206] Yamaguchi, Y.; Ochi, T.; Miyamura, S.; Tanaka, T.; Kobayashi, S.; Wakamiya, T.; Matsubara, Y.; Yoshida, Z. Rigid Molecular Architectures That Comprise a 1,3,5-Trisubstituted Benzene Core and Three Oligoaryleneethynylene Arms: Light-Emitting Characteristics and Pi Conjugation between the Arms. *J. Am. Chem. Soc.* **2006,** *128* (14), 4504-5.
[207] Archut, A.; Vogtle, F.; De Cola, L.; Azzellini, G. C.; Balzani, V.; Ramanujam, P. S.; Berg, R. H. Azobenzene-Functionalized Cascade Molecules: Photoswitchable Supramolecular Systems. *Chem. Eur. J.* **1998,** *4* (4), 699-706.
[208] Gauglitz, G.; Hubig, S. Chemical Actinometry in the Uv by Azobenzene in Concentrated Solution: A Convenient Method. *J. Photochem.* **1985,** *30* (2), 121-125.
[209] Rau, H., In *Photochromism, Molecules and Systems* (Ed.: Dürr, H.; Bouas-Laurent, H.), Elsevier, Amsterdam, **1990**; chapter 4.
[210] Connors, K. A., *Chemical Kinetics: The Study of Reaction Rates in Solution*. (Ed.: Sons, J. W.), **1990**.
[211] Dokic, J.; Gothe, M.; Wirth, J.; Peters, M. V.; Schwarz, J.; Hecht, S.; Saalfrank, P. Quantum Chemical Investigation of Thermal Cis-to-Trans Isomerization of Azobenzene Derivatives: Substituent Effects, Solvent Effects, and Comparison to Experimental Data. *J. Phys. Chem. A* **2009,** *113* (24), 6763-73.
[212] (a) van Herpt, J. T.; Areephong, J.; Stuart, M. C.; Browne, W. R.; Feringa, B. L. Light-Controlled Formation of Vesicles and Supramolecular Organogels by a Cholesterol-Bearing Amphiphilic Molecular Switch. *Chem. Eur. J.* **2014,** *20* (6), 1737-42; (b) van Herpt, J. T.; Stuart, M. C.; Browne, W. R.; Feringa, B. L. A Dithienylethene-Based Rewritable Hydrogelator. *Chem. Eur. J.* **2014,** *20* (11), 3077-83.
[213] (a) Hunter, C. A.; Sarson, L. D. Azobenzene-Porphyrins. *Tetrahedron Lett.* **1996,** *37* (5), 699-702; (b) Reddy, D. R.; Maiya, B. G. A Molecular Photoswitch Based on an 'Axial-Bonding' Type Phosphorus(V) Porphyrin. *Chemical Communications* **2001,** (1), 117-118; (c) Peters, M. V.; Goddard, R.; Hecht, S. Synthesis and Characterization of Azobenzene-Confined Porphyrins. *J. Org. Chem.* **2006,** *71* (20), 7846-9.
[214] Kim, H. J.; Jang, J. H.; Choi, H.; Lee, T.; Ko, J.; Yoon, M.; Kim, H. J. Photoregulated Fluorescence Switching in Axially Coordinated Tin(Iv) Porphyrinic Dithienylethene. *Inorg. Chem.* **2008,** *47* (7), 2411-5.
[215] Williams, D. E.; Rietman, J. A.; Maier, J. M.; Tan, R.; Greytak, A. B.; Smith, M. D.; Krause, J. A.; Shustova, N. B. Energy Transfer on Demand: Photoswitch-Directed Behavior of Metal-Porphyrin Frameworks. *J. Am. Chem. Soc.* **2014,** *136* (34), 11886-9.
[216] (a) Baskin, J. S.; Yu, H. Z.; Zewail, A. H. Ultrafast Dynamics of Porphyrins in the Condensed Phase: I. Free Base Tetraphenylporphyrin. *J. Phys. Chem. A* **2002,** *106* (42), 9837-9844; (b) Yu, H. Z.; Baskin, J. S.; Zewail, A. H. Ultrafast Dynamics of Porphyrins in the Condensed Phase: Ii. Zinc Tetraphenylporphyrin. *J. Phys. Chem. A* **2002,** *106* (42), 9845-9854.
[217] Lindsey, J. S.; Hsu, H. C.; Schreiman, I. C. Synthesis of Tetraphenylporphyrins under Very Mild Conditions. *Tetrahedron Lett.* **1986,** *27* (41), 4969-4970.
[218] (a) Guerchais, V.; Ordronneau, L.; Le Bozec, H. Recent Developments in the Field of Metal Complexes Containing Photochromic Ligands: Modulation of Linear and Nonlinear Optical Properties. *Coord. Chem. Rev.* **2010,** *254* (21-22), 2533-2545; (b) Azenha, E. G.; Serra, A. C.; Pineiro, M.; Pereira, M. M.; de Melo, J. S.; Arnaut, L. G.; Formosinho, S. J.; Gonsalves, A. M. D. R. Heavy-Atom Effects on Metalloporphyrins and Polyhalogenated Porphyrins. *Chem. Phys.* **2002,** *280* (1-2), 177-190.
[219] (a) Reddy, D. R.; Maiya, B. G. Phosphorus(V) Porphyrin–Azoarene Conjugates: Synthesis, Spectroscopy, Cis–Trans Isomerization, and Photoswitching Function. *J. Phys. Chem. A* **2003,** *107* (32), 6326-6333; (b)

Osuka, A.; Fujikane, D.; Shinmori, H.; Kobatake, S.; Irie, M. Synthesis and Photoisomerization of Dithienylethene-Bridged Diporphyrins. *J. Org. Chem.* **2001,** *66* (11), 3913-23.

[220] Pineiro, M.; Carvalho, A. L.; Pereira, M. M.; Gonsalves, A. M. d. A. R.; Arnaut, L. G.; Formosinho, S. J. Photoacoustic Measurements of Porphyrin Triplet-State Quantum Yields and Singlet-Oxygen Efficiencies. *Chem. Eur. J.* **1998,** *4* (11), 2299-2307.

[221] Lebold, T. P.; Yeow, E. K.; Steer, R. P. Fluorescence Quenching of the S1 and S2 States of Zinc Meso-Tetrakis(4-Sulfonatophenyl)Porphyrin by Halide Ions. *Photochem. Photobiol. Sci.* **2004,** *3* (2), 160-6.

[222] (a) Higashiguchi, K.; Matsuda, K.; Irie, M. Photochromic Reaction of a Fused Dithienylethene: Multicolor Photochromism. *Angew. Chem., Int. Ed.* **2003,** *42* (30), 3537-40; (b) Higashiguchi, K.; Matsuda, K.; Tanifuji, N.; Irie, M. Full-Color Photochromism of a Fused Dithienylethene Trimer. *J. Am. Chem. Soc.* **2005,** *127* (25), 8922-3.

[223] (a) Norsten, T. B.; Branda, N. R. Photoregulation of Fluorescence in a Porphyrinic Dithienylethene Photochrome. *J. Am. Chem. Soc.* **2001,** *123* (8), 1784-5; (b) Norsten, T. B.; Branda, N. R. Axially Coordinated Porphyrinic Photochromes for Non-Destructive Information Processing. *Adv. Mater.* **2001,** *13* (5), 347-349.

[224] Ishida, H.; Bünzli, J.-C.; Beeby, A. Guidelines for Measurement of Luminescence Spectra and Quantum Yields of Inorganic and Organometallic Compounds in Solution and Solid State (Iupac Technical Report). *Pure Appl. Chem.* **2016,** *88* (7).

[225] (a) Lee, J. W.; Klajn, R. Dual-Responsive Nanoparticles That Aggregate under the Simultaneous Action of Light and Co2. *Chem. Commun.* **2015,** *51* (11), 2036-9; (b) Moldt, T.; Brete, D.; Przyrembel, D.; Das, S.; Goldman, J. R.; Kundu, P. K.; Gahl, C.; Klajn, R.; Weinelt, M. Tailoring the Properties of Surface-Immobilized Azobenzenes by Monolayer Dilution and Surface Curvature. *Langmuir* **2015,** *31* (3), 1048-57; (c) Udayabhaskararao, T.; Kundu, P. K.; Ahrens, J.; Klajn, R. Reversible Photoisomerization of Spiropyran on the Surfaces of Au25 Nanoclusters. *Chem. Phys. Chem.* **2016,** *17* (12), 1805-1809; (d) Raimondo, C.; Crivillers, N.; Reinders, F.; Sander, F.; Mayor, M.; Samori, P. Optically Switchable Organic Field-Effect Transistors Based on Photoresponsive Gold Nanoparticles Blended with Poly(3-Hexylthiophene). *Proc. Natl. Acad. Sci. USA* **2012,** *109* (31), 12375-80.

[226] (a) Li, Y.; Yu, D.; Dai, L.; Urbas, A.; Li, Q. Organo-Soluble Chiral Thiol-Monolayer-Protected Gold Nanorods. *Langmuir* **2011,** *27* (1), 98-103; (b) Xue, C.; Gutierrez-Cuevas, K.; Gao, M.; Urbas, A.; Li, Q. Photomodulated Self-Assembly of Hydrophobic Thiol Monolayer-Protected Gold Nanorods and Their Alignment in Thermotropic Liquid Crystal. *J. Phys. Chem. C* **2013,** *117* (41), 21603-21608; (c) Ouhenia-Ouadahi, K.; Yasukuni, R.; Yu, P.; Laurent, G.; Pavageau, C.; Grand, J.; Guerin, J.; Leaustic, A.; Felidj, N.; Aubard, J.; Nakatani, K.; Metivier, R. Photochromic-Fluorescent-Plasmonic Nanomaterials: Towards Integrated Three-Component Photoactive Hybrid Nanosystems. *Chem. Commun.* **2014,** *50* (55), 7299-302.

[227] Cao, J.; Wu, S.; Zhai, B.; Wang, Q.; Li, J.; Ma, X. Photo-Responsive Spiropyran Monolayer Protected Gold Nanorod. *Dyes Pigm.* **2014,** *103*, 89-94.

[228] Burrows, N. D.; Vartanian, A. M.; Abadeer, N. S.; Grzincic, E. M.; Jacob, L. M.; Lin, W.; Li, J.; Dennison, J. M.; Hinman, J. G.; Murphy, C. J. Anisotropic Nanoparticles and Anisotropic Surface Chemistry. *Journal of Physical Chemistry Letters* **2016,** *7* (4), 632-41.

[229] Berkovic, G.; Krongauz, V.; Weiss, V. Spiropyrans and Spirooxazines for Memories and Switches. *Chem. Rev.* **2000,** *100* (5), 1741-1754.

[230] Ivashenko, O.; van Herpt, J. T.; Feringa, B. L.; Rudolf, P.; Browne, W. R. Uv/Vis and Nir Light-Responsive Spiropyran Self-Assembled Monolayers. *Langmuir* **2013,** *29* (13), 4290-7.

[231] Nikoobakht, B.; El-Sayed, M. A. Preparation and Growth Mechanism of Gold Nanorods (Nrs) Using Seed-Mediated Growth Method. *Chem. Mater.* **2003,** *15* (10), 1957-1962.

[232] Jiang, G.; Hore, M. J.; Gam, S.; Composto, R. J. Gold Nanorods Dispersed in Homopolymer Films: Optical Properties Controlled by Self-Assembly and Percolation of Nanorods. *ACS Nano* **2012,** *6* (2), 1578-88.

[233] Jana, N. R.; Gearheart, L.; Murphy, C. J. Wet Chemical Synthesis of High Aspect Ratio Cylindrical Gold Nanorods. *J. Phys. Chem. B* **2001,** *105* (19), 4065-4067.

[234] (a) Nikoobakht, B.; El-Sayed, M. A. Evidence for Bilayer Assembly of Cationic Surfactants on the Surface of Gold Nanorods. *Langmuir* **2001,** *17* (20), 6368-6374; (b) Gomez-Grana, S.; Hubert, F.; Testard, F.; Guerrero-Martinez, A.; Grillo, I.; Liz-Marzan, L. M.; Spalla, O. Surfactant (Bi)Layers on Gold Nanorods. *Langmuir* **2012,** *28* (2), 1453-9.

[235] Funston, A. M.; Novo, C.; Davis, T. J.; Mulvaney, P. Plasmon Coupling of Gold Nanorods at Short Distances and in Different Geometries. *Nano Lett.* **2009,** *9* (4), 1651-1658.

[236] Nie, S.; Emory, S. R. Probing Single Molecules and Single Nanoparticles by Surface-Enhanced Raman Scattering. *Science* **1997,** *275* (5303), 1102-6.

[237] Zhu, M. Q.; Zhang, G. F.; Li, C.; Aldred, M. P.; Chang, E.; Drezek, R. A.; Li, A. D. Reversible Two-Photon Photoswitching and Two-Photon Imaging of Immunofunctionalized Nanoparticles Targeted to Cancer Cells. *J. Am. Chem. Soc.* **2011,** *133* (2), 365-72.

[238] Sivapalan, S. T.; Vella, J. H.; Yang, T. K.; Dalton, M. J.; Swiger, R. N.; Haley, J. E.; Cooper, T. M.; Urbas, A. M.; Tan, L. S.; Murphy, C. J. Plasmonic Enhancement of the Two Photon Absorption Cross Section of an Organic Chromophore Using Polyelectrolyte-Coated Gold Nanorods. *Langmuir* **2012,** *28* (24), 9147-54.

[239] (a) Fukaminato, T.; Doi, T.; Tamaoki, N.; Okuno, K.; Ishibashi, Y.; Miyasaka, H.; Irie, M. Single-Molecule Fluorescence Photoswitching of a Diarylethene-Perylenebisimide Dyad: Non-Destructive Fluorescence Readout. *J. Am. Chem. Soc.* **2011,** *133* (13), 4984-90; (b) Berberich, M.; Natali, M.; Spenst, P.; Chiorboli, C.; Scandola, F.; Wurthner, F. Nondestructive Photoluminescence Read-out by Intramolecular Electron Transfer in a Perylene Bisimide-Diarylethene Dyad. *Chem. Eur. J.* **2012,** *18* (43), 13651-64.

LIST OF ABBREVIATIONS

4,4'-BPE	1,2-bis(4-pyridyl)ethylene
ADC	Analog-to-digital converter
ATD	Arrival time distribution
AuNP	Gold nanoparticle
AuNR	Gold nanorod
AzDC	Azobenzene-4,4'-dicarboxylate
BSE	Backscattered electrons
CCD	Charge-coupled device
CCS	Collisional cross-section
CE	Chemical enhancement
CFD	Constant function discriminator
CL	Condenser lens
CMC	Critical micellar concentration
COF	Covalent organic framework
CTAB	Hexadecyltrimethylammonium bromide
CW	Continuous-wave (laser)
DAE	Diarylethene
DDA	Discrete dipole approximation
DFT	Density functional theory
DLS	Dynamic light scattering
DMSO	Dimethyl sulfoxide
DTE	Dithienylethene
DTIMMS	Drift tube ion-mobility mass spectrometry
EF	Enhancement factor
EM	Electromagnetic enhancement
ESEM	Environmental scanning electron microscopy
ESI	Electrospray ionisation
FEG	Field emission gun
FRET	Förster resonance energy transfer
FWHM	Full width at half maximum
H_2TPP	Free-base tetraphenylporphyrin
HOMO	Highest occupied molecular orbital
HOPG	Highly ordered pyrolytic graphite
HPLC	High performance liquid chromatography
IM	Ion mobility
IMMS	Ion mobility mass spectrometry
IRF	Instrument response function
KO*t*Bu	Potassium *tert*-butoxide
LbL	Layer-by-layer
LDOS	Local density of states
LED	Light emitting diode
LSPR	Longitudinal surface plasmon resonance (mode or band)
LUMO	Lowest unoccupied molecular orbital
MC	Merocyanine
MD	Molecular dynamics
MLCT	Metal-to-ligand charge transfer
MM	Molecular mechanics
MOF	Metal organic framework
MS	Mass spectrometry

NMR	Nuclear magnetic resonance
OL	Objective lens
OTFT	Organic thin film transistor
PBC	Periodic boundary conditions
PEG	Poly(ethylene glycol)
PGA	Programmable gain amplifier
phen	1,10-Phenantroline
PMI	Perylenemonoimide
PMT	Photomultiplier tube
PPD	Picosecond photon detection (module)
PSS	Photostationary state
rt	Room temperature
SAM	Self-assembled monolayer
SE	Secondary electron
SEM	Scanning electron microscopy
SERS	Surface-enhanced Raman scattering
SP	Spiropyran
SPR	(Localised) Surface plasmon resonance
STM	Scanning tunnelling microscopy
TAC	Time-to-amplitude converter
TCBPB	1,3,5-tris[4-carboxy(1,1'-biphenyl-4-yl)]benzene
TCDB	1,3,5-tris(10-carboxydecyloxy)benzene
TCSPC	Time correlated single photon counting
TERS	Tip-enhanced Raman scattering
TFA	Trifluoroacetic acid
THF	Tetrahydrofuran
TLC	Thin layer chromatography
TOF	Time-of-flight
TPP	Tetraphenylporphyrin
TSPR	Transverse surface plasmon resonance (mode or band)
TWIMMS	Travelling wave ion mobility mass spectrometry
UHV	Ultrahigh vacuum
UPLC	Ultra performance liquid chromatography
WD	Window discriminator
ZnTPP	Zinc tetraphenylporphyrin

ACKNOWLEDGEMENTS

First and foremost, I wish to express my deepest gratitude to my advisor, Prof. Paolo Samorì for accepting me being part of his research team and for his supervision throughout these years. Working under his guidance has been an extremely exciting and formative experience that allowed me to open my eyes towards the research world and also to expand my scientific interests. I am grateful for his patient teaching and for the confidence and the freedom he gave me to chase my ideas, obviously very rarely leading to success at first attempt.

A word of gratitude goes also to the members of this PhD jury: Prof. De Feyter, Prof. Montalti and Prof. Hermans, for accepting to be referees and for the time they have dedicated to this thesis.

Very special thanks must go to the present and past colleagues in the Nanochemistry Group with whom I have shared these special years, for being source of inspiration, for their invaluable scientific and human support, for their help and encouragement or simply for the great time we spent together. Emanuele, Sara, Marco S., Matilde, Marco C., Marco G. and Marc-Antoine, Alessandro, Tim, Oliver, Simone, Thomas and Maria, Chang-Bo, Yifan, Rafael, Stefano D. B., Stefano C. and Stefano I., Lei, Nicolas, Lili, Mohamed, Artur I am indebted with you.

It has been an enormous privilege to take part of the Marie Skłodowska-Curie ITN network "iSwitch" coordinated by Prof. Paolo Samorì, which gave me the opportunity to travel around Europe and most importantly to meet fantastic people and brilliant colleagues.

I dedicate this thesis to my family and friends who always supported me throughout this challenge. As last in the list, the most important mention goes to you Caroline, for providing me energy, happiness and love. This would not have been possible without you.

PUBLICATIONS

- Exploring the Effect of Ligand Structural Isomerism in Langmuir-Blodgett Films of Chiral Luminescent Eu(III) Self-Assemblies. Galanti, A.; Kotova, O.; Blasco, S.; Johnson, C. J.; Peacock, R. D.; Mills, S.; Boland, J. J.; Albrecht, M.; Gunnlaugsson, T. *Chem. Eur. J. 22* (28), **2016**, 9709-23.
- Photoisomerisation and Light-Induced Morphological Switching of a Polyoxometalate-Azobenzene Hybrid. Markiewicz, G.; Pakulski, D.; Galanti, A.; Patroniak, V.; Ciesielski, A.; Stefankiewicz, A. R.; Samorì, P. *Chem. Commun. 53* (53), **2017**, 7278-7281.
- Fluorescence Commutation and Surface Photopatterning with Porphyrin Tetradithienylethene Switches. Biellmann, T.; Galanti, A.; Boixel, J.; Wytko, J. A.; Guerchais, V.; Samorì, P.; Weiss, J. *Chem. Eur. J. 24* (7), **2018**, 1631-1639.
- Electronic Decoupling in C_3-Symmetrical Light-Responsive Tris(Azobenzene) Scaffolds: Self-Assembly and Multiphotochromism. Galanti, A.; Diez-Cabanes, V.; Santoro, J.; Valášek, M.; Minoia, A.; Mayor, M.; Cornil, J.; Samorì, P. *J. Am. Chem. Soc.*, **2018**, *140*, 16062-16070.
- A new class of rigid multi(azobenzene) switches featuring electronic decoupling: unravelling the isomerization in the individual photochrome. Galanti, A.; Santoro, J.; Mannancherry, R.; Duez, Q.; Diez-Cabanes, V.; Valášek, M; De Winter, J.; Cornil, J; Gerbaux, P.; Mayor, M.; Samorì, P. *in preparation*.

CONFERENCE PRESENTATIONS

- « *Fabrication of Light Responsive Anisotropic Gold Nanocrystals Passivated by Photochromic Thiols* », A. Galanti, B. Zyska, S. Hecht, P. Samorì. *E-MRS Spring Meeting* – Strasbourg, 25/05/2017. Oral communication.
- « *Novel Conjugated Multi-Azobenzene Photochromic Rigid Systems* », A. Galanti, V. Diez-Cabanes, J. Santoro, M. Valášek, J. Cornil, M. Mayor, P. Samorì. *28th International Conference on Photochemistry (ICP 2017)* – Strasbourg, 18/07/2017. Oral communication.
- « *Fluorescence Switching in Tetra-Dithienylethene Porphyrin Scaffolds* », T. Biellmann, A. Galanti, J. Boixel, J. A. Wytko, V. Guerchais, P. Samorì, J. Weiss. *12th Phenics International Network Symposium* – Strasbourg, 21/07/2017. Oral communication.
- « *Novel Star-Shaped Azobenzene Systems: an Insight into their Multi-Photochromism and Self-Assembly Properties* », A. Galanti, V. Diez-Cabanes, J. Santoro, Q. Duez, J. De Winter, M. Valášek, P. Gerbaux, J. Cornil, M. Mayor, P. Samorì. *Minisymposium "Complex molecular systems towards adaptive materials"* – Strasbourg, 21/06/2018. Oral communication.

Agostino GALANTI

Multi-Photochromic Architectures: from Structure to Function

Résumé

L'objectif de cette thèse a été axé sur le développement des systèmes capable de répondre à des stimuli externes, basés sur des unités photochromiques. Le but d'une telle quête est d'augmenter la complexité des dispositifs et des machines moléculaires synthétiques. Avec l'objectif de développer des dispositifs et des machines artificiels plus complexes, nous avons réalisé de systèmes comprenant de multiples interrupteurs moléculaires. En vue de la réalisation de cette thèse, des nouveaux systèmes multi-photochromiques, où hybrides photochrome/nanomatériaux contenant des fragments azobenzène, diaryléthène ou spiropyrane ont été réalisés et étudiés. D'abord, on s'est focalisés sur des systèmes multi-azobenzènes capables de subir de grands réarrangements géométriques lors de la photoisomérisation, ils pourraient être utilisés à l'avenir comme éléments constitutifs des matériaux *host-guest* ou *metal-organic frameworks* contrôlables par des stimuli lumineux. Dans un second exemple, des commutateurs photochromiques de type dithiényléthène ont été utilisés pour déclencher l'émission d'une porphyrine. Cette dyade à montré une modulation réversible de son émission, affichant un contraste particulièrement élevé. Comme dernier exemple, un dérivé de spiropyrane a été combiné avec des nanoparticules d'or anisotropes. En induisant l'isomérisation de l'interrupteur moléculaire dans les dispersions colloïdales des nanorods d'or en liquide, nous avons visualisé une grande variation du spectre d'extinction des colloïdes, dépendante de la longueur d'onde du mode LSPR et du recouvrement spectrale avec le *photoswitch*.

Mots-clés: multi-photochromic, in-situ photoswitching, interfaces, scanning tunnelling microscopy, self-assembly, gold nanorods, fluorescence photoswitching

Résumé en anglais

The aim of this thesis has been to develop systems capable of responding to external stimuli, based on photochromic units. The goal of such a quest is to increase the complexity of devices and synthetic molecular machines. With the goal of developing more complex artificial devices and machines, we have realised systems containing multiple molecular switches. For the realisation of this thesis, new multi-photochromic systems, or photochromes/nanomaterials hybrids containing azobenzene, diarylethene or spiropyran moieties have been realised and studied. Firstly, we focused on multi-azobenzene systems capable of undergoing large geometric rearrangements during photoisomerisation, as they may be used in the future as constituent elements of host-guest or metal-organic frameworks controllable by luminous stimuli. In a second example, dithienylethene-type photochromic switches have been used to trigger the emission of a porphyrin. This dyad exhibited a reversible modulation of its emission, displaying a particularly highly contrasted response. As a final example, a spiropyran derivative has been combined with anisotropic gold nanoparticles. By inducing the isomerisation of the molecular switch in the AuNR colloidal liquid dispersions, we visualised a large variation of the colloid extinction spectrum, dependent on the LSPR mode wavelength and the spectral overlap with the photoswitch.